



University of  
**Nottingham**  
UK | CHINA | MALAYSIA

Awaji, Safhi (2020) A New 3D Printing-Based Approach to Understand Drug Release Mechanisms from Amorphous Solid Dispersion Tablets. PhD thesis, University of Nottingham.

**Access from the University of Nottingham repository:**

**Copyright and reuse:**

The Nottingham ePrints service makes this work by researchers of the University of Nottingham available open access under the following conditions.

This article is made available under the University of Nottingham End User licence and may be reused according to the conditions of the licence. For more details see:

For more information, please contact [eprints@nottingham.ac.uk](mailto:eprints@nottingham.ac.uk)

**A New 3D Printing-Based Approach to Understand Drug  
Release Mechanisms from Amorphous Solid Dispersion  
Tablets. PhD thesis, University of Nottingham.**

School of Pharmacy

Division of Molecular Therapeutics and Formulations

**Awaji Yahya Safhi**

BSc, MSc in Pharmaceutical Sciences

**Thesis submitted to the University of Nottingham  
for the degree of Doctor of Philosophy**

## **Acknowledgements**

I would like to express my very great appreciation for my main supervisor, Dr Jonathan Burley, Assistant Professor in Pharmaceutical Nanotechnology, Faculty of Science, for allowing me to undertake this work and for his valuable and constructive suggestions during the planning and development of this research. Additionally, I am grateful for his enthusiastic encouragement and help in coordinating my project, especially in writing this report. Moreover, the time he provided to me so generously is very much appreciated.

Furthermore, I would also like to express my deep appreciation for my supervisor, Prof Clive Roberts, Chair of Pharmaceutical Nanotechnology, Head of School, for his continuous guidance, advices, and valuable suggestions throughout the research.

I would like to extend a special vote of thanks to Dr Vincenzo Taresco, Research Fellow, Faculty of Science, Dr Salah Abdelrazig, Mass Spectrometry Research officer, Faculty of Science, and Dr Martin Corfield, Research Fellow, Faculty of Engineering, for their advice on and assistance in keeping my progress on schedule. Also, the advice given by Dr Gilon Hagit is greatly appreciated.

I would also like to extend my thanks to the technicians of the laboratory, Mr Paul Cooling, Mr Thomas Booth, and Mrs Esme, for their valuable advices, training, and assistance during the lab work. Also, I would like to express my gratitude to my colleagues in the D19 office, BSB, Mohammad Alnatour, Wathiq Alhashmi, Waleed Rizg, Mohammed

Alissa, Ayman Mohammed, and Vijender, for their help and support on this work.

I would also like to express my sincere appreciation towards my family members, especially my mother, Rana Safhi, who always looked after me and supported me throughout my study. My wife, Afnan, and my daughter, Lana, are always with me and encourage me, especially during my study in the UK. I also thank my brothers and sisters for their inspiration and support.

Finally, I would like to express my gratitude to Jazan University and the department of Pharmaceutics for providing me with the opportunity to pursue my higher education in the UK. I would also like to thank the Saudi Arabia Cultural Bureau in London for their unlimited support.

## Declaration

I hereby declare that this thesis titled, *a new 3D printing-based approach to understand drug release mechanisms from amorphous solid dispersion tablets*, and the work presented in it is the result of my own work conducted at the University of Nottingham between February 2017 and June 2020, with the guidance of my supervisors Dr Jonathan Burley and Professor Clive Roberts. No part of my work has been submitted for any other degree at the university of Nottingham or any other institution. The source is always given when I quoted from the work of others. Help from others is acknowledged as appropriate.

Signed:

---

Date

---

## **Abstract**

Amorphous solid dispersions (ASDs) can be a successful approach to improve the apparent solubility and hence the bioavailability of poorly water-soluble drugs, specifically BCS class II ingredients. However, it has been reported that an increase in active pharmaceutical ingredient (API) loading can lead to a decrease in the API release rate from the formulation, due to recrystallisation *in vitro/vivo*, often driven by crystalline seeds in random locations in formulation. Up to now, it has been difficult to fabricate ASD tablets with controlled distribution of crystalline seeds in various positions of the formulation to study the release of APIs, because conventional tableting methods do not easily afford precise spatial control of these impurities during tablet manufacturing. Consequently, fabrication of such solid dosage forms spiked with crystalline impurities may be possible by employing three-dimensional (3D) printing technologies due to their ability to control numerous parameters during the printing process.

Therefore, we aim to investigate the dissolution behaviour of the API from ASD tablets by fabricating two basic ASD model tablets (pure ASD and spiked) by employing one of the 3D printing techniques in which the effect of spatial location of crystal seeds can be systematically controlled and evaluated to understand drug release mechanisms from such type of dosage forms and offer recommendations.

The present thesis investigates the dissolution behaviour of two basic ASD model tablets i.e. pure ASD and amorphous tablets spiked with

crystalline seeds, which is a tablet manufactured as compartment with an outer shell (amorphous or spiked) and an inner core (amorphous or spiked), fabricated utilising fused deposition modelling (FDM) 3D printing technique. A well-documented low water-soluble drug i.e., felodipine (FELD) was selected once and used as a model drug throughout the present thesis. Also, polyvinyl alcohol (PVA), which is one of the most commonly used thermoplastic polymers with the FDM 3D printer, was selected as the main polymer with which to fabricate the two basic ASD formulations. The steps that were taken towards fabricating the model tablets were detailed in chapter 3, 4, and 5. Starting in chapter 3 by predicting the miscibility of FELD with two polymers, namely PVA, and Soluplus®, utilising the Flory-Huggins theory and the melting point depression approach (dissolution endpoint) to select the drug loadings which then used to manufacture the printer feedstocks utilising hot melt extruder (HME). For the FELD-PVA system the miscibility was calculated for the first time in the present work. The FELD has shown complete miscibility with both polymers, PVA and Soluplus®, for all the drug-polymer compositions (5%- 75%) at temperatures above 140°C. In contrast, The FELD was predicted to be miscible with both polymers for drug loadings lower than 10% (w/w) at room temperature. Moreover, the composition phase diagrams for both systems, FELD-PVA and FELD-Soluplus®, were successfully constructed. Accordingly, different drug loadings, including 10% (metastable zone), and 50% (unstable zone), were selected for the formulation of the FDM 3D printer feedstocks and model tablets in chapter 4.

In chapter 4, the selected drug loadings were successfully used to manufacture the FDM 3D printer feedstocks utilising HME. It was possible to fabricate the pure ASD model tablets with different geometries utilising the FDM 3D printer due to the high temperature (above 160°C) used during both process, the formulation of the printer feedstocks using HME and fabrication of the model tablets utilising the FDM 3D printer. In contrast, it was challenging to manufacture spiked model tablets with controlled spatial distribution of crystalline seeds during the model tablets fabrication process. Thus, relative humidity (RH) storage conditions were used as an approach to achieve equilibrium (crystallinity) in the manufactured materials in order to fabricate the spiked model tablets.

In chapter 5, we successfully manufactured the FDM 3D printer drug loaded feedstock utilising HME. Then, the manufactured printer feedstock was used to fabricate different compartment model tablets i.e., fresh shell- fresh core (control), fresh shell- aged core, aged shell- fresh core, and aged shell- aged core (control), utilising the FDM 3D printer and 75% humidity. The crystallinity % of the FELD in the spiked models, fresh shell-aged core, aged shell- fresh core, and aged shell- aged core, was quantified using DSC and found to be about 6%. The spiked model tablets were fabricated for the first time in the present work. The dissolution performance of the different model tablets was investigated utilising USP dissolution apparatus I (basket). The FELD release from the fabricated formulations has shown a sustained release (SR) for a period of 10 hours in two pH media, pH 2 and pH 6.8. In both media, the

observed dissolution of the FELD from the fabricated model tablets was ranked as fresh shell-fresh core > fresh shell-aged core > aged shell-fresh core > aged shell-aged core. The obtained dissolution profiles from the utilised spiked formulations suggested that the model tablets fabricated with a fresh shell-aged core have shown drug release close to that obtained from the model tablets fabricated as a pure amorphous tablet. Accordingly, this result suggests that the fresh outer shell of the fabricated model tablets may have dissolved, and the release was predominantly controlled by the outer shell rather than the spiked inner core. In contrast, the obtained dissolution of the aged shell-fresh core model tablets has shown FELD drug release close to that obtained for the control fabricated as aged shell-aged core model tablets, which suggests that the drug release was predominantly controlled by the spiked outer shell rather than the fresh inner core due to the induced crystallinity in the outer shell with time.

The FDM 3D printing technique is promising as a fabrication process to build better ASD test model tablets with controlled spatial distribution and amount of crystalline seeds than the conventional tableting method in order to investigate why ASD tablets fail dissolution testing. Following this work, the FDM 3D printing technique can be considered for future development of ASD tablets in the industry to build model tablets with defined amount and location of crystalline seeds to understand the dissolution behaviour from these formulations.

# Table of Contents

Acknowledgements .....	II
Declaration.....	IV
Abstract.....	V
Table of Contents .....	IX
List of Figures.....	XVII
List of Tables.....	XXIV
List of Abbreviation .....	XXVI
1. Chapter 1: Introduction .....	1
1.1. Poorly Soluble Active Pharmaceutical Ingredients (APIs) .....	1
1.2. Biopharmaceutical Classification System (BCS) and the Developability Classification System (DCS) .....	2
1.3. Solubility and Dissolution Rate .....	5
1.4. Strategies to Overcome Problems of Poorly-Water Soluble Active Pharmaceutical Ingredients .....	7
1.4.1. Salt Formation .....	7
1.4.2. Pro-drugs .....	8
1.4.3. Particle Size Reduction.....	8
1.4.4. Cyclodextrins .....	9
1.4.5. Amorphisation and Amorphous Solid Dispersions (ASDs). 9	
1.5. Amorphous Materials .....	10
1.5.1. Formation and Physical Stability of the Amorphous Form	10

1.6.	Amorphous Solid Dispersions (ASDs).....	12
1.6.1.	Common Polymers Utilised to Formulate ASDs .....	13
1.6.2.	Manufacturing of Amorphous Solid Dispersions .....	14
1.6.2.1.	Hot Melt Extrusion (HME).....	15
1.6.2.2.	Spray Drying.....	16
1.6.3.	Physical Stability of ASDs.....	17
1.6.4.	Mechanisms of Drug Release from Polymeric Matrix Devices.....	18
1.6.4.1.	Swelling.....	19
1.6.4.2.	Diffusion .....	20
1.6.4.3.	Erosion .....	20
1.6.4.4.	Osmosis .....	21
1.6.5.	Possible Failure Modes in ASDs.....	22
1.7.	Three-Dimensional (3D) Printing Techniques.....	28
1.7.1.	Applications of 3D Printing Techniques in Different Fields.....	30
1.7.2.	3D Printing for Commercial Pharmaceutical Products .....	31
1.7.3.	The Recent Technologies in 3D Printing.....	32
1.7.3.1.	Stereolithography (SLA) .....	33
1.7.3.2.	Fused Deposition Modelling (FDM).....	33
1.7.3.3.	Selective Laser Sintering (SLS).....	35
1.7.3.4.	Inkjet 3D Printing Technology (IJ) .....	36
1.7.3.5.	Extrusion Based 3D Printing Techniques.....	37

1.7.4.	3D Printing Techniques Versus Conventional Tablet Production.....	37
1.8.	Aims and Objectives.....	39
2.	Chapter 2: Materials and Experimental Techniques.....	42
2.1.	Materials.....	42
2.1.1.	Active Ingredient Used in this Project .....	43
2.1.1.1.	Felodipine (FELD) .....	43
2.1.2.	Carriers used in this Project.....	44
2.1.2.1.	Polyvinyl alcohol (PVA) .....	44
2.1.2.2.	Soluplus®.....	45
2.2.	Experimental Techniques.....	46
2.2.1.	Manufacturing of the Drug-Loaded Filaments.....	46
2.2.1.1.	Hot Melt Extruder (HME) .....	46
2.2.2.	Fabrication of the Drug-Loaded Model Tablets.....	48
2.2.2.1.	Fused Deposition Modeling (FDM).....	48
2.2.3.	Characterisation Techniques .....	49
2.2.3.1.	Scanning Electron Microscopy (SEM) .....	49
2.2.3.2.	Differential Scanning Calorimetry (DSC) .....	52
2.2.3.3.	Raman Spectroscopy .....	55
2.2.3.4.	Attenuated Total Reflectance-Fourier Transformed Infrared Spectroscopy (ATR-FTIR) .....	59
2.2.3.5.	X-Ray Powder Diffractometer (XRPD) .....	61
2.2.4.	In-Vitro Drug Release Study .....	64
2.2.4.1.	In-Vitro US Pharmacopoeia Dissolution Apparatus ...	64

3.	Chapter 3: Utilising the Flory-Huggins Theory to Predict Felodipine Miscibility in Polyvinyl Alcohol (PVA) and Soluplus® .....	68
3.0.	Novelty in this Chapter .....	68
3.1.	Introduction.....	68
3.2.	Aims and Objectives.....	72
3.3.	Materials and Methods .....	73
3.3.1.	Materials .....	73
3.3.2.	Methods.....	73
3.3.2.1.	Physical Preparation of Different Drug-Polymer Compositions.....	73
3.3.2.2.	Melting Point Depression (MPD) .....	73
3.3.2.3.	T <sub>g</sub> Measurements of Different Drug-Polymer Mixtures.....	74
3.3.2.4.	Determination of Gibb's Free Energy of Mixing.....	75
3.3.2.5.	Determination of the F-H Interaction Parameter- $\chi$ .....	76
3.3.2.6.	Construction of Composition Phase Diagram.....	79
3.4.	Results and Discussion .....	81
3.4.1.	Drug-Polymer Miscibility Utilising Solubility Parameters Approach.....	81
3.4.2.	Thermal Analysis .....	83
3.4.3.	F-H Interaction Parameter $\chi$ and Gibb's Free Energy of Mixing.....	86
3.4.4.	Extrapolation of the F-H Interaction Parameter $\chi$ .....	91
3.4.5.	Determination of Miscibility .....	97

3.4.6.	Construction of the Compositions Phase Diagram .....	101
3.5.	Conclusion.....	104
4.	Chapter 4: Formulation of Felodipine-Polyvinyl Alcohol Printer Feedstocks and Model Tablets Fabrication.....	106
4.0.	Novelty in this Chapter .....	106
4.1.	Introduction.....	106
4.2.	Aims and Objectives.....	109
4.3.	Materials and Methods .....	110
4.3.1.	Materials .....	110
4.3.2.	Methods.....	110
4.3.2.1.	Formulation of Different FELD-PVA Loaded Filaments.....	110
4.3.2.2.	Fabrication of the Model Tablets .....	111
4.3.2.3.	Characterisation Techniques.....	114
4.3.2.3.1.	Scanning Electron Microscopy (SEM).....	114
4.3.2.3.2.	Measurements .....	114
4.3.2.3.3.	Differential Scanning Calorimetry (DSC).....	115
4.3.2.3.4.	Attenuated Total Reflectance- Fourier Transform Infra-Red Spectroscopy (ATR-FTIR) .....	115
4.3.2.3.5.	Raman Spectroscopy .....	115
4.3.2.3.6.	X-Ray Powder Diffractometer (XRPD) .....	116
4.3.2.4.	Stability Study.....	116
4.4.	Results and Discussion .....	118

4.4.1.	Fabricated Drug-Free Model Tablets .....	118
4.4.2.	Manufactured Drug Loaded Filaments and Fabricated FELD-PVA Model Tablets .....	121
4.4.3.	Morphological Observations, and Measurements of the Manufactured Filaments and 3D Fabricated Model Tablets.....	127
4.4.4.	Thermal Analysis of FELD-PVA Filaments and 3D Printed Model Tablets Utilising DSC .....	138
4.4.5.	FTIR Spectra of Prepared Filaments and 3D Printed Tablets.....	142
4.4.5.1.	FTIR Spectra of Prepared Filaments.....	142
4.4.5.2.	FTIR Spectra of 3D Fabricated Model Tablets .....	143
4.4.6.	Raman Spectra of the Raw Materials and the Fabricated FELD-PVA Model Tablets .....	147
4.4.7.	XRPD Patterns of the Raw Materials and Fabricated Model Tablets.....	151
4.4.8.	Stability Study .....	153
4.5.	Conclusion.....	155
5.	Chapter 5: In-Vitro Study to Investigate Drug Release from 3D Fabricated Model Tablets.....	157
5.0.	Novelty in this Chapter .....	157
5.1.	Introduction.....	157
5.1.1.	Drug Release Kinetics .....	159
5.1.1.1.	Zero-Order .....	160

5.1.1.2.	First-Order .....	160
5.1.1.3.	Higuchi Model.....	161
5.1.1.4.	Korsmeyer-Peppas Model.....	162
5.2.	Aims and Objectives.....	163
5.3.	Materials and Methods .....	164
5.3.1.	Materials .....	164
5.3.2.	Methods .....	164
5.3.2.1.	Fabrication of FELD-PVA Model Tablets Employing FDM 3D Printer.....	164
5.3.2.2.	Characterisation of Aged Samples .....	167
5.3.2.2.1.	FTIR .....	167
5.3.2.2.2.	Raman Spectroscopy .....	167
5.3.2.2.3.	X-Ray Powder Diffractometer (XRPD) .....	167
5.3.2.3.	Quantification of Crystallinity Utilising DSC .....	167
5.3.2.4.	In-Vitro Drug Release Studies .....	167
5.3.2.4.1.	Stock Solution and Sample Preparation.....	167
5.3.2.4.2.	Determination of FELD Absorbance Wavelength.....	168
5.3.2.4.3.	Investigating Drug Release Utilising USP Apparatus.....	168
5.3.2.5.	X-Ray Micro Computed Tomography (X $\mu$ CT) .....	169
5.4.	Results and discussion.....	170
5.4.1.	Manufactured Drug Loaded Filaments and Fabricated Model Tablets .....	170
5.4.2.	Characterisation of Aged Samples.....	173

5.4.2.1.	FTIR Spectra .....	173
5.4.2.2.	Raman Spectra .....	176
5.4.2.3.	XRPD Patterns .....	180
5.4.3.	Quantification of Crystallinity.....	182
5.4.4.	Preliminary In-vitro Drug Release .....	186
5.4.4.1.	X $\mu$ CT of the Fabricated Model Tablets.....	191
5.4.4.2.	Modification of the Model Tablets.....	192
5.4.4.3.	X $\mu$ CT of the Modified Model Tablets .....	193
5.4.5.	In-vitro Drug Release of Modified Model Tablets .....	194
5.4.5.1.	Drug Release Kinetics.....	198
5.5.	Conclusion.....	200
6.	Chapter 6: Conclusion and Future Work .....	202
6.1.	Conclusion.....	202
6.2.	Future Work.....	206
7.	References .....	208
8.	Appendix .....	226

## List of Figures

<b>Figure 1.1.</b> Biopharmaceutics Classification System (BCS) . . . . .	3
<b>Figure 1.2.</b> BCS modification for more realistic fluid volumes available in the GI tract and the compensatory nature of permeability on low solubility (alterations from the BCS to DCS are shown in red). Figure adapted from- [9]. . . . .	5
<b>Figure 1.3.</b> A schematic of free-energy temperature phase diagram...11	
<b>Figure 1.4.</b> Recrystallisation of the API from ASD tablet during the dissolution process . . . . .	24
<b>Figure 1.5.</b> Different applications of 3D printing techniques in medicine . . . . .	30
<b>Figure 1.6.</b> Images of 3D fabricated tablets loaded with (A) paracetamol and (B) 4-ASA. From top to bottom: tablets containing 35% PEGDA, 65% PEG300, 65% PEGDA, 35% PEG300, 90% PEGDA, and 10% PEG300 . . . . .	31
<b>Figure 1.7.</b> The basic principle of the stereolithography apparatus.....33	
<b>Figure 1.8.</b> Schematic diagram of the FDM 3D printer working principles. . . . .	34
<b>Figure 1.9.</b> Schematic diagram of the SLS 3D printer..... 36	
<b>Figure 2.1.</b> Chemical structure of felodipine. . . . .	44
<b>Figure 2.2.</b> Chemical structure of PVA..... 45	
<b>Figure 2.3.</b> Soluplus® chemical structure. . . . .	46
<b>Figure 2.4.</b> Single screw extruder instrument, a) Schematic diagram of the HME components, b) photographic image of the Noztek single screw HME utilised in the current thesis. . . . .	48

<b>Figure 2.5.</b> A photographic image (left) and a schematic diagram (right) of the Ultimaker <sup>2+</sup> FDM 3D printer. ....	49
<b>Figure 2.6.</b> A schematic diagram of the SEM components (a), and a photographic images of the Scanning Electron Microscope (SEM) and display system (b). The figure was adapted from [170]. ....	51
<b>Figure 2.7.</b> Schematic diagram of the DSC principles (a), Photographic images of the discovery DSC, cooling unit, and the TRIOS software interface (b). ....	54
<b>Figure 2.8.</b> Schematic representations of the Raman and Rayleigh scattering processes: (a) Rayleigh scattering, (b) Stokes Raman scattering, and (c) Anti-Stokes Raman scattering. The figure was inspired from [178]. ....	57
<b>Figure 2.9.</b> Photographic image of the Raman instrument (confocal Horiba-Jobin-Yvon LabRAM system). ....	58
<b>Figure 2.10.</b> Photograph image of the ATR-FTIR (Agilent Cary 360 FTIR), and schematic diagram of the ATR-FTIR principles. ....	61
<b>Figure 2.11.</b> Schematic diagrams of the essential components of the XRPD. The figure was inspired from [170]. ....	62
<b>Figure 2.12.</b> Photographic image of a dissolution apparatus (Dis8000, Copley Scientific Limited, UK). ....	66
<b>Figure 3.1.</b> DSC thermograms of FELD-PVA mixtures prepared using different drug loadings, from top to bottom (crystalline FELD, 75%, 50%, 35%, 25%, 20%, 10%, 5% FELD-PVA w/w %). (Endo Up in the thermogram). ....	83

**Figure 3.2.** DSC thermograms of FELD-Soluplus® mixtures prepared using different drug loadings, from top to bottom (crystalline FELD, 75%, 50%, 35%, 25%, and 20% FELD-Soluplus® w/w %). Area in the box is the magnification of the melting endotherm of the 20% (FELD-Soluplus® w/w). (Endo Up in the thermogram). ..... 84

**Figure 3.3.** Flory-Huggins interaction plot utilised to determine the F-H interaction parameter  $\chi$  values for the FELD-PVA system (a) and the FELD-Soluplus® system (b) utilising equation 3.5 ( $n=1$ ). ..... 86

**Figure 3.4.** Alteration of the F-H interaction parameter  $\chi$  as a function of temperature for FELD-PVA and FELD-Soluplus® systems. The linear line represents the best experimental data fit to equation (3.6). ..... 91

**Figure 3.5.** A plot of  $\Delta G_{\text{mix}}/RT$  as a function of the FELD volume fraction for FELD-PVA and FELD-Soluplus® systems. The open symbols show data calculated using the interaction parameter  $\chi$  obtained from MPD method (**Table 3.6,  $\chi^a$** ), while the filled symbols show data using the interaction parameter  $\chi$  obtained from equation (3.6) at 140°C (**Table-3.6,  $\chi^b$** )..... 94

**Figure 3.6.** A plot of  $\Delta G_{\text{mix}}/RT$  as a function of the FELD volume fraction for a) FELD-PVA and b) FELD-Soluplus® systems at different temperatures (25, 50, 80, 100, 120, and 140 °C). ..... 97

**Figure 3.7.** Binary phase diagram of, a) FELD-PVA system, and b) FELD-Soluplus® system. .... 101

**Figure 4.1.** Schematic illustration of the different tablet designs with different dimensions utilised in this chapter to fabricate different drug-free and drug-loaded model tablets. a, b, c, and d used to fabricate

drug-free tablets, while e, f, g, h utilised to fabricate drug-loaded tablets.  
 ..... 112

**Figure 4.2.** Photographic images represent the morphology of the 3D printed tablets with plain PVA and PLA filaments using Ultimaker <sup>2+</sup> FDM 3D printer. .... 118

**Figure 4.3.** (a, b, and c) are photographic images of the manufactured drug-loaded filaments using HME, while d, e, f, g and h) are photographic images of the fabricated FELD-PVA model tablets utilising the FDM 3D printer. .... 122

**Figure 4.4.** SEM images of the fabricated PLA drug free tablet utilising the Ultimaker 2+ FDM 3D printer, a), and b) are the images of the tablet surface, while c), and d) are the images of the tablet the inner layers, and e) is the image of the tablet outer layers..... 127

**Figure 4.5.** SEM images of the fabricated PVA drug free tablets utilising the Ultimaker <sup>2+</sup> FDM 3D printer after optimisation of the printing parameters. a), and b) are the images of the tablet surface, while c), and d) are the images of the tablet inner layers, and e) is the image of the tablet outer layers. .... 128

**Figure 4.6.** a) SEM images of the fabricated FELD-PVA filament after the extrusion process using the HME, and b) SEM images of the FELD-PVA filament after being extruded through the FDM 3D printer nozzle.  
 ..... 133

**Figure 4.7.** SEM images of the pre-optimised fabricated FELD-PVA model tablet. a), b), c), and d) are the images of the tablet surface, while e) is the image of the tablet outer layers. .... 135

<b>Figure 4.8.</b> SEM images of the post-optimised FELD-PVA model tablets fabricated using the FDM 3D printer. a), and b) are the images of the tablet surface, while c), and d) are the images of the tablet outer layers.....	136
<b>Figure 4.9.</b> DSC thermograms of the first and the second heating cycles of FELD, 10%, and 25% (w/w) 3D printed model tablets and manufactured filaments. (Endotherm upward in the thermogram).....	140
<b>Figure 4.10.</b> FTIR spectra of the crystalline FELD, quenched cooled FELD, FELD-PVA physical mixture, FELD-PVA extrudates of 25%, and 10% drug-loading respectively, and PVA. ....	142
<b>Figure 4.11.</b> FTIR spectra of the crystalline FELD, quenched cooled FELD, FELD-PVA physical mixture, 3D printed model tablets of 25%, and 10% drug-loading respectively, and PVA. ....	143
<b>Figure 4.12.</b> Raman spectra of the crystalline FELD, FELD-PVA physical mixture, quench cooled FELD, fabricated model tablets, and PVA in the molecular-region ( $1100-1750\text{ cm}^{-1}$ ).....	147
<b>Figure 4.13.</b> Raman spectra of the crystalline FELD, FELD-PVA physical mixture, quench cooled FELD, fabricated model tablets, and PVA in the phonon region ( $50-450\text{ cm}^{-1}$ ). ....	148
<b>Figure 4.14.</b> XRPD patterns of the crystalline FELD, PVA, FELD-PVA physical mixture, and freshly fabricated model tablets (10%, and 25% w/w). ....	151
<b>Figure 4.15.</b> DSC thermograms of a) crystalline FELD (blue), FELD-PVA 25% physical mixture (red), and $T_g$ region ( $2^{\text{nd}}$ heating cycle) of the same samples, and b) DSC thermograms of the crystalline FELD	

(blue), and FELD-PVA 25% aged sample after seven days exposure to RH (red). (Endotherm upward in the thermogram). .....	153
<b>Figure 5.1.</b> Model tablet designs, a) control design, b) model tablets (formulations) outer shell and inner core designs. ....	164
<b>Figure 5.2.</b> Formulation steps of the FELD-PVA model tablets. ....	166
<b>Figure 5.3.</b> Photographic images of the prepared filament (a), FDM printing of the model tablets (b), one-part tablet (c), outer shell (d), and inner core (e). ....	170
<b>Figure 5.4.</b> Photographic images of the fabricated model tablets a) outer shell, and b) inner core, after seven days of storage in 75% RH. ....	171
<b>Figure 5.5.</b> FTIR spectra of the FELD as received, the quenched cooled FELD, the FDM 3D printed tablets (aged and freshly prepared), and FELD-PVA extrudate. ....	173
<b>Figure 5.6.</b> Raman spectra of the crystalline FELD, aged model tablet, quench cooled FELD, fresh tablet, and PVA in the molecular-region (1100-1750 $\text{cm}^{-1}$ ). ....	176
<b>Figure 5.7.</b> Raman spectra of the crystalline FELD, aged model tablet, quench cooled FELD, fresh tablet, and PVA in the phonon region (50-450 $\text{cm}^{-1}$ ). ....	177
<b>Figure 5.8.</b> XRPD patterns of the crystalline FELD, 25% aged and fresh tablets, and the PVA. (Black arrows indicate the main peaks appeared in the aged tablet in relative to the crystalline FELD).....	180

<b>Figure 5.9.</b> DSC thermogram of the FELD-PVA (25% w/w) fresh and aged tablets (red represents aged samples, and blue represents fresh samples) (n=3). .....	182
<b>Figure 5.10.</b> Photographic images of the 3D printed model tablets, a) 1, 2, 3, and 4, are the manufacturing steps of the fresh shell-aged core model tablet, while b) 1, 2, 3, and 4, are the manufacturing steps of the aged shell- fresh core model tablet.....	184
<b>Figure 5.11.</b> In-vitro cumulative drug release profiles of 3D fabricated (controls and formulations) model tablets in a) pH 2, and b) pH 6.8 (n=3). (Error bars represents standard deviation).....	186
<b>Figure 5.12.</b> A representative of X $\mu$ CT scan reconstructed 3D images of FELD-PVA 3D printed two-compartment model tablets.....	191
<b>Figure 5.13.</b> Modified model tablet designs (outer shell and inner core designs).....	192
<b>Figure 5.14.</b> X $\mu$ CT scan reconstructed 3D images of the modified 3D printed model tablets. ....	193
<b>Figure 5.15.</b> In-vitro cumulative drug release profiles of modified 3D fabricated model tablets in a) pH 2, and b) pH 6.8 (n=3). (Error bars represents standard deviation). ....	194
<b>Figure 5.16.</b> FELD release kinetics of fresh shell-fresh core control (blue), fresh shell-aged core (green), aged shell-fresh core (purple), and aged shell-aged core control (red), fitted to various models: a) Zero-order, b) First-order, c) Higuchi model, and d) Korsmeyer-Peppas. ...	198

## List of Tables

<b>Table 1.1.</b> Different examples of FDA-approved medicines manufactured as ASDs.....	14
<b>Table 1.2.</b> A summary for the fabrication of tablets using 3D printing in the pharmaceutical research.....	29
<b>Table 1.3.</b> A summary of commonly established 3D printing methods with advantages and disadvantages of each technique.....	32
<b>Table 2.1.</b> A summary of the applications, advantages, and disadvantages of XRPD in ASD characterisation.....	63
<b>Table 2.2.</b> Official dissolution apparatus types and their applications..	67
<b>Table 3.1.</b> Physical properties for FELD, PVA, and Soluplus®. ....	82
<b>Table 3.2.</b> Data used to estimate the F-H interaction parameter $\chi$ values for the FELD-PVA system. ....	89
<b>Table 3.3.</b> Data used to estimate the F-H interaction parameter $\chi$ values for the FELD-Soluplus® system. ....	90
<b>Table 3.4.</b> Data utilised to extrapolate $\chi$ for FELD-PVA system. ....	92
<b>Table 3.5.</b> Data used to extrapolate $\chi$ for FELD-Soluplus® system.....	93
<b>Table 3.6.</b> The F-H interaction parameter $\chi$ values obtained using MPD method and the $\chi$ values obtained using equation (3.6) at 140 °C. ....	93
<b>Table 3.7.</b> Determination of the A and B constants using the linear regression analysis of experimental DSC data and the interaction parameter $\chi$ , calculated using MPD approach and solubility parameters method at 25 °C. ....	96
<b>Table 3.8.</b> Predicted miscibility of the FELD-PVA and FELD-Soluplus® systems. ....	100

<b>Table 4.1.</b> Default and optimised printing parameters that have been utilised while fabricating the drug-free tablets.....	120
<b>Table 4.2.</b> The main parameters optimised for printing of the PVA tablets relate to the PLA tablets.....	121
<b>Table 4.3.</b> Temperatures and motor speed during the manufacturing process of different drug-loaded filaments.....	124
<b>Table 4.4.</b> The optimised parameters utilised while fabricating the drug-loaded (FELD-PVA) model tablets.....	125
<b>Table 4.5.</b> Represents the dimensions of the designed tablets and the dimensions of the model tablets after the printing process using the FDM 3D printer.....	131
<b>Table 4.6.</b> Dimensions of the designed and the 3D printed model tablets measured using electronic callipers before and after optimisation. ....	138
<b>Table 5.1.</b> R <sup>2</sup> drug release kinetics values obtained for all the formulations.....	199

## List of Abbreviation

<b>3D</b>	Three-Dimensional
<b>ATR-FTIR</b>	Attenuated Total Reflectance Fourier Transform Infrared Spectroscopy
<b>AM</b>	Additive Manufacturing
<b>API</b>	Active Pharmaceutical Ingredients
<b>ASDs</b>	Amorphous Solid Dispersions
<b>BSED</b>	Backscatter Electron Detector
<b>CAD</b>	Computer Aided Design
<b>CIJ</b>	Continuous Inkjet
<b>CR</b>	Controlled Release
<b>CRDDs</b>	Controlled Release Drug Delivery Systems
<b>CT</b>	Compressed Tablet
<b>DOD</b>	Drop on Demand
<b>DSC</b>	Differential Scanning Calorimetry
<b>ECT</b>	Enteric Coated Tablet
<b>ER</b>	Extend Release
<b>FDA</b>	Food and Drug Administration
<b>FDM</b>	Fused Deposition Modelling
<b>FELD</b>	Felodipine
<b>HME</b>	Hot Melt Extrusion
<b>HPMC</b>	Hydroxypropyl Methyl Cellulose
<b>HPMCAS</b>	Hydroxypropyl Methyl Cellulose Acetate Succinate
<b>HPMCP</b>	Hydroxypropyl Methyl Cellulose Phthalate
<b>HME</b>	Hot Melt Extruder
<b>IJ</b>	Inkjet

<b>IMC</b>	Indomethacin
<b>IR</b>	Immediate Release
<b>MCR</b>	Multi-Variate Curve Resolution
<b>MCT</b>	Multiple Compressed Tablet
<b>NCE</b>	New chemical entities
<b>ODT</b>	Orally Disintegrating Tablet
<b>PC</b>	Poly Carbonate
<b>PEG</b>	Polyethylene Glycol
<b>PEGDA</b>	Polyethylene Glycol Dicylate
<b>PLA</b>	Poly Lactic Acid
<b>PVA</b>	Polyvinyl alcohol
<b>PVAP</b>	Polyvinyl Acetate Phthalate
<b>PVC</b>	Chloride
<b>PVP</b>	Polyvinylpyrrolidone
<b>PVP/VA</b>	Polyvinylpyrrolidone/Vinyl Acetate
<b>PXRD</b>	Powder X-ray Diffractometer
<b>SCF</b>	Super Critical Fluid
<b>SD</b>	Solid Dispersion
<b>SLA</b>	Stereolithography
<b>SLS</b>	Selective Laser Sintering
<b>SR</b>	Sustained Release
<b>SEM</b>	Scanning Electron Microscopy
<b>SED</b>	Secondary Electron Detector

# 1. Chapter 1: Introduction

## 1.1. Poorly Soluble Active Pharmaceutical Ingredients (APIs)

The oral route remains the most favourable and frequently utilised route of drug delivery due to the high patient compliance, ease of administration, flexibility in the design of dosage form, and cost-effectiveness [1]. Conversely, inadequate bioavailability is the main challenge associated with the oral route of administration. There are different factors that can influence the oral bioavailability of the APIs, including the rate of dissolution, aqueous solubility, permeability of APIs, and first-pass metabolism. The most important factor to accomplish sufficient bioavailability and the desired pharmacological response for orally administered APIs, specifically low water-soluble ingredients, is the aqueous solubility [2]. The API molecule must go through different steps to reach the site of action with a sufficient quantity, such steps including the API should be dissolved in the gastrointestinal (GI) liquids, and then absorbed across the membrane of the GI into the systematic circulation. The absorption step is both dissolution rate and solubility limited for low water-soluble ingredients [2].

Unfortunately, the majority of the new chemical entities (NCE), about 80%-90%), developing from the pharmaceutical development pipelines (PDP) are characterised by poor solubility and limited dissolution profile and consequently may lead to low bioavailability [3]. As a result, the pharmaceutical industries need to generate new formulations to accomplish

the desired in-vivo efficacy as well as sufficient oral bioavailability [4]. Enhancing the concentration of the API in the GI fluids is one way to boost the bioavailability of the low water-soluble ingredients. Enhancing the water solubility, the rate of the dissolution, or a blend of both can lead to increasing the API concentration in the GI fluids. Changing the crystalline solids into amorphous is presented as an example to increase the dissolution characteristics of poorly water-soluble ingredients [5]. A crystalline material is characterised by three-dimensional long-range order, which is lost in the amorphous materials. Consequently, the API molecules energy barriers to go to into solution is reduced.

In order to understand the physicochemical and biopharmaceutical features of APIs, the APIs can be classified into four categories by the biopharmaceutics classification system (BCS) depending on the solubility (hydrophilic and hydrophobic drugs) and the permeability of the API in the gastrointestinal tract (GI).

## **1.2. Biopharmaceutical Classification System (BCS) and the Developability Classification System (DCS)**

The APIs have been distributed into four classes according to the Biopharmaceutics Classification System (BCS),: Class I- High solubility, high permeability, Class II - Low solubility, high permeability Class III - High solubility, low permeability Class IV - Low solubility, low permeability (**Figure 1.1**) [6].

Based on this system, class I are the most favourable candidates to proceed to the clinical trials due to their high solubility in addition to their high permeability characteristics. The poor solubility of low water-soluble APIs in the gastrointestinal (GI) fluids frequently leads to insufficient bioavailability, particularly for class II APIs. Depending on the BCS, the bioavailability may be boosted by improving the solubility and dissolution rate of the API in the GI liquids. The bioavailability of class III ingredients (high soluble, low permeable) is dependent on the permeability rate since their solubility is most likely high. Class IV ingredients are characterised by poor solubility as well as poor permeability, which make them unfavourable candidates for drug development. Thus, there is a growing interest in formulation approaches to enhance the solubility and dissolution of BCS class II, and IV ingredients [7].

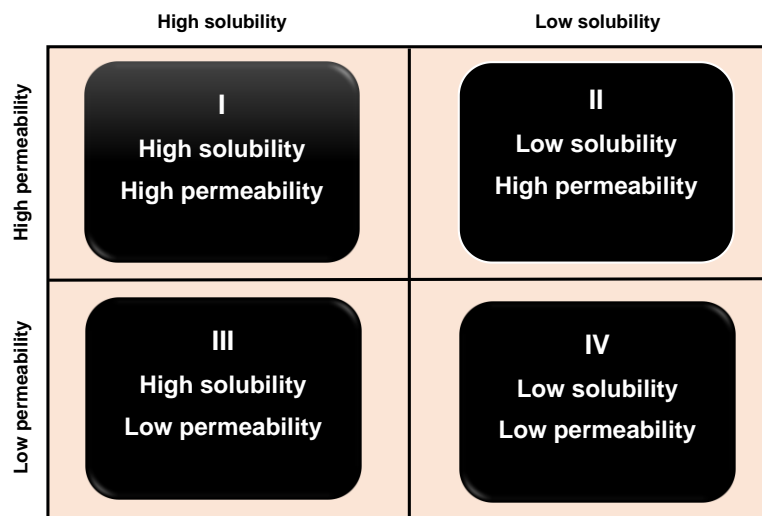


**Figure 1.1.** Biopharmaceutics Classification System (BCS) [8].

The BCS classification system was modified by Dressman and Butler in 2010, in which they used 500 mL as realistic dissolution volume in the GI tract rather than 250 mL which was used by Amidon et al. [9]. With the BCS as the starting point, the developability classification system (DCS) was presented as the modified system for oral drugs [9]. Whereas the BCS is established as a regulatory categorisation for bio-equivalence assurance, the DCS more effectively classifies APIs depending on factors that influence oral absorption. Consequently, the DCS offers a more effective categorisation method for the problems associated with oral product development.

Two essential modifications of the DCS from the BCS were introduced, including the addition of two sub-classes for class II compounds and the establishment of the solubility limited absorbable dose (SLAD) concept (**Figure 1.2**) [9]. Depending on the idea that solubility and permeability are compensatory for class II ingredients, the SLAD is illustrated by the border between class 2a and class 2b [10].

For dissolution of rate-limited ingredients (class IIa), because of the compensatory nature of high permeability on low solubility, a crystalline API maybe designed to accomplish the full oral absorption from a solid dosage form without the use of complex solubilisation technologies [10]. However, for this specific class, the release and absorption of the API from a typical formulation will depend on different factors i.e., area of the surface, wettability and size of the particle [10]. For solubility-limited ingredients,

class IIb, formulation of the API as a solubilised form is a pre-requisite to be absorbed at the absorption site. Thus, class IIb remains a major challenge to manufacturers [10].

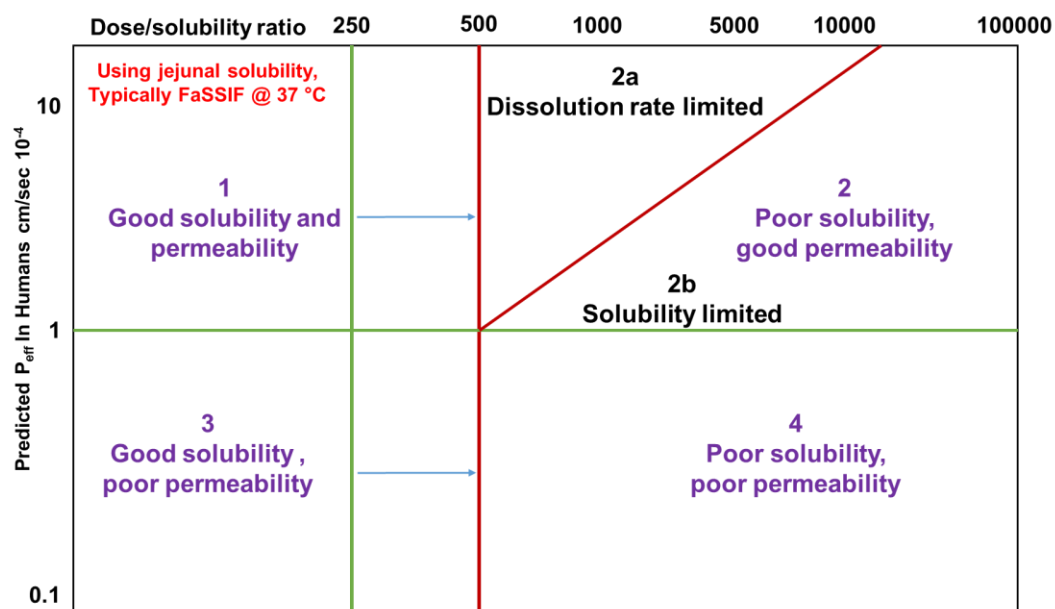


**Figure 1.2.** BCS modification for more realistic fluid volumes available in the GI tract and the compensatory nature of permeability on low solubility (alterations from the BCS to DCS are shown in red). Figure adapted from-[9].

### 1.3. Solubility and Dissolution Rate

Dissolution rate and aqueous solubility are important features to take into account during the development of APIs for oral administration. Solubility can be defined as “the amount of a solute that gets dissolved in a solvent when equilibrium is achieved between the solute and the excess of undissolved material”. Dissolution is defined as “the rate/or extent at which

the molecules or ions transferred from solid-state and dissolve in a solvent and form a solution” [11]. Solubility can be changed by changing the chemical structure of an API molecule i.e., salt formation, and pro-drug strategies, whereas utilising strategies, such as complexation, and reduction of the particle size, can change the dissolution rate.

The Noyes-Whitney equation has described the relationship between dissolution rate and solubility (**Equation 1.1**) [12].

$$dx/dt = C (S - x) \quad (1.1)$$

Where  $S$  represents the substance solubility or the concentration of its saturated solution,  $x$  represents the concentration at the expiration of time  $t$ , and  $C$  a constant. Then, the Noyes-Whitney equation was developed by Nernst-Brunner and the development showed that the dissolution rate depends on both, the exposed surface area and the solubility of the substance (**Equation 1.2**) [13].

$$dc/dt = K_D A (C_s - C_t) \quad (1.2)$$

Where  $dc/dt$  is the dissolution rate of drug,  $K_D$  is the diffusion coefficient (dependent on the dissolution constant and the stirring rate),  $A$  is the solid

surface area,  $C_s$  is the drug solubility,  $C_t$  is the concentration of the drug dissolved at time  $t$ . It is evident from the equation that the rate of dissolution is proportional to the solid surface area and the drug solubility, with respect all other factors being constant. As a consequence, the low water-soluble compounds will be characterised by a limited dissolution rate and inadequate bioavailability. Thus, a review of the present formulation strategies to overcome the problems of the low water-soluble APIs is detailed in the next sections.

#### **1.4. Strategies to Overcome Problems of Poorly-Water Soluble Active Pharmaceutical Ingredients**

Different strategies that tend to improve the bioavailability of poorly water-soluble APIs, specifically BCS class II APIs, are divided into two main categories which are either to enhance the dissolution rate or solubility of low water-soluble ingredients, such strategies includes: the formation of salt [14], prodrug [15], particle size reduction [16], cyclodextrins [17], and amorphisation and amorphous solid dispersions [5].

##### **1.4.1. Salt Formation**

Salt formation, which is an example of the crystal modification techniques, is one of the most frequently employed ways in the pharmaceutical industry to enhance the dissolution features of the low water-soluble basics or acidic APIs [14]. The resulted enhancement in dissolution rate of salt relative to its free base or free acid under the pH environment of the GI tract is because

of the greater solubility of the free API in the pH microclimate of the aqueous dissolution layer encompassing the solid created by the counterion [18] [19]. For instance, the sodium salt form of tolbutamide is known to dissolve 5,000 times faster in acidic pH media relative to its free acid [20].

Moreover, strongly acidic salts of chlorpromazine and ranitidine (weakly basic drugs) have improved dissolution profiles in the GI tract media relative to their free base forms [21]. However, this strategy is not appropriate for un-ionisable APIs. Furthermore, salts can precipitate inside the GI tract after oral administration and form aggregates, hence diminishing the enhancement in the bioavailability [14].

#### **1.4.2. Pro-drugs**

Using pro-drugs, which is a strategy involves chemically functionalising an API with a hydrophilic group, such as a phosphate ester group, will enhance the solubility compared to the pure drugs. [22]. Since the pro-drug strategy utilises chemicals with low or no pharmacological activity, the inert substance undergoes biotransformation in vivo to produce an active metabolite after oral administration [23]. For instance, fosamprenavir has been produced from phosphorylated amprenavir [22]. However, pro-drug formulation has challenges such as the cost and time for production, pharmacokinetic, toxicological, and physicochemical assessment [23].

#### **1.4.3. Particle Size Reduction**

Particle size reduction can increase the surface area of the powder and therefore the dissolution rate and the solubility as per Nernst-Brunner

equation. Moreover, decreasing the particle size can result in increased wetting properties of the particles through decreasing of its surface roughness [24]. For instance, when griseofulvin particle size was decreased from 10 to 2.7  $\mu\text{m}$ , its amount in the blood was found to be about double [25]. Particle size reduction can be achieved by utilising a milling technique [26]. There are different limitations with this strategy including the creation of cohesive and charged particles which can rapidly aggregate. Also, reduction in particle size can result in amorphisation and/or polymorphic transformation, which are considered as unstable forms that might cause stability problems over time in the final products [27].

#### **1.4.4. Cyclodextrins**

The use of cyclodextrins is another technique that is utilised to boost the solubility and bioavailability of the low water-soluble ingredients. In addition, they are employed as taste-making. Cyclodextrins are cyclic oligosaccharides comprising a water-soluble (hydrophilic) outer surface and a hydrophobic central cavity, which is capable of forming complexes with hydrophobic and weakly water-soluble APIs [28]. However, there are some limitations of cyclodextrins including nephrotoxicity after parenteral administration, and GI tract diarrhoea [29].

#### **1.4.5. Amorphisation and Amorphous Solid Dispersions (ASDs)**

Changing the drug crystalline forms to amorphous form is one of the most commonly utilised strategies to enhance the dissolution characteristics of

low water-soluble APIs [5]. Typically, improvement in dissolution rate will lead to an enhancement in oral absorption and bioavailability.

Since ASD is the main focus of the current thesis, ASDs strategy will be discussed in more detail in the following sections. However, it is important to start with a brief discussion about the formation and physical stability of the amorphous form before commencing a full discussion about ASDs.

## 1.5. Amorphous Materials

### 1.5.1. Formation and Physical Stability of the Amorphous Form

As mentioned earlier in section (1.1) the three-dimensional long-range order is lost in the amorphous form in comparison to the crystalline phase [30]. **Figure 1.3** shows a schematic free-energy temperature diagram [31]. **Figure 1.3** displays that, once the temperature is enhanced, the crystal free energy is significantly reduced until the temperature of melting ( $T_m$ ) of the crystal is reached. When the  $T_m$  is reached, the crystal goes through a spontaneous change to the liquid form. Depending on the cooling rate of the formed liquid, the liquid phase will change to the crystal if the formed system is cooled slowly below its  $T_m$  and there is an adequate time for crystal nucleation and crystal growth. In contrast, the system will keep the liquid phase features (supercooled liquid) in case the system is quickly cooled and the crystallisation step is avoided. Also, the supercooled liquid viscosity increases with further cooling of the system. Consequently, the unstable glassy state will be formed, as it appears as a distinct discontinuity in the

free-energy temperature phase diagram (**Figure 1.3**). The glass transition temperature ( $T_g$ ) is defined as a temperature below which amorphous solids exist as a solid material, and above this temperature, it changes to a liquid material [32]. Thus, one method of preparing the amorphous form is basically by melting the crystalline form of an API and then quench cool the melt to a temperature under its  $T_m$  and the  $T_g$  [30].

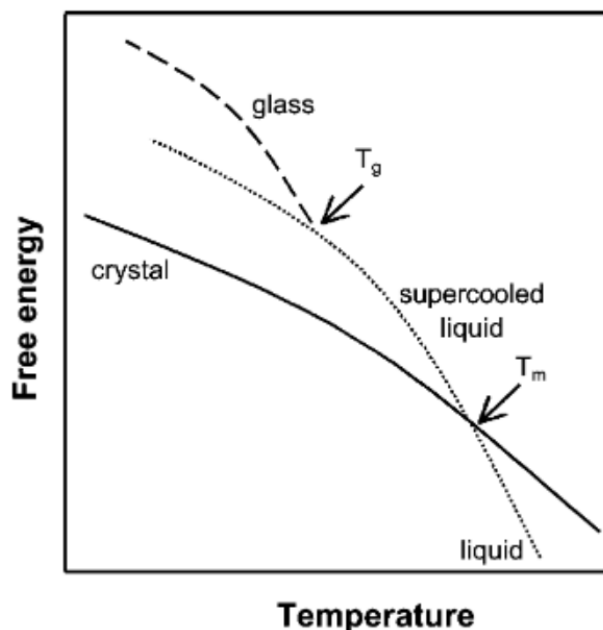


**Figure 1.3.** A schematic of free-energy temperature phase diagram [31].

Moreover, **Figure 1.3**, represents that the glassy state of the amorphous is in a higher free energy in relative to the crystalline form at all temperatures. Consequently, the amorphous phase will undergo spontaneous crystallisation over time to change to more stable state (crystalline form). Thus, due to this re-crystallisation, the advantage of utilising the amorphous

form to increase the dissolution rate of poorly water-soluble APIs will be lost. It was reported by Aso et al. that the mobility of the molecule and re-crystallisation tendency of the amorphous, for numerous pharmaceutical compounds, significantly enhances above the  $T_g$  [33]. Therefore,  $T_g$  is an important sign of an amorphous form physical stability.

As stated earlier, improving the dissolution properties of poorly water-soluble compounds, especially class II APIs, is the main advantage of the amorphous form relative to the crystalline form because the amorphous form does not possess a three-dimensional long-rang order. However, due to the physical instability of the amorphous materials, they have a tendency to rapidly re-crystallise to more stable form (crystal form) during manufacturing, storage, or during the dissolution process [34], which may lead to unpredictable bioavailability. Consequently, nucleation inhibitors that decrease the system molecular mobility i.e., polymers, can be utilised to stabilise the system by resisting the re-crystallisation process and improve the dissolution properties [35].

### **1.6. Amorphous Solid Dispersions (ASDs)**

Nearly three decades ago, many researchers and pharmaceutical scientists, guided by George Zografi, began exploiting the solubility benefit of the amorphous forms of APIs in solid dispersions [36]. Among the several types of solid dispersions, ASDs have presented to be successful and significantly enhances the apparent solubility of the poorly water-soluble drugs,

especially BCS II API [37] [38] [39]. ASD is defined as a group of solid products comprising at least two different components, commonly a hydrophobic drug and a hydrophilic inert carrier matrix [40]. Numerous polymers and formulation techniques were extensively reported in the literature to stabilise and manufacture ASD formulations.

Thus, the next sections (**1.6.1** and **1.6.2**) are a brief discussion about the most commonly used polymers and the most frequently utilised techniques to manufacture ASDs.

### **1.6.1. Common Polymers Utilised to Formulate ASDs**

Numerous polymers are used to prepare ASDs utilising different manufacturing techniques. Polymer plays an essential role in stabilising the amorphous form of a drug and attaining solubility benefit [5][41]. The most commonly employed carriers for the preparation of ASDs are cellulose derivatives such as hypromellose acetate succinate (HPMCAS), hydroxypropyl methylcellulose (HPMC), hydroxypropyl methylcellulose phthalate (HPMCP), and methylcellulose. Moreover, polyvinylpyrrolidone (PVP) and poloxamers can be employed as carriers for ASD as shown below in (**Table 1.1**) [42] [43]. Recently, polyvinyl alcohol (PVA, synthetic, biodegradable polymer) has been utilised for the preparation of ASD through 3D printing fabrication methods due to its printable ability [44].

The polymer carrier is not only added to boost the solubility and the dissolution of the APIs; also, they are added to maintain the solid-state physical stability of the API by decreasing its molecular mobility and

enhancing its glass transition temperature ( $T_g$ ) [45]. Moreover, polymer has been used to retain supersaturation solution in the GI tract for an adequate period to maximise the absorption at the site [45]. There are different examples of the marketed products as ASDs as listed below in (**Table 1.1**).

**Table 1.1.** Different examples of FDA-approved medicines manufactured as ASDs [46].

Product Name	API	Polymer	Maximum API Dose per Tablet or Capsule (mg)	API Tm (°c)	Solid Dispersion Preparation Method	Year of Approval
Cesamet	Nabilone	PVP	1	160	-	1985
Sporanox	Itraconazole	HPMC	100	160	Spray drying	1992
Prograf	Tacrolimos	HPMC	5	128	Spray drying	1994
Kaletra	Lopinavir/ritonavir	PVP/VA	200/50	125/122	Melt extrusion	2005
Onmel	Itraconazole	HPMC	200	166	Melt extrusion	2010
Novir	Ritonavir	PVP/VA	100	122	Melt extrusion	2010
Zotress	Everolimus	HPMC	0.75	115	Spray drying	2010
Intelence	Etravirine	HPMC	200	265	Spray drying	2008
Incivek	Telaprevir	HPMCAS	375	246	Spray drying	2011

### 1.6.2. Manufacturing of Amorphous Solid Dispersions

In the early 1960s, the concept of solid dispersions of low water-soluble drugs in the inert carrier was becoming popular. Accordingly, different methods were reported to manufacture the ASD, such as hot melt extrusion

(HME), and spray drying, which are the two main techniques to manufacture of ASD as evident above in (Table 1.1) [47]–[49].

#### 1.6.2.1. Hot Melt Extrusion (HME)

HME is a method of mixing an API with a thermoplastic polymer and/or with a binder and then heating the mixture above its  $T_g$  or above the melting point of all the ingredients used in the mix until softening. The dispersion results mainly from high shear mixing between the drug and the polymer [50]–[53]. Typically, the drug-polymer blend is processed with a twin-screw extruder or a single-screw extruder at a high rotational speed. Then, the blend is concurrently melted and homogenised. After that, the mix is extruded and shaped to the desired product [54]. In this method, the drug-polymer blend is only exposed to a high temperature for about 1 min [55].

HME is preferred over spray drying in the manufacturing of ASD formulations because HME is a single process, more environmentally friendly (solvent free process), and shorter time in relative to the spray drying method [50]–[53] [56]. The main disadvantage with HME method is that it is contraindicated in processing of heat sensitive materials because it might cause thermal degradation of the materials during manufacturing process [52].

Different drug-polymer systems have been manufactured using a HME process, for example itraconazole with HPMC [57], and felodipine with PVA [58]. The HME method will be discussed in more detail in chapter 2, section (2.2.1.1).

### 1.6.2.2. Spray Drying

Spray drying technique is one of the most frequently used methods in the formulation of ASD. In this method, the required API, and a polymer, are dispersed in an appropriate solvent. Then, the solvent is evaporated from the formed solution to transform it into a solid mass [59]–[61].

Spray drying is used in several pharmaceutical operations, such as encapsulation, pulmonary dosage form development, and in granulation [59]. ketoconazole ASD with polyvinylpyrrolidone K25 was prepared by spray drying method [62]. Spray drying process is suitable for processing thermo sensitive materials relative to the HME, which is an inappropriate technique for the formulation of thermosensitive materials [52]. Regardless of this advantage, there are many limitations for this technique, including the usage of solvent that results in long time needed for the formulation production, hazard and cost, in the case of using organic solvents during production. Also, the residual solvent might become entrapped in the product, which might result in a stability issue [63].

Even though there are different polymers and techniques which can be used to manufacture homogenous and stable ASD formulations, it is important to predict the solubility and miscibility between the drug and the polymer prior to the manufacturing process to select the appropriate method of manufacture and appropriate drug-polymer compositions.

### 1.6.3. Physical Stability of ASDs

Formulation of a homogenous single phase ASD is important to maintain supersaturation in the dissolution medium to enhance the absorption and the bioavailability of the dispersed drug [43]. Typically, a single phase ASD is made when a single  $T_g$  is achieved between the drug and the polymer [43]. It was mentioned earlier in section (1.6.1) that the presence of polymer in ASD results in maintaining the solid-state physical stability of the API by inhibiting the solid-state crystallisation [45] [64]. Moreover, the polymer is used to retain supersaturation state in the GI tract for an adequate period to maximise the absorption at the site by inhibiting the solvent-mediated crystallisation [45] [64]. However, this is not necessarily the case within the presence of moisture [65]. Moisture might result in re-crystallisation of the active in the ASD by the plasticising effect of water ( $T_g$  reduction) due to the low  $T_g$  of water (about  $-134\text{ }^\circ\text{C}$ ) [66]. Temperature is another factor that may worsen the stability of ASDs. For example, storage of ASD at a temperature higher than its  $T_g$  may results in re-crystallisation of the API [67]. ASDs stability is the interest of several researchers, such as Healy [68] [69], Guy Van den Mooter [70], Ann Newman [43], Lynne Taylor [71], and many others [69]–[73].

Miscibility between the drug and polymer is presented as a valuable aspect in predicting the stability of the ASD formulations [58] [59]. Miscible system means a single  $T_g$  is produced between API and polymer which can be determined utilising a DSC method [78]. It is important to predict the

miscibility of a drug-polymer mixture in order to select the appropriate API loading, the suitable carrier, and the appropriate procedure to manufacture a homogenous and stable ASD system [76]. Consequently, numerous approaches have been noted in the literature [53] [175]–[177] to predict the miscibility of a binary drug-polymer system. For example, the melting point depression method (MPD) [76] [69], [81]–[83], and solubility parameters calculation approach [53] [175]–[177]. Also, the Flory-Huggins interaction parameter is another prediction model that is used for the prediction of a binary drug-polymer system [76]. Prediction of a drug-polymer binary system miscibility will be discussed in more detail in chapter (3).

The presence of the polymeric carrier in the ASD formulations can affect drug release mechanisms from these formulations. Thus, the next section is a summary about different release mechanisms from polymeric matrix devices.

#### **1.6.4. Mechanisms of Drug Release from Polymeric Matrix**

##### **Devices**

In many therapeutic situations, there can be an advantage in delivering the pharmacological agent over a sustained period rather than as a bolus dose. Examples of this requirement include patients receiving pain relief or who experience adverse effects when full doses are administered in immediate-release preparations. In other situations, the active drug may be acid labile, so the dosage form must be capable of passing through the acidic environment of the stomach, only releasing its contents once in the small

intestine. Other drugs may require mucoadhesion or simply taste-masking; in many of these cases, polymeric formulations can be of substantial importance.

There are several different mechanisms through which drug release can occur, and the dominant release mechanism is generally determined by the design of the polymer. Some polymer types are designed to swell while other types are eroded. More complex multi-component systems can also produce biphasic drug release, with more than just a single release type. In contrast, some polymer formulations can release their therapeutic payload by passive diffusion or osmotic processes. Each of these mechanisms is visited in turn here.

#### **1.6.4.1. Swelling**

Polymers containing combinations of hydroxyethyl cellulose and sodium carboxymethyl cellulose have been shown to swell and float, which is of particular value if the therapeutic payload is to be released in the stomach [84]. In this example, the active drug is physically constrained within the polymer matrix and is unable to leave until the dosage form is exposed to gastric solution. Over the course of several hours, the polymer then swells, generating pores that are large enough to allow the passage of drug.

The kinetics of drug release from polymers such as those described by Chen et al, are not only affected by the rate of swelling of the polymer, but also by the dissolution profiles of the drug in question [84]. Chen et al tested three model drugs, noting that the freely water-soluble drug metformin was

released from the polymer primarily under diffusion, whereas the less soluble drug ciprofloxacin and the slightly soluble esomeprazole were subject to anomalous diffusion [84].

#### **1.6.4.2. Diffusion**

Arguably, diffusion is a key process in all of the mechanisms through which drugs are released from polymeric dosage forms. In each case, processes such as swelling or erosion expose the drug to the environment external to the polymer, but it is the rate of diffusion that can ultimately affect the rate of drug release into that environment.

The diffusion equation is a parabolic partial differential equation derived from Fick's laws of diffusion, and it describes the behaviour of particles such as drug molecules which are subject to the random movements and collisions [85]. In essence, the process of diffusion describes the net movement of molecules from an area of high concentration, such as inside the polymer dosage form, to an area of lower concentration, such as the target area, in line with a concentration gradient [85].

#### **1.6.4.3. Erosion**

The erosion of a polymer dosage form involves its gradual disintegration either as a result of physical or chemical processes occurring in the body, such as acidic or enzymatic processes or persistent peristaltic motions, or a combination thereof. The kinetics of polymer erosion can be complex, with surface erosion and bulk erosion often taking place simultaneously, which may be the case if the polymer is ingested. Rate of surface erosion changes

gradually as the active surface area decreases, while bulk erosion is a function of the overall volume of the polymer, which also decreases over time [86]. Polyesters such as poly lactic acid (PLA) is example of a bulk eroding polymer, whereas polyorthoester and polyanhydrides are examples on surface erosion [88] [89].

#### **1.6.4.4. Osmosis**

Osmosis refers to the spontaneous movement of a solvent, usually water, through a semipermeable membrane towards an area with higher solute concentration; the movement of solvent brings about an equalisation of solute concentrations on either side of the membrane [89] [90].

The osmotic process can be harnessed in drug delivery through the production of a tablet that presents an osmotic pump. In such designs, osmosis drives water into the tablet, which then effectively pushes the drug out of the tablet at a predictable rate [91]. This mechanism requires a dosage form with an internal osmotic pressure that is created by use of a suitable osmotically active excipient and semipermeable polymer excipients. Control of the rate at which water enters the tablet results in a known rate of dissolution, and output of the drug occurs through a hole in the membrane created with a laser. For example, Sapna et al. prepared an osmotic device to control the release of the 60mg pseudoephedrine HCl utilising a semipermeable membrane of cellulose acetate over period of 12 hours [92]. Procardia XL® (Nifedipine) and Ditropan XL® (oxybutynin chloride 5, 10 mg) are other examples of drug release from osmotic devices [93].

As mentioned earlier, the main aim of manufacturing a physically stable homogenous ASD system is to improve the bioavailability of the low water-soluble APIs. However, due to the metastable nature of amorphous APIs, they have a tendency to crystallise. Consequently, this benefit is lost as the dissolution will slowly convert to that of the crystalline counterpart. Crystallisation of amorphous APIs can occur throughout manufacturing, storage or inside the body during contact with the gastrointestinal fluids leading to formulations failure [7].

#### **1.6.5. Possible Failure Modes in ASDs**

Improving the dissolution and the oral bioavailability are the main advantages with utilising ASD as a strategy to overcome the problems associated with low water-soluble ingredients, specifically BCS class II APIs, in comparison to their crystalline counterparts. However, ASD formulations are thermodynamically unstable and have a tendency to crystallise with time as mentioned in the previous sections.

The instability of the ASD formulations, which is maybe the greatest challenge with these formulations, is highly dependent on their thermal history, i.e. which method of preparation has been utilised to produce the ASDs and what is the glass state produced? For instance, it has been reported by Mahmah, et al. that the physical stability of the ASDs could be significantly influenced by the technique utilised, solvent evaporation or heat melt, to produce the formulations [94]. Also, different characteristics of glass would be produced through using solvent evaporation technique as a

fabrication process depending on different factors such as how fast the solvent is removed and the amount of residual solvent [94][95]. Moreover, the glassy products may relax over time; therefore, the freshly prepared glass properties may be different from the aged glassy product [95][96].

In addition, before distribution of the ASDs to the consumers, they undergo further manufacturing processes and exposure to storage conditions. For example, compaction, and milling during the formulation process may generate defects and cracks, which may cause phase changes in the ASD matrix, leading to dissolution failure [97]. Furthermore, the strength of the activity or interaction of the API with the carrier may change due to moisture exposure during product storage [98].

Re-crystallisation of ASDs may occur due to the amorphous-amorphous phase separation (AAPS) [99]. AAPS is a condition in which amorphous phases of a drug-rich and a polymer-rich regions coexist and is believed to be a sign to re-crystallisation step [100].

The crystallisation step may occur during the manufacturing process, during storage, and during contact with an aqueous medium, which may lead to dissolution failure [7]. For example, Tres, et al. [101] have studied the dissolution behavior of felodipine with copovidone VA64 (5% and 50% w/w) amorphous solid dispersions utilising Raman mapping during the dissolution process to study the impact of increasing the drug loading on the dissolution performance. They found that the 5% dispersions were completely dissolved after 280 minutes.

On the other hand, API releases from the 50% dispersions was extremely low, and the compacts did not dissolve after 1705 minutes. Multi Curve Resolution (MCR) Raman mapping, XRPD, and classical Raman characterisation revealed that felodipine re-crystallised after an initial loss of copovidone from the extrudates, which led to a release dynamics dependent on high hydrophobicity and poor water solubility of felodipine (**Figure 1.4**) [101].

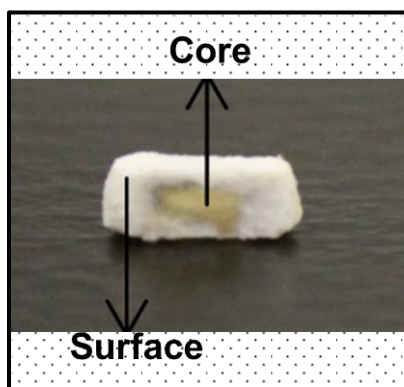


**Figure 1.4.** Recrystallisation of the API from ASD tablet during the dissolution process [101].

It was stated by Craig that the release of the APIs from the ASD formulations may be categorised as drug-controlled or polymer-controlled, depending on the drug-polymer compositions and the chemical nature of the compounds used in the formulation [102]. Numerous processes are included during the dissolution step of the ASD formulations [101]. The behaviour of the solvent, the generation of micro and nanoparticles suspended in the dissolution medium, and the nucleation and crystallisation of the API in the solid-state

and/or from a super-saturated solution. All the above mentioned factors can severely affect the whole dissolution profile [103]–[106]. Because of the several processes included the dissolution behaviour of the ASD formulations remains complicated and difficult to understand. Subsequently, different approaches have been reported to give a clear idea about the API release from the ASD formulations during the dissolution process. Such approaches have included UV imaging [107]–[109], ATR-FTIR [110]–[112], and Raman spectroscopy [4] [7] [101].

For example, Hulse et al., have utilised UV imaging to compare the dissolution rates of indomethacin ( $\alpha$  and  $\gamma$  forms) [107]. The rate of the dissolution ratio between the  $\alpha$  form upon the  $\gamma$  form was found to be about 1.7. Moreover, in another research, the amlodipine besylate dissolution performance of three different solid forms, including dihydrate, free base, and amorphous, was monitored employing the UV imaging [108]. The amorphous form re-crystallisation into the monohydrate form was indicated utilising UV imaging combined by Raman spectroscopy. In addition, the dissolution of the amorphous of both sodium salt and free acid of furosemide in relative to the corresponding crystalline forms was studied utilising UV imaging [95]. The transformation of the amorphous acid into crystalline acid was indicated by Raman spectroscopy.

Also, Raman spectroscopy was utilised in different studies to monitor physio-chemical transitions during dissolution process of many pharmaceuticals [4] [7] [101]. For instance, in-situ Raman spectroscopy was

also utilised by Savolainen, et al., to monitor indomethacin solid phase transition during dissolution [7]. It was shown that amorphous indomethacin dissolution rate was decreased due to the re-crystallisation of the drug into the  $\alpha$  form. Moreover, real-time in-situ Raman mapping was employed by Tres, et al., to study the solvent-mediated phase transformations of bicalutamide with copovidone VA64 [4]. The dissolution behaviour was tested as a function of the drug loading (5% and 50% w/w). The information from the spatially time-resolved Raman maps obtained utilising MCR showed that the amorphous bicalutamide present in the 50% drug-loaded extrudate undergoes simultaneous conversion into metastable low-energy polymorphic form I and polymorphic form II [4].

In addition, attenuated total reflection (ATR) FT-IR was utilised by Kazarian and Chan to image ibuprofen-PEG ASD crystallisation process during dissolution in water [10] [96]. Combining FT-IR with ATR spectroscopy produced an approach with high spatial resolution and high chemical specificity. In another study, a combined compaction and flow-through cell, which was built by the same group, was utilised to investigate the dissolution of a tablet comprised of HPMC and caffeine [111]. Improving the images quality due to the good contact between the ATR surface and the sample, and a more controlled penetration of water into the compact were the main advantages of the specially designed flow cell. In another study conducted by the same group, a UV detector was linked to the combined compaction

and flow-through cell, which is similar to the typical dissolution test, to quantify the nicotinamide amount released from HPMC tablets [98].

Although there are several publications and reviews on the subject, the mechanisms pertaining to both the observed improvements and failure in dissolution remain to be understood. Current methods of understanding why formulations fail dissolution testing use tablet samples in which the spatial distribution of material is uncontrolled. However, if we can control the distribution and position of the crystals within the tablet and build better model test tablets, maybe we can then look at a testing hypotheses about how the micro-structure of a tablet affects the drug release mechanisms from ASD tablets.

So far, it is challenging to fabricate ASD tablets with controlled distribution of crystalline seeds in various positions of the dosage form to test the release of the APIs utilising conventional tableting methods, such as single punch press, rotary press, and tablet moulding, because conventional tableting processes do not easily afford precise spatial control of these impurities during tablet formulation.

3D printing techniques have been utilised in different studies [113]–[115] to fabricate tablets with complex geometries due to their ability to manage several factors throughout the printing process compared to the conventional tableting methods. Moreover, 3D printing techniques have the ability to fabricate a tablet without using an excipient, commonly a drug and a polymer are used during the fabrication process. For example, Saviano,

et al. have used FDM 3D printer to fabricate different drug-loaded tablets utilising ciprofloxacin hydrochloride as active and PVA as polymer [116]. Consequently, 3D printing techniques could potentially be utilised in the present thesis to fabricate better test model tablets compared to the typical tableting methods in order to investigate the drug release mechanisms from ASD tablets.

Thus, the next section will deliver a brief discussion about the use of 3D printing technologies and their applications in the medical field, with more focus on utilising 3D printing techniques for the fabrication of pharmaceutical products for research.

### **1.7. Three-Dimensional (3D) Printing Techniques**

Recently, 3D printing techniques have been implemented in pharmaceutical research and fabrication of tablets (**Table 1.2**) [114]. These techniques can control different variables during the printing process in comparison with the conventional tablet manufacturing methods [113]–[115]. 3D printing is a process where the raw material, in a powder form, liquid, or solid filament, is deposited layer by layer to construct a physical 3D object. In the 3D printing system, the material to be printed is created by utilising a computer-aided-design (CAD) software and then exported as a file for printing. Next, this file splits the 3D object into a sequence of layers; after which, the object is printed layer by layer [117].

**Table 1.2.** A summary for the fabrication of tablets using 3D printing in the pharmaceutical research [113]

Dosage form	3D technique	API	Summary	References
Tablet, ER	Powder bed inkjet (Fochif Co.)	Acetaminophen	Manufactured tablets to achieve near zero-order release utilising radial gradients of different rate regulating excipients and impermeable top and bottom EC.	[118]
Tablet, ER	Powder bed inkjet (TheriForm/	Pseudoephedrine HCl	An outer rate-limiting shell material controlled water-soluble API release. No sensitivity to pH and hydrodynamics was displayed in vitro experiments. Level A IVIVC for near-zero-order release was shown in vivo tests.	[115]
Orally disintegration tablet		Levetiracetam	ODT with rapid dissolving (510 s) that requires a little amount of water about 515 mL, and with up to 1 g of water-soluble API was prepared. Printer with high saturated fluid was employed on outer edges, top, and bottom to enhance ODT hardness.	[119]
Tablet, ER	Powder bed inkjet (Fochif Co.)	Acetaminophen	Tablets with doughnut-shape and with impermeable top and bottom to generate zero-order release from sides were manufactured.	[120]
Tablet IR/ER bilayer	Extrusion 3D printer	Guaifenesin	Two pastes of IR and ER preparations extruded into double layers tablets. When compared to the commercial products, lower friability, hardness, and slightly faster release profiles were observed.	[121]
Tablet, IR/SR	FDM (Fab@home)	Pravastatin, atenolol, ramipril, aspirin, hydrochlorothiazide	A similar paste to the above work was prepared. IR release profiles reached for two APIs, including aspirin and hydrochlorothiazide. While the rest exhibited SR release profiles.	[122]
Tablet	FDM (RegenHU 3D Printer)	Fluorescein	The API was impregnated by incubation with PVA filaments at 0.29% drug-loading. SR tablets were fabricated with 0 to 100% infill density (slower release from the tablet was observed with more infill due to less porosity).	[123]
Tablet	FDM (RegenHU 3D Printer)	MR 5-ASA, 4-ASA	Because of poor solvent solubility during the incubation process, only 0.06% drug-loading was accomplished for 5-ASA. Because of high temperature (210 °C) used during the printing process, most of 4-ASA, about 50%, was decomposed.	[44]
Tablet, ER	FDM (Makerbot Replicator® 2)	Prednisolone (2–10 mg)	The API was saturated by incubation with PVA filaments at 1.9% drug-loading; thus, the theoretical dose of strength 88.7–107% was achieved. Most of the drug in the final produced tablet was amorphous.	[124]
Tablet	FDM (Makerbot Replicator® 2)	Acetaminophen	The impact of different parameters was examined during this study, including surface area to volume ratio, surface area, and weight of tablet on dissolution of varying geometries. Higher volume-to-surface ratios showed faster release rates. Less variation in release suggesting erosion-mediated release from PVA matrix was shown by constant weights.	[125]
Tablet, IR and MR	FDM (Makerbot Replicator® 2X)	Acetaminophen, CAF	Drug-loaded PVA filaments of each drug were manufactured using HME. Then, these filaments were utilised to formulate FDC with a multi-layered tablet for immediate release and tablet-in-tablet (DuoCaplet) for the delayed release. 100% infill density, 0% friability, and high hardness tablets were successfully manufactured. Comparable to a Size 4 capsule, the tablet model showed the ability to create more rounded features to make swallowing easier. Amorphous solid dispersion of APAP and PVA formulated during HME process.	[126]

### 1.7.1. Applications of 3D Printing Techniques in Different Fields

3D printing technology was first utilised to fabricate dental implants and custom prosthetics in the early 2000s [127][128]. Since then, the applications of this technology in the medical field have increased significantly. Currently, several published reviews explain the use of the 3D printing technology to fabricate different models such as a jawbone, eyeglasses, vascular networks, cell culture, stem cells, tissues, blood vessels, ears, bones and organs. Moreover, it used for the fabrication of novel dosage forms and drug delivery devices (**Figure 1.5**) [129][130].

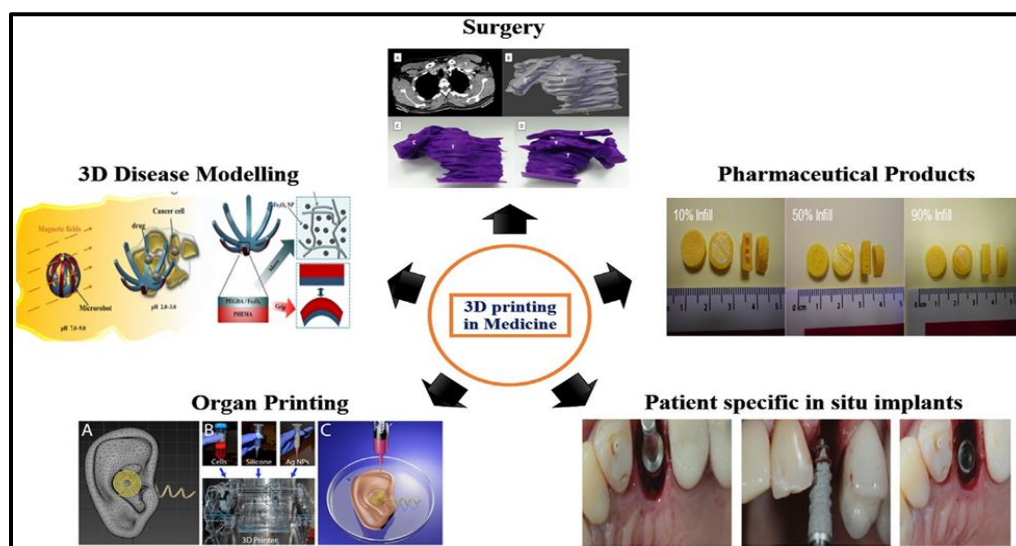


**Figure 1.5.** Different applications of 3D printing techniques in medicine [131].

### 1.7.2. 3D Printing for Commercial Pharmaceutical Products

3D printing has advantages in the fabrication of dosage forms over the use of the conventional tableting methods, such as the capability to manufacture dosage forms with complex drug-release profiles, and high reproducibility, [114]. For example, Wang, et al., used SLA to manufacture drug-loaded 3D printed tablets with sustained-release profiles (**Figure 1.6**) [132]. In their study, polyethylene glycol diacrylate (PEGDA) was employed as a monomer, and diphenyl (2,4,6-trimethyl benzoyl) phosphine oxide was utilised as a photo-initiator, while, paracetamol (acetaminophen) and 4-aminosalicylic acid (4-ASA) were selected as model APIs. They successfully fabricated extended-release paracetamol and 4-ASA tablets containing three different loading (35 %, 65 %, and 90 %) of PEGDA.



**Figure 1.6.** Images of 3D fabricated tablets loaded with (A) paracetamol and (B) 4-ASA. From top to bottom: tablets containing 35% PEGDA, 65% PEG300, 65% PEGDA, 35% PEG300, 90% PEGDA, and 10% PEG300 [132].

### 1.7.3. The Recent Technologies in 3D Printing

Nowadays, several types of 3D printers are available on the market. However, the most common technologies used in medicine are stereolithography (SLA), fused deposition modelling (FDM), selective laser sintering (SLS), inkjet 3D printing technology, and extrusion-based 3D printing technique (**Table 1.3**) [55][135]. The next sections include a brief discussion about the most common commercially available 3D printing techniques.

**Table 1.3.** A summary of commonly established 3D printing methods with advantages and disadvantages of each technique [136].

Technique	Starting materials	Typical polymers	principle	Advantages	Disadvantages
<b>SLA</b>	Liquid photopolymer	Epoxy and/or acrylate-based resin	Ultraviolet (UV) induced curing and laser scanning	High printing resolution	Limited materials, cytotoxicity, expensive
<b>FDM</b>	Filament	Thermoplastics polymers, such as PCL, ABS, PLA, PVA, and nylon	Extrusion and deposition	Cheap, good strength, multi-material capability	Clogging of the nozzle
<b>SLS</b>	Powder	Polyamide powder, and PCL	Temperature-induced sintering, and laser scanning	Good strength, easy cleaning of support materials	Expensive, rough surface
<b>3D plotting (Extrusion based 3D)</b>	Liquid or paste	PLA, PCL, and hydrogel	UV-assisted curing or pressurised syringe extrusion, and heat	High printing resolution, ability to process soft materials	Low mechanical strength, and slow
<b>Inkjet 3D (drop on demand &amp; continuous inkjet printing)</b>	Powder	Any materials can be supplied as a powder; however, a binder is needed	DOD binder printing process	Cheap, multi-material capability, and easy to clean support powder	Binder clogging, and contamination

The table was modified from Wang, Xin, et al. "3D printing of polymer matrix composites: a review and prospective."

### 1.7.3.1. Stereolithography (SLA)

The technology relies on the concept that each layer is created by curing a photosensitive resin using a UV laser. After each layer is formed, the platform moves up and down by one-layer thickness. Then, the process is continued until the final shape of the product is achieved (Layer by layer process) (**Figure 1.7**). For example, Wang, et al., used a SLA 3D printer to print 4-aminosalicylic acid and acetaminophen extended-release tablets [132] [134].

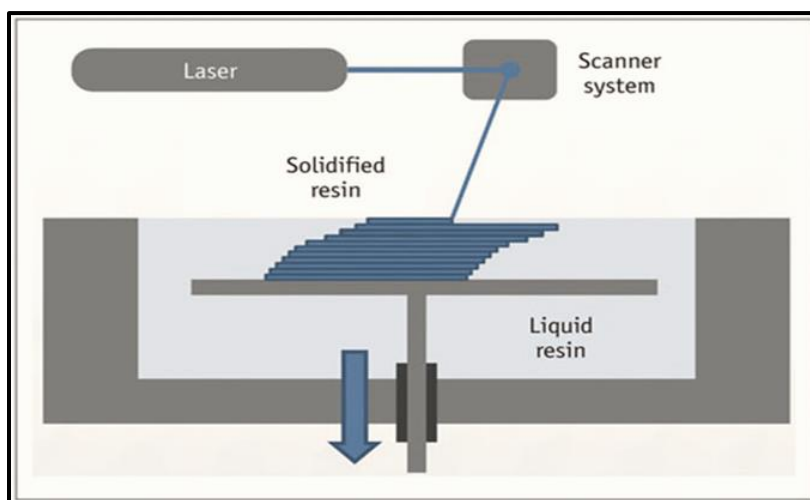


**Figure 1.7.** The basic principle of the stereolithography apparatus [137].

### 1.7.3.2. Fused Deposition Modelling (FDM)

The FDM technology was developed by Crump of Stratasys; also, known as Fused Filament Modelling. In recent years, FDM is one of the most commonly utilised processes for tablet manufacture in the pharmaceutical research field [127]. Thermoplastic polymers such as acrylonitrile butadiene

styrene, PVA, PCI, and polylactic acid (PLA) are commonly used filaments with FDM technology [113]. In FDM, the thermoplastic materials (filaments) are fed through the printer feeding tube utilising drive wheels (rollers). Then, the rollers push up the loaded filaments towards the liquefier head. At this stage, the filaments are heated by temperature control units and converted into a semisolid state. After that, the semi-molten materials are extruded out of the nozzle and solidify in the wanted areas. Each layer is fabricated through the same steps. These steps are then repeated to fabricate the 3D object in a layer by layer process (**Figure 1.8**) [127].

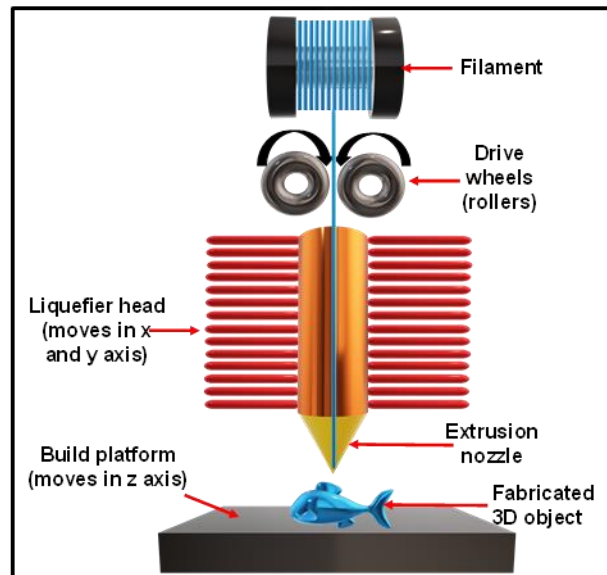


**Figure 1.8.** Schematic diagram of the FDM 3D printer working principles.

### 1.7.3.3. Selective Laser Sintering (SLS)

SLS technology was developed by Carl and Beaman, at the University of Texas-Austin, in 1980 [138]. SLS 3D printing is similar to inkjet printing. However, SLS utilises a high power laser beam to sinter powder materials to produce a 3D model [139], while the inkjet 3D printing uses binding materials to bind the powder particles together. In SLS, the powder of the first layer is dispersed equally onto a platform using a roller [139]. Then, the powder is heated to a temperature under the melting point of the powder [139]. After a cross-sectional profiles designated as steriolithography file, the laser beam is selectively scanned upon the powder to increase the temperature above the melting point and fuse the powder particles together [139]. When the first layer is fabricated, a second layer is added, distributed and sintered in the required place. These steps are then repeated until a 3D model is fabricated (**Figure 1.9**) [139]. An advantage of the SLS system, is that different materials can be used with this technology as shown above in (**Table 1.3**), for example, acrylonitrile butadiene styrene (ABS), resin, polyester[140], poly carbonate (PC), polyvinyl chloride (PVC), nylon, metal, and ceramic powders [141]. SLS fabricated models however can suffer from deformation because of the thermal heating produced by the laser and subsequent cooling [127][142].

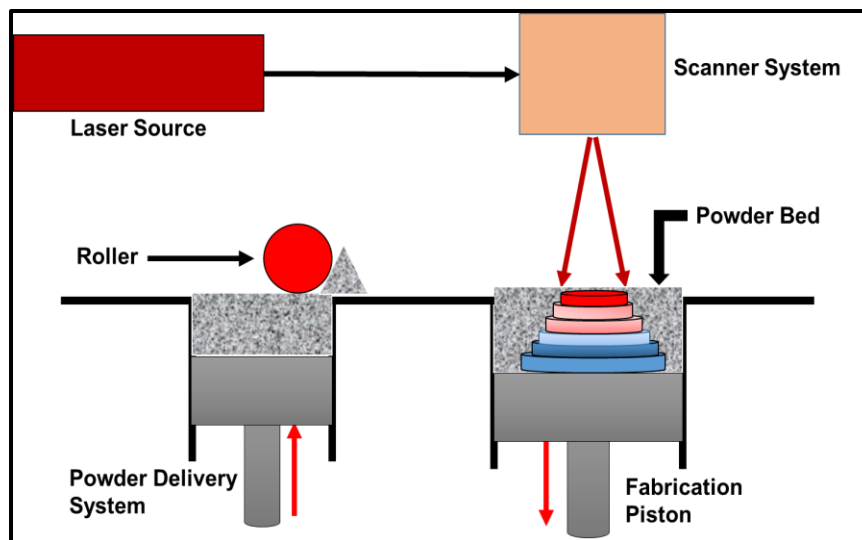


**Figure 1.9.** Schematic diagram of the SLS 3D printer.

#### 1.7.3.4. Inkjet 3D Printing Technology (IJ)

Inkjet 3D printing technology is a powder-based technique. This technology has been used to print pharmaceutical formulations [143]. For example, Yu, Deng-Guang, et al., used powder bed inkjet (Fochif Co.) to fabricate tablets with a doughnut-shape with water-resistant top and bottom to generate zero-order release from the sides [120]. In this process, a layer of solid particles (powder materials) with around 200  $\mu\text{m}$  height and particle sizes ranging from 50-100  $\mu\text{m}$  are collected together by a liquid printed material to fabricate a 3D model. The first layer of the powder is dispersed equally on the support stage by a roller. Then, the head of the inkjet printer prints liquid droplets and binds material onto the powder layer at chosen areas of solidification. Then, when the first layer is finished, the platform moves down, and a second layer of powder is dispersed and selectively combined

with the printed binding material. Then, the above mentioned steps are repeated until a 3D object is created (layer by layer process) [127]. Inkjet printers can have two different mechanisms, including drop-on-demand (DOD) inkjet printing and continuous inkjet (CI) printing [144]. The two types can generate drops of fluid with diameters in the range of 10 to 150  $\mu\text{m}$ . (CI) printing droplets are generated continually by an electric charge imparted to them. The drop diameter in an inkjet printer is of approximately 100  $\mu\text{m}$ . On the other hand, in (DOD) inkjet printers, droplets are generated only when they are needed.

#### **1.7.3.5. Extrusion Based 3D Printing Techniques**

This is a process like the other 3D printing techniques, where the 3D model is fabricated on a layer by layer manner. Several materials such as hydrogels, thermoplastic materials, pastes, polymers, and hydrogels, can be extruded using a syringe tool (metallic or plastic), and then, dispensed via pneumatic, piston-driven, or screw-driven force on a building platform [135]. For example, Shaban A, et al., have used fab@home model 2 extrusion-based 3D printing to fabricate controlled release pharmaceutical bilayer tablets [121].

#### **1.7.4. 3D Printing Techniques Versus Conventional Tablet Production**

As a promising technology, 3D Printing techniques have several advantages in the fabrication of tablets over other manufacturing techniques. Compared to conventional tablet manufacturing processes, 3D printing offers a lot of

attractive qualities; for instance, the ability to achieve high drug-loading, decrease the amount of material wastage and manufacture dosage forms with complex drug-release profiles [114][115].

Moreover, it may be applied to a range of API types, such as low water-soluble peptides, proteins, and APIs with narrow therapeutic indices [114][115]. Furthermore, 3D printing has great promise for the future of manufacturing multi-prescribed medicines in one tablet. For example, Shaban A, et al. have utilised a 3D extrusion printer to fabricate a solid dosage form (Polypill), which contains five APIs. In their work, they used five compartmentalised APIs with two independently controlled and distinct release profiles to fabricate the Polypill. It shows that multiple drugs can be utilised to produce a single personalised tablet, which could possibly enhance adherence for patients who are taking different tablets at the same time. Furthermore, using 3D printers in the future could eliminate some steps in the tablet manufacturing pipeline procedure, including wet granulation, coating, dry granulation, compression of tablet, and powder milling, especially when there is a limited quantity of APIs at early stage of API development [145].

Consequently, due to the numerous advantages of the 3D printing techniques over the conventional tableting methods, as detailed in previous sections, we want to utilise one of the 3D printing techniques to fabricate some model systems to understand how and why the distribution of the excipients in the tablet can lead to formulation failure.

Therefore, we aim to investigate the dissolution behaviour of the API from the ASD tablets by working towards and manufacturing two types of model tablets, pure ASD and spiked ASD, by employing one of the 3D printing techniques in which the effect of spatial location of crystal seeds can be systematically controlled and evaluated to understand drug release mechanisms from such type of dosage forms and offer recommendations.

### **1.8. Aims and Objectives**

The general aim of the current thesis is to investigate the dissolution behaviour of the API from the ASD tablets by working towards formulating two basic formulations (pure ASD and spiked ASD) of model tablets, by employing one of the 3D printing techniques in which the effect of spatial location of crystal seeds can be systematically controlled and evaluated to understand drug release mechanisms from these formulations and offer recommendations.

In the present thesis the following objectives will be detailed:

- To predict the miscibility of the active (FELD) with the polymers (PVA and Soluplus®) through the calculation of the F-H interaction parameter ( $\chi$ ), solubility parameters calculation method, and Gibb's free energy of mixing for the drug-polymer systems.
- To construct the composition phase diagram of the drug-polymer system in order to determine which drug-polymer compositions and

conditions will produce stable ASD and which compositions and conditions will produce ASD spiked with crystalline materials.

- To manufacture the printer drug-loaded feedstocks based on the calculations obtained from the previous step using HME, which will be used to fabricate the model tablets. Also, to design, optimise, and fabricate different drug-free and drug-loaded tablets with different geometries utilising the FDM 3D printer in order to evaluate the ability of the printer on controlling different parameters during the printing process.
- To use SEM and a digital calliper to study the morphology and dimensions of the fabricated model tablets before and after optimisation of the printing parameters.
- To utilise DSC, FTIR, XRPD, and Raman to investigate the drug-polymer interaction and formation of ASD as well as to detect possible crystallinity % in the manufactured materials.
- To manufacture the drug-loaded model tablets, which have an outer shell (amorphous or spiked with crystalline material) and inner core (amorphous or spiked with crystalline material), using the FDM 3D printer as a fabrication technique based on the data obtained from the drug-polymer compositions phase diagram.
- To investigate the drug release from the 3D printed model tablets and to evaluate the effect of the spatial crystallinity on the dissolution

behavior using dissolution testing United States Pharmacopeia (USP).

- To use the drug release kinetics in order to understand the drug release mechanisms from the fabricated model tablets.

## 2. Chapter 2: Materials and Experimental Techniques

This chapter aims to deliver an overview of the materials and the major experimental techniques utilised in the present thesis to predict the drug-polymer solubility/miscibility, to prepare the FELD-PVA filaments, to fabricate the model tablets, to investigate the drug-polymer interaction and formation of ASDs, and Moreover, to study the dissolution behaviour of the API from the different fabricated model tablets. The theory of the utilised methods and the purposes for their use will be briefly discussed in this chapter. Complete experimental descriptions will be discussed in "Materials and methods" sections of Chapters 3, 4, and 5.

### 2.1. Materials

Felodipine (FELD), pale yellow crystals, was purchased from Carbosynth Limited (Compton, Berkshire, UK). Polyvinyl alcohol (PVA), synthetic, biodegradable, water-soluble polymer (2.85 mm diameter), and polylactic acid (PLA) (Black, 2.85 mm diameter) filaments were purchased from the Ultimaker (Lancashire, UK). Soluplus® was kindly gifted by BASF SE Pharma Ingredients & Services (Ludwigshafen, Germany). Sodium chloride (NaCl), potassium chloride (KCl), potassium phosphate monobasic (KH<sub>2</sub>PO<sub>4</sub>), sodium phosphate dibasic (Na<sub>2</sub>HPO<sub>4</sub>), hydrochloric acid (HCl),

sodium hydroxide (NaOH), and sodium lauryl sulphate (SLS), were provided by Sigma Aldrich (Gillingham, UK).

### **2.1.1. Active Ingredient Used in this Project**

#### **2.1.1.1. Felodipine (FELD)**

FELD (**Figure 2.1**), (4 RS)-4-(2,3-dichlorophenyl)-2,6-dimethyl-1, 4-dihydropyridine-3,5-dicarboxylate, is known as a calcium channel blocker and is widely utilised in the treatment of hypertension and angina pectoris [146] [147]. It is a BCS class II API, which is characterised by low water solubility and high permeability. According to that, felodipine has poor dissolution as well as poor bioavailability after oral administration. Moreover, felodipine goes through extensive first-pass metabolism with a bioavailability of about 15% [148]. Low water solubility, which is approximately 19.17 mg/L at room temperature, is the main challenge in terms of the therapeutic application and efficacy of felodipine as an oral dosage form. Consequently, enhancement of its water solubility and dissolution is of therapeutic importance [149] [150]. Homogenous ASDs of felodipine with different polymers, such as PVP, copovidone, Soluplus, HPMCAS and PVA have been successfully formulated over a range of compositions (0-70% drug loading), indicating some enhancements in both dissolution performance and physical stability [73] [88] [141] [142]. According to the information available from these studies, FELD may be is an appropriate model drug for the current thesis.

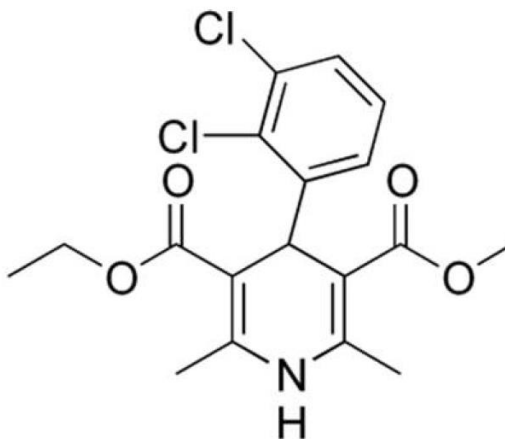


**Figure 2.1.** Chemical structure of felodipine [10].

## 2.1.2. Carriers used in this Project

### 2.1.2.1. Polyvinyl alcohol (PVA)

PVA (**Figure 2.2**) is a synthetic, hydrophilic, and thermoplastic polymer [153]. Because PVA is chemically inert, biocompatible, safe, drug compatible, water-soluble, and has good swelling and mechanical properties, it is commonly employed for numerous pharmaceutical applications, including in transdermal delivery systems, controlled release formulations, implants, ophthalmic formulations, and tablet coatings [154]. Lately, PVA is extensively used as a polymer to fabricate tablets using 3D printing techniques due to its printable features (thermoplastic polymer). For example, Saviano, et al., successfully used PVA to fabricate a tablet loaded with Ciprofloxacin hydrochloride employing FDM as the 3D printing technique [116]. PVA was utilised in the present thesis as a polymer to print the different drug-loaded model tablets.

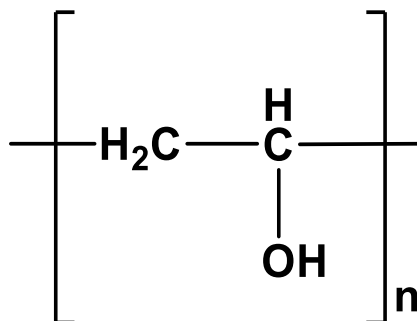


**Figure 2.2.** Chemical structure of PVA.

#### 2.1.2.2. Soluplus®

Soluplus®, (**Figure 2.3**), is a graft copolymer that is consisting of three different homopolymers, i.e. polyvinyl caprolactam-polyvinyl acetate-polyethylene glycol (PCL-PVAc-PEG), and is considered as an amphiphilic copolymer, where PCL and PVAc are the hydrophobic part, whereas PEG qualifies as the hydrophilic component [155] [156]. Soluplus® has been reported in different literature [151] [157]–[159] to prepare ASD of poorly water-soluble API by hot-melt extrusion technology. Also, it was utilised as a surfactant to improve the aqueous solubility of poorly water-soluble drugs [160].

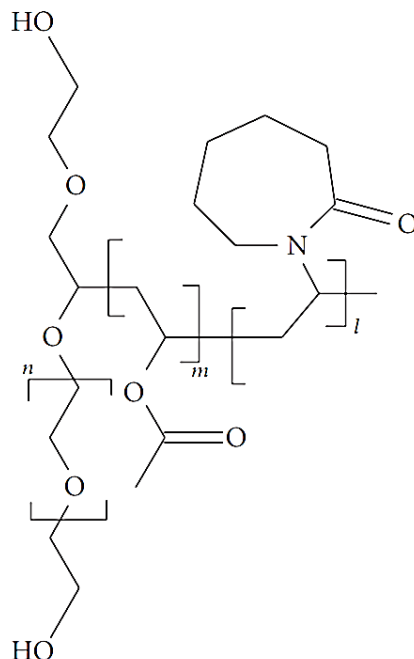


**Figure 2.3.** Soluplus® chemical structure [161].

## 2.2. Experimental Techniques

### 2.2.1. Manufacturing of the Drug-Loaded Filaments

#### 2.2.1.1. Hot Melt Extruder (HME)

HME technique was started as a processing technology in the plastic, rubber, and food industry in the early 1930s. In the 1970s, the use of the HME was expanded to the pharmaceutical industry and was used in the formulation, manufacturing, and development of pharmaceutical products [53], for example, implants [162], transdermal applications [163] and amorphous solid dispersion (ASD) to improve the bioavailability of poorly-water soluble APIs [164] [165]. HME, as described previously in section

(1.6.2.1), is a fusion process utilised to formulate ASDs [50]–[53]. An extruder generally consists of three parts: the feed zone (the hopper), the compression zone (the screw), and the metering zone (the die) (**Figure 2.4, a**) [10]. After the feeding step, the material is forced through the extruder by the rotating screws (single, or twin) which are positioned inside a cylindrical heated barrel [10]. At this stage, the material is melted compressed, and homogenised due to both the temperature from the barrel wall and the rotating screws [10]. The material thickness can be controlled by stabilising the extrudate flow in the metering zone. The sections in the barrel are interchangeable in most extruders to allow several configurations to be utilised and hence more flexibility during formulation. Then, the molten product is forced through the die plate. Following the exit from the die, it is cooled and moulded into the desired shape [10] [166]. The HME technique has been reported in a number of different studies as a suitable fabrication tool to produce ASD formulations [8] [167]–[169].

A benchtop single screw HME (Noztek Touch, Noztek LTD, West Sussex) (**Figure 2.4, b**) was utilised in this project to prepare different drug-loaded filaments (10%, 25%, and 50% FELD-PVA w/w), which were been used to fabricate the model tablets. This HME is equipped with two temperature-controlled barrels (T1 and T2) with a maximum of 300 C° for both zones, one screw, and a motor with 40 rpm. Moreover, it has two interchangeable extrusion nozzles (1.75 mm, and 3.00 mm) and a fan to cool the produced materials.

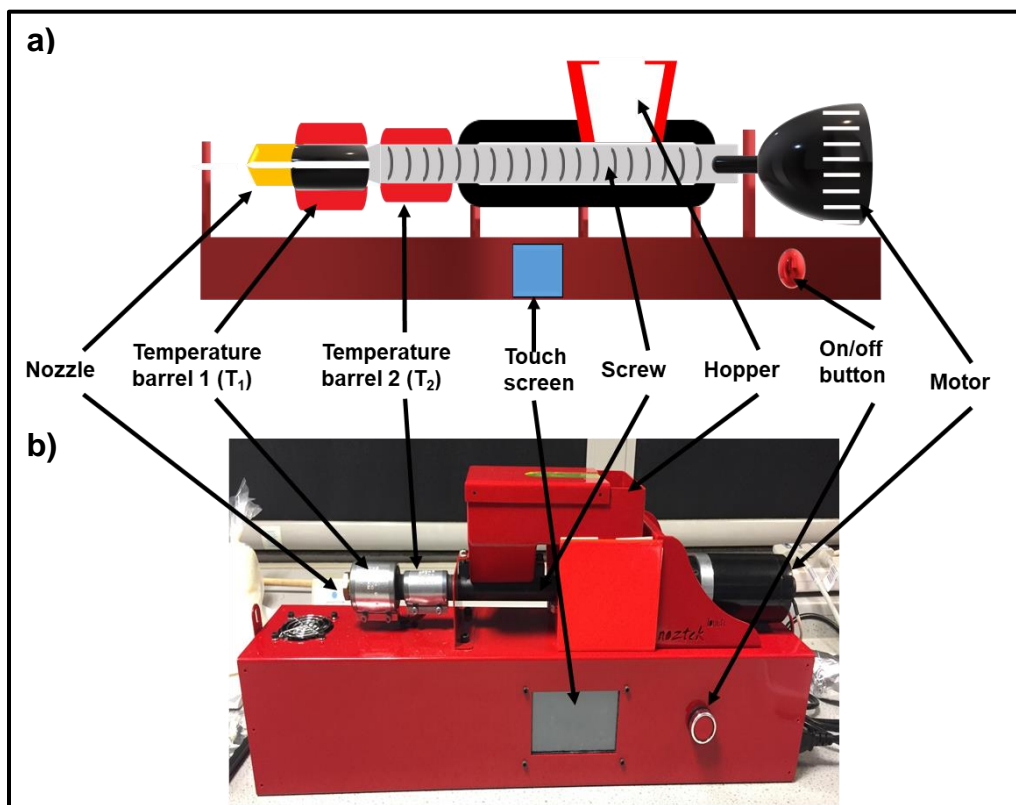


**Figure 2.4.** Single screw extruder instrument, a) Schematic diagram of the HME components, b) photographic image of the Noztek single screw HME utilised in the current thesis.

## 2.2.2. Fabrication of the Drug-Loaded Model Tablets

### 2.2.2.1. Fused Deposition Modeling (FDM)

As detailed in chapter 1, section (1.7.3.2). The FDM 3D printing instrument Ultimaker <sup>2+</sup> (Ultimaker, Netherlands) (**Figure 2.5**) was utilised in this research project to fabricate several drug-free and drug-loaded model tablets with different geometries, which have been used for the dissolution study.

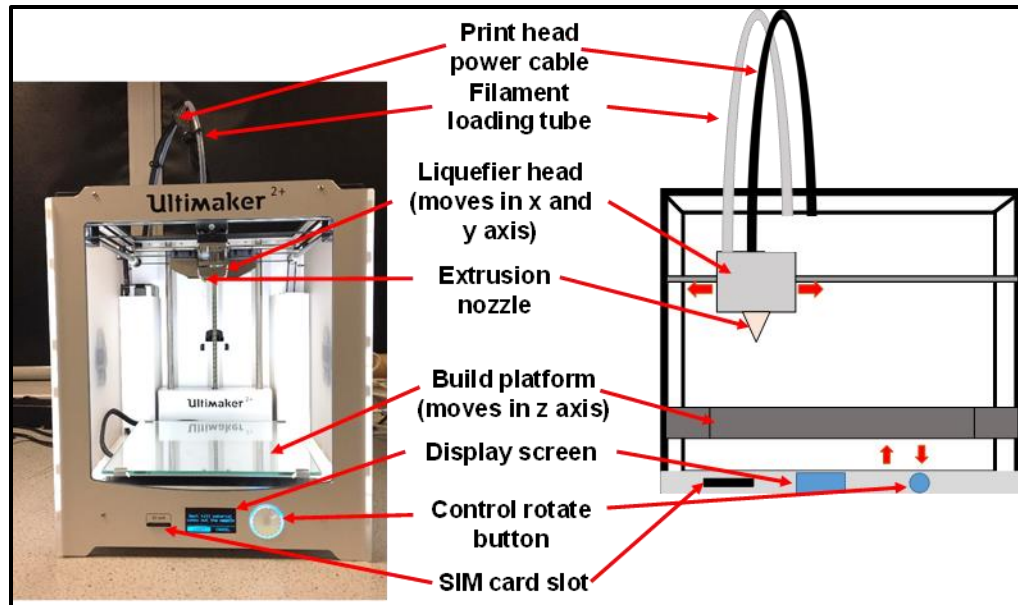


**Figure 2.5.** A photographic image (left) and a schematic diagram (right) of the Ultimaker<sup>2+</sup> FDM 3D printer.

### 2.2.3. Characterisation Techniques

#### 2.2.3.1. Scanning Electron Microscopy (SEM)

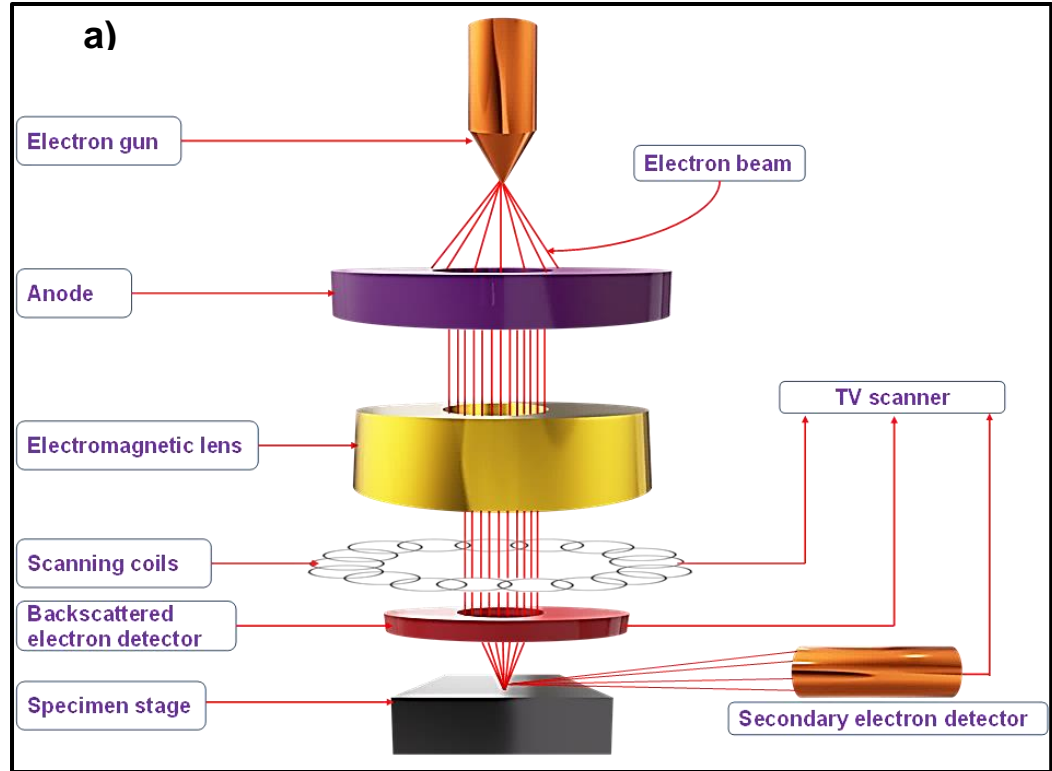
Scanning electron microscopy (SEM) is a powerful magnification tool that uses an electron beam instead of visible light to produce a high-resolution image [170]. As a result, SEM offers higher resolution, better magnification control, and larger depth of field (DOF) than the typical light microscope [170]. SEM spatial resolution can reach as low as 50-100 nm. Also, due to the use of a larger DOF with SEM in comparison to light microscopy, it allows more of a sample to be in focus at one time [170].

In the SEM, the produced focused beam interacts with the atoms on a sample surface, which generates different signals of various energy that contains information on the sample's composition and topography. An

electron optical column is used in the SEM to produce a focused beam. The SEM is composed of an electron source, anode, electromagnetic lens, scanning coil, sample stage, TV scanner and different detectors. The detectors can include secondary scatter electron detector (SED), backscatter electron detector (BSED), and X-ray detectors (**Figure 2.6, a**) [170] [171].

Utilising the SEM can provide various information about the material under study such as sample morphology, crystalline structure, and chemical composition. The SED is used to obtain morphological and topographic information about the sample. The BSED is useful to distinguish between numerous components. X-ray signals detected during the procedure are characteristic of the elements in the sample and could be used to determine the specimen chemical composition. Furthermore, the SEM can generate 3D images of the sample in black and white [170] [171].

A Scanning Electron Microscope SEM (XL30, Philips) fitted with an Oxford Instruments INCA EDX microanalysis system (**Figure 2.6, b**), was utilised to characterise the microstructure of manufactured filaments, and printed drug-free, and drug-loaded model tablets.



b)

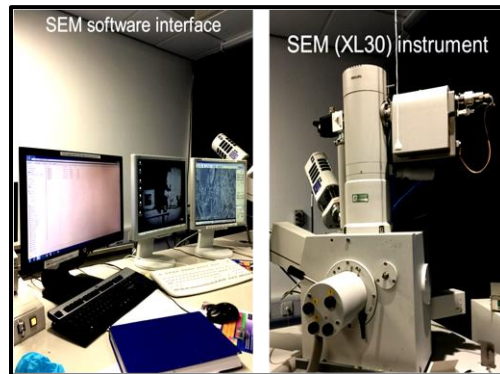


**Figure 2.6.** A schematic diagram of the SEM components (a), and a photographic images of the Scanning Electron Microscope (SEM) and display system (b). The figure was adapted from [170].

### 2.2.3.2. Differential Scanning Calorimetry (DSC)

DSC is one of the most widely used thermal analysis techniques in the characterisation of a variety of materials, including crystalline and amorphous pharmaceutical materials [172]. DSC can be used to measure thermal changes in a material as a function of time and temperature. In the DSC, both the sample and the reference are subjected to nearly the same temperature during the experiment. The changes in the material can be determined by measuring the changes in the heat flow related to the heating of a sample relative to heat flow to a reference material (**Figure 2.7, a**).

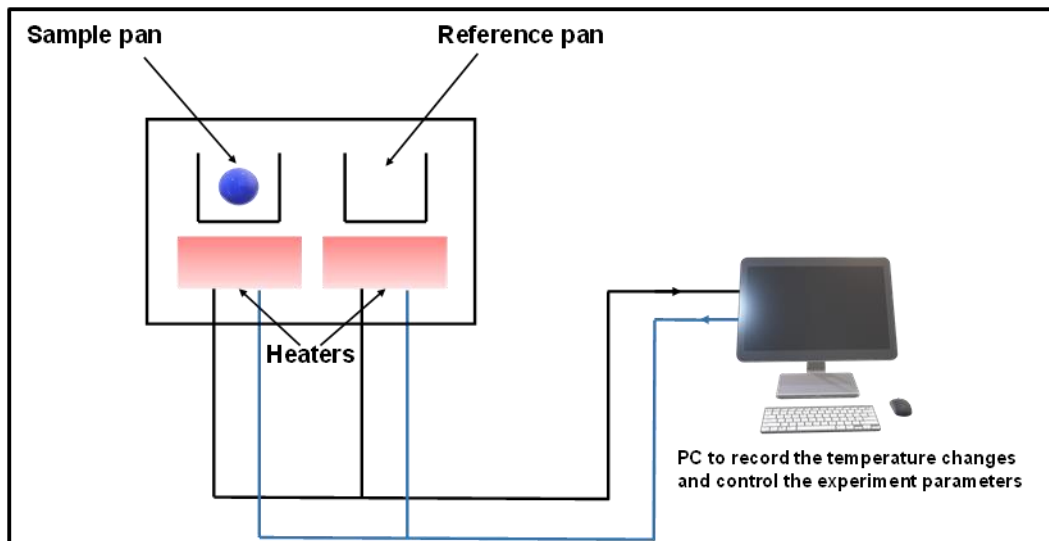
In case of endothermic event, heat is absorbed by the sample; thus, heat flow to the reference is lower than that to the sample. In contrast, the exothermic transition takes place when the heat flow to the reference is higher than the heat flow to the sample (in this case, the sample releases energy).

Moreover, DSC is capable of measuring numerous thermal changes related to a sample when it is heated or cooled in a controlled manner. The thermal transition that occurs in a material under study could be due to a chemical reaction or a physical transformation. Different physical transformations, such as exothermic, endothermic, and polymorph conversion, which are related to a change in enthalpy, can be detected utilising the DSC. Therefore, the DSC is a useful technique to provide fundamental information about the crystalline structure of a material. Furthermore, it could be used to investigate the changes in the heat capacity that happen during solid-state

transformation by measuring the heat flow when the sample is heated or cooled in a controlled manner. Consequently, it is a useful thermal technique to determine the glass transition temperature ( $T_g$ ) of amorphous materials [170] [172].

A TA discovery Q 2000 differential scanning calorimetry (DSC) instrument equipped with a refrigerated cooling unit (TA Instruments, New Castle, Delaware) (**Figure 2.7, b**) was utilised in this project to thermally analyse the model drug FELD and the polymers (PVA, and Soluplus®). Moreover, it was used to analyse the FELD-PVA, FELD-Soluplus® compositions and the prepared drug-loaded filaments and model tablets. In this aspect, the DSC was used to detect the  $T_g$  and the melting point of the crystalline FELD, PVA, and Soluplus®. In addition, it was utilised to determine the melting point depression of the different FELD-PVA and FELD-Soluplus systems used in this study, which were used to calculate the F-H interaction parameter ( $\chi$ ). Moreover, the DSC was used to investigate drug-polymer interactions and formation of ASD of the manufactured filaments as well as the fabricated model tablets. Also, it was employed to determine and quantify the crystallinity of the aged samples.

a)



b)

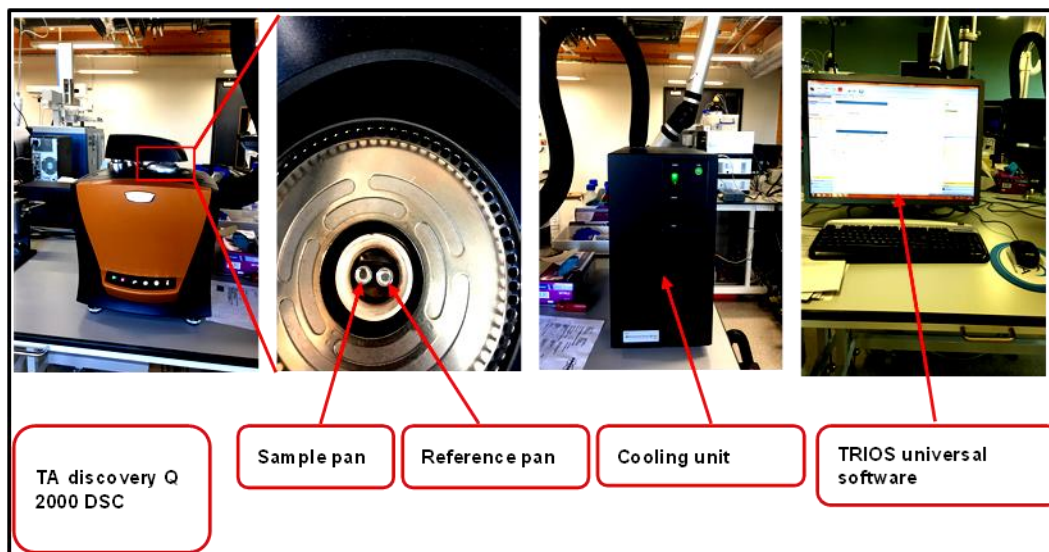


**Figure 2.7.** Schematic diagram of the DSC principles (a), Photographic images of the discovery DSC, cooling unit, and the TRIOS software interface (b).

### 2.2.3.3. Raman Spectroscopy

Raman spectroscopy is a commonly employed method to observe rotational, vibrational, and other low-frequency modes in a sample under study [173]. The vibrational energy range typically used is  $3500\text{-}50\text{ cm}^{-1}$  for Raman spectroscopy [170]. Raman spectroscopy has the ability to measure the Raman scattering, which is a phenomenon discovered by C. V Raman in 1928 [174]. It relies upon the inelastic light-scattering process between incident light (monochromatic light) and an irradiated ingredient [175]. Scattering occurs when the incident light (typically from a laser source) hits a sample. In this step, the light interacts with the substance molecules and polarises the electron cloud to form a short-lived state called (virtual state). Since the virtual state is unstable, the photons are immediately scattered to another relatively stable state [176]. Different scattering events are produced during the light-sample interaction, including, elastic scattering (Rayleigh scattering) and inelastic scattering (Raman scattering). In Rayleigh scattering, when the photons collapse to the ground state, the scattered light and the incident light have the same energy level and thus there is no change in the wavelength and photon frequency (**Figure 2.8, a**) [176] [177].

In Raman scattering, the scattered photons fall to a new energy level different from the ground state (initial level), energy transfer occurs, i.e., the photon gains or loses some amount of energy, resulting in the laser photon being shifted down or up, which provides information related to the

vibrational process in the system [176]. Raman scattering is directly related to the vibrated molecules [170]. Raman scattering (inelastic scattering) can be classified into two types including, Stokes Raman scattering and anti-Stokes Raman scattering. In Stokes Raman scattering, when the photons are excited from the ground state to the virtual state, they fall back to higher energy level rather than falling to the initial state, a new photon with less energy and longer wavelength is released (**Figure 2.8, b**). The difference in wavelength between the released photon and the incoming photon is called Raman shift. In anti-Stokes Raman scattering, photons fall back from the excited state to the ground state after being irradiated by the monochromatic light and thus the scattered photon is characterised by higher energy and shorter wavelength than the incoming photon (**Figure 2.8, c**) [170].

A Raman spectrometer is composed of three primary parts: an excitation source, a detector, and a sampling apparatus, in which a laser source acts as an excitation source, a microscope acts as a sampling apparatus, and a charged coupled device (CCD) acts as a detector. In the spectrometer, gratings are used to spatially split the different wavelengths. Moreover, the optical filter is utilised to remove the Rayleigh scattering [170].

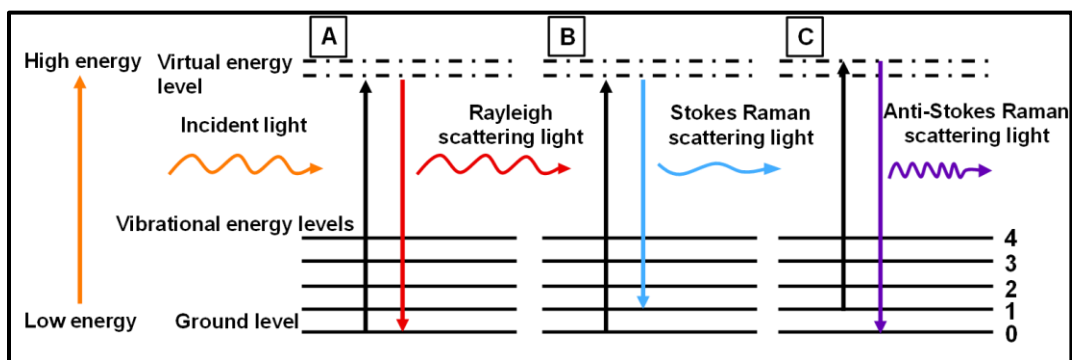


**Figure 2.8.** Schematic representations of the Raman and Rayleigh scattering processes: (a) Rayleigh scattering, (b) Stokes Raman scattering, and (c) Anti-Stokes Raman scattering. The figure was inspired from [178].

A confocal Horiba-Jobin-Yvon LabRAM system (Horiba-Jobin-Yvon Ltd., Middlesex, UK), (**Figure 2.9**), was utilised in this work. This instrument is equipped with four different laser excitation capabilities including A) NIR (785 nm), B) red (660 nm), C) green (532 nm), and D) UV (325 nm). In this work, characterisation of all the samples was performed by using a 785 nm laser. The detector that was used in this study is a 1024-pixel silicon charge-coupled device detector (CCD).

The Raman spectroscopy was employed in this work to determine the Raman spectra of the raw materials, including crystalline FELD, quenched cooled FELD, PVA polymer, and different FELD-PVA physical mixtures. Moreover, it was utilised to characterise the prepared drug-loaded filaments (10%, 25%, and 50% FELD-PVA w/w) and the fabricated model tablets of

the same compositions to determine the formation of the ASD. In addition, it was utilised to determine the distribution of the FELD in the 3D fabricated model tablets. Also, it was used to characterise the freshly printed and the aged model tablets to differentiate between the crystalline and the amorphous forms of the FELD within the fabricated tablets.

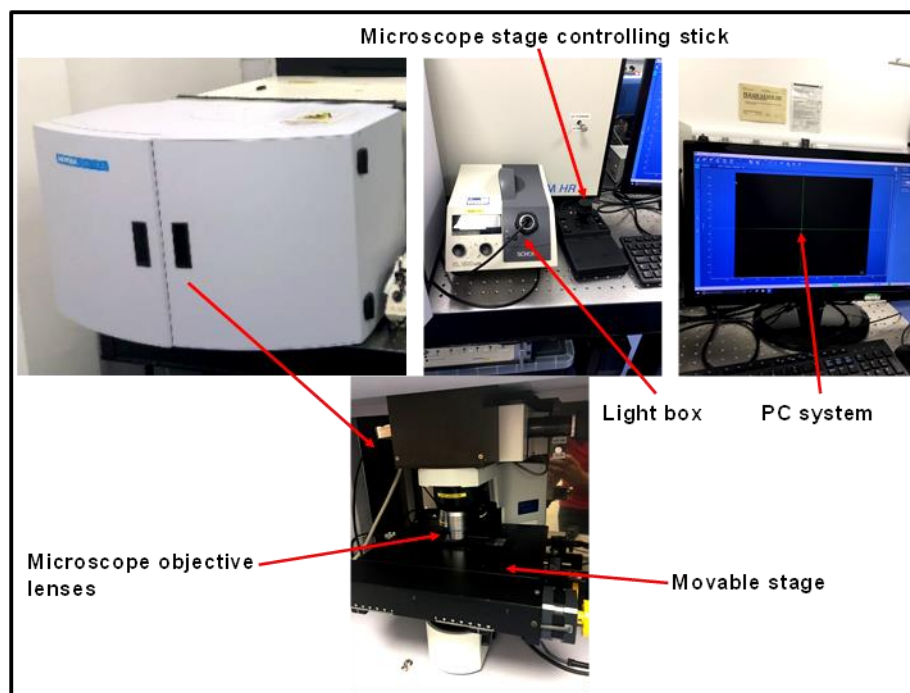


**Figure 2.9.** Photographic image of the Raman instrument (confocal Horiba-Jobin-Yvon LabRAM system).

#### **2.2.3.4. Attenuated Total Reflectance-Fourier Transformed Infrared Spectroscopy (ATR-FTIR)**

ATR-FTIR spectroscopy is a rapid and non-destructive absorption technique, and it is commonly utilised to analyse samples in liquid, semisolid, and solid states with minimal sample preparation [170]. FT-IR is utilised generally to probe the middle infrared range from 400-4000  $\text{cm}^{-1}$  [170]. FT-IR spectra offer information on the rotational and vibrational changes within the molecules under analysis. The general regions in which several types of FT-IR vibrational bands are found can be divided into two main regions, including a) the fingerprint region, and b) the group frequency region. For the fingerprint region, the infrared spectrum can be found in the 1450-600  $\text{cm}^{-1}$  region. This region is usually complicated and it is hard to allocate all the absorption peaks for the material under study [170]. In contrast, for the group frequency region, the infrared spectrum can be found in the 4000-1450  $\text{cm}^{-1}$  region. Bands in the group frequency region usually have reasonable separation and are related to diatomic units stretching vibrations [170]. This region is useful for structure elucidation and organic compound identification [170].

FT-IR spectroscopy technique is widely utilised to differentiate between solid forms, such as salts, solvates, polymorphs, and amorphous forms [170]. Moreover, it also utilised for raw material identification and qualification, quantitative analysis of material compositions, and phase transformation analysis at controlled humidity and temperature [170]. Recently, ATR-FTIR

spectroscopy has been widely applied to generate chemical imaging during the dissolution process. For example Chan et al., have used ATR-FTIR spectroscopy to study solid dispersions of nifedipine (BCS class II drug) in poly(ethylene glycol) (PEG) and dissolution in water [179].

In ATR-FTIR, an infrared beam is passed onto an optically dense crystal, which has a high refractive index, at an angle greater than the critical angle; thus, total internal reflection occurs [180]. Then, this internal reflection generates an evanescent wave which extends beyond the crystal surface into the sample in contact with the crystal [180]. This evanescent wave penetrates on a few microns ( $0.5\ \mu\text{m}$  -  $5\ \mu\text{m}$ ) of the sample under analysis [180]. After that, when the sample absorbs energy in the infrared spectrum regions, the evanescent wave will be altered or attenuated (**Figure 2.10**) [181].

An ATR-FTIR spectrometer (Agilent Technologies FTIR, Cary 360, Santa Clara, CA, USA) (**Figure 2.10**) was utilised in this research project to obtain the spectra of the crystalline FELD, PVA, as received, the FELD-PVA physical compositions. In addition, it was used to characterise the prepared filaments, and the fabricated model tablets (fresh and aged) to assess the formation of the ASD and, hence, to determine the formation of the crystals in the aged model tablets.

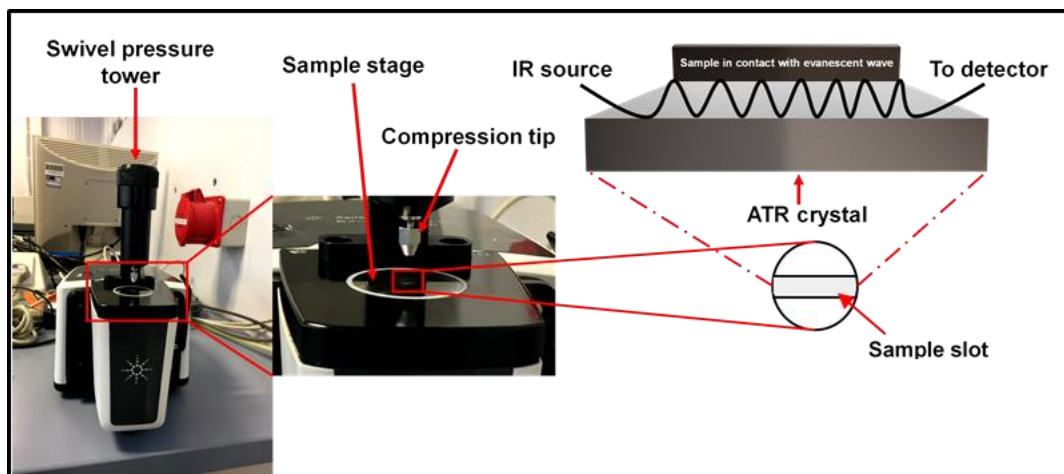


**Figure 2.10.** Photograph image of the ATR-FTIR (Agilent Cary 360 FTIR), and schematic diagram of the ATR-FTIR principles.

#### 2.2.3.5. X-Ray Powder Diffractometer (XRPD)

XRPD is a technique utilising X-ray diffraction that allows the operator to characterise the solid-state properties of pharmaceutical material such as amorphous, crystalline, or a mixture, in powder form [170]. Classically, these various materials can be easily distinguished by XRPD, since an amorphous form does not possess long-range order and shows diffuse diffraction (broad Bragg peaks), whereas, in contrast, a solid crystalline material has an ordered structure, which shows sharp, distinct diffraction peaks at different diffraction angles [170].

XRPD has shown great ability for the quantification, and fingerprinting of the amorphous pharmaceutical formulations [182]. It is commonly used for ASD solid-state characterisation [183]. **Table 2.1** illustrates different applications of XRPD in ASD characterisation [183]. XRPD utilises X-ray diffractometers

to collect data of pharmaceutical materials. An X-ray diffractometer is consists of an X-ray source, sample holder, and a detector (**Figure 2.11**) [170]. In XRPD, an X-ray source generates a divergent monochromatic beam. Then, the divergent beam bombards target material and produces a divergent diffraction beam. Thereafter, the diffracted beam is focused on the detector, which records and processes the generated X-ray signal and converts them to a count rate, which is then output to a device such as a computer monitor [170] [184].

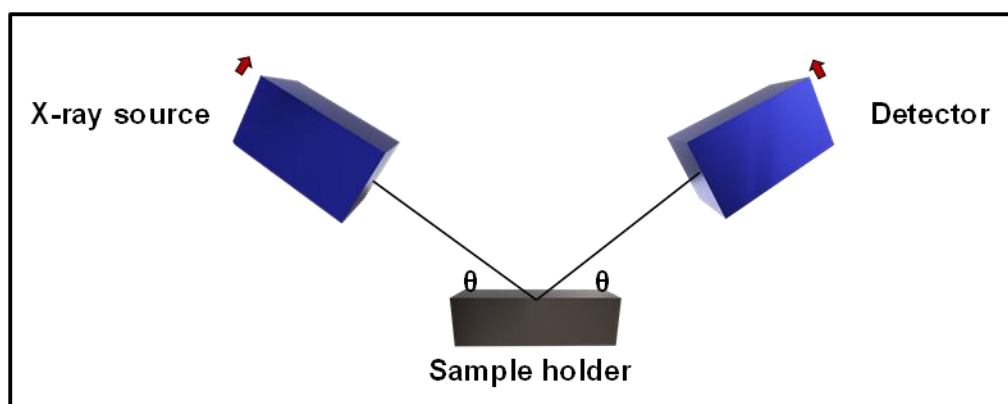


**Figure 2.11.** Schematic diagrams of the essential components of the XRPD. The figure was inspired from [170].

An X'Pert PRO (PANalytical, Almelo, Netherlands) XRPD was used in the current thesis to obtain the x-ray patterns of the crystalline FELD, and the PVA. Moreover, it was employed to determine the formation of the ASD of the manufactured filaments as well as the 3D fabricated model tablets. Furthermore, it was used to detect the crystallinity of the aged model tablets.

**Table 2.1.** A summary of the applications, advantages, and disadvantages of XRPD in ASD characterisation [183].

Technique	Applications	Advantages	Disadvantages	Reference
XRPD	<ul style="list-style-type: none"> <li>- Differentiating between crystalline and amorphous forms</li> <li>- Evaluating degree of crystallinity</li> <li>- investigating phase transformation such as dehydration, hydration, polymorph conversion, and the crystallisation of amorphous materials</li> <li>- Quantitatively analysing the polymorph, amorphous forms, and hydrates, content in a crystalline material</li> </ul>	<ul style="list-style-type: none"> <li>- Small sample size</li> <li>- Easy to use</li> <li>- Qualitative and quantitative</li> <li>- Very little sample preparation</li> <li>- Non-destructive technique</li> </ul>	<ul style="list-style-type: none"> <li>- No chemical structure information</li> <li>- Less sensitive than Raman and FTIR(&gt; 5% crystallinity)</li> </ul>	<ul style="list-style-type: none"> <li>[185]</li> <li>[186]</li> <li>[187]</li> <li>[188]</li> </ul>

## **2.2.4. In-Vitro Drug Release Study**

### **2.2.4.1. In-Vitro US Pharmacopoeia Dissolution Apparatus**

Dissolution studies are mainly conducted to study various drug products for different purposes, for instance, batch to batch product quality assessment, and to guide new formulation development. Furthermore, it is utilised to monitor API performance and quality after certain changes in formulation, method, location, and scale-up process [170]. It is usually used to evaluate drug release profiles of API from products such as tablets, transdermal patches, and capsules. For a conventional dissolution study, a dosage form is placed in a dissolution vessel which has a fixed volume of dissolution medium in a specific USP dissolution apparatus and operated at a certain agitation rate. Then, the quantity of drug dissolved in the medium is investigated by using different instruments such as high-performance liquid chromatography (HPLC) or UV spectrophotometric. The dissolution experiment data is usually plotted as percentage drug released as a function of time, which is commonly called a dissolution profile. Dissolution experiment is usually designed to fit the products release profiles, either controlled release or immediate release [170].

Dissolution testing is a time-dependent process, which involves several physical alterations such as the disintegration of tablets or capsules to their primary particles, drug molecules movement from the solid surface, and the API molecules diffusion across the diffusion layer that is adjacent to the solid surface [170].

A successful dissolution testing depends on suitable process development. For example, selecting an appropriate dissolution medium for the study, medium volume, apparatus type, rate of stirring, and method of analysis. Identifying an appropriate dissolution apparatus and a suitable dissolution medium are the most critical steps associated with a dissolution experiment [170].

There are seven types of the US Pharmacopoeia (USP) dissolution apparatuses that are available to study several dosage forms as illustrated in (**Table 2.2**). Apparatus I (basket apparatus), and apparatus II (paddle apparatus), are both commonly utilised in quality control assessment of capsules and tablets with delayed, extended, and immediate release features. Furthermore, both apparatuses have a simple design and both methods employ a large volume of dissolution media (500–1000 mL). Apparatus III (reciprocating cylinder), and apparatus IV (flow-through cell apparatus), are both considered to have hydrodynamics which are mimicking gastrointestinal tract (GIT) physiological conditions. Testing immediate-release (IR) and extended-release (ER) pharmaceutical oral dosage forms are mostly applicable with dissolution apparatus III. Whereas, Apparatus IV is commonly used for poorly water-soluble APIs and ER oral dosage products. Apparatus V (paddle over disk) and Apparatus VI (cylinder apparatus) are both apparatuses which are utilised to examine transdermal dosage forms. Apparatus VII (reciprocating holder) is appropriate to

evaluate non-disintegrating oral modified release pharmaceutical dosage forms [170].

In this research project, USP dissolution (Dis8000, Copley Scientific Limited, UK) apparatus I, (**Figure 2.12**) was utilised to investigate the FELD drug release form the fabricated 3D printed model tablets including fresh and aged model tablets (controls and formulations). After that, the concentration of the FELD in the dissolution medium was analysed by UV vis spectroscopy (Cary, 50 Bio, Australia).

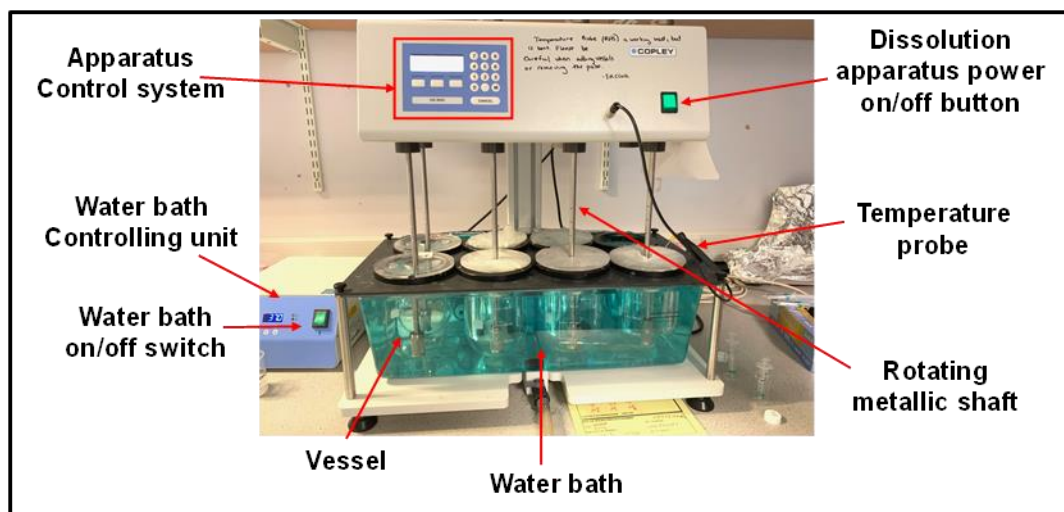


**Figure 2.12.** Photographic image of a dissolution apparatus (Dis8000, Copley Scientific Limited, UK).

**Table 2.2.** Official dissolution apparatus types and their applications [170].

Sr.No	Official name	Description	Rotation speed (RPM)	Uses
1	USP Apparatus I	Basket	50-120	Tablets, capsules, Floating dosage forms, and chewable tablets
2	USP Apparatus II	Paddle	25-100	Tablets, capsules, and enteric forms
3	USP Apparatus III	Reciprocating cylinder	6-35	Beads, pellets, soft gelatin capsules, suppositories, and implants
4	USP Apparatus IV	Flow-through cell	_____	Suppositories, modified-release tablets, implants, Soft gelatin capsules, and poorly soluble drugs
5	USP Apparatus V	Paddle over disk	25-50	Transdermal dosage form
6	USP Apparatus VI	Cylinder apparatus	_____	Transdermal dosage form
7	USP Apparatus VII	Reciprocating holder	30	Extended-release drug products, and transdermal dosage form

## **3. Chapter 3: Utilising the Flory-Huggins Theory to Predict Felodipine Miscibility in Polyvinyl Alcohol (PVA) and Soluplus®**

### **3.0. Novelty in this Chapter**

Recently, the temperature-composition phase diagram based on the Flory-Huggins theory, has been presented as a pre-formulation tool for polymer selection to gain insight to drug-polymer interactions and to decide an API loading in the polymer [151]. In the present study, the miscibility of FELD with PVA was estimated for the first time using the F-H interaction parameter,  $\chi$ , that was calculated from the DSC data utilising the melting point depression endset ( $T_{\text{end}}$ ) approach [76] [62] [74]–[76]. Also, the F-H theory-based temperature composition phase diagram of the FELD-PVA system was successfully constructed for the first time in the present study.

### **3.1. Introduction**

As previously mentioned in chapter 1, incorporation of APIs, specifically BCS class II ingredients (low water-soluble/high permeable), into a polymer matrix to formulate solid dispersions is a promising method to improve the dissolution behaviour of the low water-soluble APIs [21] [163] [164]. Moreover, ASDs have shown an ability to sustain an API in

the amorphous state during manufacturing and storage. However, as soon as the API concentration in the polymeric matrix exceeds a particular drug-polymer ratio, the API will tend to re-crystallise, leading to low bioavailability [8] [69] [166].

Several hydrophilic carriers (polymers) have been successfully utilised to improve oral bioavailability through either increasing the API concentration and/or improving the API dissolution rate [67] [181] [182]. Each polymer possesses several physical and chemical features, such as melting temperature ( $T_m$ ), molecular weight, functional groups, and glass transition temperature ( $T_g$ ). Thus, every polymer has a distinctive ability to inhibit the API re-crystallisation at a particular drug-polymer ratio and to maintain the amorphous form in the dispersion at a particular drug-polymer concentration [193].

As previously discussed in chapter 1, different factors can affect the stability of the ASD, such as temperature and relative humidity [65]-[67]. Therefore, these properties have to be considered during the selection of appropriate API/polymer combinations to prepare a homogenous one phase ASD system in order to maintain supersaturation during dissolution and long-term stability [43].

Lately, thermodynamic models, which were originally established for polymer-solvent and polymer-polymer systems, have been successfully utilised to predict drug-polymer solubility and miscibility in the polymeric matrix [68] [71] [72] [73] [75] [187]–[189]. The term solubility is defined as the ability of a polymer to dissolve a crystalline API. In contrast, the

term miscibility can be defined as the ability of an amorphous API to mix with an amorphous polymer producing one-phase system [64] [71]. ASD systems are considered to be stable only below the solubility limit of the API in the polymer without any concern for the API re-crystallisation [197]. However, due to the limited solubility of most drugs in the commonly used polymers, the preparation of ASDs is generally restricted to only very low dose APIs [197]. Thus, because the miscibility is always greater than the solubility of the API in a particular polymer, certain works are invested to predict the drug miscibility with the polymer [197]. Under the limit of miscibility, only significant temperature and/or compositions variations can destabilise drug-polymer system toward drug re-crystallisation [197]. Thus, it is important to estimate the drug-polymer miscibility in order to choose the appropriate drug loading, the suitable polymer, and the proper method to manufacture a homogenous single-phase ASD system [76]. Thermodynamic modelling enables the free energy of mixing between the polymer and the API to be estimated with regards to temperature and compositions of the formulation. This approach, depending on Flory-Huggins theory [198], enables construction of composition-temperature phase diagrams. The composition-temperature phase diagram, which separates the drug-polymer binary system in to three regions, i.e. stable, metastable, and unstable zones, helps the formulation scientist to select proper processing conditions and drug-polymer compositions during ASD formulation [197].

Consequently, different approaches have been reported in the literature [53] [175]–[177] to estimate the drug-polymer miscibility for numerous

ASD systems. Such strategies include the use of differential scanning calorimetry (DSC) experimental data to calculate the Flory-Huggins interaction parameter  $\chi$  using the endset ( $T_{\text{end}}$ ) melting point depression (MPD) method, which may be used to construct drug-polymer binary phase diagrams [62] [76] [74]–[76]. Moreover, the solubility parameters calculation method was used to estimate the drug-polymer miscibility [53] [175]–[177]. For example, Tian et al. have successfully estimated solubility/miscibility of two ASD systems, namely felodipine (FELD)-hydroxypropyl methylcellulose (HPMC) and FELD-Soluplus® systems utilising both the DSC endset MPD method, and the solubility parameter calculations approaches [76]. They found that the interaction parameter  $\chi$  of the FELD-HPMC is slightly positive, indicating immiscibility between the drug and the polymer. Moreover, they found that the interaction parameter  $\chi$  of the FELD-Soluplus systems is slightly negative, which indicates that the FELD-Soluplus® system is a miscible system [76]. In another study, Marsac et al. used the MPD and the solubility parameters methods to estimate the F-H interaction parameters,  $\chi$ , for two drugs, namely felodipine and nifedipine with polyvinyl pyrrolidone (PVP). The derived F-H interaction parameter,  $\chi$ , from the MPD method were negative indicating that mixing was favourable for both systems [199]. Also, Baghel et al., has investigated different ASD systems of cinnarizine and dipyridamole in polyacrylic acid (PAA) and (PVP) at different drug loadings, utilising practical and theoretical examinations related to drug-polymer miscibility, including solubility parameter method and the MPD approach based on the F-H theory in the presence of moisture and effect

of drug loading on F-H interaction parameter [80]. The composition dependent F-H interaction parameter,  $\chi$ , and the miscibility were predicted utilising moisture and thermal analysis in their study. Dipyridamole-PVP, dipyridamole-PAA, and cinnarizine-PAA systems demonstrated mixing at the molecular level for all the utilised drug loadings, while cinnarizine-PVP showed immiscibility for drug loadings over 50% (w/w) [80].

Consequently, in the present piece of work, we intended to examine the strength of FELD interactions with two polymers, namely PVA and Soluplus®. Moreover, we also estimated the miscibility limits of FELD with both polymers (PVA and Soluplus®) through the calculation of the F-H interaction parameter,  $\chi$ , using both the DSC melting point depression (MPD) method and solubility parameters approach.

### **3.2. Aims and Objectives**

As mentioned in chapter 1, section (1.7), we intended to predict the miscibility limits of one low water-soluble ingredient, which is FELD, in two polymeric carriers, including PVA and Soluplus®, in which below this limit we can formulate a homogenous one phase ASD tablet and above it, we can produce a tablet spiked with crystalline seeds.

This aim can be achieved through the use of the solubility parameter calculations method to estimate the miscibility of the FELD with the PVA and Soluplus®. Also, the DSC was utilized to determine the MPD for the FELD-PVA and FELD-Soluplus® systems. Then, to calculate the F-H interaction parameter  $\chi$  from the DSC data utilising the MPD endset ( $T_{\text{end}}$ )

approach. Next, Gibb's free energy of mixing of the different FELD-PVA and FELD-Soluplus® compositions was predicted. After that, to construct the composition phase diagram for both systems. This procedure can be utilised as a road map to guide the selection of suitable drug/polymer compositions and to optimise the processing conditions to formulate two different formulations (homogenous one phase ASD and spiked SD), which will be used later as model systems to test the impact of crystallinity on the drug release behaviour using the USP dissolution apparatus.

### **3.3. Materials and Methods**

#### **3.3.1. Materials**

As detailed in chapter 2, section (2.1)

#### **3.3.2. Methods**

##### **3.3.2.1. Physical Preparation of Different Drug-Polymer Compositions**

Prior to the thermal analysis experiments, the FELD-PVA, and FELD-Soluplus® with different drug loadings, including (5/95, 10/90, 20/80, 25/75, 35/65, 50/50, and 75/25) (FELD/PVA w/w %), and (20/80, 25/75, 35/65, 50/50, and 75/25) (FELD-Soluplus® w/w %) were physically mixed using a mortar and pestle to achieve the maximum physical uniformity between the drug and the polymer.

##### **3.3.2.2. Melting Point Depression (MPD)**

The melting point of the crystalline FELD and the dissolution-end point ( $T_{\text{end}}$ ) of the different drug-polymer compositions were determined

utilising TA discovery Q 2000 differential scanning calorimetry (DSC) instrument equipped with a refrigerated cooling unit (TA Instruments, New Castle, Delaware). A minimum amount of the previously prepared samples were weighed within the size range of 5-10 mg. After that, the measured samples were sealed in new Tzero aluminium hermetic pans and sealed with a hermetic lid. The heating rate was 10 °C/min and nitrogen gas was as a purge gas with a flow rate of 50 ml/min. All the samples were heated from 25-200 °C. Then, the thermogram of each sample was recorded using TRIOS data analysis software (n=1).

### **3.3.2.3. T<sub>g</sub> Measurements of Different Drug-Polymer Mixtures**

Similar compositions as used in section (3.3.2.1) were used to determine the T<sub>g</sub> of the raw materials, FELD-PVA, and FELD-Soluplus® systems. The same method, as detailed in section (3.3.2.2), was used to measure the T<sub>g</sub> of the mixtures; however, a heat/cool/heat cycle was utilised in this case to detect the T<sub>g</sub> of the different drug-polymer compositions. All samples, including the pure drug, were heated to 200 °C at 10 °C/min followed by cooling cycles to 0 °C at 10 °C/min. After that, the samples were immediately heated up to 200 °C at 10 °C/min. Then, the T<sub>g</sub> mid-value was detected from the second heating cycle [77] (n=1).

### 3.3.2.4. Determination of Gibb's Free Energy of Mixing

Gibb's free energy changes of mixing a drug-polymer binary system may be expressed according to the F-H theory as in (Equation 3.1):

$$\Delta G_{\text{mix}} = \Delta H_{\text{mix}} - T\Delta S_{\text{mix}} \quad (3.1)$$

Then, Gibb's free energy of mixing may be expressed as a function of the F-H interaction parameter  $\chi$  as in (Equation 3.2) [76]:

$$\Delta G_{\text{mix}} = RT \left( \frac{\Phi_{\text{drug}}}{N_A} \ln \Phi_{\text{drug}} + \frac{\Phi_{\text{polymer}}}{N_B} \ln \Phi_{\text{polymer}} + \chi_{\text{drug-polymer}} \Phi_{\text{drug}} \Phi_{\text{polymer}} \right) \quad (3.2)$$

Where  $\varphi$  is the volume fraction of the drug and the polymer,  $N$  is the drug or polymer molecular volume,  $\chi$  is the F-H interaction parameter,  $R$  is the universal molar gas constant, and  $T$  is the temperature. In a drug-polymer blend,  $N_A$  may be defined as the drug molecular size, in which  $N_B = mN_A$ , where  $m$  is the ratio of the volume of a polymer chain to drug molecular volume (Equation 3.3) [76].

$$m = \frac{\frac{Mw_{\text{poly}}}{\rho_{\text{poly}}}}{\frac{Mw_{\text{drug}}}{\rho_{\text{drug}}}} \quad (3.3)$$

Where  $Mw_{poly}$  is the molecular weight of the solvent (polymer),  $Mw_{drug}$  is the molecular weight of the solute (API), the  $\rho_{poly}$ , and  $\rho_{drug}$  are the density of polymer and drug respectively. The drug and the polymer densities utilised in the present chapter were obtained from the literature [82] [200].

Thus, the free energy of mixing for a drug-polymer binary system may be written alternatively as in (Equation 3.4) [76]:

$$\Delta G_{mix} = RT (\varphi_{drug} \ln \varphi_{drug} + \frac{\varphi_{polymer}}{m} \ln \varphi_{polymer} + \chi_{drug-polymer} * \varphi_{drug} \varphi_{polymer}) \quad (3.4)$$

Where  $\varphi$  is the volume fraction of the drug and the polymer,  $\chi$  is the F-H interaction parameter, R is the universal molar gas constant, T is the temperature, and  $m$  is the ratio of the volume of a polymer chain to drug molecular volume, as shown previously in (Equation 3.3) [76].

### 3.3.2.5. Determination of the F-H Interaction Parameter-

#### $\chi$

The values of the F-H interaction parameter,  $\chi$ , of the drug-polymer blend may be predicted using MPD data obtained from DSC experiments in the current chapter utilising (Equation 3.5) [25] [26].

$$\left(\frac{1}{T_{m_{mix}}} - \frac{1}{T_{m_{pure}}}\right) = -\frac{R}{\Delta H_{fusion}} \left[ \ln \varphi_{drug} + \left(1 - \frac{1}{m}\right) \varphi_{polymer} + \chi_{drug-polymer} \varphi_{polymer}^2 \right] \quad (3.5)$$

Where  $\varphi$  is the volume fraction of the drug and the polymer,  $T_{m_{mix}}$  is the melting point of the crystalline drug in the drug/polymer mixture,  $T_{m_{pure}}$  is the melting point of the pure drug,  $R$  is the universal molar gas constant, and  $\Delta H_{fusion}$  is the heat of fusion of the pure drug.  $m$  is the ratio of the volume of a polymer chain to drug molecular volume and can be obtained from (Equation 3.3) [76].

Consequently, the calculated  $\chi$  values derived from the MPD data at temperature close to the FELD melting point were employed in equation (3.4) to construct the plot of Gibb's free energy of mixing as a function of temperature and composition [71]. However, the F-H interaction parameter  $\chi$  values obtained from the MPD approach are applicable only at the FELD melting point temperature and cannot be employed to estimate the drug-polymer miscibility at temperatures below the FELD melting point. It has been shown that F-H interaction parameter,  $\chi$ , changes with composition and temperature [196] [201]. In comparison to the effect of the temperature on the F-H interaction parameter  $\chi$ , the effect of the composition on  $\chi$  is considered negligible; hence, the temperature dependence of the  $\chi$  can be extrapolated using (Equation 3.6) [76]:

$$\chi_{\text{drug-polymer}} = A + \frac{B}{T} \quad (3.6)$$

Where A is referred to as the non-combinational (entropic) contribution to the F-H interaction parameter  $\chi$ , while B/T is referred to as the enthalpic contribution [202]. By plotting  $\chi$  versus 1/T, a linear relationship was obtained in the present study for FELD-PVA, and FELD-Soluplus® systems, which allowed calculation of constant “A” (intercept) and “B” (slope). Consequently, the obtained values of constant “A” and “B” allowed us to calculate the  $\chi$  at temperatures lower than the FELD melting point (147 °C). Then, the F-H interaction parameter  $\chi$  obtained from equation (3.6) at different temperatures were used in equation (3.4) to predict Gibb’s free energy of mixing as function of temperature and compositions for both systems (FELD-PVA, and FELD-Soluplus®) in the temperature range of 25 °C to 140 °C.

Also, the F-H interaction parameter  $\chi$  can be determined at room temperature using the solubility parameters approach [76]. In this chapter, the solubility parameters approach was used to calculate  $\chi$  and to compare it with the  $\chi$  that was calculated at room temperature using equation (3.6). Moreover, it was used to predict the miscibility of the FELD-PVA and FELD-Soluplus® systems. The solubility parameters values for the API (FELD) and the carriers (PVA and Soluplus®) used in the present chapter were obtained from the literature and used to calculate  $\chi$  at room temperature using (Equation 3.7) [201]:

$$\chi = \frac{V_0}{RT} (\delta_{\text{drug}} + \delta_{\text{polymer}})^2 \quad (3.7)$$

Where  $V_0$  is the volume of lattice site,  $\delta$  is the solubility parameter of the drug and the polymer,  $R$  is the universal gas constant, and  $T$  is the absolute temperature [76].

### 3.3.2.6. Construction of Composition Phase Diagram

The solid-liquid transition curve (solubility) of the drug-polymer mixtures was obtained by employing the  $\chi$  values obtained from the MPD data at different temperatures in equation (3.5) allowing the  $T_{m_{\text{mix}}}$  of each drug-polymer composition to be predicted [19] [24]. Moreover, the spinodal curve (miscibility) of the drug-polymer mixtures was predicted using Equation 3.8, which can be obtained by equating the second derivative of Gibb's free energy to zero, equation (3.4), and combining it with equation (3.6) as follows [196]:

$$\chi(T) = \frac{2B}{\left(\frac{1}{\phi_{\text{drug}}}\right) + \left(\frac{1}{m - (1 - \phi_{\text{polymer}})}\right) - 2A} \quad (3.8)$$

Where  $A$  is the non-combinational (entropic) contribution to the F-H interaction parameter  $\chi$ , while  $B$  is the enthalpic contribution [202],  $\phi$  is the volume fraction of the drug and the polymer, and  $m$  is the ratio of the volume of a polymer chain to drug molecular volume.

The  $T_{g_{mix}}$  of the FELD-PVA and FELD-Soluplus® systems were predicted using the Gordon-Taylor equation for two components as expressed in (Equation 3.9) [203]:

$$T_{g_{mix}} = \frac{w_1 T_{g1} + K w_2 T_{g2}}{w_1 + K w_2} \quad (3.9)$$

Where  $w_1$  and  $w_2$  are the weight fraction of drug and polymer respectively,  $T_{g1}$  and  $T_{g2}$  is the glass transition temperature of drug and polymer respectively, while  $K$  can be calculated using the  $T_g$  and densities,  $\rho$ , of each component as represented in (Equation 3.10):

$$K \approx \frac{\rho_1 T_{g1}}{\rho_2 T_{g2}} \quad (3.10)$$

The obtained solid-liquid transition curve ( $T_{m_{mix}}$ ) and the spinodal curve (miscibility) for both systems were plotted as a function of drug weight fraction and temperature. Then, this information accompanied by the predicted  $T_{g_{mix}}$  obtained using equation 3.9 [203] and 3.10 along with the experimental  $T_{g_{mix}}$  of both systems obtained using DSC in the present study were used to construct the composition phase diagrams for the FELD-PVA and FELD-Soluplus® systems [76].

### 3.4. Results and Discussion

#### 3.4.1. Drug-Polymer Miscibility Utilising Solubility

##### Parameters Approach

The difference in the solubility parameters between the model drug and the carriers was utilised to estimate the miscibility of two systems [204] [205]. It has been reported that ingredients with a difference in solubility parameters lower than  $\sim 7 \text{ (MPa)}^{1/2}$  are most likely to be miscible, while ingredients with solubility parameters differing by more than  $\sim 10 \text{ (MPa)}^{1/2}$  are more likely to be immiscible [206].

**Table 3.1** below illustrates that the reported solubility parameters for FELD was found to be  $24.39 \text{ (MPa)}^{1/2}$  whereas the values reported for PVA and Soluplus® were 30.50 and  $31.22 \text{ (MPa)}^{1/2}$  respectively. Depending on the reported data for PVA and Soluplus®, and the obtained data for FELD in **Table 3.1**, the difference in the solubility parameters was found to be 6.11 and  $6.83 \text{ (MPa)}^{1/2}$ , for the FELD-PVA system and FELD-Soluplus® system respectively. According to this rule, FELD is expected to be miscible with both polymers as  $\Delta SP < 7 \text{ (MPa)}^{1/2}$ .

Even though the solubility parameters method is considered the easiest way to calculate  $\chi$  and does not need any experiment, it has been reported that calculated  $\chi$  using the solubility parameters approach can fail in prediction of drug-polymer miscibility [199]. This is may be because of the solubility parameters limitations, especially when dealing with drug-polymer systems including highly directional bonds (e.g., hydrogen bonding) or long-range interactions (e.g., ionic interactions) [81] [207].

Also, the solubility parameters approach does not consider possible exothermic mixing as the determined F-H interaction parameter  $\chi$  is always positive [195]. Thus, alternate methods, such as MPD method, have been noted in the literature [76] [69], [81]–[83] to estimate the F-H interaction parameter  $\chi$  and to predict drug-polymer miscibility.

**Table 3.1.** Physical properties for FELD, PVA, and Soluplus®.

Materials	Molecular weight (g/mol)	Density (g/cm <sup>3</sup> )	molecular volume (cm <sup>3</sup> /mol)	solubility parameter (MPa) <sup>1/2</sup>	$\Delta SP$ in (MPa) <sup>1/2</sup> (SPdrug - SPpolymer)	$\Delta H_{\text{fusion}}$ (kJ/mol)	T <sub>m</sub> (°C)
FELD	384.25 <sup>a</sup> [76]	1.28 <sup>a</sup> [82]	300.19 <sup>b</sup>	24.39 <sup>a</sup> [76]	—	30.45 <sup>c</sup>	147.82 <sup>c</sup>
PVA	38160	1.30 <sup>a</sup> [200]	29354 <sup>b</sup>	30.50 <sup>a</sup> [208]	6.11	—	—
Soluplus®	115000 <sup>a</sup> [76]	0.99 <sup>a</sup> [76]	116161.62 <sup>b</sup>	31.22 <sup>a</sup> [76]	6.83	—	—

<sup>a</sup> Data reported in the literature, <sup>b</sup> Data obtained by dividing the molecular weight by density, and

<sup>c</sup> Value obtained in the present work using DSC.

### 3.4.2. Thermal Analysis

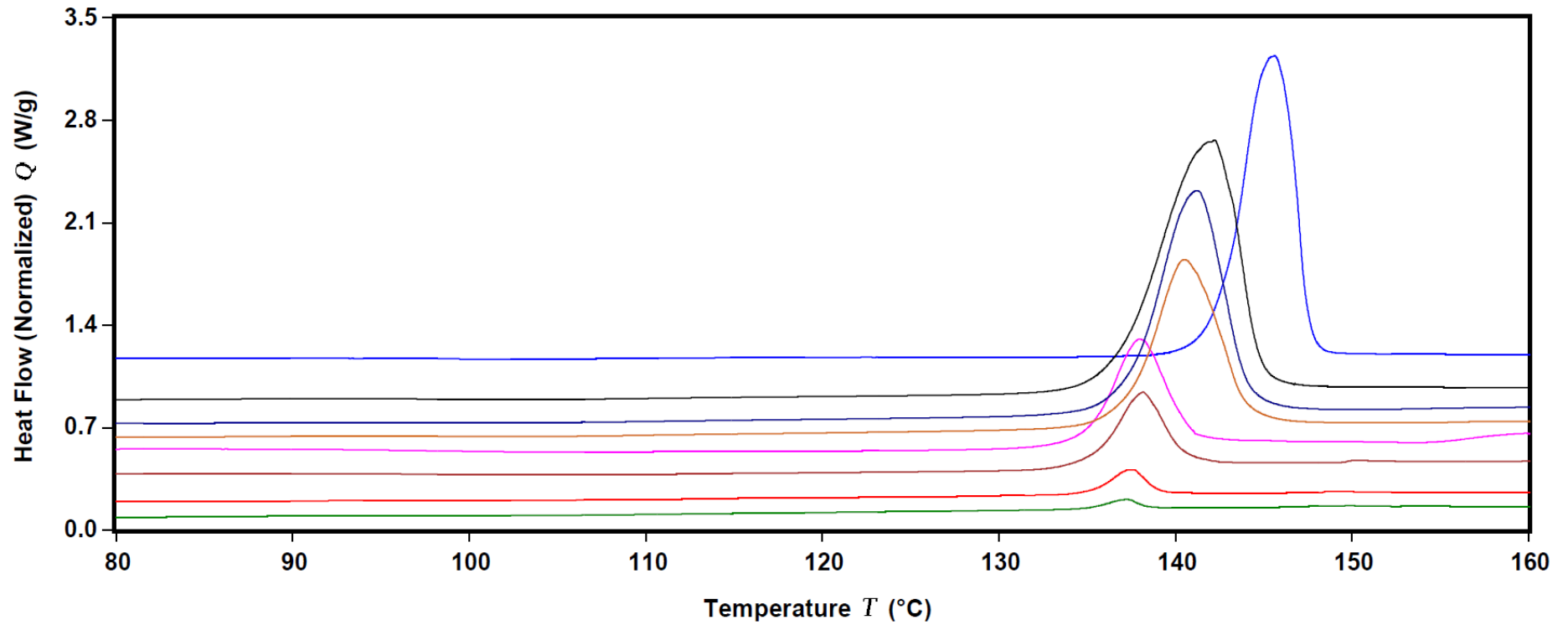


**Figure 3.1.** DSC thermograms of FELD-PVA mixtures prepared using different drug loadings, from top to bottom (crystalline FELD, 75%, 50%, 35%, 25%, 20%, 10%, 5% FELD-PVA w/w %). (Endo Up in the thermogram).

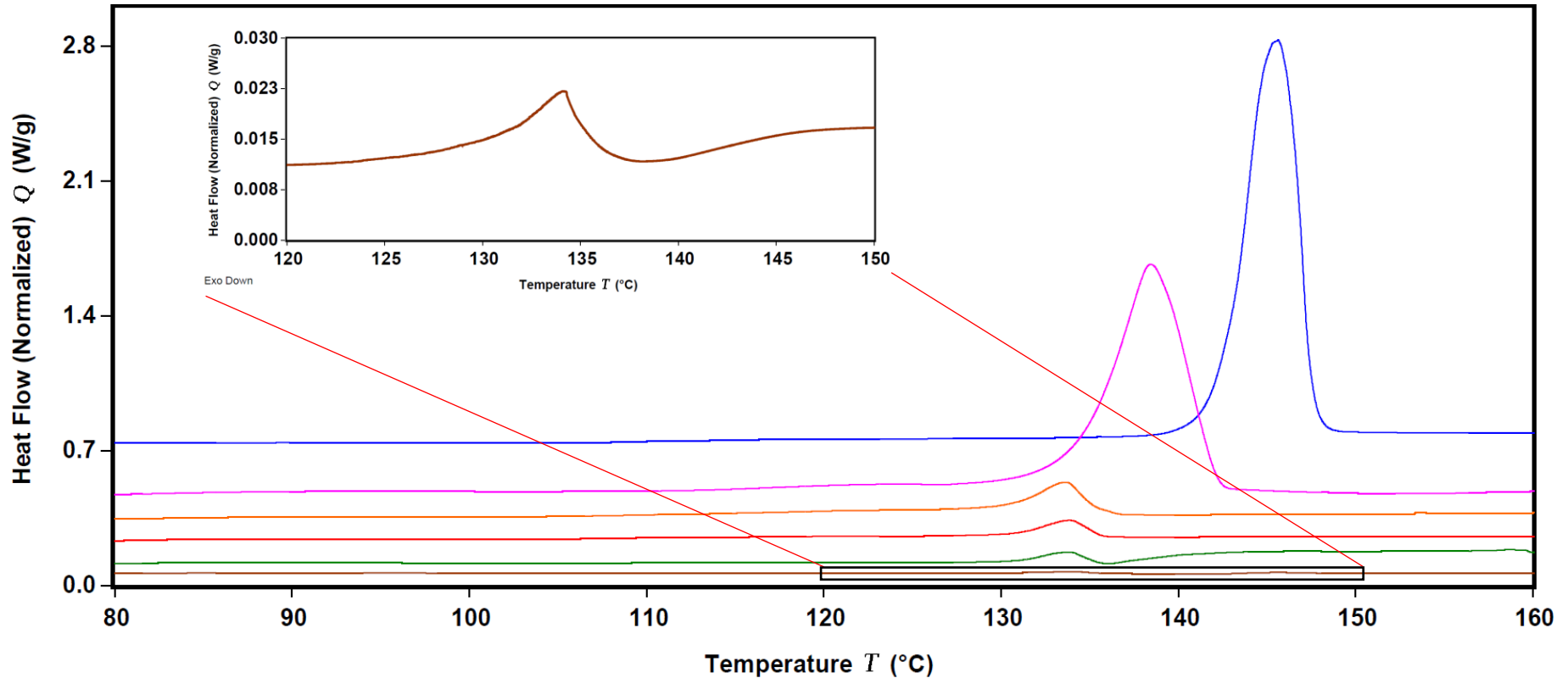


**Figure 3.2.** DSC thermograms of FELD-Soluplus® mixtures prepared using different drug loadings, from top to bottom (crystalline FELD, 75%, 50%, 35%, 25%, and 20% FELD-Soluplus® w/w %). Area in the box is the magnification of the melting endotherm of the 20% (FELD-Soluplus® w/w). (Endo Up in the thermogram).

**Figure 3.1 and Figure 3.1** show DSC thermograms obtained for the FELD, as received, FELD-PVA, and FELD-Soluplus® mixtures prepared using different drug loadings (w/w %). Firstly, the melting point ( $T_{\text{end}}$ ) of the crystalline FELD was obtained using DSC in the current experiment and it was found to be 148 °C [76]. Also, the  $T_g$  of the FELD was obtained from the second heating and it was found to be 46 °C (**Appendix Figure-1**). From the figures shown above, it is clear that there is a significant indication of melting point depression of FELD as a function of polymer addition, which is suggesting a substantial degree of mixing at the drug melting temperature. It is clear that the melting endset for mixing of the drug and the polymers in the liquid state decreased when the fraction of PVA or Soluplus® increased [76].

Further investigation into the miscibility between the FELD and the polymers was conducted by using the MPD data to calculate the F-H interaction parameter  $\chi$  for FELD with both carriers.

### 3.4.3. F-H Interaction Parameter $\chi$ and Gibb's Free Energy of Mixing

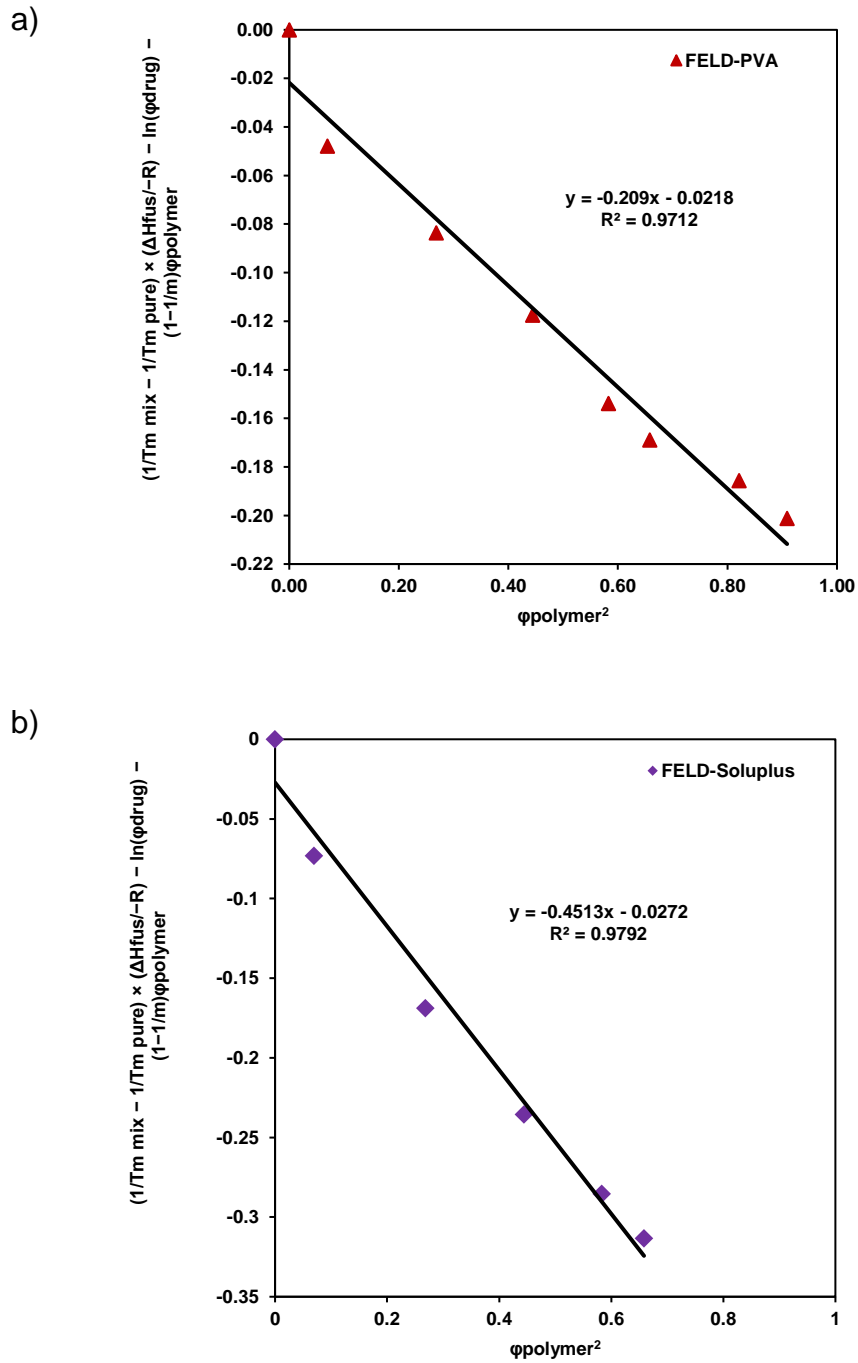


**Figure 3.3.** Flory-Huggins interaction plot utilised to determine the F-H interaction parameter  $\chi$  values for the FELD-PVA system (a) and the FELD-Soluplus® system (b) utilising equation 3.5 ( $n=1$ ).

**Figure 3.3, a and b** show that By plotting of  $(1/T_{m_{mix}} - 1/T_{m_{pure}}) * (\Delta H_{fus} / -R) - \ln(\phi_{drug}) - (1 - 1/m)\phi_{polymer}$  versus  $\phi_{polymer}^2$ , a linear plot for the different drug-polymer systems was obtained, and the values of  $\chi$  were estimated from the slope of the plotted graphs. Depending on the MPD method, a positive value of  $\chi$  is indicative of weak interactions between drug-polymer molecules and, hence, low miscibility [209]. In contrast, a negative value of  $\chi$  is a suggestion of strong drug-polymer interactions and, thus, high miscibility [209]. In our work, the obtained values of  $\chi$  were found to be negative for both systems (- 0.21,  $r^2 = 0.97$  for FELD-PVA and -0.45,  $r^2 = 0.98$  for FELD-Soluplus®), indicating that FELD is miscible with both polymers at a temperature close to the melting point of the drug for all the studied compositions.

This result is consistent with the predicted miscibility of FELD-Soluplus® system that was previously recorded by Tian, et al [76]. They found that the interaction parameter  $\chi$  of the FELD-Soluplus® system is negative (- 0.37), indicating that the FELD-Soluplus® system is a miscible system [76]. Also, this result is consistent with the predicted miscibility of FELD with both carriers (PVA and Soluplus®) using the solubility parameters method, as both polymers are predicted to be miscible with the drug. The data used to determine the F-H interaction parameter,  $\chi$ , values for the FELD-PVA system and the FELD-Soluplus® system can be found below in **(Table 3.2 and 3.3)**.

However, it would be difficult to use this information to predict the level of drug-polymer miscibility at a lower temperature, i.e., storage temperature. Consequently, with constructing an appropriate

compositions phase diagram, one could be able to determine the miscibility and if crystallisation would occur at lower temperatures.

In the next section, we plotted the  $\chi$  values obtained from the MPD data against  $1/T_m$  to determine the F-H constants A and B.

**Table 3.2.** Data used to estimate the F-H interaction parameter  $\chi$  values for the FELD-PVA system.

FELD-PVA weight fraction	T <sub>m</sub> <sub>mix</sub>	T <sub>m</sub> <sub>mix</sub> (Kelvin)	$\phi_{\text{drug}}$	$\phi_{\text{polymer}}$	R	$\Delta H_{\text{fus}}$	m	Term 1= (1/T <sub>m</sub> <sub>mix</sub> - 1/T <sub>m</sub> <sub>pure</sub> )	Term 2= ( $\Delta H_{\text{fus}}/R$ )	Term 3= ln( $\phi_{\text{drug}}$ )	Term 4= (1-1/m) $\phi_{\text{polymer}}$	chi	(1/T <sub>m</sub> <sub>mix</sub> - 1/T <sub>m</sub> <sub>pure</sub> ) × ( $\Delta H_{\text{fus}}/R$ ) - ln( $\phi_{\text{drug}}$ ) - (1-1/m) $\phi_{\text{polymer}}$	$\phi_{\text{polymer}}^2$
1.00	147.80	420.80	1.00	0.00	8.3	30450	98	0.000000	-3669	0.00	0.00	0.00	0.00	0.00
0.75	145.50	418.50	0.74	0.26				0.000013		-0.31	0.26	-0.69	-0.05	0.07
0.50	143.80	416.80	0.48	0.52				0.000023		-0.73	0.51	-0.31	-0.08	0.27
0.35	142.20	415.20	0.33	0.67				0.000032		-1.10	0.66	-0.26	-0.12	0.44
0.25	140.50	413.50	0.24	0.76				0.000042		-1.44	0.76	-0.26	-0.15	0.58
0.20	139.80	412.80	0.19	0.81				0.000046		-1.67	0.80	-0.26	-0.17	0.66
0.10	139.02	412.02	0.09	0.91				0.000051		-2.37	0.90	-0.23	-0.19	0.82
0.05	138.30	411.30	0.05	0.95				0.000055		-3.07	0.94	-0.22	-0.20	0.91

**Table 3.3.** Data used to estimate the F-H interaction parameter  $\chi$  values for the FELD-Soluplus® system.

FELD-Solplus weight fraction	T <sub>m</sub> <sub>mix</sub> (°C)	T <sub>m</sub> <sub>mix</sub> (Kelvin)	$\phi_{\text{drug}}$	$\phi_{\text{polymer}}$	R	$\Delta H_{\text{fus}}$	m	Term 1= (1/T <sub>m</sub> <sub>mix</sub> - 1/T <sub>m</sub> <sub>pure</sub> )	Term 2= ( $\Delta H_{\text{fus}}/R$ )	Term 3= ln( $\phi_{\text{drug}}$ )	Term 4= (1-1/m) $\phi_{\text{polymer}}$	chi	(1/T <sub>m</sub> <sub>mix</sub> - 1/T <sub>m</sub> <sub>pure</sub> ) × ( $\Delta H_{\text{fus}}/R$ ) - ln( $\phi_{\text{drug}}$ ) - (1-1/m) $\phi_{\text{polymer}}$	$\phi_{\text{polymer}}^2$
1.00	147.80	420.80	1.00	0.00	8.30	30450	387	0.000000	-3669	0.00	0.00	0.00	0.00	0.00
0.75	144.30	417.30	0.74	0.26				0.000020		-0.31	0.26	-1.05	-0.07	0.07
0.50	139.80	412.80	0.48	0.52				0.000046		-0.73	0.52	-0.63	-0.17	0.27
0.35	136.73	409.73	0.33	0.67				0.000064		-1.10	0.66	-0.53	-0.24	0.44
0.25	134.46	407.46	0.24	0.76				0.000078		-1.44	0.76	-0.49	-0.29	0.58
0.20	133.20	406.20	0.19	0.81				0.000085		-1.67	0.81	-0.48	-0.31	0.66

### 3.4.4. Extrapolation of the F-H Interaction Parameter $\chi$

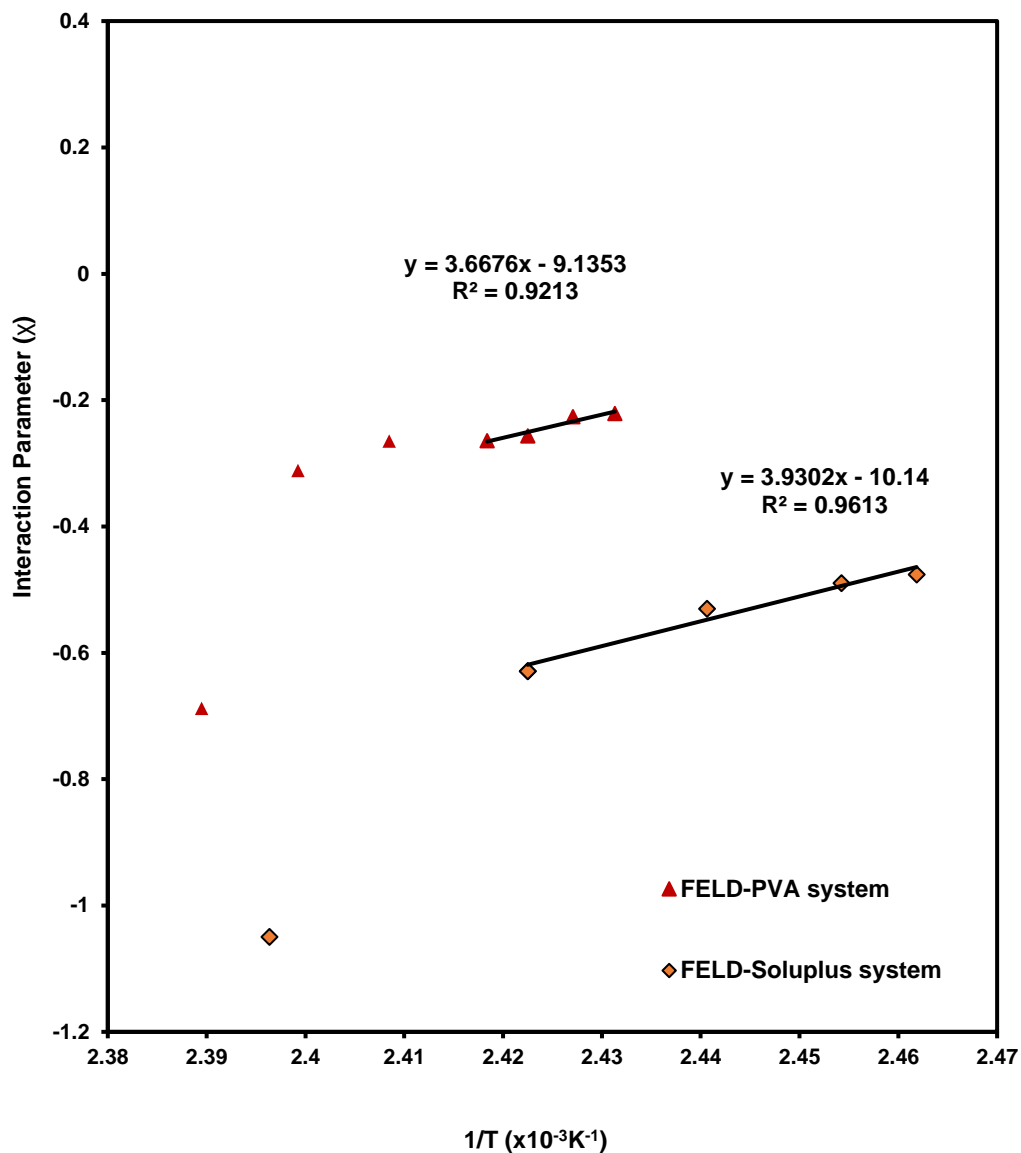


**Figure 3.4.** Alteration of the F-H interaction parameter  $\chi$  as a function of temperature for FELD-PVA and FELD-Soluplus® systems. The linear line represents the best experimental data fit to equation (3.6).

**Figure 3.4** shows the  $\chi$  plotted versus  $1/T_m$ . A linear relationship was detected between the F-H interaction parameter,  $\chi$ , and  $1/T_m$  for the FELD-PVA system in the composition range of 5-25 % (w/w) with  $R^2$  value of 0.92, whereas a linear relationship was determined between  $\chi$  and  $1/T_m$  for the FELD-Soluplus® system in the composition range of 20-50 % (w/w) with a determination coefficient ( $R^2$ ) value of 0.96.

On the other hand, a non-linear relationship was detected for the FELD-PVA system at drug loadings greater than 35% (w/w), and a non-linear relationship was observed for the FELD-Soluplus® system at drug loadings greater than 50 % (w/w). The deviation from the linearity at high drug loadings during extrapolation of the  $\chi$  against  $1/T_m$  for different drug-polymer systems was previously reported in the literature [76] [79]. From the plotted graphs, we were able to obtain the F-H constants A (intercept) and B (slope), which allowed us to estimate the F-H interaction parameter  $\chi$  at lower temperatures using equation (3.6). Data used to extrapolate the F-H interaction parameter  $\chi$  against  $1/T_m$  for FELD-PVA and FELD-Soluplus® systems is shown below in (**Table 3.4, and 3.5**).

**Table 3.4.** Data utilised to extrapolate  $\chi$  for FELD-PVA system.

FELD-PVA weight fraction	Tm (°C)	Tm (Kelvin)	1/T x10 <sup>3</sup> (K <sup>-1</sup> )	chi ( $\chi$ )
1.00	147.80	420.80	2.38	0.00
0.75	145.50	418.50	2.39	-0.69
0.50	143.80	416.80	2.40	-0.31
0.35	142.20	415.20	2.41	-0.26
0.25	140.50	413.50	2.42	-0.26
0.20	139.80	412.80	2.42	-0.26
0.10	139.02	412.02	2.43	-0.23
0.05	138.30	411.30	2.43	-0.22

**Table 3.5.** Data used to extrapolate  $\chi$  for FELD-Soluplus® system.

FELD-Solplus weight fraction	Tm (°C)	Tm (Kelvin)	1/T x(10 <sup>3</sup> K <sup>-1</sup> )	chi ( $\chi$ )
1.00	147.80	420.80	2.38	0.00
0.75	144.30	417.30	2.40	-1.05
0.5	139.80	412.80	2.42	-0.63
0.35	136.73	409.73	2.44	-0.53
0.25	134.46	407.46	2.45	-0.49
0.20	133.20	406.20	2.46	-0.48

For more investigation on the miscibility between the FELD and the polymers, we used equation (3.4) along with the values obtained for the F-H interaction parameter  $\chi$  using MPD method and equation (3.6), as summarised in (**Table 3.6**), to study the alteration in Gibb's free energy of mixing during mixing of FELD with the polymers at temperature close to the melting point of the drug [80].

**Table 3.6.** The F-H interaction parameter  $\chi$  values obtained using MPD method and the  $\chi$  values obtained using equation (3.6) at 140 °C.

	FELD-PVA system	FELD-Soluplus® system
$\chi^a$	-0.21	-0.45
$\chi^b$	-0.26	-0.62

<sup>a</sup>Determined from the slope of the plotted graph of the  $\chi$  values obtained for FELD-PVA and FELD-Soluplus® systems (**figure 3.3 a and b**). <sup>b</sup> $\chi$  values calculated using equation (3.6) at 140.00 °C.

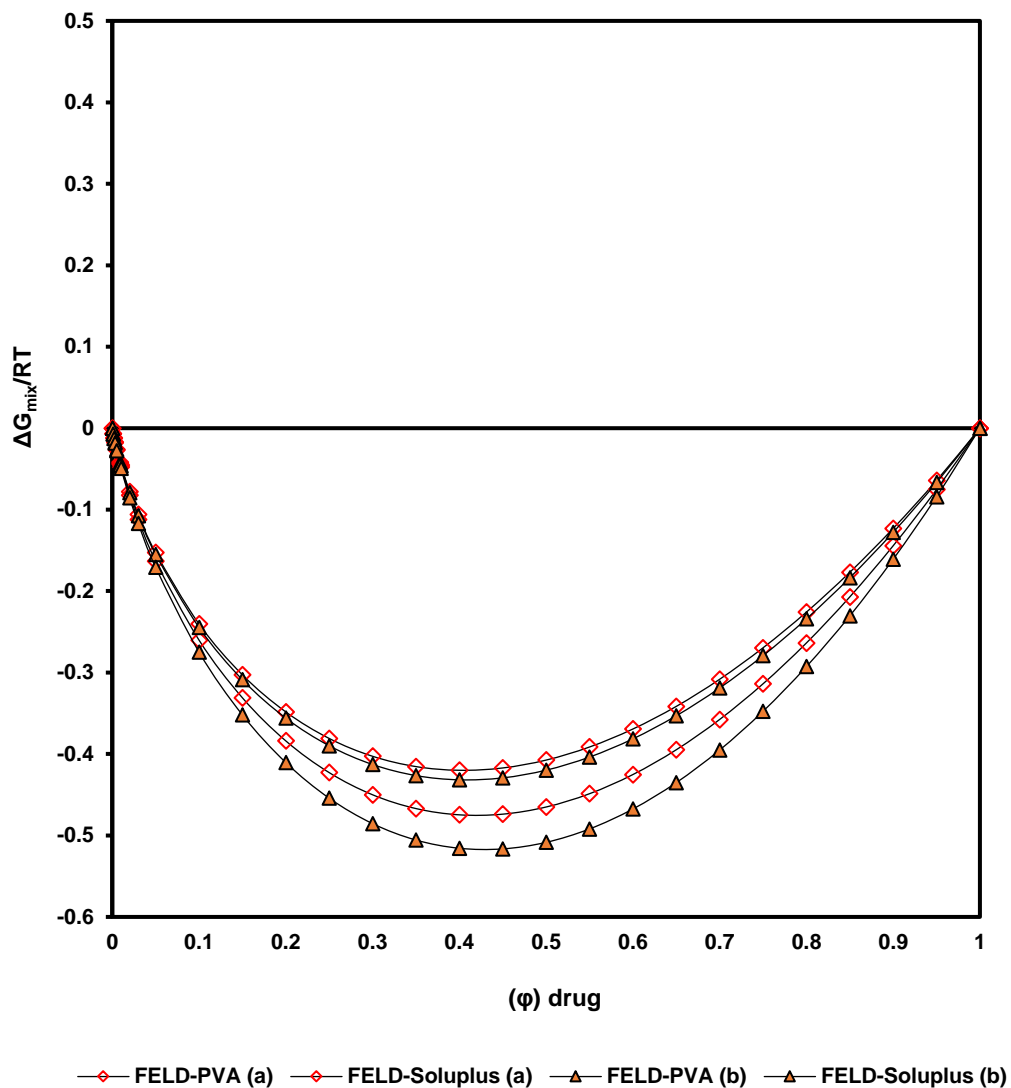


**Figure 3.5.** A plot of  $\Delta G_{\text{mix}}/RT$  as a function of the FELD volume fraction for FELD-PVA and FELD-Soluplus® systems. The open symbols show data calculated using the interaction parameter  $\chi$  obtained from MPD method (**Table 3.6,  $\chi^a$** ), while the filled symbols show data using the interaction parameter  $\chi$  obtained from equation (3.6) at 140°C (**Table-3.6,  $\chi^b$** ).

**Figure 3.5** shows the change in Gibb's free energy upon mixing of the FELD with the PVA and Soluplus® at 140°C. Depending on the drug composition and  $\chi$  values, Gibb's free energy of mixing for a binary system can be either positive, promoting instability and phase separation or negative, which is indicating of miscibility and system stability [80].

Due to the negative values of the  $\chi$ , as shown in (**Table 3.6**), used to plot the graph, Gibb's free energy of mixing, as expected, was concaved towards the negative value with all the drug loadings for both systems, which suggests that the mixing is thermodynamically favourable between the FELD and both carriers (PVA and Soluplus®) for all the compositions at a temperature close to the melting point of the model drug. Thus, these results suggest that it would be possible to formulate miscible ASD of FELD-PVA and FELD-Soluplus® systems at a temperature equal to or higher than 140°C utilising HME.

The F-H interaction parameter,  $\chi$ , values for both systems were also determined using the solubility parameters approach at 25 °C. The values of the F-H constants (A and B) and the calculated values of the F-H interaction parameter  $\chi$  are summarised below in (**Table 3.7**).

**Table 3.7.** Determination of the A and B constants using the linear regression analysis of experimental DSC data and the interaction parameter  $\chi$ , calculated using MPD approach and solubility parameters method at 25 °C.

	FELD-PVA system	FELD-Soluplus® system
<b>A</b>	<b>- 9.14</b>	<b>- 10.14</b>
<b>B</b>	<b>3667.6</b>	<b>3930.2</b>
$\chi^a$	<b>3.17</b>	<b>3.05</b>
$\chi^b$	<b>3.81</b>	<b>5.65</b>

<sup>a</sup> Determined through extrapolation of melting point depression data at 25 °C. <sup>b</sup> Calculated using van Krevelen solubility parameter method at 25 °C.

Regardless of the method employed to calculate the F-H interaction parameter  $\chi$  at 25 °C, the obtained values were positive for the FELD with both carriers. This information suggests limited miscibility occurred between the FELD-PVA or FELD-Soluplus® systems at storage temperature (25 °C).

For more understanding on the phase behaviour of the ASD, we investigated the effect of the F-H interaction parameter  $\chi$  on Gibb's free energy of mixing at different temperature profiles by plotting the  $(\Delta G_{\text{mix}}/RT)$  against the FELD volume fraction.

### 3.4.5. Determination of Miscibility

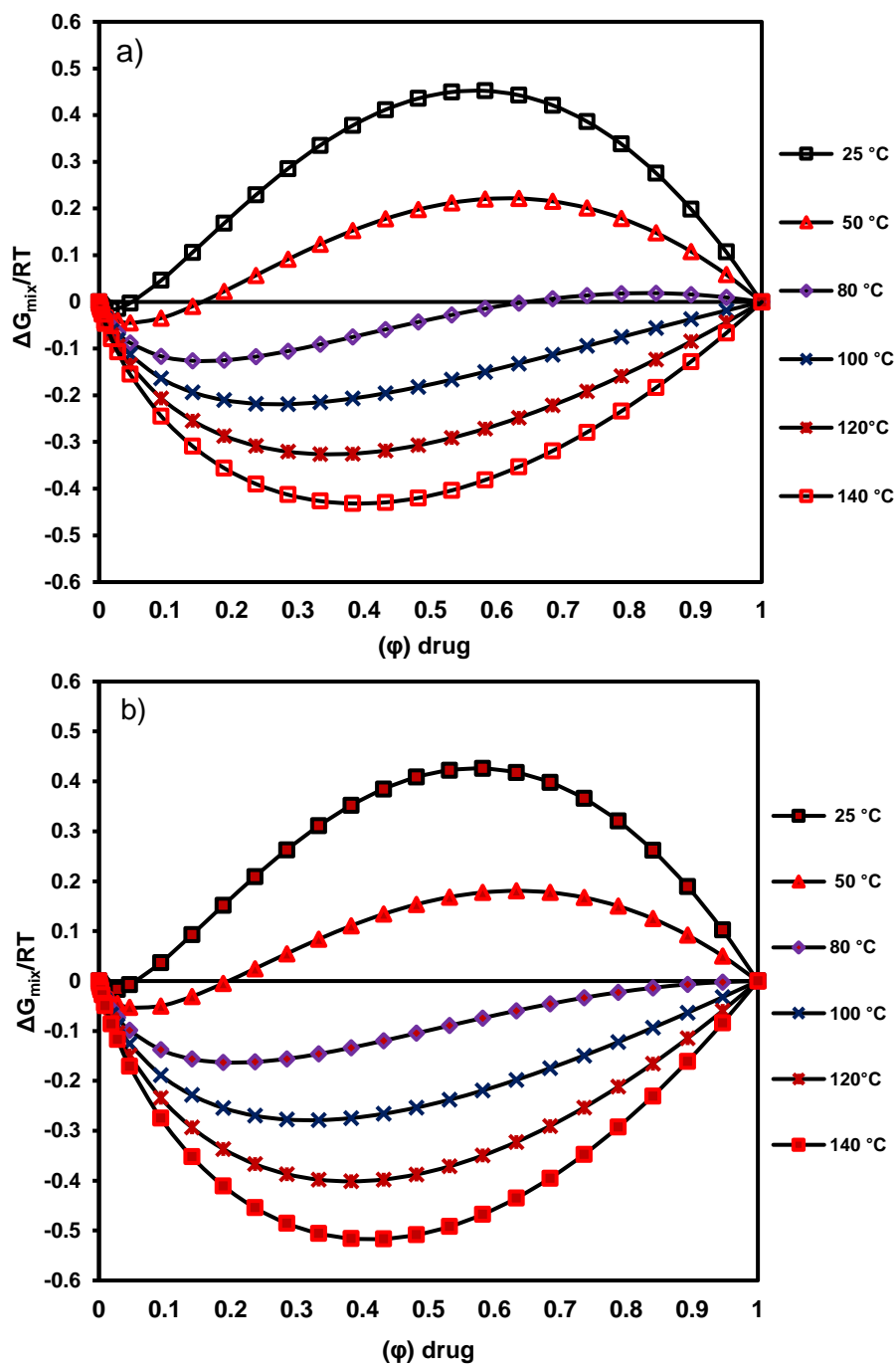


**Figure 3.6.** A plot of  $\Delta G_{\text{mix}}/RT$  as a function of the FELD volume fraction for a) FELD-PVA and b) FELD-Soluplus® systems at different temperatures (25, 50, 80, 100, 120, and 140 °C).

Abu-Diak et al., have previously reported that Gibb's free energy of mixing of a drug-polymer binary system is significantly affected by values of the F-H interaction parameter,  $\chi$  [210].

**Figure 3.6** (a and b) illustrate a plot of changes in Gibb's free energy of mixing as a function of temperature and drug compositions for FELD with PVA and Soluplus®. As discussed previously in section (3.4.3), the negative value of Gibb's free energy of mixing is an indicative of miscibility, whereas the positive value is an indicative of immiscibility and phase separation at specific drug-polymer compositions [80]. Consequently, Gibb's free energy of mixing of the FELD-PVA and FELD-Soluplus® systems, as shown in (**Figure 3.6, a and b**), are negative only with drug  $\phi < 0.094$  at storage temperature (25 °C), suggesting similar miscibility and stability for both systems at 25 °C.

In addition, both systems have revealed immiscibility and possible phase separation for the drug  $\phi$  higher than 0.094 as estimated by Gibb's free energy of mixing at the storage temperature. However, with increasing temperature, the FELD-Soluplus® has shown higher miscibility with the model drug than the FELD-PVA system.

As illustrated in the graphs, the miscibility of the FELD-Soluplus® system has increased as Gibb's free energy of mixing turns out to be negative for the drug  $\phi < 0.24$  at 50 °C, while Gibb's free energy of mixing became negative for the drug  $\phi < 0.19$  in case of FELD-PVA system at the same temperature. Moreover, Gibb's free energy of mixing of the FELD-Soluplus® system is negative with all the drug compositions at

temperature above 80 °C indicating miscibility and stability at elevated temperatures as shown in (**Figure 3.6, b**).

In contrast, Gibb's free energy of mixing of the FELD-PVA system changed to a negative value only when the temperature exceeded 100-°C for all the drug compositions as revealed in (**Figure 3.6, a**). This result is consistent with the previous results, in which the miscibility of the FELD-Soluplus® system is higher than the miscibility of the FELD-PVA system. The predicted miscibility values for FELD with both polymers are summarised below in (**Table 3.8**).

**Table 3.8.** Predicted miscibility of the FELD-PVA and FELD-Soluplus® systems.

Maximum values	FELD-PVA system	FELD-Soluplus system
<b>Miscibility of FELD</b>		
<b>(wt %) at</b>		
<b>25 C°</b>	10	10
<b>50 C°</b>	19	24
<b>80 C°</b>	68	94
<b>100 C°</b>	100	100

Understanding how Gibb’s free energy of mixing changes as a function of temperature for FELD-PVA and FELD-Soluplus® systems allows the solid-liquid transition curve (solubility) and the spinodal curve (miscibility) of the FELD with both carriers to be plotted as a function of the FELD weight fraction and temperature. This information was combined with the glass transition temperatures to construct the composition phase diagram as detailed below.

### 3.4.6. Construction of the Compositions Phase Diagram

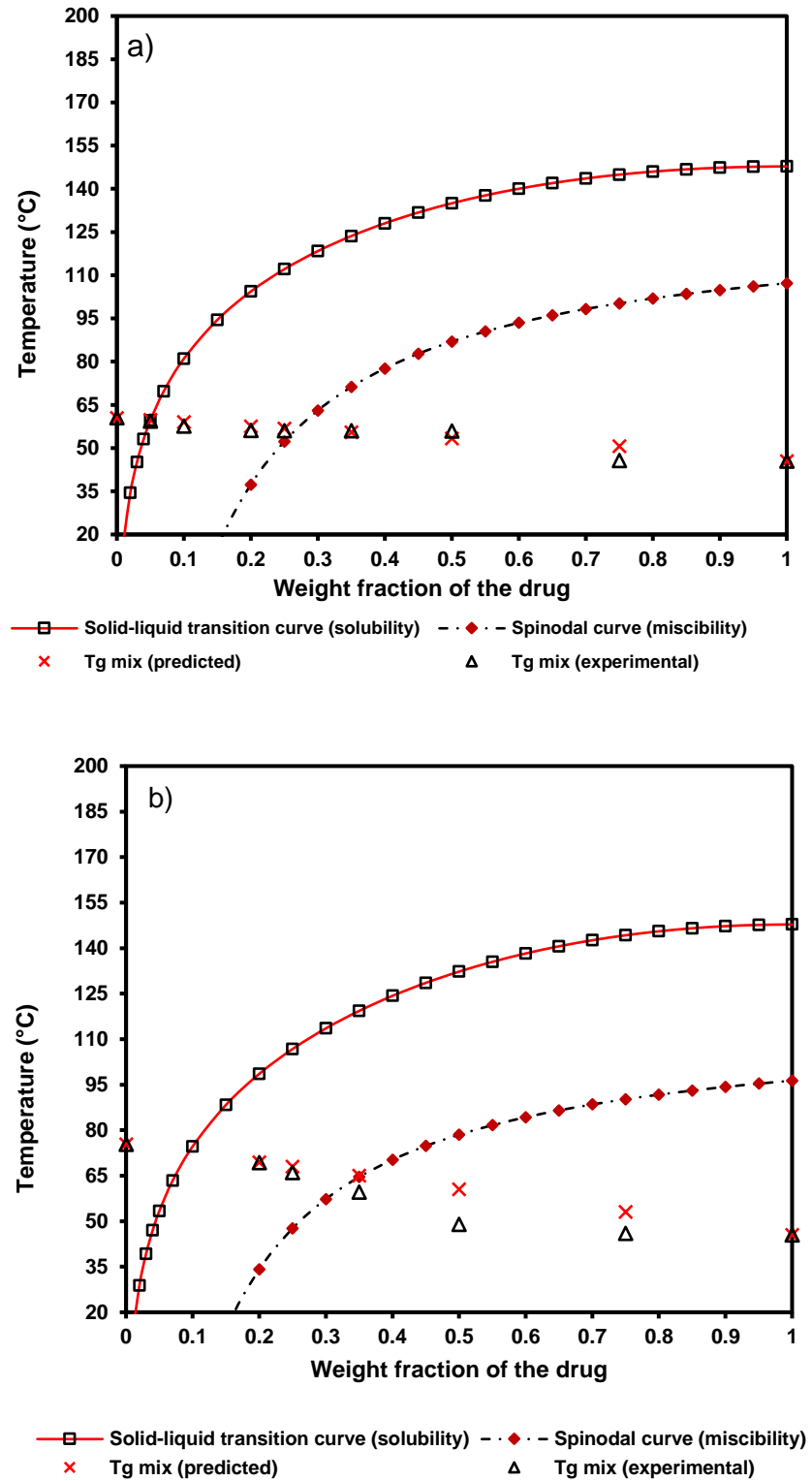


Figure 3.7. Binary phase diagram of, a) FELD-PVA system, and b) FELD-Soluplus® system.

A phase diagram can offer a fair estimation by which we can better understand the behaviour of the solute (FELD) within the solvents (PVA and Soluplus®). Moreover, it allows prediction of the phase behaviour (stability and phase separation) of the ASD as a function of changes in the composition or temperatures. Also, it can identify the drug-polymer binary system phase boundaries [19] [80]. Using the phase diagram to estimate the drug-polymer phase boundaries may offer detailed information on the appropriate drug-polymer compositions, and the required temperature to produce ASD formulations utilising HME [76].

**Figure 3.7** Illustrates the composition phase diagrams of the FELD-PVA system (a) and FELD-Soluplus® system (b). We constructed the composition phase diagrams of the model drug (FELD) with two polymeric carriers, namely PVA and Soluplus® using a combination of DSC experimental data (MPD method) and the F-H theory.

As shown in the graph, above the solid-liquid curve (solubility curve), the drug-polymer mixtures are expected to remain thermodynamically stable with respect to the insignificant changes in the system. Below the solid curve and above the miscibility curve (spinodal curve), the metastable zone exists. In this zone, the drug-polymer compositions, at specific loadings, have the ability to phase separate into two amorphous phases, including drug-rich phase and polymer-rich phase, without changing directly to the crystalline state, which may re-crystallise over time.

Thus, the drug is expected to remain stable for small alterations in the system, but significant changes in the system will lead to re-

crystallisation through a growth mechanism and nucleation. However, in the metastable region, the nucleation step will be kinetically impeded until a significant energy barrier is overcome, specifically when the drug-polymer mixture temperature is under the  $T_g$  curve of the system. Below the spinodal curve, the API is present in the carrier in an unstable state, where spontaneous crystallisation is expected to occur without any significant kinetic barrier [76] [80].

However, it is important to report that all the drug-polymer compositions used to measure the  $T_g$  of the mixtures have shown complete miscibility by showing only a single  $T_g$ , and no melting endotherm was detected between the drug and the polymers after the second heating cycle (**Appendix Figure 2, a and b**). This is an indication of the ability of both polymers to diminish the re-crystallisation process and to produce a homogenous one phase and stable ASD system at a particular temperature and drug loading.

It is clear from the (**Figure 3.7, b**) that the FELD-Soluplus® system temperature-composition phase curves have shifted towards high compositions range, which is indicating higher solubility and miscibility of the FELD in the Soluplus® compared to the FELD-PVA system. The high solubility and miscibility observed here with the FELD-Soluplus® system are consistent with the result reported by Tian et al., for the same system [76].

According to the results obtained from the predicted miscibility limit using Gibb's free energy of mixing and the constructed temperature-

compositions phase diagrams of the FELD with PVA and Soluplus®, it should be possible to formulate the homogenous ASD and the spiked formulation using a particular drug-polymer composition and temperature.

Consequently, in the current thesis, we selected the FELD-PVA system to fabricate the filaments and the model tablets. The selection of the PVA as a carrier for this work was based on its advantages over the Soluplus® during the printing process as the PVA is ready 3D printable, especially with the FDM 3D printer. Moreover, it is may be possible to manufacture drug loaded printer feedstocks without adding of excipients i.e. plasticiser, during the production of the filaments and printing of the tablets using the PVA polymer compared to the Soluplus® [58]. Consequently, two different loadings were selected to formulate the filaments based on the information obtained from the FELD-PVA graph (**Figure 3.7, a**). These loadings were 10% (located in the metastable zone), and 50%, which is located below the miscibility curve (unstable zone).

### 3.5. Conclusion

In this chapter, we have successfully predicted the miscibility limits of the FELD-PVA and FELD-Soluplus® systems utilising two approaches, including a quantitative approach (MPD method) and a qualitative method (solubility parameters) in combination with the F-H interaction parameter  $\chi$ . Moreover, we successfully determined the temperature dependence of F-H interaction parameter  $\chi$  for both systems. Also, we

successfully constructed Gibb's free energy of mixing ( $\Delta G_{\text{mix}}$ ) and the temperature-composition phase diagrams for both systems. Regardless of the method utilised to determine the F-H interaction parameter  $\chi$ , the relative rank of the miscibility estimated were consistent, in which the miscibility of the FELD in Soluplus® is greater than that in the PVA. In addition, the predicted miscibility rank obtained using Gibb's free energy of mixing ( $\Delta G_{\text{mix}}$ ) and the temperature-composition phase diagrams have shown similar ranking. The constructed composition phase diagrams have clearly identified the phase boundaries for both systems, indicating a metastable zone and an unstable zone. Due to the increasing interest in utilising HME to produce ASD formulations, the construction of the temperature-composition phase diagrams allows scientists to easily identify the required temperature and drug loading to formulate ASDs. Accordingly, two different loadings were selected, i.e. 10%, and 50% (FELD-PVA w/w), to be used to formulate the filaments utilising HME in the next chapter.

## **4. Chapter 4: Formulation of Felodipine-Polyvinyl Alcohol Printer Feedstocks and Model Tablets Fabrication**

### **4.0. Novelty in this Chapter**

Different FELD-PVA printer feedstocks with 10%, 25%, and 50% of FELD loading were manufactured utilising HME without adding of plasticiser. Moreover, the manufactured filaments were used to fabricate drug-loaded model tablets with different geometries utilising the FDM 3D printer in the present work.

### **4.1. Introduction**

As discussed in chapter 1 and 2, FDM 3D printing technique is a low-cost manufacturing method, recently explored to manufacture implantable systems [211]–[213], medical devices [214], capsular devices [215], innovative tablets [216], and dosage forms fabricated as multi-layer device [217]. Also, as detailed in chapter 2, FDM 3D printer utilises filaments, which are usually commercially available thermoplastic polymers i.e. PLA and PVA, to fabricate the final products. However, in order to fabricate personalised dosage forms loaded with an API, there are two main methods i.e. soaking method, and HME [116].

The HME method is a procedure where pressure and heat are employed to melt the thermoplastic filament and then force the molten material

through a die, under controlled conditions [218]. The HME method has been recently utilised by the pharmaceutical industry to formulate drug delivery systems, and oral dosage forms, especially in combination with FDM 3D printing technology for advanced drug formulations [116]. The soaking process involves soaking of the thermoplastic filament in a saturated solution of drug in order to allow the drug to diffuse into the polymer [219]. Although the soaking method is easier and less expensive than the HME process, it may lead to lower and not very reproducible amounts of drug in the filament [116].

Therefore, in the present chapter, we have utilised HME to manufacture different drug-loaded feedstocks for the FDM 3D printer, which will be used in chapter five to fabricate the model tablets i.e. pure ASD and amorphous tablets spiked with crystalline seeds utilising the FDM 3D printer. The spiked models, which are ASD tablets manufactured as compartment with an outer shell (amorphous or spiked with crystalline materials) and an inner core (amorphous or spiked with crystalline materials), will be utilised in the present project to investigate the effect of the tablet micro-structure on the drug release mechanisms from these formulations utilising a USP dissolution apparatus I.

In order to manufacture the final product (the compartment model tablets), we need firstly to evaluate the impact of using different materials on the printing parameters during the tablet fabrication process. For example, the effect of using different drug loadings on the flexibility of the manufactured filaments should be evaluated in comparison to utilising drug free filaments. Also, evaluating the ability of the FDM 3D printer to

fabricate tablet with a complex geometry utilising both the drug-loaded formulated feedstocks and commercially available filaments. Moreover, we need to investigate whether it is possible to use the FDM 3D printer to manufacture a pure ASD, and a spiked model tablets using the manufactured drug-loaded filaments based on the calculated miscibility values of FELD-PVA system as presented in chapter 3.

Consequently, we have used the FDM 3D printer in this chapter to fabricate different tablets with several geometries and dimensions using the formulated drug loaded filaments and two commercially available filaments, namely PLA and PVA.

PLA is a widely utilised polymer to fabricate implant devices utilising FDM 3D printing technology [210] [211]. In contrast, PVA, as detailed in chapter 2, section (2.1.2.1), has already been utilised for the production of drug loaded filament using HME and fabrication of oral dosage forms utilising the FDM 3D printer [116] due to its good thermal stability with a melting point that can vary from 180°C- 225°C [222] [223] depending on the molecular weight. However, PLA polymer was utilised in the current thesis as a starting printing material because it is the default printing material with the FDM 3D printer software.

Thus, we started the fabrication process by utilising PLA filament as a default material and by using the default printing parameters to fabricate the first PLA tablet. The same printing parameters that were used to print the PLA tablet were then used to print different tablets using PVA, which is the main polymer utilised through the current thesis due to all the

reasons stated here and previously in chapters 1 and 2. However, it was important to modify the printing parameters in order to fabricate a model tablet using PVA with better morphology than that printed using PLA. Then, the optimised printing parameters along with the formulated drug-loaded filaments were used to fabricate the drug-loaded model tablets using the FDM 3D printer.

The morphology and dimensions of the manufactured filaments and fabricated model tablets were studied utilising SEM and a digital calliper. Also, we used several techniques with different limits of detection, as reported in the literature [224], including DSC, ATR-FTIR, Raman spectroscopy, and PXRD in order to investigate drug-polymer interactions, the formation of ASD, and percentage of crystallinity in the manufactured drug-loaded filaments and model tablets.

## **4.2. Aims and Objectives**

As mentioned in chapter 1, section (1.7), the main aim of this chapter is to prepare different drug-loaded filaments, and to fabricate several drug-free and drug-loaded model tablets with different geometries in order to evaluate the ability of the printer to control different parameters during the printing process. Moreover, to investigate and to detect the formation of ASD and crystallinity percentage for both the formulated drug-loaded filaments and the fabricated model tablets.

This aim can be achieved by firstly designing and fabricating different drug-free tablets using the plain polymers, default printing parameters, and optimised printing parameters. After that, to manufacture drug-

loaded filaments using HME and then use the manufactured filaments and the previously optimised parameters to fabricate several drug-loaded model tablets utilising the FDM 3D printer. Then, to investigate the structure and the dimensions of the prepared filaments, the fabricated drug-free, and drug loaded model tablets utilising SEM and digital calliper before and after optimisation of the printing parameters. Furthermore, to investigate the possible drug-polymer interaction using different techniques, including DSC, FTIR, Raman spectroscopy, and PXRD, in order to detect the formation of ASD and possible crystallinity within the formulated filaments and 3D printed drug-loaded model tablets.

### **4.3. Materials and Methods**

#### **4.3.1. Materials**

As detailed in chapter 2.

#### **4.3.2. Methods**

##### **4.3.2.1. Formulation of Different FELD-PVA Loaded Filaments**

The amorphous form of FELD was prepared by heating the drug (as received) in an oven to 180°C, which is above the obtained FELD melting point using DSC (148 °C), as reported in chapter 3. After complete melting of the sample, it was quickly cooled to -20 °C to obtain the FELD amorphous form [101]. FTIR and Raman spectroscopy both confirmed the formation of the amorphous form within the limit of detection (FTIR 1-2%, and Raman <1% of crystalline components) [224].

Prior to the extrusion process, two batches of FELD-PVA powder (10%, and 50% of FELD loading), were weighed and transferred into a mortar. In this step, 30 g total powder weight was used for each batch. Then, the physical mixtures were geometrically titrated using a mortar and a pestle for five minutes.

Initially, the extruder was started to produce the 10% (FELD-PVA w/w) filament. The temperature was fixed at 170 °C on both temperature regions, T<sub>1</sub>, barrel 1 temperature, and T<sub>2</sub>, barrel 2 temperature, see **Figure 2.4 (chapter 2)**. Then, 15 g of the prepared powder was fed to the extruder hopper. After that, the screw speed was fixed at 10 RPM to allow proper mixing of the powder at the end of the screw (T<sub>2</sub>). Next, the screw speed was increased to 35 RPM to produce the filament. Next, while the HME running at 35 RPM, the remaining amount of the powder (15 g) was added to the HME hopper. Similar steps that were used to produce the 10% of FLED loading filament were also utilised to manufacture the 50% of FELD loading filament. However, due to the use of a higher amount of drug with the 50% filament in comparison to that used with the 10% filament and due to the plasticising effect of the drug on the polymer, the temperature was reduced to 160°C during the formulation process of the 50% drug-loaded filament.

#### **4.3.2.2. Fabrication of the Model Tablets**

In the beginning different model tablets were designed using open-source online software ([www.tinkercad.com](http://www.tinkercad.com)) (**Figure 4.1**). Then, the designed files were exported as STL files, and they were imported to Cura Ultimaker software version 2.6.2 (Ultimaker, Netherlands).

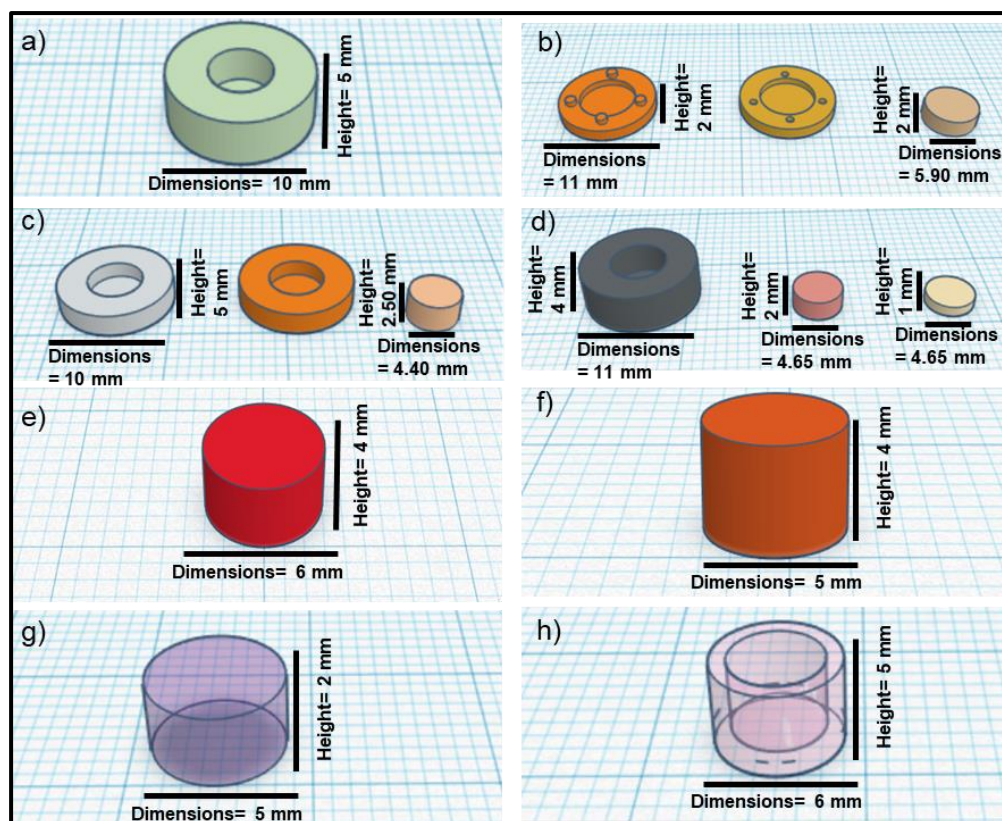


**Figure 4.1.** Schematic illustration of the different tablet designs with different dimensions utilised in this chapter to fabricate different drug-free and drug-loaded model tablets. a, b, c, and d used to fabricate drug-free tablets, while e, f, g, h utilised to fabricate drug-loaded tablets.

Initially, the FDM Ultimaker<sup>2+</sup> 3D printer was utilised to print the drug-free model tablets. The model tablets were fabricated utilising the default settings of the software for the PLA filament as follows: type of printer: FDM Ultimaker<sup>2+</sup>; type of filament: PLA; resolution: standard; temperature of nozzle: 200 °C; temperature of building plate: 10 °C; speed of extruder 20 mm/s while extruding and 120 mm/s while travelling; infill density: 100%; infill pattern: line; height of the layer: 0.10 mm; wall thickness: 1.05 mm; top/bottom thickness: 0.80 mm; build plate

adhesion type: brim; width of the brim: 0.80 mm. No supports were utilised in the printed models. The diameter of the nozzle used in this work is 0.40 mm.

Subsequently, the created files were saved as gcode file type and transferred to the printer using a SanDisk memory card. Thereafter, the printing process was established as follows:

- I. The prepared filament was inserted to the filament holder and then loaded to the Ultimaker 2<sup>+</sup> printer feeder using the rollers.
- II. The rollers pushed the loaded filament through the filament tube until it reached the printer head.
- III. The printing head heated the loaded filament and extruded it through the nozzle.
- IV. The printing stage transferred to the desired height (Z movement), as the inserted information in the gcode saved file.
- V. The printing head was moved to the desired printing site (according to information in the saved file) to fabricate the designed model (XY movement).
- VI. After the first layer was finished, the printing stage moved down slightly to allow printing of the next layer.
- VII. The printing nozzle printed the next layer.
- VIII. Step III and VII were repeated until the 3D object was completed.

Then, the FDM 3D printer was utilised to fabricate different drug-loaded model tablets utilising similar parameters used during fabrication of drug-free model tablets as detailed earlier in the current section. However, the

addition of the drug (FELD) led to the formation of a brittle filament, especially with 50% drug loading. Thus, further changes were applied during the printing of the drug-loaded model tablets. These changes were as follows temperature of nozzle: 195 °C; temperature of building plate: 60 °C; speed of extruder 15 mm/s; infill density: 20 %; build plate adhesion type: none; width of the brim: none. The diameter of the nozzle used in this work is 0.60 mm.

#### **4.3.2.3. Characterisation Techniques**

##### **4.3.2.3.1. Scanning Electron Microscopy (SEM)**

A Scanning Electron Microscope SEM (XL30, Philips) fitted with an Oxford Instruments INCA EDX microanalysis system was utilised to characterise the microstructure of the manufactured filaments, and 3D printed tablets. Firstly, a conductive carbon tape (double-adhesive) was fixed on the surface of the sample stub. After that, the samples were mounted on the carbon tape stubs. Before the microscopic imaging, all the samples were placed in a vacuum sputter coater chamber (Leica EM SCD005 sputter coater) and coated with gold for 190 seconds utilising an accelerating voltage of 25 mA. Thereafter, they were fixed in the SEM specimen holder stage. Furthermore, the samples were tilted manually from 0-45 ° to allow capturing images of the inner layers of the model tablets. Subsequently, several images were obtained for the samples.

##### **4.3.2.3.2. Measurements**

The printed tablet dimensions were measured with a digital calliper (VonHaus®) to investigate whether the FDM 3D printer had fabricated the tablets as created in the online software.

#### **4.3.2.3.3. Differential Scanning Calorimetry (DSC)**

Thermal analysis of the raw materials, manufactured filament, and the fabricated model tablets was achieved utilising a TA discovery Q 2000 DSC instrument equipped with a refrigerated cooling unit, and an auto-sampler (TA Instruments, New Castle, Delaware). Firstly, small pieces of the manufactured filaments as well as fabricated tablets, FELD, as received, and PVA, as received were weighed within the size range of 5-10 mg. Then, the measured samples were sealed in a new Tzero aluminium hermetic pan and lid. The heating rate was established to be 10°C/min and nitrogen gas was used as a purge gas with a flow rate of 50 ml/min. Then, the thermogram of each sample was recorded using Universal TA Instruments data analysis software (n=1).

#### **4.3.2.3.4. Attenuated Total Reflectance- Fourier**

#### **Transform Infra-Red Spectroscopy (ATR-FTIR)**

The spectra of the crystalline FELD, PVA, manufactured filaments and printed tablets were obtained using an ATR-FTIR spectrometer (Agilent Technologies FTIR, Cary 360, Santa Clara, CA, USA). A small amount of each sample, about 5-10 mg, was used and placed on the FTIR crystal diamond plate [78]. After that, the spectra of the samples were obtained in absorbance mode in the spectral region of 600 to 4000  $\text{cm}^{-1}$  utilising a scanning resolution of 8  $\text{cm}^{-1}$  [29] (n=1).

#### **4.3.2.3.5. Raman Spectroscopy**

A confocal Horiba—Jobin-Yvon LabRAM system (Horiba—Jobin-Yvon Ltd, Middlesex, UK) was utilised in this experiment to determine the

Raman spectra of the raw materials (crystalline FELD, quenched cooled FELD, and the PVA). Furthermore, it was used to determine the spectra of the fabricated FELD-PVA model tablets. The Raman instrument is equipped with a different laser excitation capacity including A) UV (385 nm), B) green (532 nm), C) red (660 nm), and D) near-infrared NIR (785 nm). Firstly, minimum amount of the crystalline FELD, quenched cooled FELD, PVA powder, and 3D fabricated tablets (10%, and 25% w/w) was placed on a glass slide respectively. Then, Raman spectra were obtained using the 785 nm laser type. The parameters used in the Raman experiment to obtain the spectra of the raw materials were as following; lens: 50x, acquisition: 5 seconds, grating: 600 line/mm, hole: 300  $\mu\text{m}$ . All the data was recorded using the labspec6 software (n=1).

#### **4.3.2.3.6. X-Ray Powder Diffractometer (XRPD)**

XRPD patterns of crystalline FELD, PVA, and fabricated model tablets were collected using an X'Pert PRO (PANalytical, Almelo, Netherlands) XRPD instrument. The instrument uses  $\text{Cu K}\alpha_1$  ( $\lambda = 1.54 \text{ \AA}$ ) radiation and operates in Bragg-Brentano geometry. The step size utilised was  $0.02^\circ$   $2\theta$  with total of 6 minutes collection time. The voltage of the generator was set to 40 kV and the current to 40 mA. After that, the samples were scanned from  $5^\circ$  to  $40^\circ$   $2\theta$  [101] (n=1).

#### **4.3.2.4. Stability Study**

A saturated solution of sodium chloride was prepared, and this solution was placed in a tight plastic container to achieve the required humidity, which is 75% at room temperature. Then, DSC was used to generate in-situ ASD of FELD-PVA (25% w/w FELD) from the physical mixture

utilising a heat/cool/heat cycle. A minimum amount of previously prepared physical mixtures was weighed within the size range of 5-10 mg. Thereafter, the measured sample was packed in Tzero aluminium hermetic pan and lid. However, a pinhole was made in the lid to allow moisture intake into the samples and facilitate crystallisation while exposed to RH for one week. Next, the samples were studied utilising DSC [225]. Then, the thermogram was recorded using universal TA Instruments data analysis software.

## 4.4. Results and Discussion

### 4.4.1. Fabricated Drug-Free Model Tablets

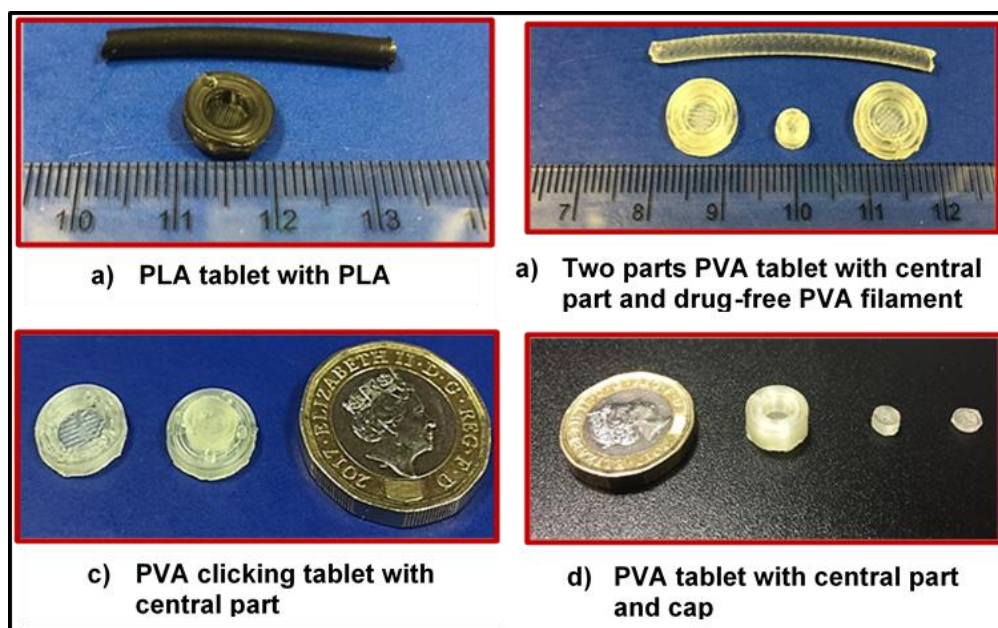


**Figure 4.2.** Photographic images represent the morphology of the 3D printed tablets with plain PVA and PLA filaments using Ultimaker<sup>2+</sup> FDM 3D printer.

**Figure 4.2** illustrates different tablets with different designs were printed using the Ultimaker<sup>2+</sup> FDM 3D printer loaded with original PLA and PVA (drug-free) filaments. Firstly, the PLA filament was loaded into the Ultimaker<sup>2+</sup> printer and passed through a 0.40 mm head nozzle to fabricate the designed tablets as presented in section (4.3.2.2).

Different challenges were faced during the fabrication of the tablets, including A) Modifying of the printer build plate (contact angle of the nozzle with the build plate), B) optimisation of the parameters for the PVA

filament using the PLA filament parameters, and C) the fabrication of the 3D printed tablets with an acceptable morphology.

**Figure 4.2 (a, b, c, and d)** shows drug-free printed model tablets using the PLA, and PVA filaments. The PLA tablet was fabricated utilising the default printing parameters, as shown above in **Figure 4.2 (a)**. Then, the default printing parameters were optimised and used to print different PVA model tablets with several geometery, as illustrated above in **Figure 4.2 (b, c, and d)**. **Table 4.1** below shows the default and optimised printing parameters utilised during the fabrication process of the PLA, and PVA model tablets.

**Table 4.1.** Default and optimised printing parameters that have been utilised while fabricating the drug-free tablets.

Parameters	PLA tablet	PVA tablet
Resolution	Standard	Standard
Nozzle temperature (°C)	190	200
Building plate temperature (°C)	60	50
Speed of extruder (while extruding, mm/s)	50	20
Speed of extruder (while travelling, mm/s)	120	120
Infill density (%)	100	100
Layer height (mm)	0.06	0.10
Wall thickness (mm)	0.80	1.05
top/bottom thickness (mm)	0.80	0.80
build plate adhesion type	Brim	Brim
Brim width (mm)	8.00	8.00
Nozzle diameter (mm)	0.40	0.40

It is clear from the table above that the main change was related to utilising a slower printing speed, 20 mm/s, while printing the PVA tablets, instead of using 50 mm/s printing speed as used for the fabrication of the PLA tablet (default printing speed). Also, higher temperature was used, 200 °C, while printing the PVA tablets rather than 190 °C that was used to fabricate the PLA tablet. **Table 4.2** below illustrates the main parameters that have been modified during the printing process of the PVA tablets.

**Table 4.2.** The main parameters optimised for printing of the PVA tablets relate to the PLA tablets.

Tablet	Nozzle temperature	Build plat temperature	Printing speed mm/s	Layer height mm	Wall thickness mm
PLA tablet	190 °C	60 °C	50	0.06	0.80
PVA tablets	200 °C	50 °C	20	0.10	1.05

A full discussion on the observed improvement on the morphology of the printed models, before and after optimisation will be provided in detail in section (4.4.3).

#### **4.4.2. Manufactured Drug Loaded Filaments and Fabricated FELD-PVA Model Tablets**

Before starting a full discussion for this section and the following sections, it is important to state that the main reason behind using different drug loadings for manufacturing several filaments was to achieve the maximum drug loading that could be manufactured using HME without the addition of a plasticiser. Plasticiser was excluded from the manufacturing steps to minimise the drug-excipients interaction in the final product (pure ASD, and spiked model tablets). Consequently, due to the lack of plasticiser in the manufactured filaments, a high temperature was utilised during the formulation steps of the printer feedstocks. Moreover, different challenges were faced during the fabrication of the drug-loaded model tablets utilising the FDM 3D printer, especially with the high drug-loaded feedstocks. These challenges were mainly related to the filament feeding to the printer feeding tube and printing difficulties due to the brittleness of the produced filaments.

Therefore, we used the drug-loaded printer feedstocks to fabricate drug-loaded model tablets with less complex geometries than the model tablets fabricated utilising the commercially available thermoplastic polymer, specifically PVA, as presented above in (Figure 4.2).

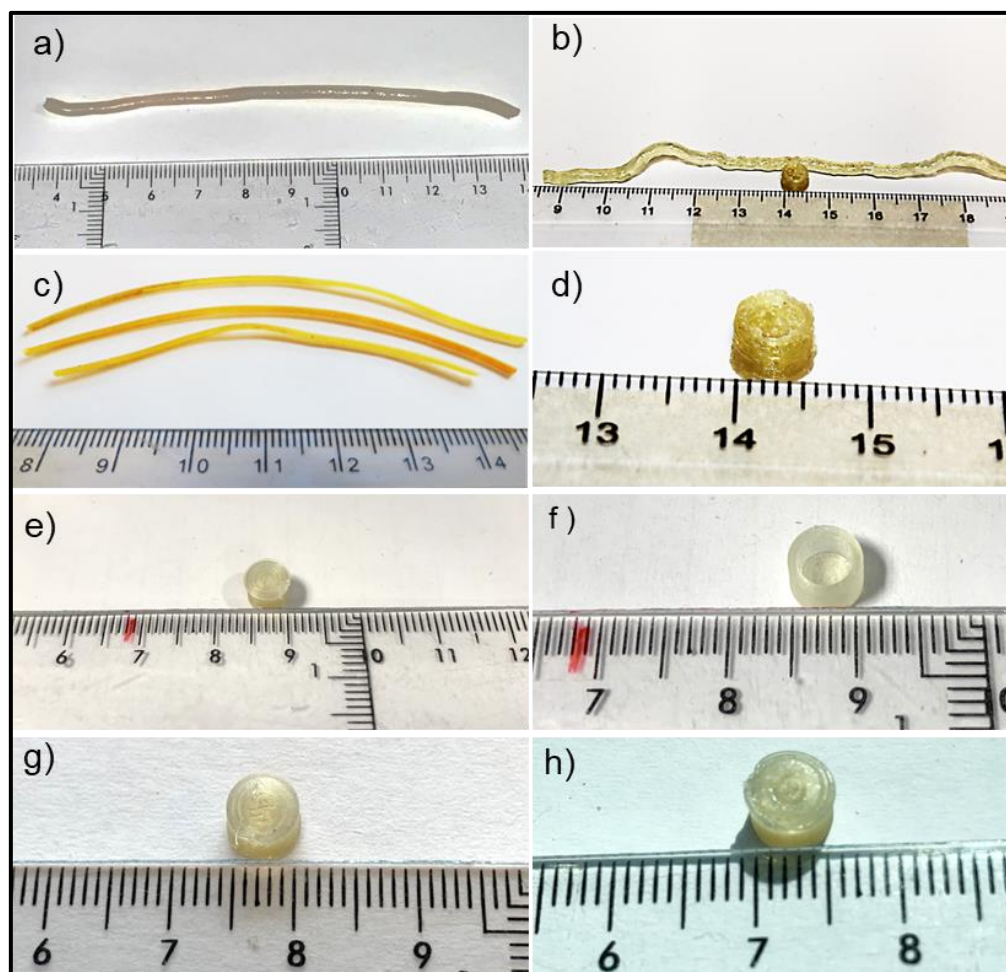


**Figure 4.3.** (a, b, and c) are photographic images of the manufactured drug-loaded filaments using HME, while d, e, f, g and h) are photographic images of the fabricated FELD-PVA model tablets utilising the FDM 3D printer.

**Figure 4.3** displays different drug-loaded filaments formulated utilising HME, and different model tablets fabricated using the FDM 3D printer. Numerous FELD-PVA filaments were successfully manufactured using HME. Initially, two drug-polymer compositions were used to produce the filaments, i.e. 10%, and 50% of FELD loading, which were selected based on our calculations in chapter 3.

For the 10%, the extrusion process was smooth, and it was possible to produce a homogenous and continuous filament, especially without plasticiser during the production step as represented in (**Figure 4.3, a**). However, due to the lack of plasticiser in the produced filament, a high temperature was used during the extrusion process (170 °C).

Then, we started to produce 50% filament. Interestingly, we managed to produce a filament containing high drug loading (50% of FELD), without adding a plasticiser, as shown in (**Figure 4.3, b**). Due to the lack of the plasticiser in the manufactured filament, the extrusion process was challenging, and the produced filament was brittle, intermittent, and very difficult to print. We managed to fabricate tablet using the high drug-loaded filament, as presented in (**Figure 4.3, d**). However, the model tablet was fabricated with poor quality due to the outlined challenges with using the 50% filament. Also, due to high material wastes and challenges encountered during filament manufacturing and tablets fabrication processes, we decided to manufacture 25% (FELD-PVA w/w) filament.

According to the calculated miscibility limits of the FELD-PVA system, as detailed in chapter 3, this drug-loading is also located in the unstable

zone. Similar production steps that were used to produce 50% filament were utilised to manufacture this filament. Even though the drug loading used with this filament was high (25% of FELD), the extrusion process was possible, and the produced filament was homogenous and continuous (**Figure 4.3, c**). However, the 25% manufactured filament was not as flexible as the 10% filament due to the impact of the high drug loading on the produced filament flexibility. Consequently, the feeding of the filament to the filament feeder tube of the FDM 3D printer during the model tablets fabrication was more difficult than when using the 10% filament. The temperature and motor speed optimised during the manufacture of the different filaments are summarised below in (**Table 4.3**).

**Table 4.3.** Temperatures and motor speed during the manufacturing process of different drug-loaded filaments.

Filament (%w/w)	T <sub>1</sub> Barrel 1 temperature (°C)	T <sub>2</sub> Barrel 2 temperature (°C)	Motor speed during mixing (rpm)	Motor speed during extrusion (rpm)	Extrusion possibility
FELD-PVA (10%)	170	170	15	35	possible
FELD-PVA (25%)	160	160	10	35	possible
FELD-PVA (50%)	160	160	10	35	challenging

**Figure 4.3 (e, f, g, and h)** demonstrates different drug-loaded (FELD-PVA) model tablets with different dimensions fabricated using the FDM 3D printer. We successfully used the manufactured filaments to fabricate the drug-loaded model tablets as designed using the TinkerCad software. Although the printing parameters were previously modified

during the fabrication of the drug-free model tablets as detailed in the previous section (4.4.1), numerous challenges were also faced during the printing process of the drug-loaded model tablets due to the use of the drug without adding plasticiser in the manufactured filaments.

For all the tablets, we started the printing process using similar parameters as were used to print the PVA drug-free tablets, as shown previously in **Table 4.1**, section (4.4.1). However, because of the presence of the drug in the produced filaments, further optimisations were applied to allow easy printing and to fabricate the model tablets with an acceptable morphology. **Table 4.4** below illustrates the main optimised parameters during the printing process.

**Table 4.4.** The optimised parameters utilised while fabricating the drug-loaded (FELD-PVA) model tablets.

Tablet FELD-PVA (%w/w)	Nozzle size (mm)	Nozzle temperature (°C)	Build plat temperature (°C)	Printing speed (mm/s)	Layer height (mm)	Wall thickness (mm)	Infill density (%)	Infill pattern	Printed tablets/10 attempts
PVA	0.40	200	50	20	0.10	1.06	100	Line	9-10
10	0.80	200	60	25	0.10	1.06	60	Line	8
25	0.60	195	60	15	0.10	1.59	20	Grid	5-6
50	0.60	195	60	15	0.10	1.59	20	Grid	1-2

As is clear from the table above, the optimised parameters were mainly related to using a bigger nozzle size (0.80 mm in case of 10%, and 0.60 mm in case of 25% and 50%), and a higher temperature for the build plate to allow more adhesion of the printed tablets on the build plate surface and prevent them from moving during the printing process. Also, the printing speed was decreased to 15 (mm/s) with the 25%, and 50%

tablet to allow better deposition of the printed layers to each other. Moreover, 20% infill density, and grid infill pattern were used to fabricate the 25%, and 50% tablets instead of using 60% infill density, and line infill pattern as were used with the 10% tablet. Lower infill density was used to minimise the materials waste during the printing process, and grid infill pattern was found to be better than using the line infill pattern, especially with 25% model tablets, to produce tablets with better morphology. Although no plasticizer was utilised to formulate the filaments as mentioned previously, it was possible to print 8 tablets out of 10 printing attempts using the 10% drug-loaded manufactured filaments and 5-6 tablets out of 10 attempts utilising the 25% drug-loaded manufactured filament.

Unfortunately, due to the reasons mentioned earlier in this section, there were a high material wastes during the printing process using the 50% filament, in which 1-2 tablets were printed out of 10 attempts. Therefore, this drug-loading was excluded from the following steps.

In the following section, SEM was utilised to investigate the morphology of the fabricated model tablets, including drug-free, and drug-loaded model tablets, for both pre-optimised, and post-optimised fabricated tablets. Also, it was used to study the morphological structure of the formulated filaments. Moreover, the dimensions of the fabricated model tablets were measured using electronic callipers to compare the dimensions of the manufactured model tablets with the software tablet designs.

### 4.4.3. Morphological Observations, and Measurements of the Manufactured Filaments and 3D Fabricated Model Tablets

Firstly, we started to investigate the microstructure of the drug-free model tablets. Then, we measured the dimensions of these model tablets as detailed below.

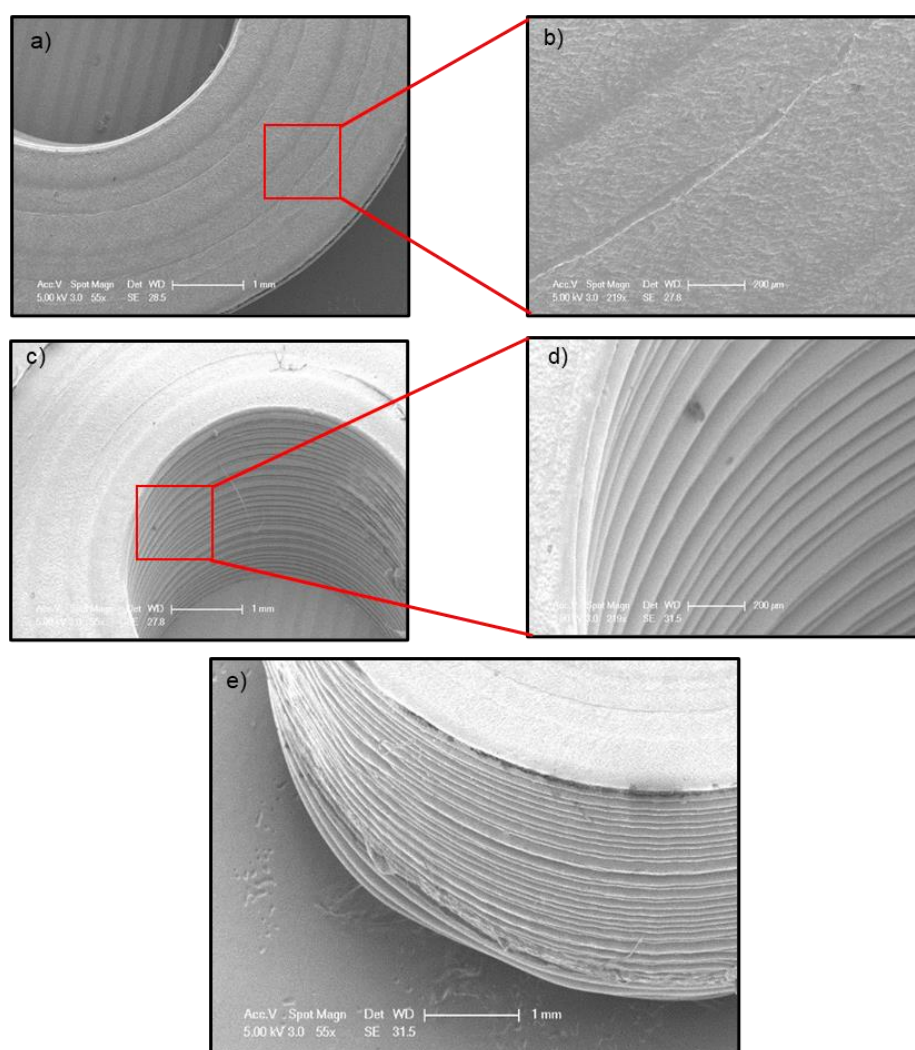


**Figure 4.4.** SEM images of the fabricated PLA drug free tablet utilising the Ultimaker 2+ FDM 3D printer, a), and b) are the images of the tablet surface, while c), and d) are the images of the tablet the inner layers, and e) is the image of the tablet outer layers.

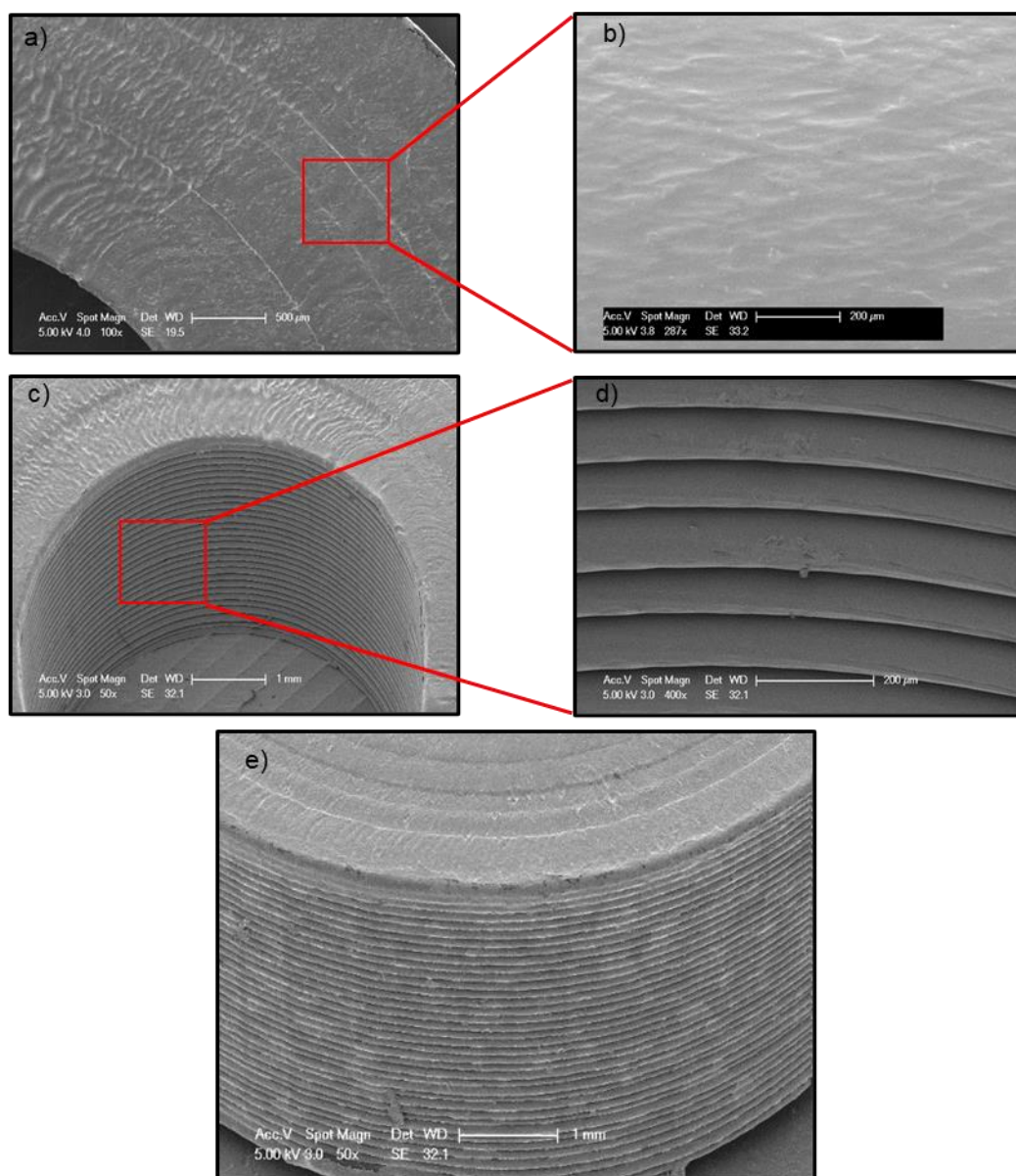


**Figure 4.5.** SEM images of the fabricated PVA drug free tablets utilising the Ultimaker <sup>2+</sup> FDM 3D printer after optimisation of the printing parameters. a), and b) are the images of the tablet surface, while c), and d) are the images of the tablet inner layers, and e) is the image of the tablet outer layers.

**Figure 4.4** represents SEM images of the PLA drug-free model tablets fabricated using the FDM 3D printer and default printing parameters. The SEM images of the PLA printed tablet surface (**Figure 4.4, a and b**) indicate that the printed layers are uniformly organised and connected, which led to a smooth surface. Furthermore, the images of the inner layers (**Figure 4.4, c and d**), demonstrate that the fabricated layers were uniformly connected to each other and organised. Moreover, the images of the outer layers of the fabricated PLA tablet (**Figure 4.4, e**) shows that the bottom printed layers were overlapped while the upper layers were fabricated with better resolution and more organised than the bottom layers. The layers overlapping maybe due to the printing speed utilised during the printing process, which may have affected the adhesion of the layers to each other.

Although the fabricated PLA tablet has illustrated an acceptable shape and morphology after the printing process, as shown in **Figure 4.4**, we modified the previously used parameters to achieve better morphology while printing the PVA tablets, as detailed in section (4.4.1).

**Figure 4.5** represents SEM images of the PVA drug-free tablets fabricated utilising the FDM 3D printer and the optimised printing parameters. The images captured for the PVA tablet show a smooth surface (**Figure 4.5, a and b**). Furthermore, the images that were captured for the inner layers of the PVA tablet indicate a uniformity, and well-connected layers to each other with no layers overlapping in any

parts of the printed layers as deposited in (**Figure 4.5, c and d**); hence, better resolutions were achieved than for the PLA printed tablet.

Moreover, SEM images captured for the outer layers, as shown in (**Figure 4.5, e**) revealed that all the printed layers were uniformly organised, well connected, and no overlapping between layers was detected. Thus, better morphology was achieved than that with the PLA tablet.

Moreover, an electronic calliper was used to see the alterations that may occur on the dimensions of the designed tablets after the printing process and to also see the ability of the printer to produce objects with dimensions that are same as or close to the designed models. **Table 4.5** below summarised all the dimensions of the designed and the fabricated model tablets.

**Table 4.5.** Represents the dimensions of the designed tablets and the dimensions of the model tablets after the printing process using the FDM 3D printer.

Designed and fabricated tablets		First main tablet (mm)		Second main tablet (mm)		Central part (mm)		Surface cap (mm)		Hollow (mm)
		Diameter	Height	Diameter	Height	Diameter	Height	Diameter	Height	Diameter
<b>PLA tablet</b>	Designed	11.00	5.00	-	-	-	-	-	-	5.00
	Fabricated	11.09	4.91	-	-	-	-	-	-	4.80
<b>PVA tablet</b>	Designed	11.00	4.00	-	-	4.65	2.00	4.65	1.00	5.00
	Fabricated	11.02	3.95	-	-	4.66	2.09	4.69	0.83	4.94
<b>PVA tablet</b>	Designed	10.00	2.00	10.00	2.00	4.40	2.50	-	-	5.00
	Fabricated	10.01	2.01	10.01	2.01	4.42	2.52	-	-	4.67
<b>PVA tablet</b>	Designed	11.00	2.00	11.00	1.33	5.90	2.00	-	-	6.40
	Fabricated	11.00	2.03	11.00	1.38	5.91	2.02	-	-	6.30

It is clear from the table above that the FDM 3D printer was able to fabricate the model tablets as designed using TinkerCad software, especially after optimising the default parameters used to print the PLA tablet. This result is consistent with the result obtained using SEM, in which better morphology was observed for the PVA tablets rather than the PLA tablet after optimisation of the printing parameters. We can conclude from these two results that the FDM 3D printer has the ability to control different parameters during the fabrication process. Also, it has the ability to fabricate objects with different and complicated geometries. Therefore, the FDM 3D printer will be utilised in the current thesis to manufacture the model tablets that will be fabricated as compartment tablets with an outer shell and an inner core using the optimised parameters.

In the following section, SEM was used to study the morphology of the manufactured drug-loaded filament after it was extruded using HME at 160°C, and after it was extruded from the FDM 3D printer nozzle at 195°C.

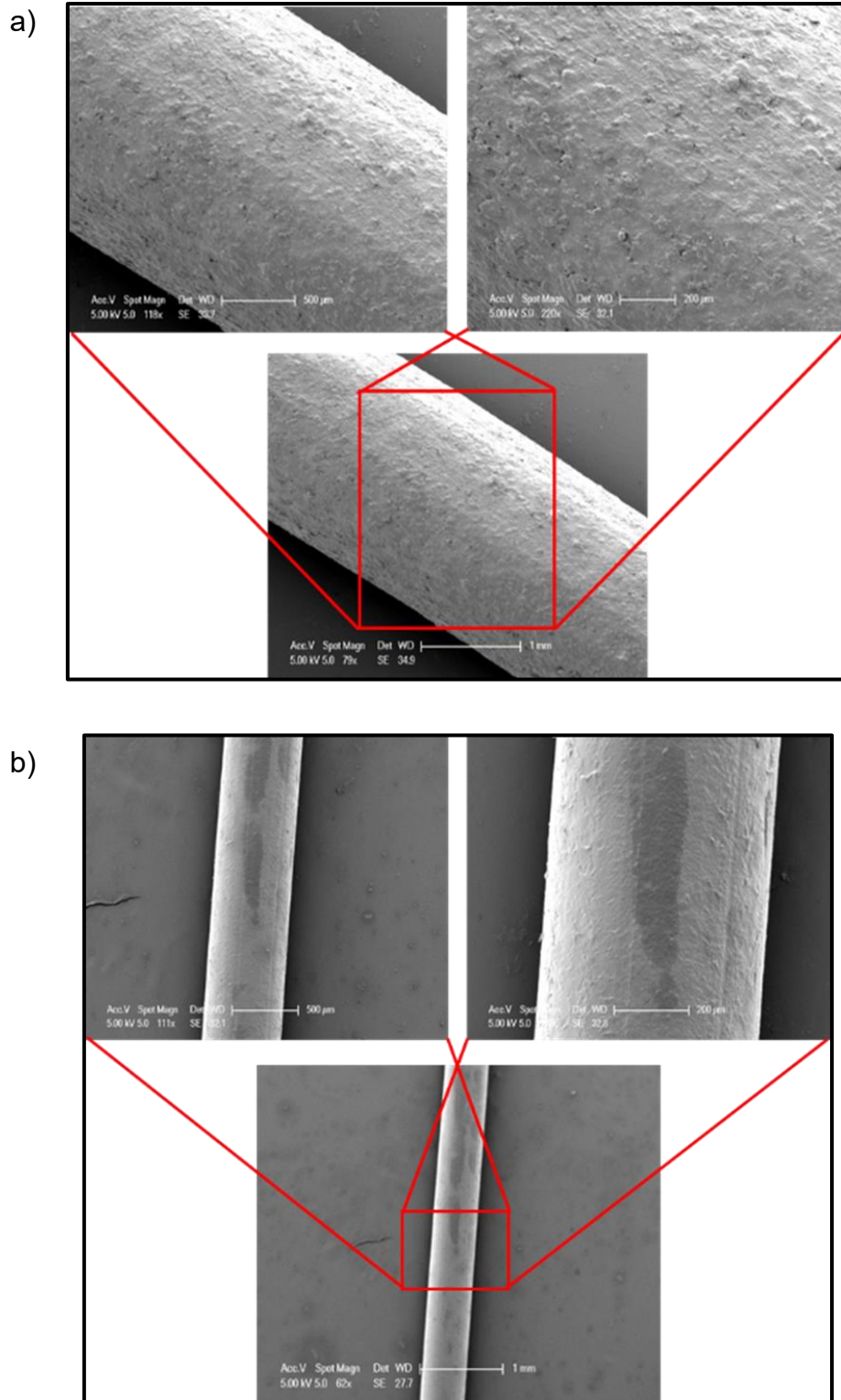


**Figure 4.6.** a) SEM images of the fabricated FELD-PVA filament after the extrusion process using the HME, and b) SEM images of the FELD-PVA filament after being extruded through the FDM 3D printer nozzle.

**Figure 4.6 (a, and b)** show SEM images of the FELD-PVA filament after it was extruded using HME and FDM 3D printer. The SEM images after the first extrusion process, (**Figure 4.6, a**), have revealed that the fabricated filament has a rough surface; however, no pores or cracks were observed on the prepared filament.

**Figure 4.6 (b)** shows SEM images of the FELD-PVA filament after being extruded through the FDM 3D printer nozzle. The SEM images revealed that the extruded filament has a smoother surface than the filament that was prepared using the HME. This may be due to the further mixing happening because of the use of high temperature during the printing process, which has led to a more homogenous system.

Next, we studied the morphology of the fabricated drug-loaded model tablets utilising SEM, and we used electronic callipers as well to measure the dimensions of the printed model tablets, as shown below.

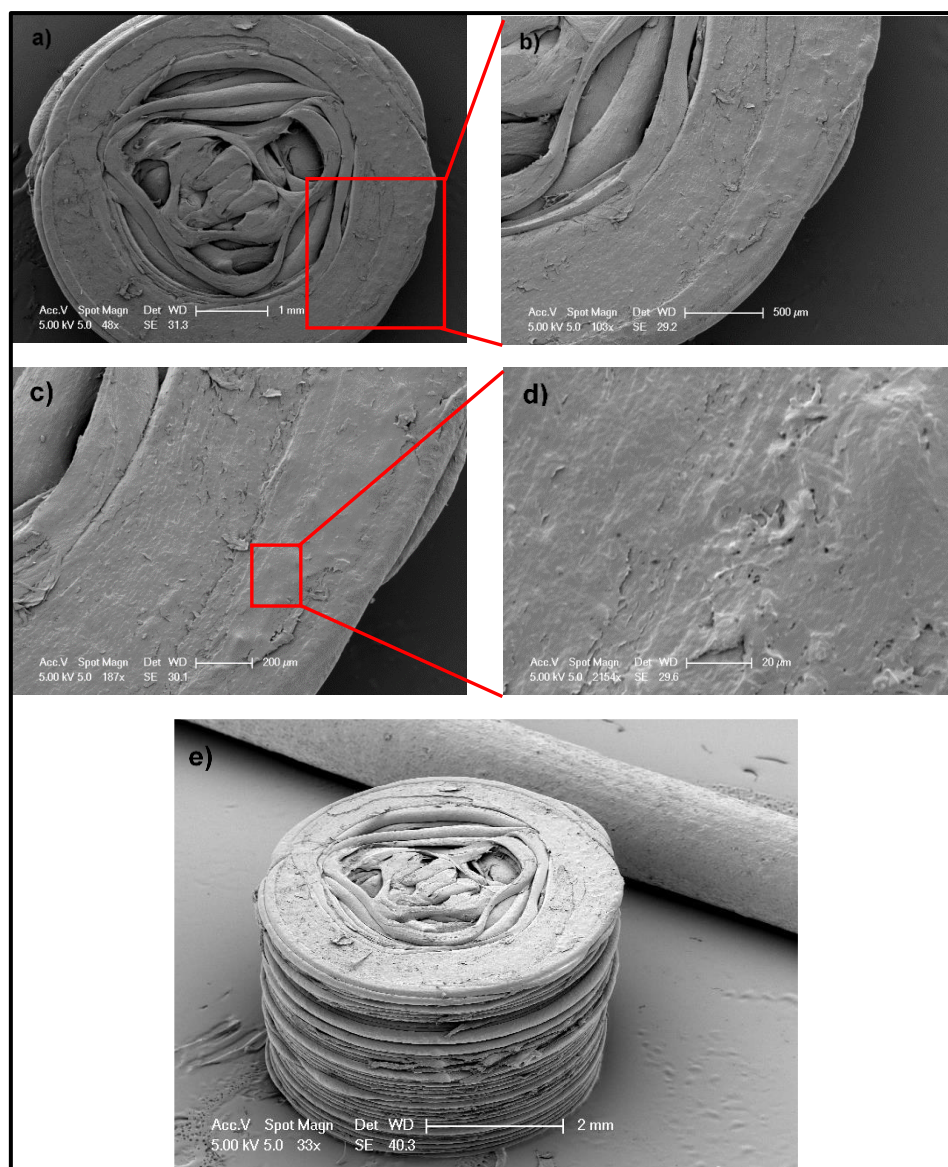


**Figure 4.7.** SEM images of the pre-optimized fabricated FELD-PVA model tablet. a), b), c), and d) are the images of the tablet surface, while e) is the image of the tablet outer layers.

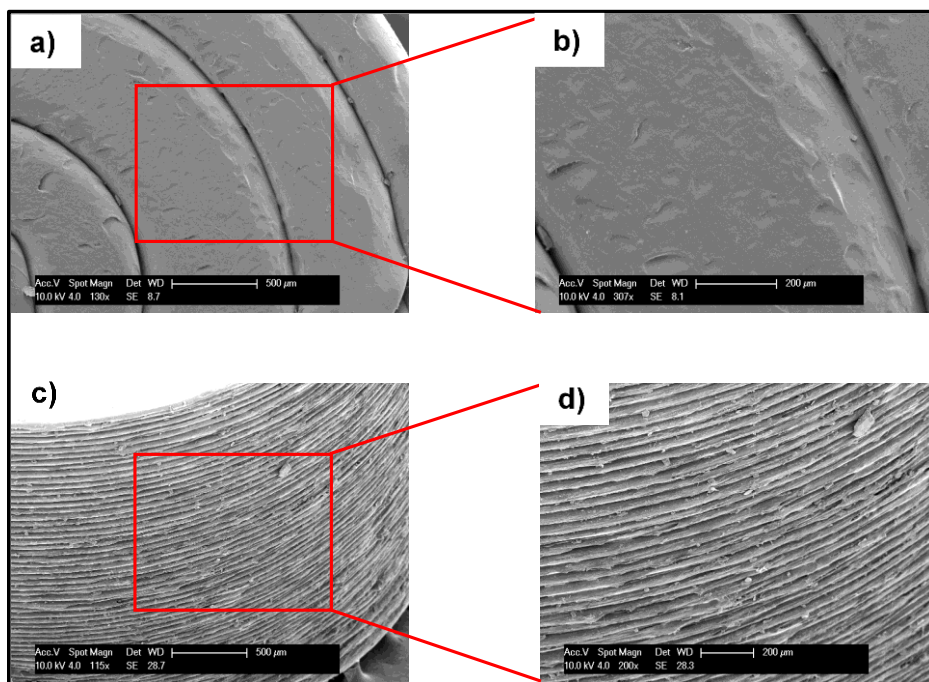


**Figure 4.8.** SEM images of the post-optimised FELD-PVA model tablets fabricated using the FDM 3D printer. a), and b) are the images of the tablet surface, while c), and d) are the images of the tablet outer layers.

**Figure 4.7** represents SEM images of the drug loaded model tablet fabricated utilising the FDM 3D printer before optimisation of the printing parameters. The printing process of this tablet was established at 200-°C (nozzle temperature) (**Appendix Figure 3, a**). The top view images (**a, b, c, and d**) showed that the layers on the surface of the fabricated tablet were not uniformly connected and overlapped. Moreover, the SEM images showed that the printed tablet was characterised by a rough surface. Furthermore, the image of the tablet outer layers (**Figure 4.8, e**) revealed that the layers were not consistently connected, and layers overlapping was detected. This may be due to the parameters that were

used during the printing process, such as the printing speed, infill density, and the temperature utilised during the printing process.

Another model tablet was also characterised using SEM. However, due to the use of high temperature during the printing process (206 °C), the morphology of the produced tablet was poor (**Appendix Figure 4**). Thus, further optimisations were made to the previously used parameters to fabricate a tablet with better morphology than the previously fabricated models.

**Figure 4.8** shows SEM images of the drug-loaded model tablet fabricated utilising the FDM 3D printer after optimisation of the printing parameters. The printing process of this tablet was established at 195 °C (nozzle temperature) (**Appendix Figure 3, b**). The top view (**a, b, c, and d**) images revealed that the surface of the fabricated tablet is smoother than the previous tablet and the layers were organised and uniformly connected to each other. In addition, no layers overlapping was detected in the printed tablet. The improvement observed on this tablet was due to the changes that were made to the printing parameters, especially the printing temperature and the infill density.

The dimensions of the fabricated model tablets were measured before and after the optimisation process using electronic callipers, as shown in (**Table 4.6**).

**Table 4.6.** Dimensions of the designed and the 3D printed model tablets measured using electronic callipers before and after optimisation.

Tablet	Designed tablet dimensions (mm)	Fabricated tablet dimensions (mm)
FELD-PVA (Pre-optimised)	5.00x4.00	5.32 x3.63
FELD-PVA (post-optimised)	6.00x4.00	6.07 x 3.95

The measured dimensions revealed defects in the dimensions of the pre-optimised fabricated tablets, which may be due to the use of high temperature while printing which causes layers overlapping and size shrinkage. However, the post-optimised printed model tablets have shown better dimensions than pre-optimised tablets. The defects that was found in the dimensions of the fabricated tablets is consistent with the previously observed in the morphology of the printed tablets studied using SEM. We can conclude from these results that the FDM 3D printer has the ability to print the designed tablets with an acceptable morphology using the manufactured 25% and 10% drug loading filaments that were prepared utilising HME.

#### 4.4.4. Thermal Analysis of FELD-PVA Filaments and 3D Printed Model Tablets Utilising DSC

Before commencing a full discussion for the following sections, it is important to state that according to the calculations obtained for the FELD-PVA system as discussed in chapter 3, all the drug loadings were predicted to be completely miscible at or above the drug melting point temperature. On the other hand, phase separation and re-crystallisation

are possible for drug loadings higher than 10% (FELD-PVA w/w) as soon as the temperature reaches 25 °C. Consequently, it may be possible to manufacture ASD filaments and model tablets by operating both the extruder and the printer at a temperature above or close to the FELD melting point, 140 °C, for all the drug loadings. As detailed previously in the current chapter, high temperatures were used during both the feedstock manufacturing using HME and the tablet fabrication utilising the FDM 3D printer due to the lack of plasticiser. Consequently, it was possible to manufacture a homogenous one phase ASD feedstock and model tablets utilising an HME and the FDM 3D printer techniques at temperature above 140°C for all the drug loadings. In contrast, it was challenging to fabricate model tablets spiked with crystallinity at the utilised temperatures. However, based on the calculations obtained in chapter 3, it may be possible to prepare a spiked model tablet by storing the freshly fabricated samples at room temperature. After that, the aged samples may then be used along with the fresh samples to fabricate the spiked model tablets.

Also, it is important to mention that different methods with a different limit of detection were used to characterise the manufactured filaments as well as the fabricated model tablets to investigate the possible drug-polymer interactions and formation of ASD. Moreover, these methods were used to detect a possible % of crystallinity in formulated filaments and fabricated tablets. As reported in the literature [224], PXRD and DSC can detect about 5-10% crystallinity, which is less sensitive than FTIR (1-

2%) and Raman (<1%) in detecting the degree of crystallinity in ASD formulations [224].

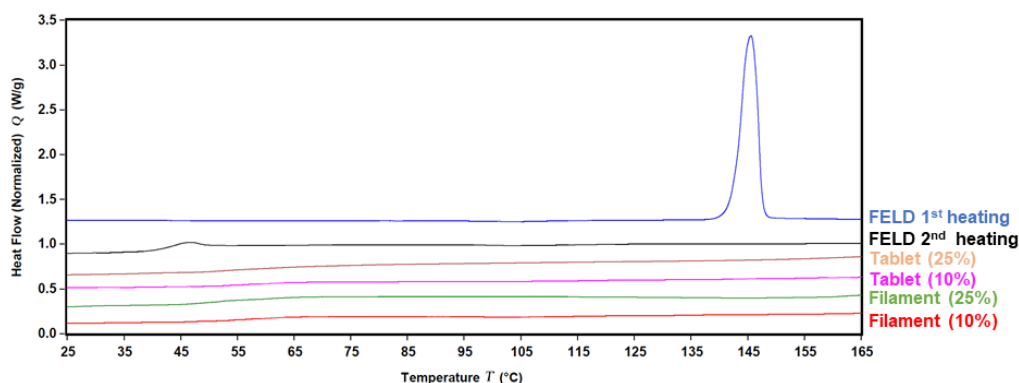


**Figure 4.9.** DSC thermograms of the first and the second heating cycles of FELD, 10%, and 25% (w/w) 3D printed model tablets and manufactured filaments. (Endotherm upward in the thermogram).

**Figure 4.9** represents the DSC thermograms of the 1<sup>st</sup> and 2<sup>nd</sup> heating events of the crystalline FELD, formulated filaments, and fabricated model tablets. As it is clear from the figure, DSC thermogram of the crystalline FELD showed a sharp melting peak 148°C during the 1<sup>st</sup> heating event. Interestingly, the sharp melting peak that was observed during the first heating cycle disappeared from the 2<sup>nd</sup> heating cycle, and a single  $T_g$  was detected 45°C, indicating that the drug was changed to the amorphous form.

Turning to DSC thermograms of the manufactured filaments (10%, and 25%), interestingly, no melting endotherm was detected for the prepared filaments during this analysis, and a single  $T_g$  was observed for both filaments, at 58.20°C, and 54.12°C for 10%, and 25% respectively (**Appendix Figure 5**). The disappearance of the melting peak and the

appearance of a single  $T_g$  indicated that the felodipine was molecularly dispersed in the polymer matrix resulting in the formation of ASD filaments [43] [58].

Similarly, no endotherm melting peak was detected with both fabricated tablets. Moreover, only a single  $T_g$  was observed, at 58 °C, and 55 °C, with 10%, and 25% fabricated model tablets respectively (**Appendix Figure 5**). The detected single  $T_g$  and the absence of the melting endotherm event of the fabricated tablets indicated that the FELD was molecularly dispersed in the polymer matrix resulting in the formation of ASD tablets [43] [58]. This result is in agreement with the result obtained from chapter 3, in which all the drug-polymer compositions used have indicated complete miscibility between FELD and PVA when manufactured at a temperature more than 140°C.

Also, in the next sections, FTIR, Raman, and PXRD were utilised for further investigation of the possible drug-polymer interactions and formation of ASD within both the formulated feedstocks and fabricated model tablets.

## 4.4.5. FTIR Spectra of Prepared Filaments and 3D Printed Tablets

### 4.4.5.1. FTIR Spectra of Prepared Filaments

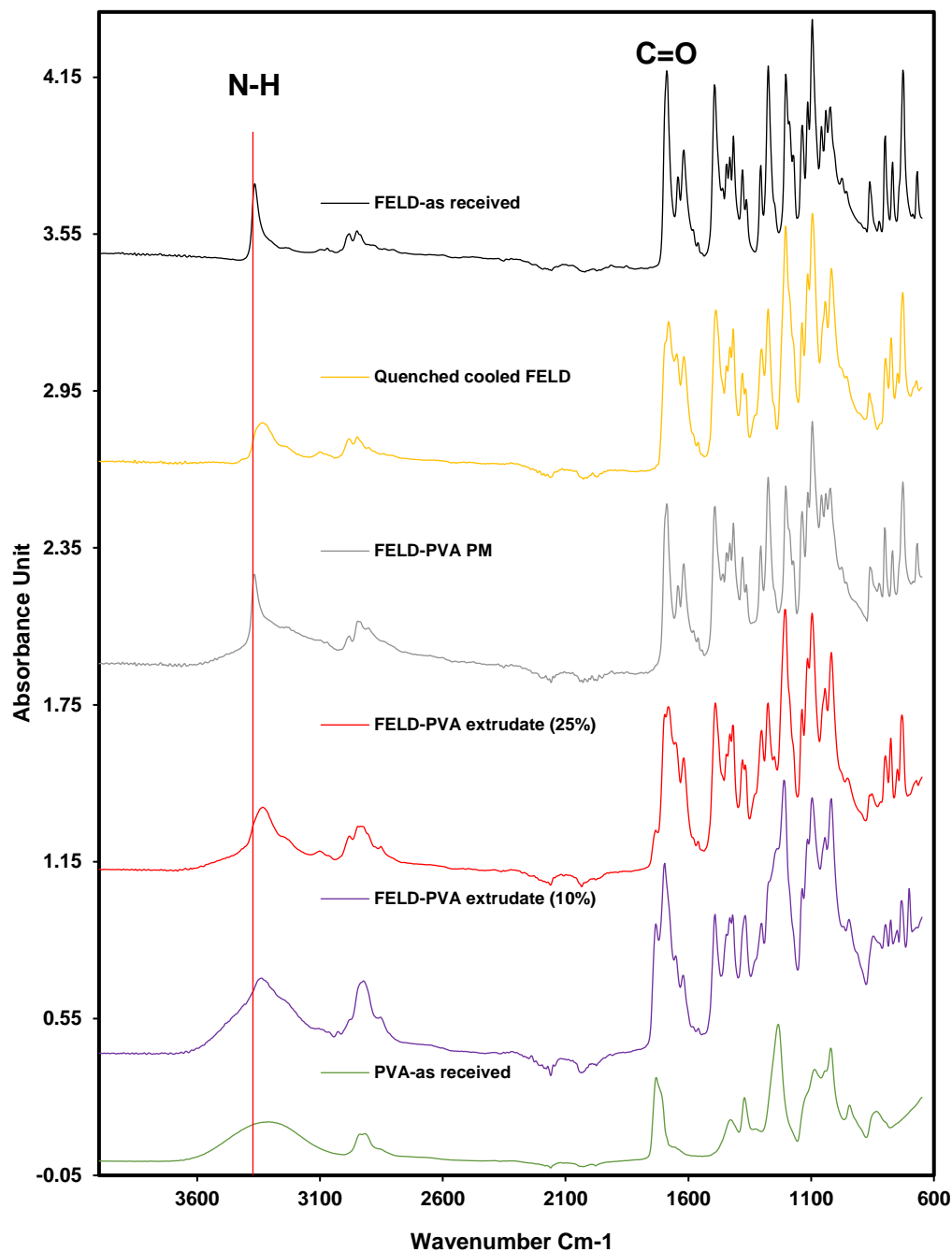


**Figure 4.10.** FTIR spectra of the crystalline FELD, quenched cooled FELD, FELD-PVA physical mixture, FELD-PVA extrudates of 25%, and 10% drug-loading respectively, and PVA.

### 4.4.5.2. FTIR Spectra of 3D Fabricated Model Tablets

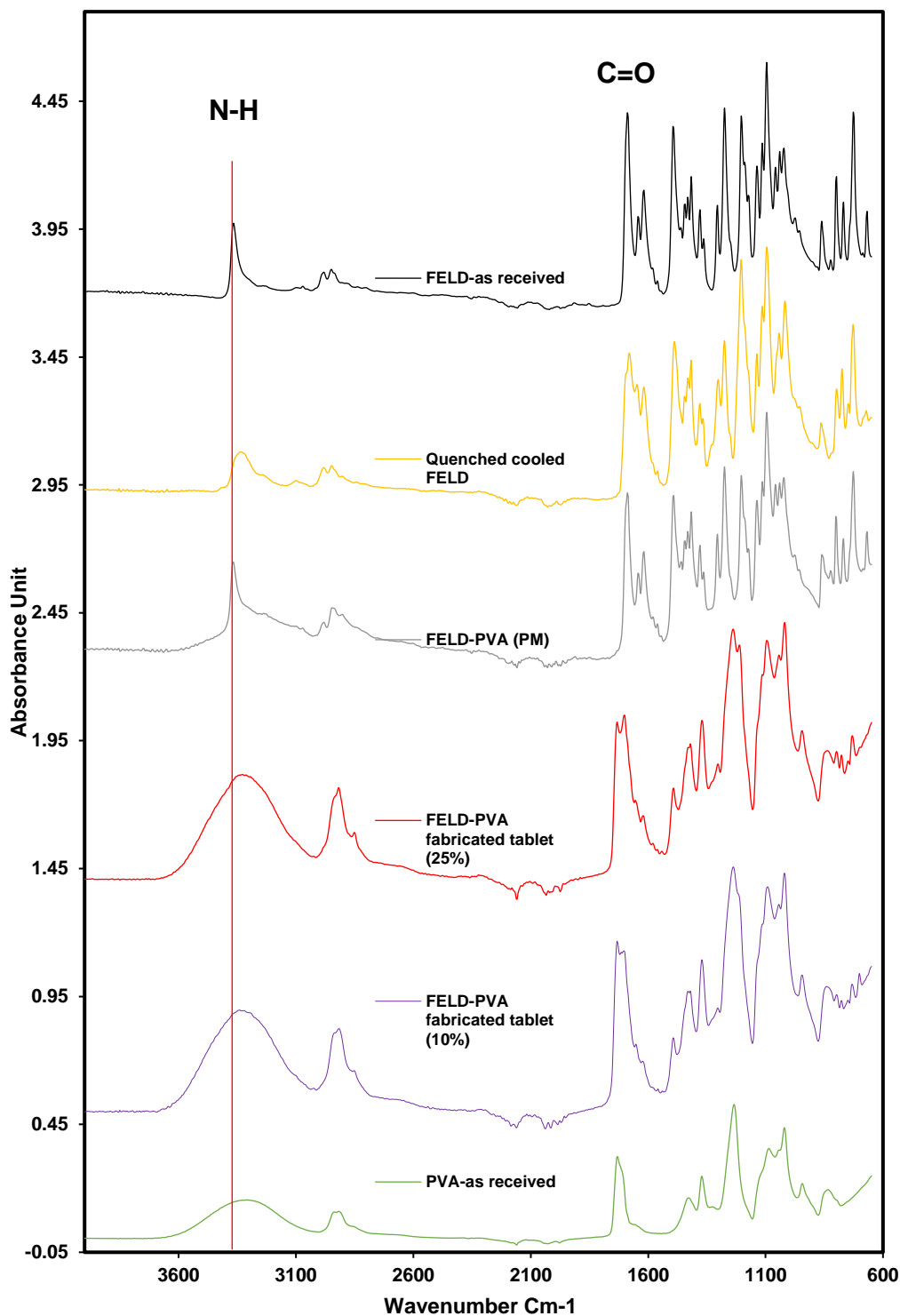


**Figure 4.11.** FTIR spectra of the crystalline FELD, quenched cooled FELD, FELD-PVA physical mixture, 3D printed model tablets of 25%, and 10% drug-loading respectively, and PVA.

Initially, the crystallinity of FELD and the formation of FELD amorphous form, using the melting method, were confirmed using different approaches, including PXRD, FTIR, and Raman (**Appendix Figure 6, 7, and 8**). Two main peaks of the FELD and one peak of PVA in the FTIR spectra were selected to compare the spectra of the manufactured materials with the raw materials.

**Figure 4.10** displays the FTIR spectra of the crystalline FELD, amorphous FELD, FELD-PVA physical mixture, manufactured extrudates, and PVA. Two peaks of the crystalline FELD, which are the amine group (N-H peak), and the carbonyl group (C=O), were selected as main peaks in order to compare between different components in the current discussion. It is apparent from the figure illustrated above (**Figure 4.10**) that the crystalline FELD, and the FELD-PVA physical mixture are characterised by two significant peaks (drug finger print), the amine group (N-H peak), located at  $3363\text{ cm}^{-1}$ , and the ethyl ester carbonyl group C=O, located at  $1685\text{ cm}^{-1}$ . For the PVA, a significant peak appears at  $1726\text{ cm}^{-1}$ , which is the carbonyl group (C=O).

Also, it is clear from the figure shown above (**Figure 4.10**) that the spectra of the quenched cooled FELD and the manufactured extrudates are significantly different in comparison to the spectra of the crystalline FELD, and the FELD-PVA physical mixture. The difference significantly appeared in the band related to the amine group in the pyridine ring of the FELD. As in the spectra of the pure FELD and the FELD-PVA physical mixture, the band appears in the range of  $3350\text{-}3380\text{ cm}^{-1}$  (N-H group), specifically at  $3363\text{- cm}^{-1}$ , it is much broadened in the spectral

region of the manufactured extrudates. Moreover, the difference is clear in the band related to the vibration of the ethyl ester carbonyl group (C=O). In the spectra of the formulated extrudates and the quenched cooled FELD, the band is much broadened with lower absorbance intensity compared to the spectra of the crystalline FELD and the FELD-PVA physical mixture. Furthermore, the spectra of the formulated extrudates and the quenched cooled FELD was shifted to lower wavenumber ( $1674\text{ cm}^{-1}$ ) compared to the spectra of the crystalline FELD, which appeared at a higher wavenumber ( $1685\text{ cm}^{-1}$ ).

**Figure 4.11** shows the FTIR spectra of the crystalline FELD, amorphous FELD, FELD-PVA physical mixture, fabricated model tablets using the FDM 3D printer, and PVA. It is clear from the figure displayed above (**Figure 4.11**) that the fabricated model tablets are characterised by more broadened band in the band related to the amine group (N-H) compared to the observed spectra of the manufactured extrudates as shown in **Figure 4.10**. Also, the fabricated model tablets showed broadened bands in the band related to the amine group (N-H) compared to the spectra of the crystalline FELD and the FELD-PVA physical mixture. The observed broadened spectra of the fabricated model tablets compared to the spectra observed with manufactured extrudate may be due to use of high temperature ( $195^{\circ}\text{C}$ ) and second extrusion process during the fabrication of the model tablets using the FDM 3D printer.

The obvious detected shift in the wavenumber, the lower absorbance intensity, and the band broadening of the manufactured filaments (extrudates), and the fabricated model tablets compared to the spectra

of the crystalline FELD and the FELD-PVA physical mixture is an indication of the strong FELD-PVA interactions, and the formation of ASD. This result is consistent with the data reported in the previous section using DSC. Similar to the DSC result, the FTIR result has indicated complete miscibility between FELD and PVA, and the formation of ASD. More investigation into the drug-polymer interaction, the formation of the ASD, and detection of crystallinity in the fabricated model tablets was conducted using Raman spectroscopy, and PXRD.

#### 4.4.6. Raman Spectra of the Raw Materials and the Fabricated FELD-PVA Model Tablets

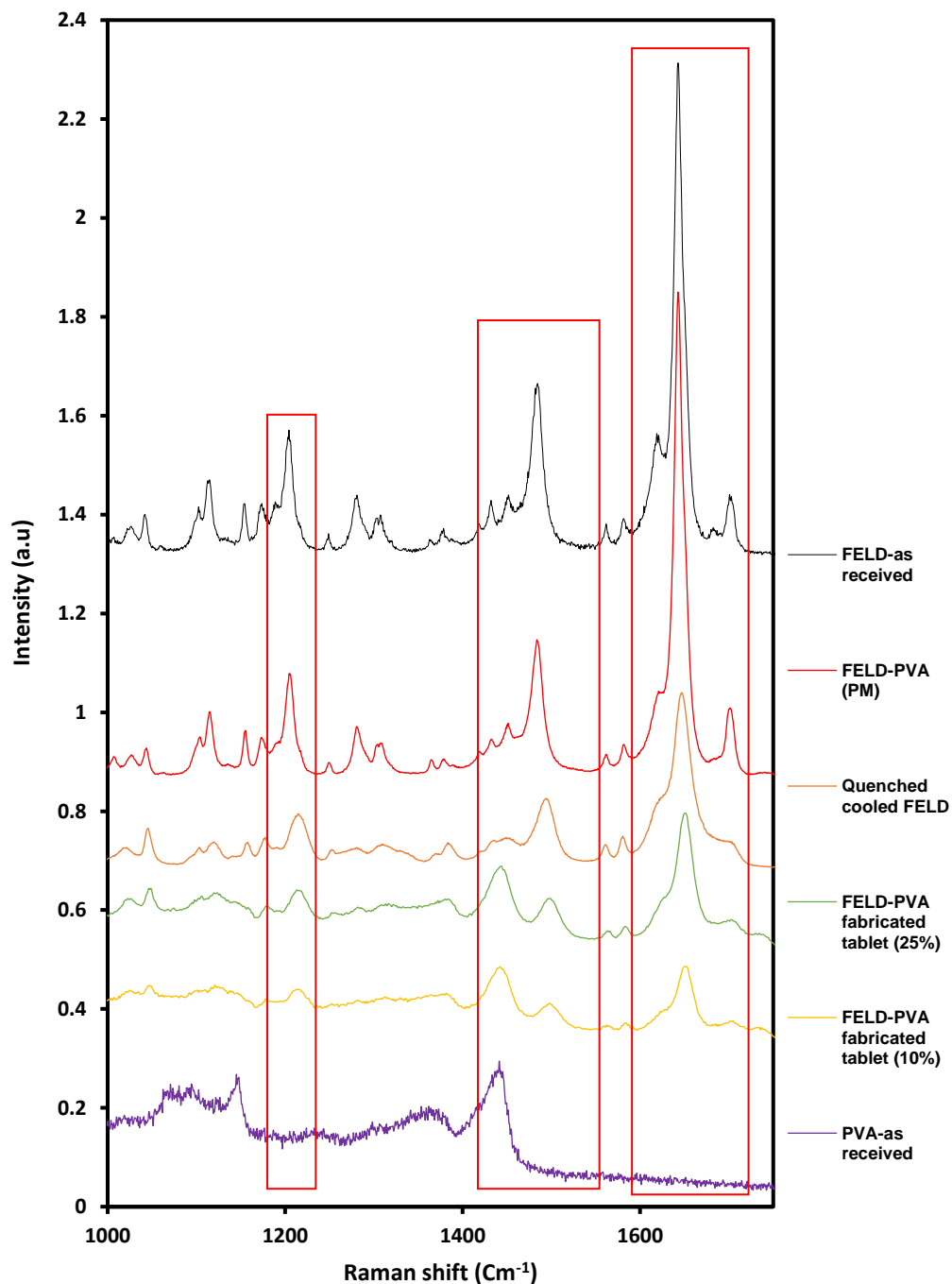


**Figure 4.12.** Raman spectra of the crystalline FELD, FELD-PVA physical mixture, quench cooled FELD, fabricated model tablets, and PVA in the molecular-region (1100-1750 cm<sup>-1</sup>).

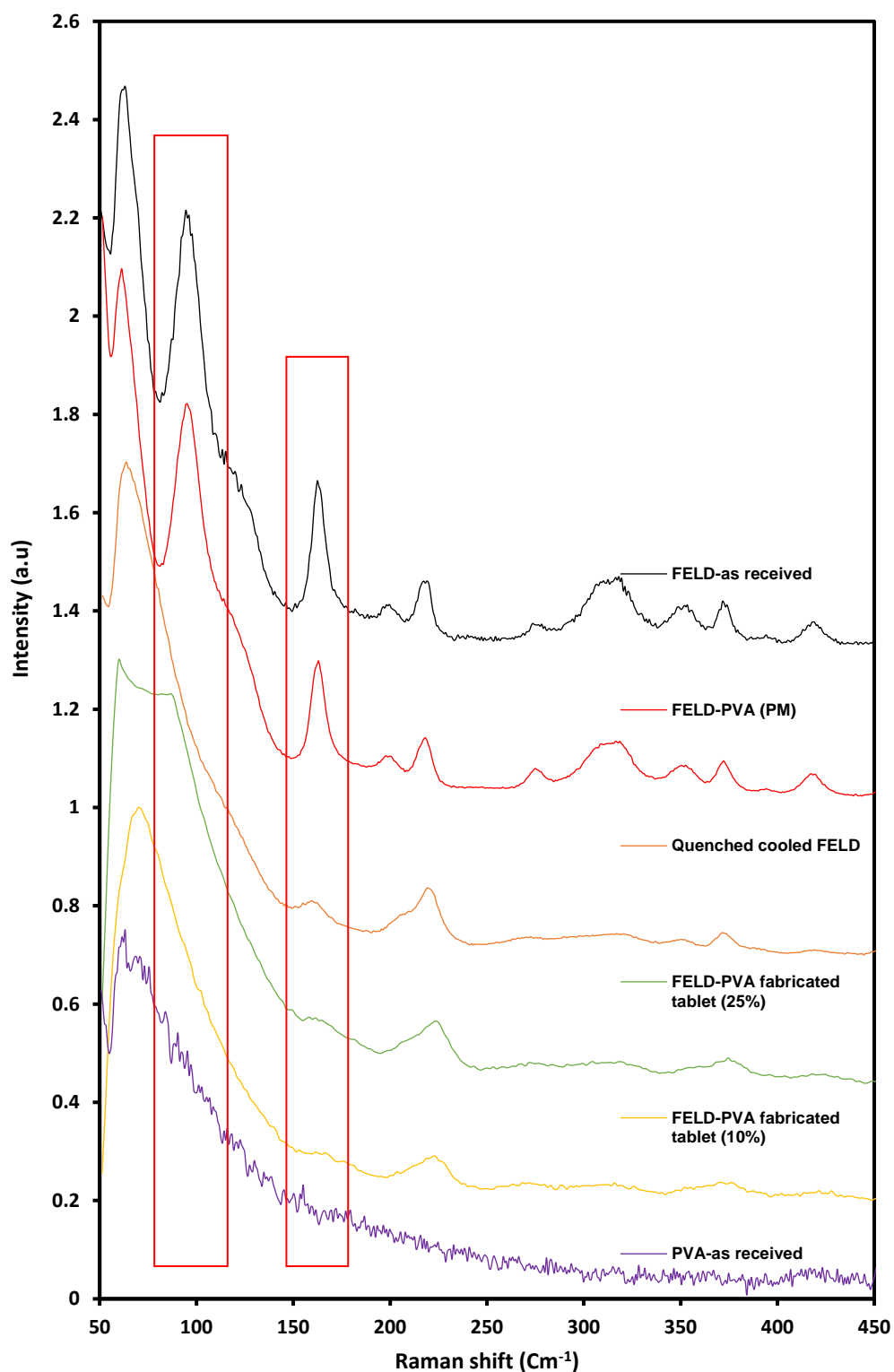


**Figure 4.13.** Raman spectra of the crystalline FELD, FELD-PVA physical mixture, quench cooled FELD, fabricated model tablets, and PVA in the phonon region (50-450- cm<sup>-1</sup>).

**Figure 4.12** and **4.13** show the Raman spectra of the raw materials, FELD-PVA physical mixture, and the 3D printed model tablets. **Figure-4.12** displays the fingerprint region ( $1100\text{-}1750\text{ cm}^{-1}$ ), while **4.13** illustrates the phonon-mode region ( $50\text{-}450\text{ cm}^{-1}$ ). Starting with the spectra of the pure ingredients, FELD and PVA, and the spectra of the FELD-PVA physical mixture, it is clear that the crystalline FELD (as received) and the FELD-PVA physical mixture are identified by sharp peaks, whereas the PVA is characterised by less-defined peaks.

Turning to the spectra of the fabricated tablets, it appears as a combination of the polymer (PVA), and the amorphous form of the drug (quenched cooled FELD). However, the peaks of the fabricated tablets were slightly shifted towards higher wavenumber in comparison to the peaks of the quenched cooled FELD. The peaks at  $1497\text{ cm}^{-1}$  appeared at  $1500\text{ cm}^{-1}$  for the fabricated tablets, and the peaks at  $1649\text{ cm}^{-1}$  moved to  $1652\text{ cm}^{-1}$  for the fabricated tablets. These shifts can be described by the drug-polymer interaction, which has been previously reported for the formation of FELD amorphous solid dispersions with PVP, and copovidone [1] [4].

When comparing the crystalline FELD with the quenched cooled FELD, it is possible to observe a significant difference between the spectra of the two forms of the FELD (quenched cooled, and crystalline FELD). It is clear that the pure FELD is characterised by sharp, and high intense peaks, while the quenched cooled FELD is identified by broad,

continuous, and less intense peaks relative to the sharp peaks of the crystalline FELD that appear in the fingerprint region (1100-1750  $\text{cm}^{-1}$ ).

These differences in the peaks shape of the two FELD forms (crystalline and quenched cooled) is due to the disorganised molecule environment of the amorphous form [101]. Moreover, the molecular bands of the pure FELD (raw material) that are located at 1205, 1485, and 1643  $\text{cm}^{-1}$ , were shifted to 1217, 1497, and 1649  $\text{cm}^{-1}$  (higher wavenumber) in the case of the quenched cooled FELD [101].

Moreover, it is evident that the two solid forms of the FELD have different spectra in the phonon-mode region, which results from inter-molecular vibrations, as displayed in **Figure 4.13**. In this region, it is evident that the crystalline FELD, and the FELD-PVA physical mixture, are characterised by sharp bands, which appear at 94  $\text{cm}^{-1}$ , and 162  $\text{cm}^{-1}$ , while the quenched cooled form is characterised by broad bands and continuous distribution of the intermolecular vibrations. The phonon-mode region has been previously reported in the literature [5] [6], to differentiate between different solid forms of a drug easily. This result is consistent with the previous results, in which the produced tablets are completely amorphous.

#### 4.4.7. XRPD Patterns of the Raw Materials and Fabricated Model Tablets

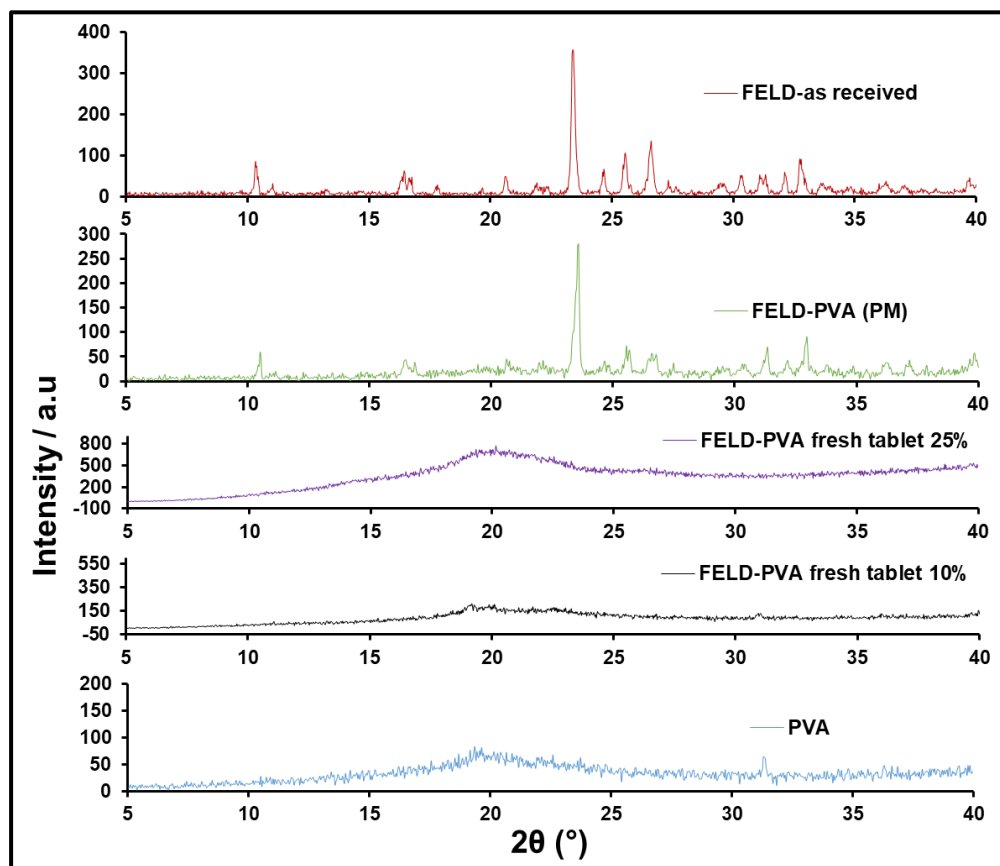


**Figure 4.14.** XRPD patterns of the crystalline FELD, PVA, FELD-PVA physical mixture, and freshly fabricated model tablets (10%, and 25% w/w).

**Figure 4.14** shows the XRPD patterns of raw materials, FELD-PVA physical mixture, and fabricated model tablets. It is clear that the crystalline FELD is characterised by sharp Bragg peaks positioned mainly at 10.19 °, 10.84 °, 16.17 °, 16.58 °, 17.68 °, 20.51 °, 23.21 °, 24.49 °, 25.41 °, 26.46 °, 27.91 °, 29.45 °, 30.16 °, 30.94 °, 31.46 °, 32.00 °, 32.63 °, and 33.46 °. Also, the FELD-PVA physical mixture is characterised by

sharp Bragg peaks similar to the crystalline FELD. Moreover, it is clear that PVA polymer is characterised by amorphous halo in relative to the sharp peaks of the crystalline FELD and the FELD-PVA physical mixture.

The sharp Bragg peaks of the crystalline FELD disappeared for the fabricated model tablets, which displayed amorphous halo, indicating that the crystalline FELD was transformed from crystalline to amorphous form within the fabricated model tablets. This result is in an agreement with the previously reported results using different techniques in the previous sections.

According to the calculations shown in chapter 3, all the FELD-PVA compositions have shown complete miscibility at 140 °C, while phase separation and re-crystallisation are possible at a temperature of 25 °C (or below) for drug loadings higher than 10% (FELD-PVA w/w). Thus, the observed complete miscibility for all the investigated compositions using the different techniques was obvious due to the lack of plasticiser in the manufactured materials, which has led to the use of high temperatures during both the printer feedstocks formulation using HME and the model tablets fabrication using the FDM 3D printer, as detailed previously in the present chapter. Thus, formulating a filament or a tablet with crystallinity was challenging for all the used drug-loadings, especially because all the produced materials were manufactured at a temperature above 140°C. As a such, exposure to high RH was utilised as an approach to facilitate crystallinity and to achieve equilibrium in the manufactured materials.

Also, due to the high materials wastes and manufacturing challenges discussed previously for the 50% filament, and for the reason that we want to study the effect of crystallinity on dissolution behaviour of ASD at a high drug-loading scenario, we decided to continue with 25% (FELD-PVA w/w) for the rest of the present thesis. Consequently, in the next section, DSC was utilised to generate ASD with a drug loading of 25% FELD and expose to RH for seven days. Then, the aged sample were re-heated using DSC to detect possible crystallinity.

#### 4.4.8. Stability Study

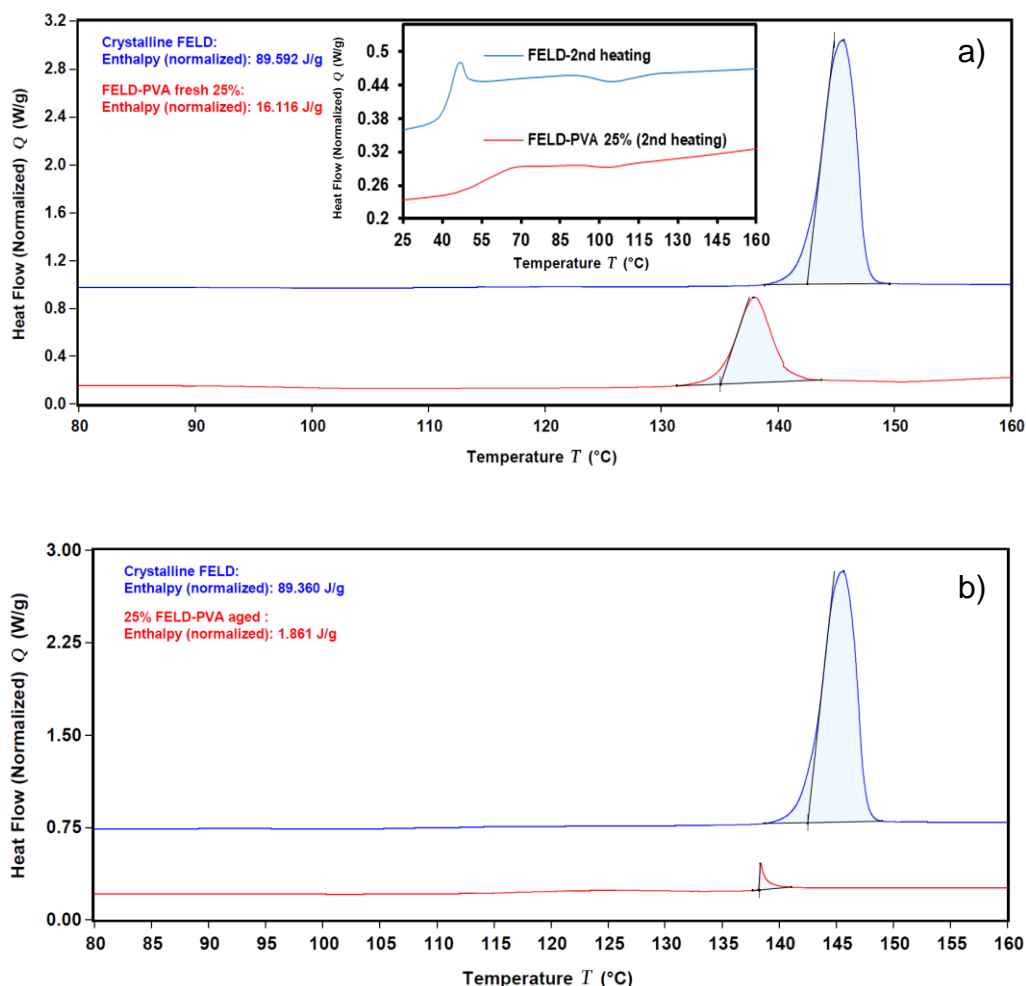


**Figure 4.15.** DSC thermograms of a) crystalline FELD (blue), FELD-PVA 25% physical mixture (red), and  $T_g$  region (2<sup>nd</sup> heating cycle) of the same

samples, and b) DSC thermograms of the crystalline FELD (blue), and FELD-PVA 25% aged sample after seven days exposure to RH (red). (Endotherm upward in the thermogram).

**Figure 4.15 (a and b)** show DSC thermograms of 1<sup>st</sup> and 2<sup>nd</sup> heating of the crystalline FELD, 25% (FELD-PVA w/w) samples, and aged sample re-heating cycle. Firstly, crystalline FELD, and physically mixed FELD-PVA with 25% drug loading samples were heated to 200 °C to produce ASD (a pinhole lid was used during this step). During this step, a sharp melting endotherm was noted for both samples. Then, the samples were cooled back to room temperature. After that, the samples were re-heated to 200 °C. No endotherm event was detected for both samples during the re-heating cycle. In addition, a single  $T_g$  was noted for both samples, indicating the formation of an ASD as shown in **(Figure 4.15, a)**.

Then, the produced ASD sample was stored at 75% RH for seven days to induce crystallisation. Next, DSC was used to investigate the re-crystallisation of the aged samples. As shown in **Figure 4.15 (b)**, the aged sample showed a melting peak indicating the re-crystallisation of the FELD-PVA system. However, smaller enthalpy was observed with the aged sample than the freshly studied sample, as shown in **(Figure 4.15, b)**. This suggests that only a small amount of the sample was re-crystallised; thus, the rest of the samples were in the amorphous state. The impact of moisture on the stability of ASD formulations was previously reported in the literature [69] [70] [221].

Consequently, based on the finding from the DSC experiment, in the next chapter, we will use 25% drug loading to fabricate a customised model tablet employing the FDM 3D printing technique. This tablet will be manufactured with an outer shell (amorphous or spiked with crystalline seeds) and an inner core (amorphous or spiked with crystalline seeds). For the spiked parts, we will print an outer shell and an inner core then we will store them in RH media for seven days to facilitate the crystallisation. After that, we will quantify the percentage of crystallinity utilising DSC. Next, the aged part will be attached with a freshly printed part to fabricate the required model tablets for dissolution study.

#### **4.5. Conclusion**

In the present work, we have successfully fabricated several drug-free model tablets using commercial filaments and FDM 3D printing as a fabrication technique. Furthermore, we were able to optimise the default printing parameters. In addition, we have successfully prepared different drug-loaded filaments, including 10%, 25%, and 50% (FELD-PVA w/w) by employing HME. Also, we managed to use the commercial and prepared filaments (10%, and 25%) and optimised parameters to fabricate drug-free and drug-loaded model tablets with better morphology than the model tablets printed using default printing parameters. SEM and electronic callipers have both revealed that better morphology was achieved for the fabricated model tablets after optimisation of the printing parameters, which validated the ability of FDM 3D printer to fabricate objects with complex geometry. Additionally, SEM

has shown that the prepared filament was characterised by a rough surface after it was extruded using HME; however, a smoother surface was observed after it was extruded from the printer nozzle, indicating more mixing between FELD and PVA. Moreover, the prepared filaments and fabricated drug-loaded model tablets were characterised using different techniques, including DSC, FTIR, Raman, and PXRD, and all the utilised techniques revealed that it was possible to manufacture ASD filaments and model tablets using different drug loadings. In addition, due to the high temperature utilised during manufacturing of the materials (printer feedstock and model tablets), the manufactured materials have not shown any crystallinity; hence, we have successfully utilised controlled RH storage conditions as an approach to achieve equilibrium (crystallinity) in the ASDs produced using DSC.

Thus, in the next chapter, FDM 3D printer along with exposure to high RH will be utilised to formulate compartment model tablets (pure ASD, and spiked model tablets); then, the impact of the crystallinity on the dissolution release mechanisms from these formulations will be studied using USP dissolution apparatus I (basket).

## **5. Chapter 5: In-Vitro Study to Investigate Drug Release from 3D Fabricated Model Tablets**

### **5.0. Novelty in this Chapter**

Compact ASD model tablets spiked with crystalline seeds, in an outer shell or in an inner core, were fabricated utilising FDM 3D printer for the first time. Then, the dissolution behaviour of the different fabricated model tablets was investigated using USP dissolution apparatus I (basket).

### **5.1. Introduction**

As detailed in chapter 1, ASD formulations are thermodynamically unstable and have a tendency to re-crystallise, which may lead to formulation failure [7] [101]. Although a large number of studies have been reported in the literature about utilising ASDs as an approach to enhance the dissolution of poorly-water soluble ingredients in comparison to the free APIs [5], the dissolution mechanisms from these formulations are not fully understood. Thus, investigating the influence of crystallinity on the dissolution behaviour of the ASDs is important to understand the drug release mechanisms from these formulations.

Based on the calculated values for the FELD-PVA system in chapter 3, and the observed miscibility between FELD and PVA in chapter 4, all the

drug loadings have shown complete miscibility between FELD and PVA at temperature above 140 °C. However, phase separation and re-crystallisation are possible when the temperature reaches 25 °C for drug loadings higher than 10%.

Also, as discussed in chapter 4, we were able to manufacture three ASD printer drug-loaded feedstocks, including 10%, 25%, and 50% (FELD-PVA w/w), using HME. Moreover, we managed to fabricate drug loaded ASD model tablets utilising the FDM 3D printer and the manufactured drug loaded feedstocks. However, the 50% drug loading was excluded due to the difficulties encountered during the model tablets fabrication process using the FDM 3D printer and due to the high materials waste. Also, the 10% drug loading was excluded because we are aiming to investigate the dissolution behaviour of the API from the ASD tablets at a high drug loading scenario.

Furthermore, according to the detailed information in the chapter 3, and 4, the 25% drug loading has shown complete miscibility between FELD and PVA and we were able to use the manufactured filaments to fabricate ASD model tablets utilising the FDM 3D printer. However, it was challenging to fabricate model tablets spiked with crystalline seeds because all the manufactured materials were miscible (ASD) due to the high temperatures used during both printer feedstock formulation using an HME and tablet fabrication utilising the FDM 3D printer. Consequently, RH was used as an approach to reach equilibrium, crystallinity, in the manufactured materials, as detailed in chapter 4.

Thus, in this chapter, two basic formulations, FELD-PVA compartment model tablets (amorphous and spiked with crystalline seeds), were fabricated with a drug loading of 25% (w/w) utilising the FDM 3D printing technique. For the spiked tablets, different outer shells and inner cores were freshly fabricated as ASD and then some of them were exposed to RH to facilitate the crystallisation process and achieve equilibrium. Next, the freshly fabricated parts were used along with the aged parts to manufacture the spiked model tablets. Then, the fabricated model formulations, pure ASD and spiked model tablets, were used to investigate the dissolution mechanisms utilising USP dissolution apparatus I (basket). Also, for more understanding on the drug release mechanisms from the fabricated model tablets, the drug release data were fitted to different kinetic models, i.e. Zero-order, first-order, Higuchi model, and Korsmeyer-Peppas model. Each of these mechanisms is visited in turn below.

### **5.1.1. Drug Release Kinetics**

Drug release can occur in a variety of ways from different types of formulation, and the ability to model these processes mathematically with a high degree of accuracy can provide valuable information when undertaking clinical decisions pertaining to dosing regimens. In general, some measure of drug release can be plotted against time, and the resulting graphs can give an indication of the types of processes that are taking place to produce the release patterns observed.

Drug release can be zero order or first order, depending upon whether the release rate is concentration-dependent or not. In addition to these,

multiple kinetic models can be applied for specific use cases such as drug release from matrices or semi-solids.

#### 5.1.1.1. Zero-Order

Zero order kinetics are described by (**Equation 5.1**) [229]:

$$C = k_o \cdot t \quad (5.1)$$

In which  $C$  indicates the fraction of drug released over time  $t$ , with the zero-order release rate constant  $k_o$ .

In essence, this means that the release rate of the drug from the formulation is constant, irrespective of the amount of drug present. Zero order release has been demonstrated for compounds such as tryptophan and theophylline from biphasic polymer hydrogels until up to 80% of the drug was released, after which the release rate became time dependent [230]. More recently, sustained zero order release of therapeutic peptides from a polyethylene glycol-treated salmon calcitonin and tannic acid film has been demonstrated, which provided consistent zero order release without any initial bolus release [231].

#### 5.1.1.2. First-Order

First order kinetics are described by (**Equation 5.2**):

$$\log C = \log C_o - kt/2.303 \quad (5.2)$$

In which  $C_0$  is the initial concentration of drug,  $k$  is the first order release rate constant, and  $t$  is the time [232]. This process involves the delivery of a given proportion of the available drug per unit of time. The data generated from the first order model is plotted as log cumulative % of drug remaining vs. time which would produce a straight line with a slope of  $-K/2.303$ . First order release kinetic model can be utilised to describe the dissolution of an API in pharmaceutical dosage forms such as those including water-soluble drugs in porous matrices [233] [234].

#### 5.1.1.3. Higuchi Model

Higuchi's equation takes into account the effect of Fickian diffusion as a function of time, and was developed to describe the release of drugs from ointments that contained active compounds in suspension [235]. Although originally intended to describe a pseudo-steady-state situation with drug suspended in an ointment applied as a thin film, the Higuchi model is valuable in a range of other circumstances such as when determining the rate of drug release through a matrix, and can be useful for drugs with various solubilities, and also for solid or semi-solid formulations, and for the release of drug from transdermal patches [236]. The Higuchi model (simplified Higuchi model) can be described by **(Equation 5.3)** [235].

$$F = k_H \cdot t^{1/2} \quad (5.3)$$

In this equation,  $k_H$  represents the Higuchi release rate constant. The data obtained from Higuchi model is typically plotted as cumulative % drug release versus square root of time [234].

#### 5.1.1.4. Korsmeyer-Peppas Model

The Korsmeyer-Peppas model was developed to describe the release of an active compound from a polymeric dosage form consisting of more than one type of functional polymer. This model accounts for the effects of the ratio between drug and excipients, and also on the effects of dynamic swelling and dissolution processes occurring within the dosage form [237]. The model is described by ( **Equation 5.4**):

$$M_t / M_\infty = kt^n \quad (5.4)$$

Where  $M_t / M_\infty$  indicates the fraction of API released at time  $t$ ,  $k$  is the Korsmeyer-Peppas release rate constant and  $n$  is the release exponent describing the mechanism of release. In Korsmeyer-Peppas model, the value of  $n$  characterises the release mechanism of drug. When the value of  $n$  is  $\leq 0.43$  indicates that the drug release is controlled by Fickian diffusion, whereas  $n \geq 0.85$  suggests that the API release is controlled by an erosion mechanism [238]. Also, for  $n$  values that are less than 0.85 and more than 0.43, the drug release is controlled by two mechanisms, including diffusion, and erosion [238]. In this model, data gained from in vitro drug release studies is usually plotted as log cumulative % drug release versus log time.

## **5.2. Aims and Objectives**

As mentioned in chapter 1, section (1.7), the main aim of this chapter is to develop FELD-PVA model tablets, pure amorphous and spiked model tablets with crystalline seeds. Also, to investigate the influence of the crystallinity on the drug release behaviour from the fabricated model tablets utilising the USP dissolution apparatus I (basket).

This aim can be accomplished by firstly using HME to manufacture FDM 3D printer feedstock. Then, the manufactured feedstock will be utilised to fabricate an outer shell (tablet with a central hole) and an inner core, which will be inserted inside the fabricated outer shell, using the FDM 3D printer. For this purpose, some of the fabricated outer shells and inner cores will be exposed to RH for seven days, to be used as spiked (aged materials), while some of them will be freshly fabricated, to be used as amorphous (fresh). Then, FTIR, Raman, and PXRD will be utilised to characterise the aged samples and compare them with the freshly prepared samples. Next, DSC will be utilised to determine the % of crystallinity of the aged samples after being exposed to 75% RH for seven days. After that, the fabricated outer shells (fresh or aged) and inner cores (fresh or aged) will be fixed together and sealed using the printer head to formulate the final compartment model tablets. Finally, USP dissolution apparatus I (basket) will be employed to study the dissolution behaviour of the fabricated model tablets.

### 5.3. Materials and Methods

#### 5.3.1. Materials

As detailed in chapter 2, section (2.1)

#### 5.3.2. Methods

##### 5.3.2.1. Fabrication of FELD-PVA Model Tablets Employing FDM 3D Printer

Initially, different model tablets were designed using TinkerCad online software, as shown below in (Figure 5.1). Then, the designed files were exported as STL files. Next, the file was imported in the FDM 3D printer to be fabricated.

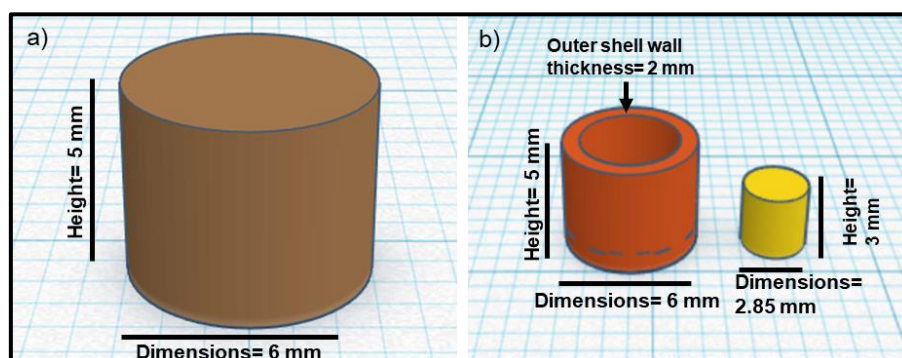


**Figure 5.1.** Model tablet designs, a) control design, b) model tablets (formulations) outer shell and inner core designs.

Then, HME was utilised to prepare 25% filament based on the same method as detailed in chapter 4. After that, the fabricated filament was loaded to the FDM 3D printer to manufacture the designed models. The printing parameters were the same as previously detailed in chapter 4. However, the one-part tablet (Figure 5.1, a) was fabricated and stored in a desiccator, to be used a fresh control, and some were exposed to

75% RH conditions to induce tablet crystallinity and to be used as aged control. The compact model tablets were printed as two parts (outer shell and inner core) as illustrated above in (**Figure 5.1, b**). Similar to the control, some of the printed outer shells and inner cores were exposed to RH for seven days to be utilised as aged (spiked) and some of them were printed and stored in a desiccator to be used as fresh (ASD). Then, the aged parts and fresh parts were used to manufacture the compartment model tablets by inserting an aged core in a fresh outer shell and/or placing a fresh core inside an aged outer shell. Finally, the formulated compacts were sealed by liquefying the PVA filament using the printer head (**Figure 5.2**). In this step, the plain PVA polymer was loaded to the printer and heated to 190 °C. Then, the liquified polymer was used to seal the top part of the fabricated model tablets with a thin layer of the polymer.

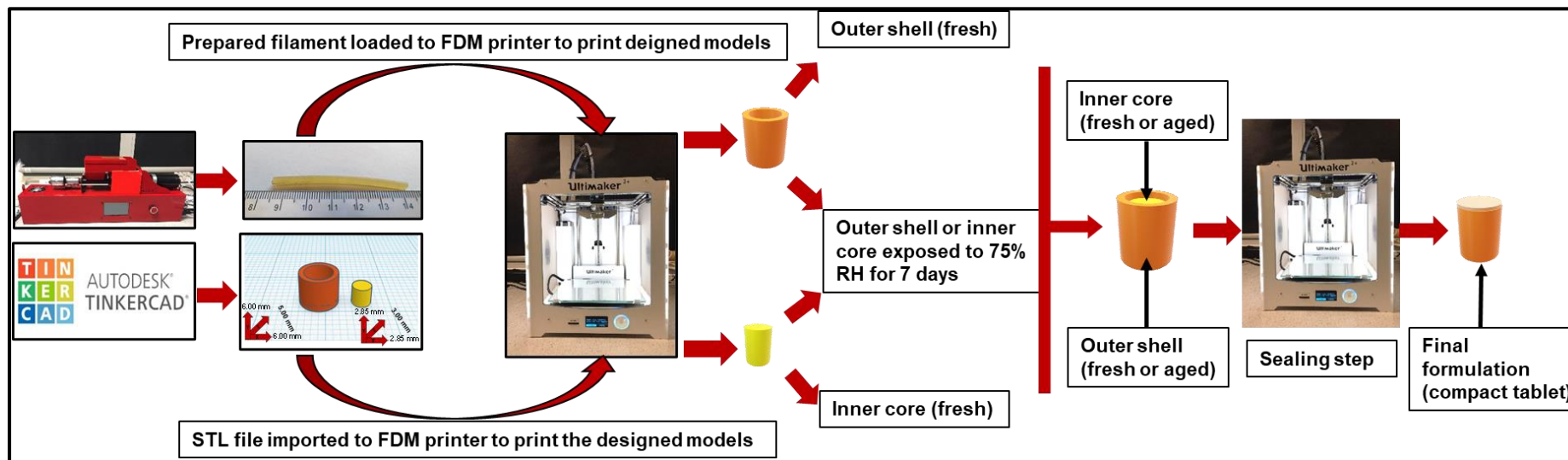


Figure 5.2. Formulation steps of the FELD-PVA model tablets.

### 5.3.2.2. Characterisation of Aged Samples

#### 5.3.2.2.1. FTIR

As detailed in chapter 4, section (4.3.2.3.4)

#### 5.3.2.2.2. Raman Spectroscopy

As detailed in chapter 4, section (4.3.2.3.5)

#### 5.3.2.2.3. X-Ray Powder Diffractometer (XRPD)

As detailed in chapter 4, section (4.3.2.3.6)

### 5.3.2.3. Quantification of Crystallinity Utilising DSC

The crystallinity percentage of the FELD in the aged model tablets was quantified utilising a DSC according to (Equation 5.5) [239] [240].

$$\%Crystallinity = \frac{\Delta H_f - \Delta H_c}{\Delta H_f^{crys}} \times 100 \quad (5.5)$$

Abbreviation	Description
$\Delta H_f$	heat fusion of the FELD in the sample
$\Delta H_c$	Heat of crystallisation of the FELD in the sample
$\Delta H_f^{crys}$	enthalpy of fusion of the crystalline drug

### 5.3.2.4. In-Vitro Drug Release Studies

#### 5.3.2.4.1. Stock Solution and Sample Preparation

In the beginning, two fresh amounts of PBS were prepared, and the pH of the PBS were adjusted to pH 6.8 and pH 2. Then, the volume of the

prepared solutions was completed by distilled water to the required quantities.

Next, FELD standard solution was prepared by accurately weighing 10 mg of the API powder. Then, the weighed powder was placed in 100 mL volumetric flask. After that, 80mL of the dissolution medium and methanol (1:1) was measured accurately by a measuring cylinder and transferred to the volumetric flask.

Thereafter, the volumetric flask was sonicated for 30 min to produce a clear solution. This solution was considered as a stock solution, and its concentration was 0.125 mg/ml. Next, a series of concentrations, including 0.325, .625, 1.25, 3.125, 6.25, 12.5, 25, 37.5, and 50 µg/mL, were diluted from the stock solutions and utilised to construct calibration curve to cover the concentration range of dissolved samples.

#### **5.3.2.4.2. Determination of FELD Absorbance Wavelength**

1 mL of the stock solution was placed in the UV quartz cuvette, and it was scanned by the UV spectrophotometer in the range of 200-600 nm to determine the absorbance wavelength.

#### **5.3.2.4.3. Investigating Drug Release Utilising USP Apparatus**

In-vitro drug release profiles were measured in dissolution testing apparatus (Dis8000, Copley Scientific limited, UK) using the basket method (USP apparatus 1). A rotation speed of 100 rpm and 900 ml of phosphate buffer pH 6.8 and/or pH 2 plus 1.5% SLS at 37.00 °C were used for the different sample measurements. The SLS was used as a surfactant as recommended in the US Pharmacopeia [241]. The 3D

printed model tablets (fresh and aged) were used in this experiment. 5 ml dissolution samples were withdrawn at (0, 5, 15, 30, 60, 120, 300, and 600 min) time intervals and directly filtered through a membrane filter with 0.45  $\mu\text{m}$  pore size (Millex®-HA filter unit, Merck Millipore, Carrigtwohill, Ireland). After that, the sample solutions were diluted with an equal volume of methanol. Then, 5 ml of fresh dissolution media was added to the dissolution vessels after each sampling. The samples were analysed utilising a UV–VIS spectrophotometer (Cary, 50 Bio, Australia) at 363 nm. All drug release studies were conducted in triplicate [58].

#### **5.3.2.5. X-Ray Micro Computed Tomography (X $\mu$ CT)**

A ZEISS XRADIA VERSA XRM-500 high-resolution X-ray micro-computed tomography scanner was used to visualise the 3D internal structure of the 3D fabricated compartment model tablets. The printed model tablets were scanned at 15  $\mu\text{m}$  (resolution)/60 minutes (scan time), and the 3D imaging was performed by rotating the objects through 180° [242] [243]. Image reconstruction was performed utilising ZEISS versa XRM software to reconstructs the 2D images (projections) that were acquired during data acquisition/tomography to create a 3D reconstructed volume. After reconstruction, the file containing the 3D image volume was loaded into XM3DViewer software and analysed.

## 5.4. Results and discussion

### 5.4.1. Manufactured Drug Loaded Filaments and Fabricated Model Tablets

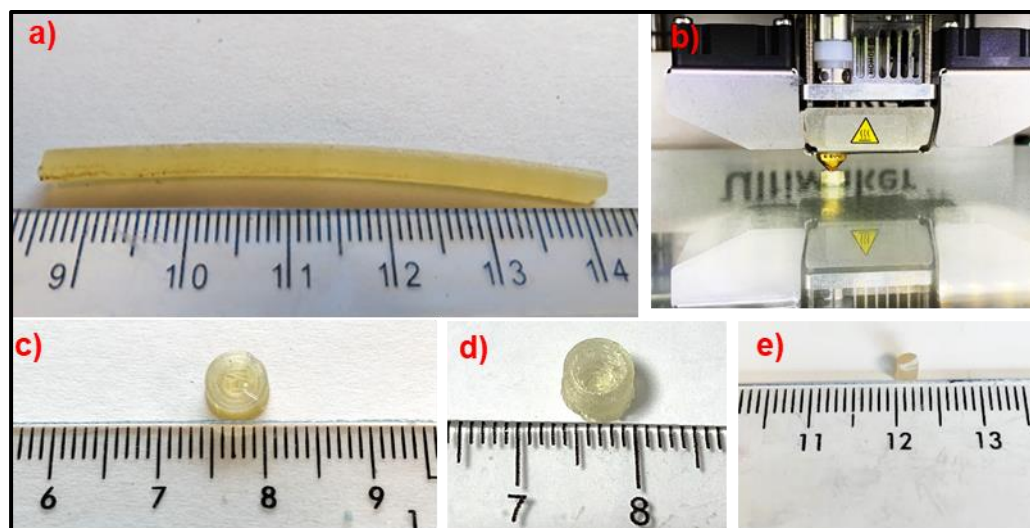


**Figure 5.3.** Photographic images of the prepared filament (a), FDM printing of the model tablets (b), one-part tablet (c), outer shell (d), and inner core (e).

We successfully prepared 25% (w/w) drug-loaded filament utilising an HME, and we managed to use the prepared filament to fabricate the designed model tablets employing the FDM 3D printer, as shown in **(Figure 5.3)**. The prepared filament was manufactured based on the manufacturing parameters that were previously detailed in chapter 4, **(Table 4.3)**. The manufactured filament was smooth, and it was possible to load it to the FDM 3D printer to fabricate the model tablets. Moreover, the designed model tablets were fabricated using the FDM 3D printer and based on the optimised parameters obtained from chapter 4 **(Table 4.4)**.

RH storage conditions was utilised as an approach to achieve equilibrium and to produce crystallinity in the manufactured materials due to the effect of the RH on the stability of ASD and its ability to facilitate the re-crystallisation process [65], [66], [228]. Therefore, some of the manufactured outer shells and inner cores were exposed to 75% RH for seven days to induce crystallisation process. RH was previously prepared based on the method used in chapter 4, section (4.3.2.6).

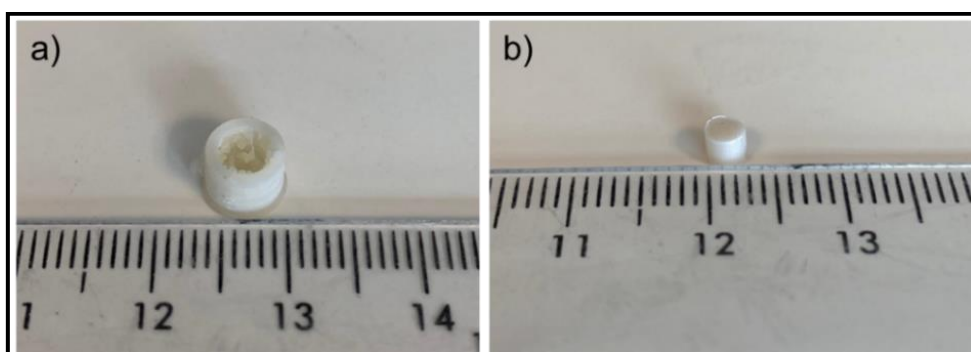


**Figure 5.4.** Photographic images of the fabricated model tablets a) outer shell, and b) inner core, after seven days of storage in 75% RH.

**Figure 5.4** displays photographic images of the aged samples exposed to RH for one week. The transparent appearance of the fresh samples was changed to opaque with the aged samples, as shown in (**Figure-5.4**). Opaque look of the aged samples has been reported to be an indication of phase separation and re-crystallisation- [244] due to the impact of the moisture on the stability of the ASD [69] [70] [87] [221]. Therefore, in the following sections, FTIR, Raman, and PXRD were utilised to investigate the crystallinity of the aged samples.

It is crucial to state that before the formulation step of the model tablets, the % of crystallinity of the aged samples was investigated to determine

whether the FELD partially or fully re-crystallised after being exposed to RH for one week. Thus, DSC was utilised in order to determine the crystallinity percentage of the aged samples. After that, we manufactured compact model tablets using freshly prepared and aged samples.

## 5.4.2. Characterisation of Aged Samples

### 5.4.2.1. FTIR Spectra

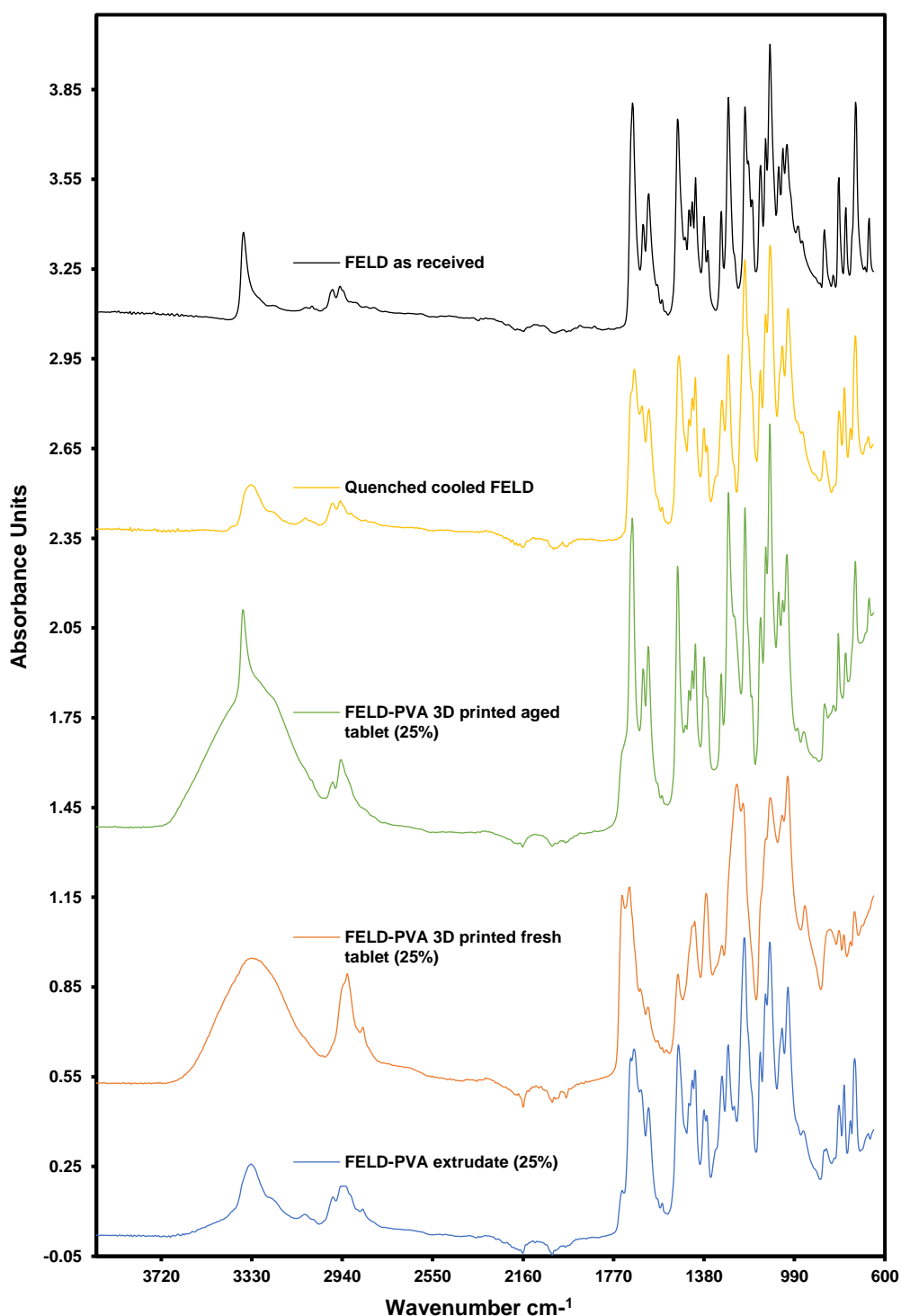


**Figure 5.5.** FTIR spectra of the FELD as received, the quenched cooled FELD, the FDM 3D printed tablets (aged and freshly prepared), and FELD-PVA extrudate.

**Figure 5.5** represents FTIR spectra of the crystalline FELD, amorphous FELD, manufactured model tablets (fresh and aged), and FELD-PVA extrudate. FTIR spectra of the freshly prepared samples, crystalline FELD, quenched cooled FELD and manufactured extrudate was previously discussed in detail in chapter 4, section (4.4.5.1). Therefore, in this chapter, we will focus mainly on comparing the spectra of the aged samples with the spectra of the other samples to investigate possible re-crystallisation of the aged samples after being exposed to 75% RH for one-week.

As in the previous chapter, two significant peaks (drug fingerprint) of the FELD will be investigated during the present study, i.e. the crystalline FELD amine group (N-H peak), located at  $3363\text{ cm}^{-1}$ , and the ethyl ester carbonyl group (C=O peak), located at  $1685\text{ cm}^{-1}$ .

Interestingly, as shown in the figure above, the amine group (N-H peak), located at  $3363\text{ cm}^{-1}$ , and the ethyl ester carbonyl group (C=O peak), located at  $1685\text{ cm}^{-1}$  have appeared with the aged fabricated model tablets, which is similar to the sharp peaks of the crystalline FELD.

In comparison to the shape of the amine group (N-H peak), which is much broadened in the spectral region of the quenched cooled FELD, manufactured extrudates, and freshly fabricated model tablets, the aged sample peak has transformed into a sharp peak and appeared in the same position as with the crystalline FELD ( $3363\text{ cm}^{-1}$ ). Moreover, the carbonyl group (C=O) has appeared with higher intensity than that

appeared with the quenched cooled FELD, manufactured extrudates, and freshly fabricated model tablets. Also, the C=O band appeared at  $1685\text{ cm}^{-1}$ , which is similar to that of the pure drug.

We can conclude from the FTIR result, and the aged samples opaque colour observed in the previous section that using controlled humidity conditions has induced crystallinity process which may have led to a partial transformation of the amorphous FELD to crystalline forms in the aged samples at or above the FTIR detection limit (1-2%) [224]. Moreover, in the next sections, Raman spectroscopy, and PXRD were utilised to conduct more investigation on the possible re-crystallisation of the aged samples.

### 5.4.2.2. Raman Spectra

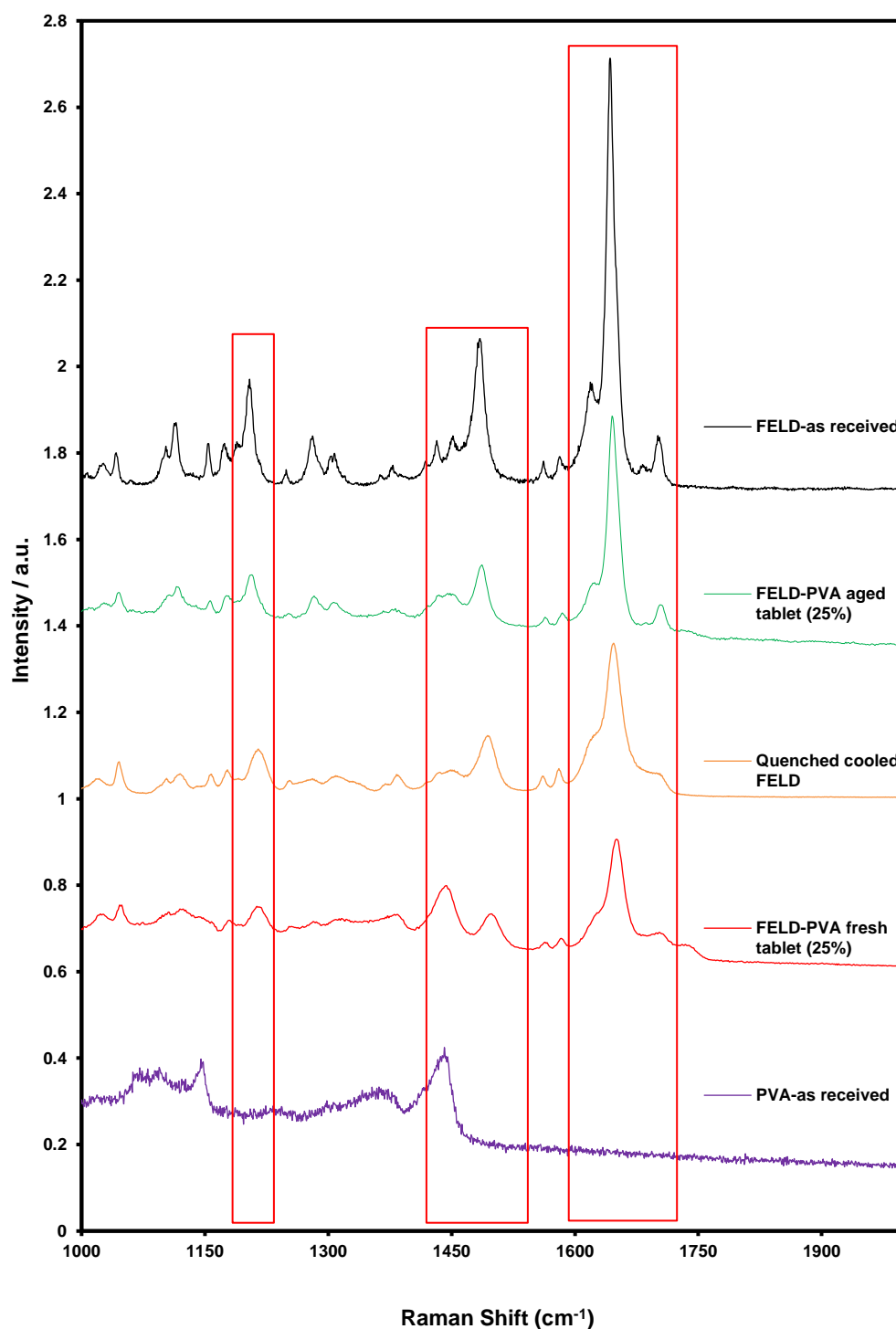


**Figure 5.6.** Raman spectra of the crystalline FELD, aged model tablet, quench cooled FELD, fresh tablet, and PVA in the molecular-region (1100-1750 cm<sup>-1</sup>).

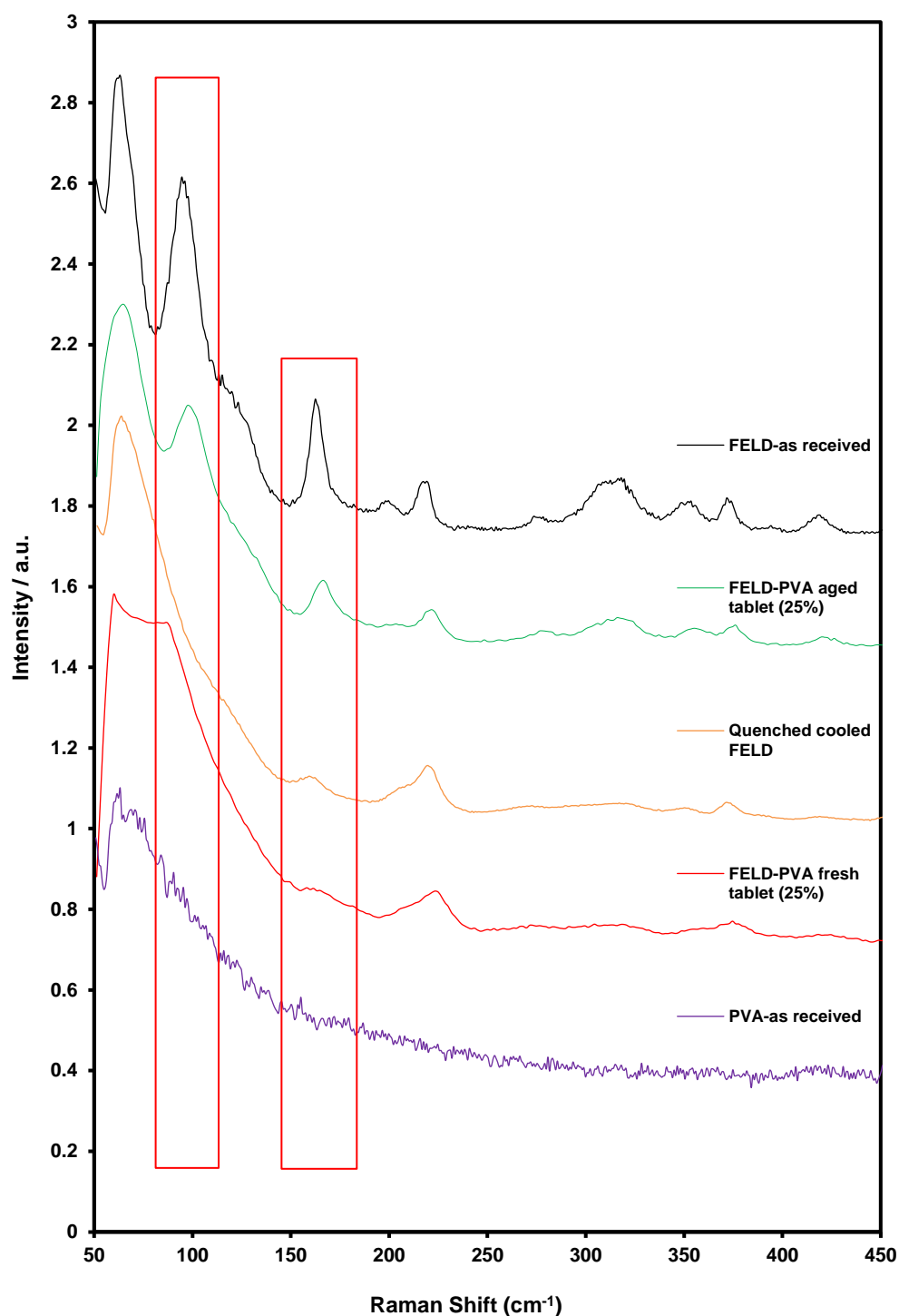


**Figure 5.7.** Raman spectra of the crystalline FELD, aged model tablet, quench cooled FELD, fresh tablet, and PVA in the phonon region (50-450 cm<sup>-1</sup>).

**Figure 5.6** and **5.7** show Raman spectra of the raw materials and the 3D fabricated model tablets (fresh and aged). **Figure 5.6** illustrates the fingerprint region ( $1100\text{-}1750\text{ cm}^{-1}$ ), while **5.7** shows the phonon-mode region ( $50\text{-}450\text{ cm}^{-1}$ ). Raman spectra of the raw materials (FELD, and PVA) with the freshly fabricated model tablets was discussed in detail in chapter 4, section (4.4.6). Based on that discussion, we found that the freshly fabricated model tablets were completely amorphous, and no crystallinity was detected at Raman detection limit. Therefore, in the present result, we will focus on comparing the spectra of the aged samples with the spectra of the other ingredients, including crystalline FELD, quenched cooled FELD, and PVA.

In the case of comparing the spectra of the aged fabricated tablets with the spectra of the crystalline FELD, and quenched cooled FELD, it is clear from the **Figure 5.6** that the peaks of the aged tablets have appeared as sharper and higher intensity peaks than those of the quenched cooled FELD. However, these peaks appeared less sharp and low intensity in comparison to that of the pure FELD. Also, the molecular bands of the aged tablets have shifted back to the original positions of the FELD molecular bands, which are located at  $1205$ ,  $1485$ , and  $1643\text{ cm}^{-1}$ .

Turning to the spectra of the pure FELD, aged tablets, and quenched cooled FELD in the phonon-mode region, it is possible to see that there is a significant difference between the pure FELD, and the aged sample bands in comparison to the bands of the quenched cooled FELD, as displayed in (**Figure 5.7**). It is evident that both the pure FELD, and the

aged tablet are characterised by two significant peaks at 94, and 162- $\text{cm}^{-1}$ , in comparison to quenched cooled form, which is characterised by broad bands in a similar region. Using of the phonon-mode region to easily differentiate between different solid forms of a drug has been previously reported in the literature [5] [6].

We can conclude from Raman results that the appearance of the aged tablet bands at similar positions to the pure drug indicate that the amorphous form of the FELD has changed to the crystalline forms due to the impact of the moisture on the ASD [69] [70] [87] [221].

However, the appearance of the aged tablets with less sharp and low intense bands, as reported in the molecular and phonon-mode regions, than the bands of the pure FELD suggest that the aged tablet was only partially re-crystallised after seven days storage at 75% RH media. This result is consistent with the FTIR result, and the opaque appearance of the aged tablet that was previously discussed in the previous sections.

## 5.4.2.3. XRPD Patterns

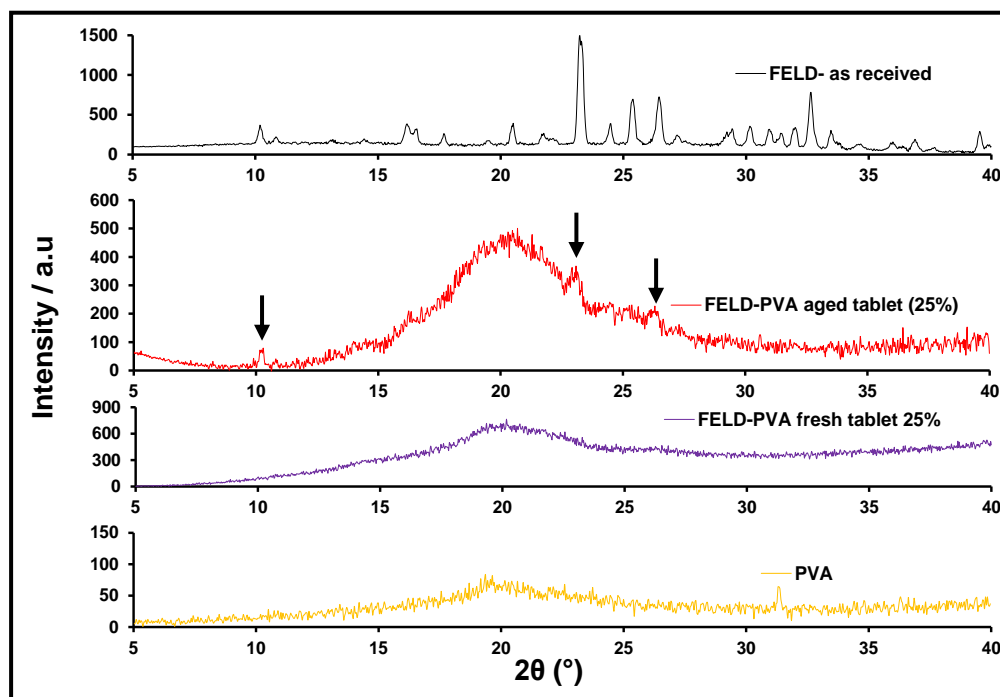


**Figure 5.8.** XRPD patterns of the crystalline FELD, 25% aged and fresh tablets, and the PVA. (Black arrows indicate the main peaks appeared in the aged tablet in relative to the crystalline FELD).

**Figure 5.8** shows XRPD patterns of raw materials and fabricated model tablets (fresh and aged). It is evident from the figure shown above that the XRPD patterns of the crystalline FELD is characterised by sharp and high intense peaks [58] in comparison to the amorphous halo of the PVA polymer [58], and the fresh FELD-PVA tablets, which displayed amorphous halo [58]. Turning to the XRPD patterns of the aged tablet in relative to the Bragg peaks of the fresh tablets, and the PVA, it is clear that the aged tablet is characterised by the appearance of Bragg peaks

positioned mainly at 10.19 °, 23.21 °, and 26.46 °, which are similar to the Bragg peaks of the crystalline FELD.

Thus, based on this result, the drug may have partially transformed from amorphous form to crystalline forms within the aged model tablet. This result is in an agreement with the previously reported results using different techniques in previous sections.

Based on the findings from the previous sections, the aged samples may have partially crystallised after seven days storage at 75% RH due to the effect of the moisture on the stability of ASDs [65], [66], [228] [100]. However, it was essential to determine the crystallinity percentage within the aged samples before the formulation of the model tablets because we are aiming to manufacture two basic formulations (pure ASD, and spiked model tablets).

Therefore, in the following section, DSC was utilised to quantify the % of crystallinity of the aged samples to see how much of the FELD amorphous form has changed to crystalline forms after one-week storage at 75% RH utilising **Equation 5.1**.

### 5.4.3. Quantification of Crystallinity

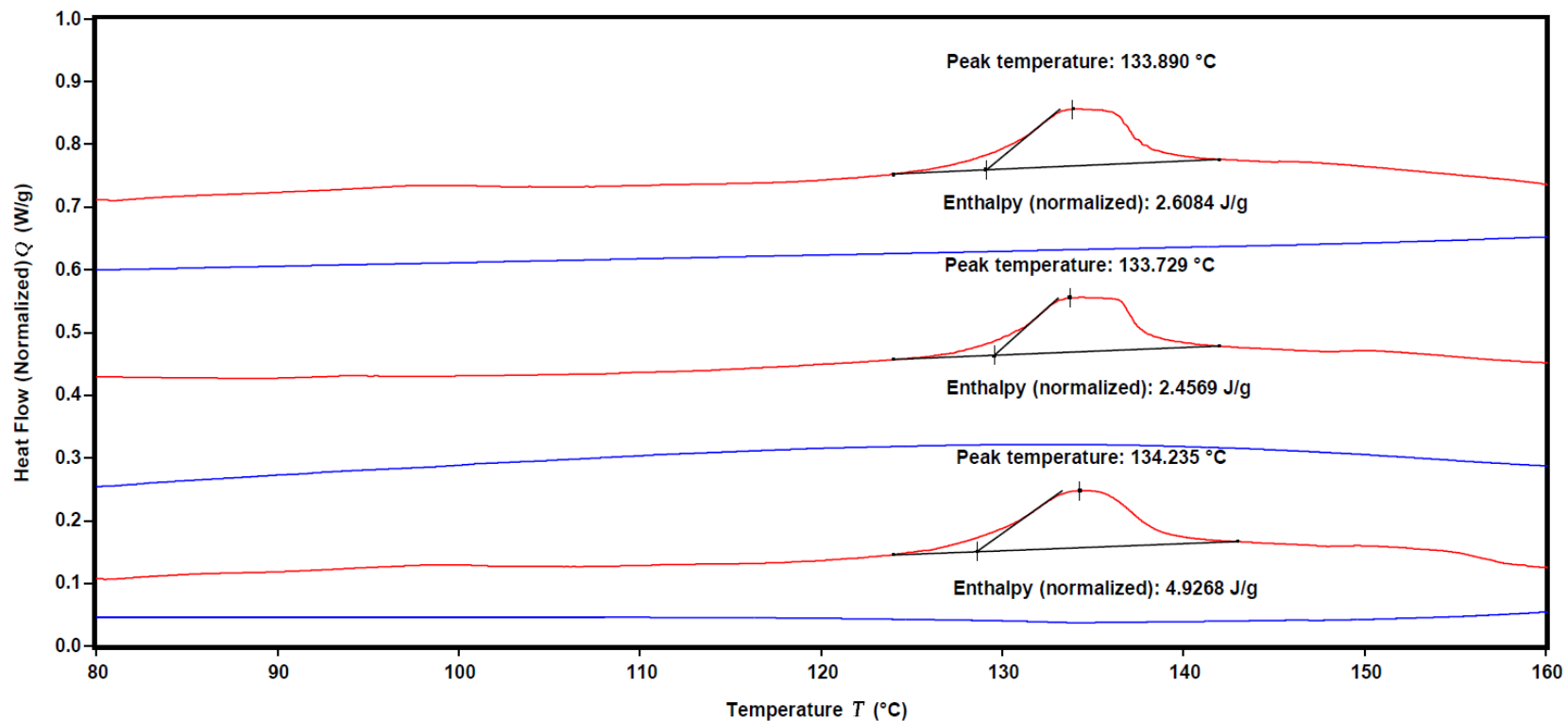


**Figure 5.9.** DSC thermogram of the FELD-PVA (25% w/w) fresh and aged tablets (red represents aged samples, and blue represents fresh samples) (n=3).

**Figure 5.9** demonstrates DSC thermograms of three freshly prepared model tablets and three aged model tablets. The crystallinity % of the FELD in the aged tablets was calculated from the DSC data using **(Equation 5.1)**. It is clear from the figure shown above that the freshly prepared model tablets did not show any melting event for all the samples in comparison to the melting endotherm determined for the pure FELD, **(Appendix Figure 1)**. The disappearance of the melting endotherm from the fresh samples is an indication of the formation and stability of ASD within the freshly printed model tablets. However, when the model tablets were stored at 75% RH for seven days, they were re-crystallised resulting in endothermic melting peaks in all the aged samples due to the humidity effect on the stability of the ASD by converting the amorphous back to its crystalline state [87] [69] [70][221].

The measured heat of fusion ( $\Delta H_f$ ) of the FELD within the aged samples, as illustrated in **Figure 5.9**, was found to be 2.61, 2.46, and 4.93 J/g felodipine from top to bottom, respectively. The  $\Delta H_f^{crys}$  of the crystalline FELD was found to be 89.37 J/g, as shown in **(Appendix Figure 9)**. The estimated crystalline content of FELD in the aged tablets was found to be approximately  $4 \pm 2$  % **(Appendix Table 1)** [239] [240]. According to the DSC result, the FELD in the aged samples have partially re-crystallised after one-week storage at 75% RH, which means that most of the aged samples remained amorphous. Thus, RH conditions approach used here was effective and produced aged samples spiked with crystalline FELD as required.

Subsequently, in the next section, the aged samples (outer shells or inner cores), along with the fresh samples (outer shells or inner cores) were utilised to manufacture the compact model tablets, which will be used later for the in-vitro drug release study.

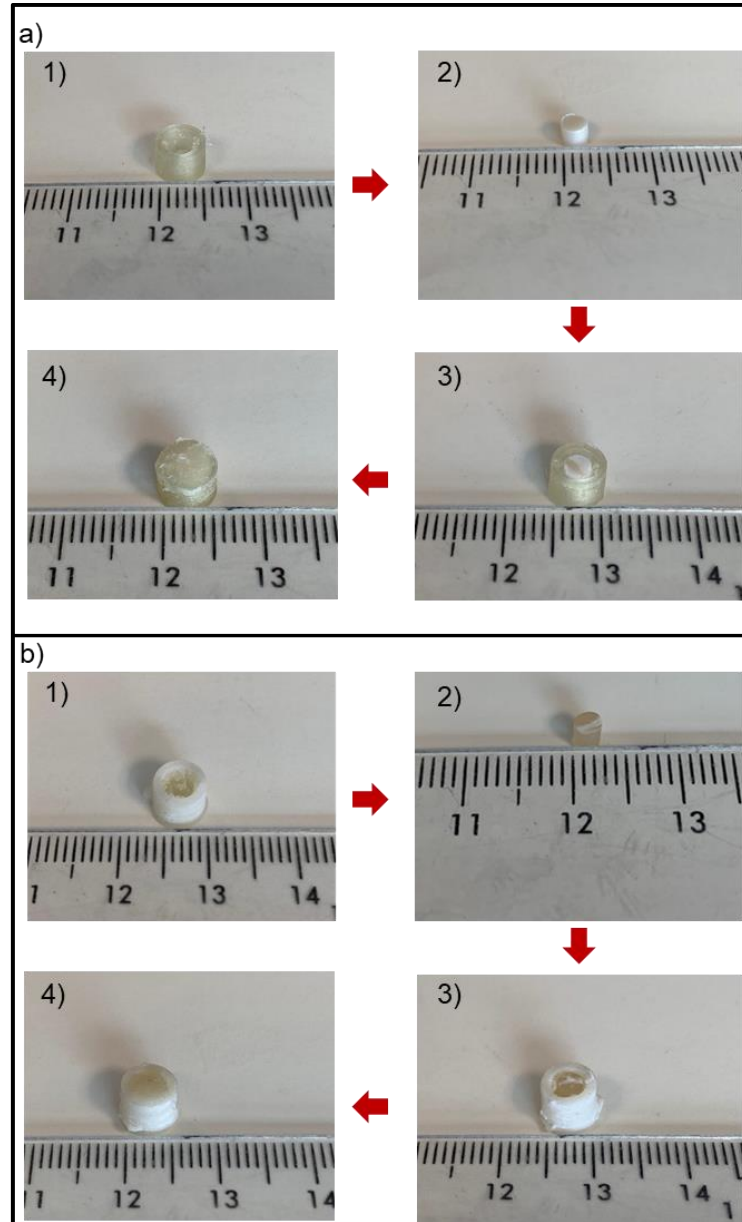


**Figure 5.10.** Photographic images of the 3D printed model tablets, a) 1, 2, 3, and 4, are the manufacturing steps of the fresh shell-aged core model tablet, while b) 1, 2, 3, and 4, are the manufacturing steps of the aged shell- fresh core model tablet.

**Figure 5.10** displays the different steps utilised to formulate the FELD-PVA compact model tablets. We have successfully formulated several spiked model tablets using the aged samples (outer shells and/or inner cores) and the freshly fabricated samples (outer shells and/or inner cores). In the beginning, we fabricated numerous fresh outer shells and inner cores using the FDM 3D printer. Next, we used the aged samples along with the fresh samples to formulate the final product (spiked model tablets) as follows: I) a fresh inner core was inserted in an aged outer shell; then, the compact was sealed using the FDM 3D printer nozzle. II) an aged inner core was inserted in a fresh outer shell and sealed with the PVA polymer using the printer nozzle, as illustrated above in (**Figure-5.10**). Then, the formulated model tablets (spiked) and pure ASD tablets were used for the in-vitro drug release study in the next sections.

### 5.4.4. Preliminary In-vitro Drug Release

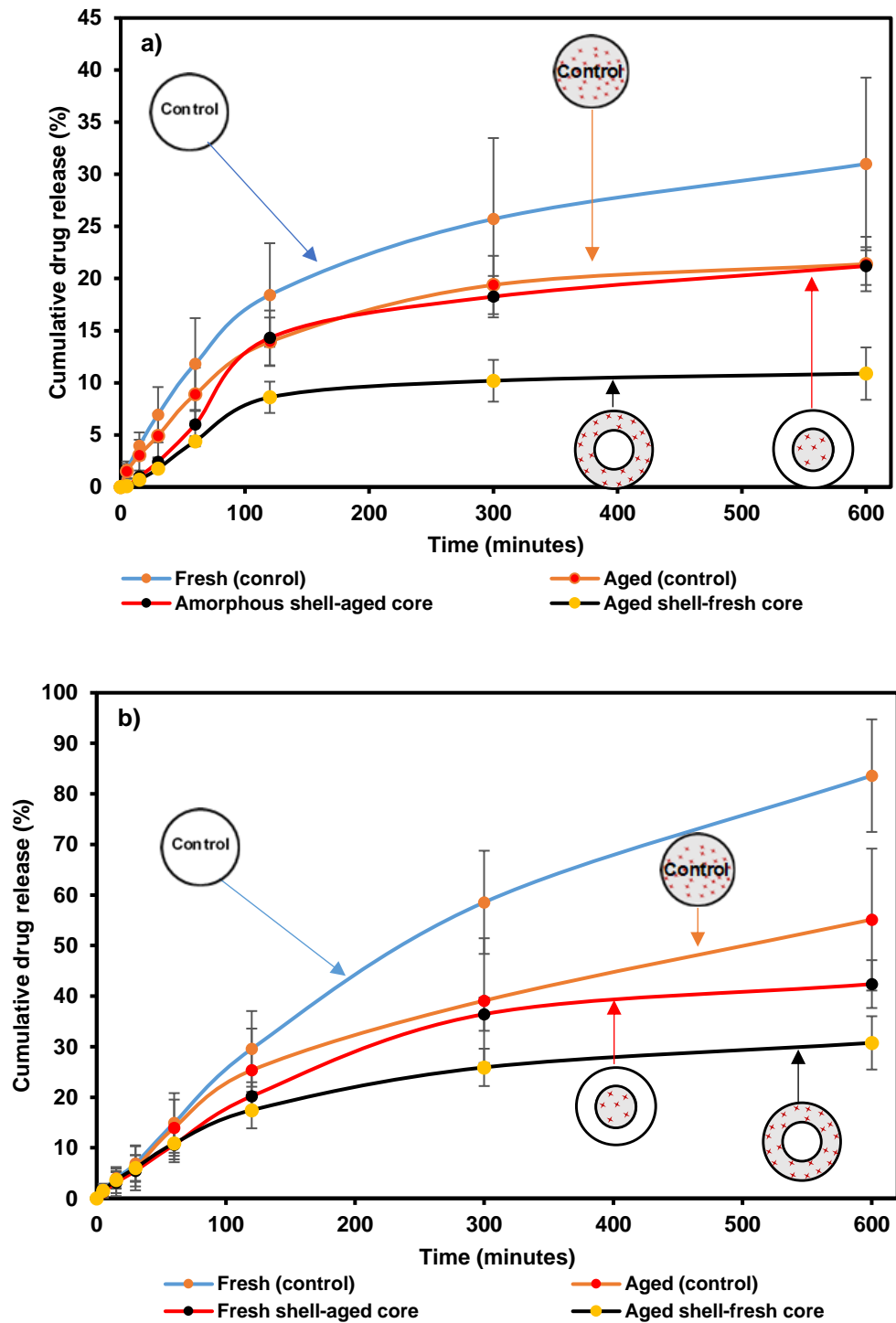


**Figure 5.11.** In-vitro cumulative drug release profiles of 3D fabricated (controls and formulations) model tablets in a) pH 2, and b) pH 6.8 (n=3). (Error bars represents standard deviation).

Before starting a full discussion of the in-vitro drug release study utilising the USP apparatus I (basket), it is important to mention that the main reason for conducting the drug release experiment in two pH media, i.e. pH 2, and pH 6.8, and for a similar time (10 hours), was to investigate the impact of the crystallinity on the behaviour of the fabricated model tablets release in both media over the same period of time. Although the SLS was used as a surfactant in the present experiment, the maximum % of drug released after 10 hours from the formulations in the current experiment was found to be about 84% indicating that the experiment was conducted under non-sink conditions. This is may be due to the high drug loading, 25% of the FELD, used for the fabricated models in the present experiment and because of the low water solubility of the crystalline FELD, which is about 19.7 mg/L [245].

Initially, 1 mL of the FELD stock solution was scanned using a UV-vis spectrophotometer in order to detect the FELD absorbance wavelength. For this purpose, 1 mL sample was scanned from 200-600 nm, and the FELD peak was observed at 363 nm (**Appendix Figure 10**). Also, the previously diluted series of concentrations were used to construct the calibration curve in order to cover the concentration range of dissolved sample (**Appendix Figure 11**). The  $R^2$  value obtained from the calibration curve was found to be 0.999, which is indicative of linearity for the utilised concentrations. Based on the data found in the literature [246], the PVA polymer has absorbance spectrum at 194 nm; hence, the PVA absorbance does not interfere with the FELD absorbance.

Drug release profiles from the fabricated model tablets, including pure ASD tablet (fresh control), aged control, spiked formulations (fresh shell-aged core, and aged shell-fresh core), in two pH media are shown above in **(Figure 5.11, a and b)**. Starting with drug release profiles in pH 2 **(Figure 5.11, a)**, it is evident that the pure ASD tablet (fresh control) has shown an improvement in the drug release relative to the aged tablet (control), and the spiked formulations over 10 hours.

The drug total release obtained from the fresh control tablet after 10 hours was 31%, while the drug total release obtained for the aged control tablet, and the fresh shell-aged core tablet after 10 hours was 21%, and 21%, respectively. Moreover, the drug release obtained for the aged shell-fresh core tablet was found to be 11%, which is lower than that obtained for the other formulations. The dissolution improvement observed with the pure ASD (fresh control) in comparison to the other model tablets may be attributed to the higher dissolution rate of the ASD in comparison to the spiked formulations [169] [247].

In addition, the structure of the compartment models [243], and the crystallinity may have affected the dissolution profiles of the aged control, and the spiked formulations, which may have led to a delayed and low drug release relative to that observed with the pure ASD one-part tablet (fresh control).

However, it is obvious that the drug release in pH 2 medium was low for all the fabricated model tablets (less than 20% in the first two hours), including the fresh control ASD model tablet. The observed limited

dissolution in pH 2 may be due to the poor dissolution and swelling properties of the PVA polymer, and the ability of the PVA to form a hydrogel in the acidic medium (**Appendix figure 12**) [58] [248]–[250].

Due to all the mentioned complications, the drug release behaviour observed for the fabricated model tablets in the pH 2 dissolution medium was not clear, especially for the compartment models (fresh shell-aged core, and aged core-fresh shell). These two formulations were expected to release more drug in comparison to the aged control because both fabricated models contained an amorphous part, either a fresh outer shell or a fresh inner core, which may induce the dissolution and produce higher drug release than that obtained for the aged control.

Thus, the drug release behaviour of the fabricated models was also investigated in pH 6.8, as shown in (**Figure 5.11, b**). The release of the FELD from the 3D fabricated model tablets has increased in pH 6.8 in comparison to the release profiles observed in pH 2 medium with all the model tablets (controls, and formulations), as shown above in the (**Figure 5.11, b**). In this medium, the obtained release of the FELD from the fresh control (ASD model tablets), was 84% after 10 hours. Moreover, the release of FELD from the aged control, fresh shell-aged core, and the aged-shell fresh core model tablets were found to be 55%, 42%, and 32% respectively, after 10 hours in the dissolution medium. The improvement in the dissolution observed may be attributed to the better dissolution, and swelling properties of the PVA in the pH 6.8 medium than that observed in pH 2 medium [248]. Moreover, the pure ASD fresh tablet has shown a better release profile, as expected, than the spiked

formulations due to the higher dissolution of the ASD [247] [169], and the impact of the crystallinity on the API release from the spiked formulations.

All the fabricated formulations showed sustained-release (SR) of the FELD over 10 hours, and this is may be due to the additional material fusion during the fabrication process, which have led to a strong drug-polymer interaction in the manufactured formulations, as reported previously in chapter 4 utilising the FTIR instrument. Also, this result is in agreement with the data reported in the literature [116].

Although the FELD release profiles obtained from the pH 6.8 medium have shown better dissolution of the active than that obtained in the pH-2 medium, the drug release behaviour from the utilised formulations was not as expected, and it was similar to that observed in pH 2 medium. As mentioned earlier in this discussion, the formulations that contain an amorphous part, either a fresh shell or a fresh inner core, were expected to release more drug than the aged tablet (control).

However, the aged control has shown drug release close to that obtained from the fresh shell-aged core model tablets, and higher than that obtained from the aged shell-fresh core model tablets in pH 2 dissolution medium. Also, the drug release of the aged control was higher than that obtained for the fresh shell-aged core and aged shell-fresh core model tablets in the pH 6.8 dissolution medium.

The observed dissolution profiles from these formulations were unexpected and difficult to explain unless there are major issues with the tablets, and micro-CT was therefore employed to probe the micro-

structure of the fabricated model tablets. Subsequently, in the next section, X $\mu$ CT was utilised to visualise the microstructure of the fabricated two-compartment model tablets.

#### 5.4.4.1. X $\mu$ CT of the Fabricated Model Tablets

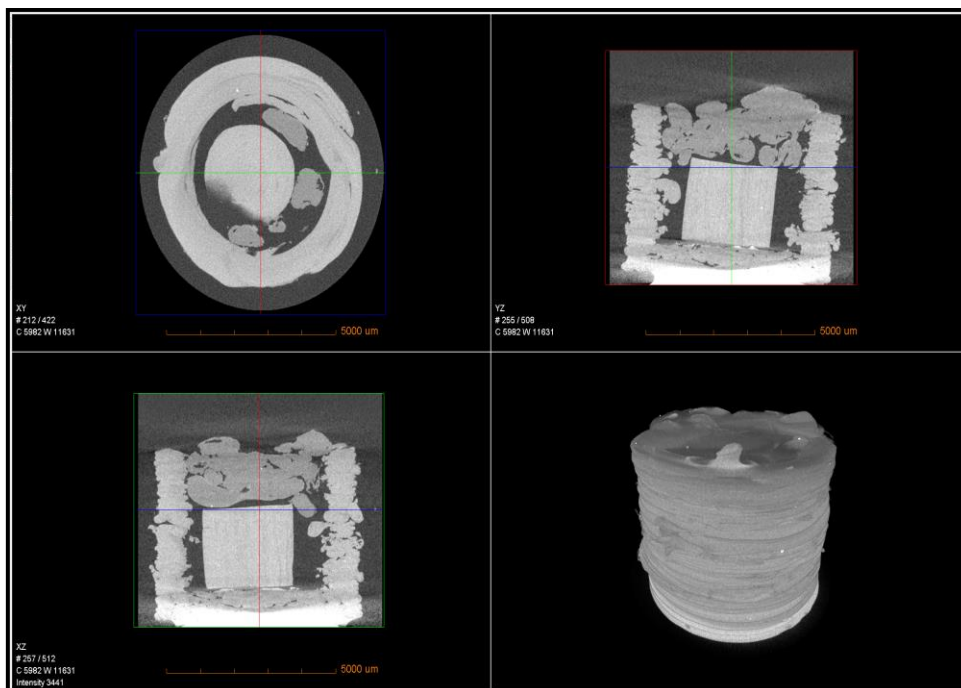


**Figure 5.12.** A representative of X $\mu$ CT scan reconstructed 3D images of FELD-PVA 3D printed two-compartment model tablets.

**Figure 5.12** displays the microstructure of the fabricated two-compartment model tablets obtained by utilising X $\mu$ CT. The X $\mu$ CT was utilised to investigate the microstructure of the model tablets (fabricated as two-compartment). The reconstructed 3D images revealed that the utilised inner core was small in size and did not fully cover the created hole in the formulated outer shell, which created a large empty area (cavity) in the centre of the fabricated model tablets. The observed cavity

in the centre of the model tablets may have air trapped inside it, which may have led to the unexpected dissolution behaviour observed for the two-compartment model tablets in the previous section. Therefore, new outer shells and inner cores were designed using TinkerCad software and fabricated utilising the FDM 3D printer in order to fabricate new model tablets with better microstructure than those observed with previous models. Then, X $\mu$ CT was utilised again in order to investigate the microstructure of the modified model tablets.

#### 5.4.4.2. Modification of the Model Tablets

In this section, modified model tablets designs were designed using TinkerCad software, as illustrated in (Figure 5.13). Then, the designed files were exported as STL files. After that, the modified designs were fabricated based on the optimised parameters obtained from chapter 4 (Table 4.3).

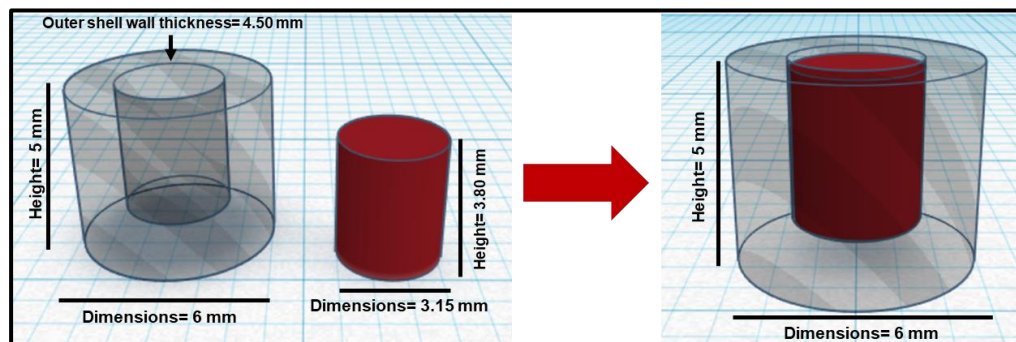


**Figure 5.13.** Modified model tablet designs (outer shell and inner core designs).

#### 5.4.4.3. X $\mu$ CT of the Modified Model Tablets

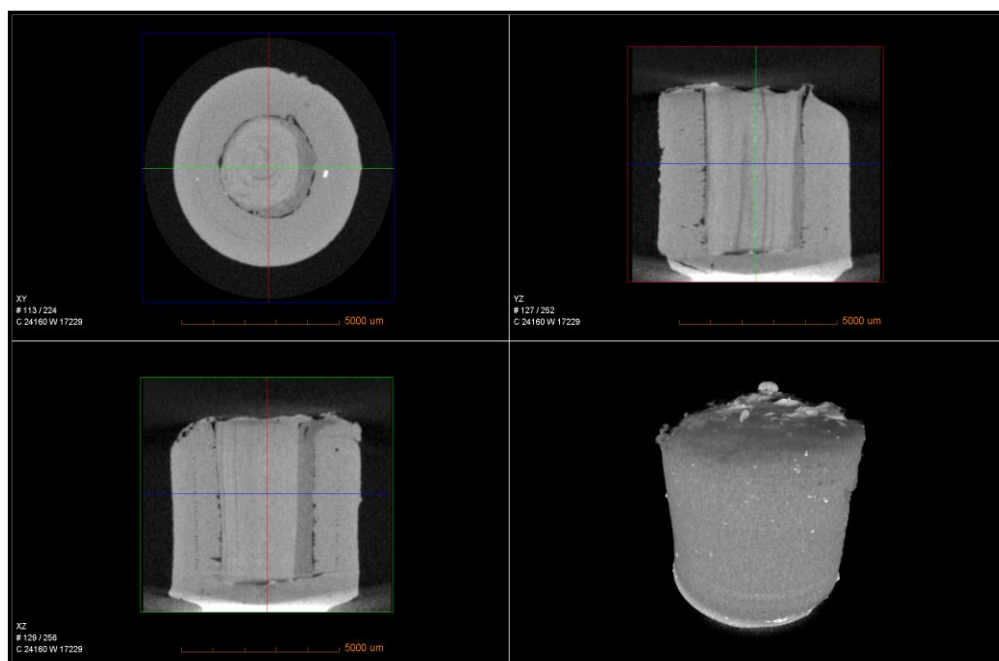


**Figure 5.14.** X $\mu$ CT scan reconstructed 3D images of the modified 3D printed model tablets.

**Figure 5.14** shows the 3D images of the fabricated model tablets after modification. The result revealed that the new modified fabricated model tablets have better microstructure than that observed for the previous models. Also, the central hole is fully filled by the new fabricated inner core. Therefore, the new modified model tablets were utilised in the next section for the in-vitro drug release study. Also, we fabricated new controls, as two-compartment tablets, instead of the one-part tablets that were utilised as fresh and aged controls in the previous drug release study, section (5.4.4). The new controls were fabricated as two-compartment tablets, fresh shell-fresh core, and aged shell-aged core, which are similar in designs to the two-compartment model tablets utilised as formulations for the drug release study.

### 5.4.5. In-vitro Drug Release of Modified Model Tablets

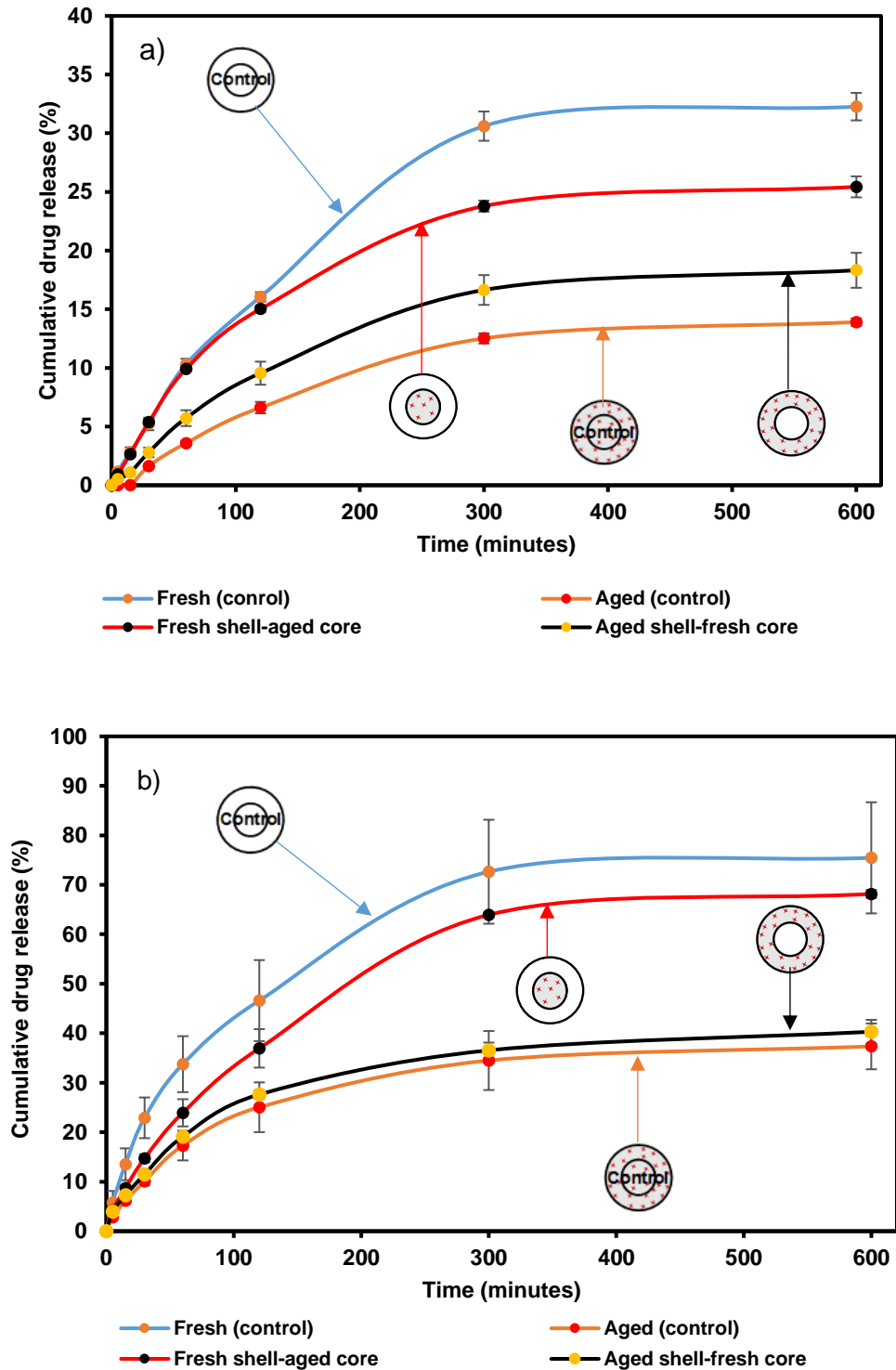


**Figure 5.15.** In-vitro cumulative drug release profiles of modified 3D fabricated model tablets in a) pH 2, and b) pH 6.8 (n=3). (Error bars represents standard deviation).

Initially, it is important to clarify that the controls and the formulations model tablets utilised in the present experiment are the modified formulations, in which both the controls (fresh shell-fresh core, and aged shell-aged core), and the formulations (fresh shell-aged core, and aged shell-fresh core), were formulated as compartment models.

The main reason to formulate both the controls and the model tablets as compartment models were to minimise the fluctuations in the drug release behaviour observed previously in section (5.4.4), between the controls, which were fabricated as one-part tablets, and the formulations, which were fabricated as compartment model tablets. Also, the modified model tablets were fabricated with better internal structure, as shown in section (5.4.4.1),

In-vitro drug release studies of the model tablets in two different dissolution media after being modified is shown above in (Figure 5.15, a and b). Starting with the release of the modified model tablets in the pH 2 dissolution medium, it is evident that the drug release in this medium was low, less than 20% with all the utilised formulations, as shown in (Figure- 5.15, a). In addition, all the formulations displayed SR of the FELD for 10 hours.

The maximum drug release was achieved after five hours with all the investigated model tablets. After that, a plateau release was observed for the utilised formulations. In comparing the FELD release for the different utilised formulations, it is evident that the FELD release obtained after 10 hours was 32% for the fresh shell-fresh core (control), 25% for the fresh

shell-aged core, 18% for the aged shell-fresh core, and 14% for the aged shell-aged core (control). The obtained release of the FELD in the pH 2 medium was low, and this was obvious due to the reasons that were stated earlier in section (5.4.4) [58] [248]–[250].

However, the behaviour and the obtained release of the active from the utilised formulations were as expected, where the obtained release was ranked as fresh shell-fresh core > fresh shell-aged core > aged shell-fresh core > aged shell-aged core. The improvement in the dissolution observed for FELD from the control (fresh shell-fresh core) may be attributed to the high dissolution of the ASD [169] [247] in comparison to the other formulations, which were spiked with crystallinity.

Also, the formulations, fresh shell-aged core, and aged shell-fresh core released more drug than the aged shell-aged core (control), and this may be attributed to the fresh part used with these model tablets, which has increased the dissolution relative to the aged shell-aged core (control).

Turning to the FELD release from the utilised formulations in pH 6.8 medium, as presented in (Figure 5.15, b). Similarly, SR was observed for all the utilised formulations in the pH 6.8 medium over a period of 10 hours. Also, it is evident that when the medium was changed to basic medium the drug release was improve indicating better dissolution of the active and the polymer in the pH 6.8 medium than the drug release observed in the acidic medium (Appendix Figure 14) [248]. The obtained release of the FELD after 10 hours was found to be 76% for the

fresh shell-fresh core (control), 68% for the fresh shell-aged core, 40% for aged shell-fresh core, and 37% for the aged shell-aged core (control). The release of the active from all the utilised formulations in the basic medium was as expected and similar to that observed in the acidic medium, in which the fresh shell-fresh core > fresh shell-aged core > aged shell-fresh core > aged shell-aged core.

Also, it was previously mentioned that the observed improvement in the dissolution of the model tablets fabricated with a fresh part in relative to the fully aged model tablets might be attributed to the high dissolution of the ASD[169] [247] in comparison to the crystalline forms. However, it is evident that the FELD release obtained from the aged shell-fresh core, 40%, was close to that obtained from the aged shell-aged core (control), 37%, even with the presence of a fresh inner core in the first model indicating that the shell was dominant over the core during the drug releases process. This is may be due to the weight of the fabricated inner core, about 30-35 mg, in comparison to the weight of the fabricated outer shell, about 160-165 mg, that were utilised to manufacture the compartment models. Also, the impact of the outer shell crystallinity on the fresh inner core may have increased with time due to the re-crystallisation of the amorphous FELD in the dissolution medium.

Moreover, for better understanding of the drug release mechanisms from the fabricated model tablets, the drug release data were fitted to different kinetic models as shown in the next section.

## 5.4.5.1. Drug Release Kinetics

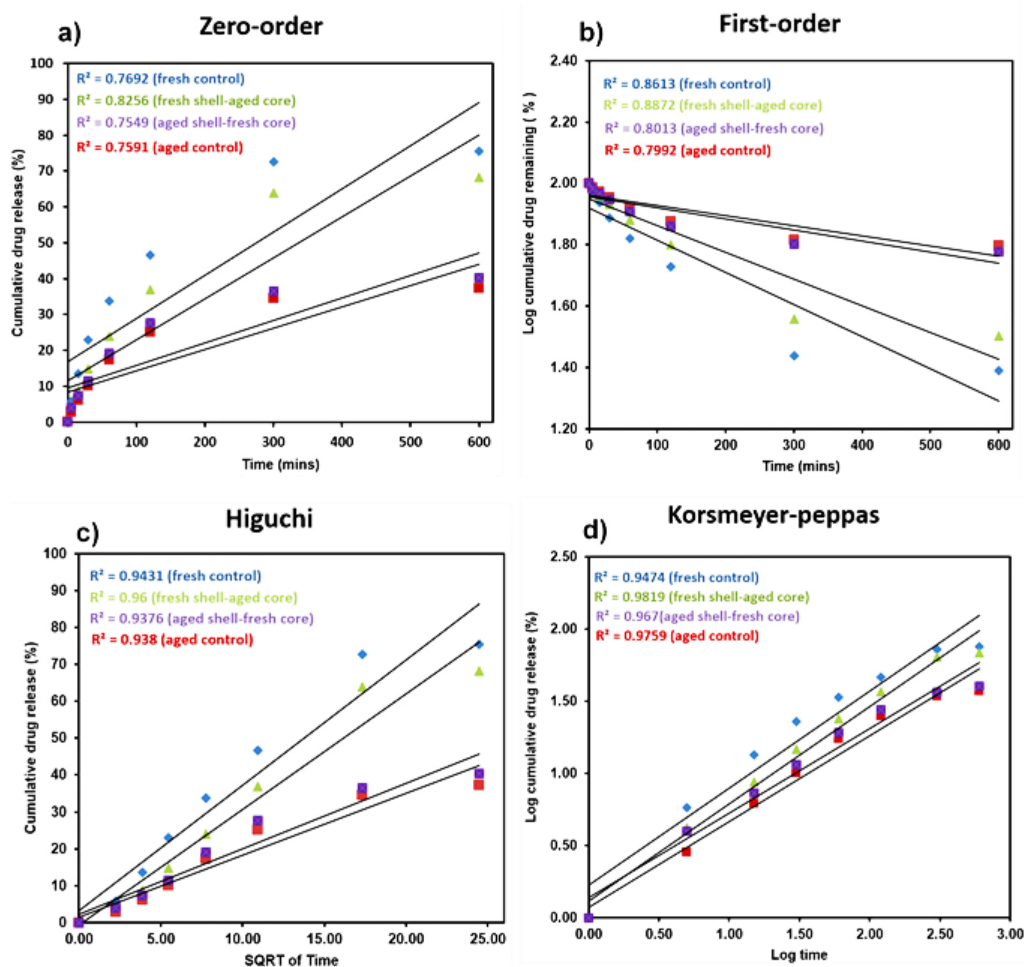


**Figure 5.16.** FELD release kinetics of fresh shell-fresh core control (blue), fresh shell-aged core (green), aged shell-fresh core (purple), and aged shell-aged core control (red), fitted to various models: a) Zero-order, b) First-order, c) Higuchi model, and d) Korsmeyer-Peppas.

The FELD release kinetics was obtained using different mathematical models, i.e. Zero-order, first-order, Higuchi model, and Korsmeyer-Peppas model, as shown above in (Figure 5.16). The obtained  $R^2$  and  $n$  values for all utilised formulations in the present study are summarised below in Table 5.1.

**Table 5.1.** R<sup>2</sup> drug release kinetics values obtained for all the formulations.

Model name	Fresh shell-fresh core (control)	Fresh shell-aged core	Aged shell-fresh core	Aged shell-aged core (control)
Zero order	0.77	0.83	0.75	0.76
First order	0.86	0.89	0.80	0.80
Higuchi model	0.94	0.96	0.94	0.94
Korsmeyer-Peppas	0.95	0.98	0.98	0.97
n value (obtained from Korsmeyer-peppas model)	0.41	0.42	0.39	0.41

It is clear from the table shown above that the regression values (R<sup>2</sup>) obtained for all the utilised formulations were best fitted to the Korsmeyer-Peppas model. Also, it is clear that R<sup>2</sup> values obtained for all the formulations were 0.95 for the fresh shell-fresh core, and 0.98 for the fresh shell-aged core, aged shell-fresh core, and 0.97 for the aged shell-aged core model tablets. According to the Korsmeyer-Peppas kinetic model, when the n (the exponent of release) value  $\leq 0.43$  indicates that the drug release is controlled by Fickian diffusion, whereas  $n \geq 0.85$  suggests that the API release is controlled by an erosion mechanism [238]. Also, for n values that are less than 0.85 and more than 0.43, the drug release is controlled by two mechanisms, including diffusion, and erosion [238].

According to the obtained n values for all the utilised formulations, as listed above in (**Table 5.1**), it is evident that all the n values were less than 0.43 suggesting that the drug release from the fabricated model tablets was predominantly controlled by Fickian diffusion mechanism.

We can conclude from the in-vitro drug release study that the modified formulations were successfully fabricated, and we were able to overcome

the observed dissolution failure that occurred previously with the non-modified formulations due to the effect of the internal structure on the drug release from the fabricated formulations. Moreover, the drug release from the modified formulations was as expected, in which the model tablets fabricated with a fresh part have released more drug than those fabricated as fully aged model tablets.

According to the observed dissolution profiles of the different utilised formulations, especially with the fresh shell-aged core model tablet, it is evident that the obtained drug release from this model tablet was (68%), which was close to that obtained for the fresh shell-fresh core (76%) model used as a control in the present study. On the other hand, the FELD release obtained from the aged shell-fresh core was 40%, which was close to that obtained from the aged shell-aged core 3%. This may indicate that the shell was dominant over the core during the drug release process.

## **5.5. Conclusion**

In this chapter, we successfully fabricated different compartment model tablets spiked with crystallinity utilising FDM 3D printer as a fabrication technique. Also, we used RH conditions as an approach to achieve equilibrium in the manufactured materials by ageing some of the fabricated models at 75% RH for seven days. Then, we quantified the crystallinity % of the aged samples after being stored exposed to RH for one-week utilising DSC instrument. Also, we have successfully utilised the USP dissolution apparatus I (basket) to track the dissolution profiles

of all the utilised compartment model tablets to measure the dissolution performance of the fabricated formulations in two pH media. The observed dissolution of the FELD from the fabricated model tablets was ranked as fresh shell-fresh core > fresh shell-aged core > aged shell-fresh core > aged shell-aged core. The obtained dissolution profiles from the utilised formulations, which were fabricated with a controlled quantity and position of crystallinity, suggests that the model tablets fabricated with a fresh shell-aged core have shown drug release close to that obtained from the model tablets fabricated as a pure amorphous tablet. Accordingly, this result has suggested that the fresh outer shell of the fabricated model tablets may have dissolved, and the release was controlled by the outer shell rather than the spiked inner core. In contrast, the observed dissolution of the aged shell-fresh core model tablets has shown FELD drug release close to that obtained for the control fabricated as aged shell-aged core model tablets, which suggests that the drug release was predominantly controlled by the spiked outer shell rather than the fresh inner core due to the induced crystallinity in the outer shell. Thus, the main aim and the detailed objectives of the present chapter were successfully achieved.

## **6. Chapter 6: Conclusion and Future Work**

### **6.1. Conclusion**

The aim of the work presented in the current thesis was to investigate the dissolution behaviour of the APIs from ASD tablets by working towards fabricating two basic ASD formulations (pure ASD, and spiked model tablets) utilising one of the 3D printing techniques, in which the effect of spatial location of crystal seeds can be systematically controlled and evaluated to understand drug release mechanisms from these formulations and offer recommendations. Gaps in the present knowledge of ASDs include a lack of understanding the dissolution behaviour of the API from ASD tablets due to the outlined drug release mechanisms complexity from these formulations. Also, current methods utilised to investigate tablets dissolution failure use tablet models in which the spatial distribution of crystals is uncontrolled due to the limitations of the conventional tableting methods on building such test models.

The novelty of utilising FDM 3D printer as a fabrication technique to build better test model tablets arises from the ability of the FDM 3D printer to control different parameters during the printing process in comparison to the conventional tableting methods, such as fabricating a tablet with either simple or complex geometry and the ability to manufacture tablets using only an API and a polymer. Thus, we have successfully formulated two basic formulations utilising the FDM 3D printer technique as a main

fabrication process in the present thesis. Also, we have successfully investigated the dissolution behaviour of the FELD from the fabricated model tablets utilising USP dissolution apparatus I (basket) in different media. The steps that were taken towards fabricating the two ASD basic models were detailed through the present thesis chapters (chapter 3, 4, and 5).

In chapter 3, the miscibility limit of the felodipine, with two polymers, namely PVA and Soluplus®, was determined utilising two approaches, including a quantitative approach (MPD method) and a qualitative method (solubility parameters) in combination with the F-H interaction parameter  $\chi$ . The calculated interaction parameter  $\chi$  values were found to be negative (-0.21 for FELD-PVA system, -0.45 for FELD-Soluplus® system) suggesting that FELD is miscible with both polymers at a temperature close to or above 140°C for all the drug loadings. Moreover, the observed single  $T_g$  has indicated a complete miscibility of the FELD with PVA and Soluplus® at 140 °C for all the drug loadings. The miscibility of the FELD in the Soluplus® obtained in the current thesis is in agreement with that obtained for the same system by Tian, et al [76]. In addition, Gibb's free energy of mixing have shown that the FELD may undergoes phase separation and re-crystallisation at or below room temperature for drug loadings higher than 10%. Also, the composition phase diagram was successfully constructed for both systems, FELD-PVA and FELD-Soluplus®, in the present work. Based on the data obtained from the compositions phase diagram of the FELD-PVA system, two drug loadings located in the metastable zone (10% of

FELD), and in the unstable zone (50% of FELD) were selected to formulate different filaments in chapter 4.

In chapter 4, several feedstocks for the FDM 3D printer with different drug loadings, including 10%, 25%, and 50%, were successfully prepared utilising HME. Also, the printing parameters were successfully optimised in the present chapter. The optimised printing parameters along with the manufactured filaments (10% and 25%) were utilised to fabricate several drug-loaded model tablets with different dimensions and geometries. Depending on the observations from the SEM and electronic callipers, the fabricated model tablets have shown better morphology than those fabricated using the default printing parameters, indicating that the printing parameters optimisation step was successful. Thus, the ability of the FDM 3D printer to control different parameters during tablet fabrication process was successfully evaluated. Due to the high temperature utilised during both filament manufacturing and tablets fabrication (above 160 °C), all the manufactured materials have shown complete miscibility of the FELD with the PVA (as predicted previously in chapter 3) based on the data obtained in chapter four using different techniques, including DSC, FTIR, Raman spectroscopy, and PXRD. Therefore, RH storage conditions was utilised as an approach to facilitate crystallisation in the manufactured materials by storing the manufactured materials at 75% RH for one-week.

In chapter 5, two basic model tablets: pure ASD and spiked with crystalline seeds, were fabricated utilising the FDM 3D printer as fabrication technique. Also, the impact of the micro-structure on the

dissolution behaviour of the fabricated model tablets was investigated utilising USP dissolution apparatus I (basket). Moreover, the crystallisation of the spiked models after being exposed to RH storage conditions were investigated utilising different techniques, including FTIR, Raman, and PXRD. All the utilised techniques revealed that the aged materials (spiked outer shell and inner cores) have partially re-crystallised after seven days of storage at 75% RH. Also, the % of crystallinity in the aged materials was found to be about  $4\pm 2$  % by utilising DSC.

The dissolution of all formulations was investigated in two media (pH 2 and pH 6.8). The observed dissolution of the FELD from the fabricated model tablets was ranked as fresh shell-fresh core > fresh shell-aged core > aged shell-fresh core > aged shell-aged core, which has suggested that the model tablets fabricated with a fresh shell-aged core have shown drug release close to that obtained from the model tablets fabricated as a pure amorphous tablet. Consequently, this result has suggested that the fresh outer shell of the fabricated model tablets may have dissolved, and the release was controlled by the outer shell rather than the spiked inner core. On the other hand, the observed dissolution of the aged shell-fresh core model tablets has shown drug release close to that obtained for the control fabricated as aged model tablets.

In summary, different methodologies and steps were discussed in the current thesis to build better model tablet systems to investigate why ASD tablets fail dissolution test and to provide additional information on drug release mechanisms from ASD tablets. From the data generated

through the different chapters, it was possible to fabricate different model tablets and it was possible to make a number of explanations regarding the impact of the micro-structure on the dissolution performance of the FELD from ASD tablets. Thus, the main aim of the current thesis was successfully achieved through all the detailed information in the chapters 3, 4, and 5.

Recommendations:

The FDM 3D printer along with thermoplastic polymers has shown promising approach to manufacture model test tablets with controlled amount and position of crystalline seeds to investigate why ASDs tablet fail dissolution testing. The current work has shown that it is not only the amount of impurity has affected the release of the drug but the location of the spatially distributed impurity in the fabricated model tablets. For example, the fabricated models with amorphous outer shell and spiked core have shown drug release close to the drug release from the pure ASD models. In contrast, the fabricated models with spiked outer shell and amorphous core have shown drug release close to the drug release from the completely spiked models. Thus, regulators and manufacturers may have to consider both the amount and the location of the impurity during manufacturing and assessing the bioavailability of the ASDs formulations.

## **6.2. Future Work**

The present work showed that the FDM 3D printing technology is a promising method to manufacture better test model tablets with

controlled position and amount of crystalline materials to investigate the dissolution failure mechanisms of different API during dissolution process using only a drug and a polymer without adding any excipients in comparison with the conventional tableting methods. It is also possible to do more modifications on the fabricated model tablets in the current work utilising the FDM 3D printer. For example, to use the printer to fabricate model tablets in which the crystallinity can be spatially distributed in different positions of the tablets i.e. close to the tablet edges rather than the centre of the tablet.

Another potential work that can be done to the fabricated model tablets in the present thesis is to investigate the dissolution behaviour of the API using Raman spectroscopy accompanied by flow-through cell in order to obtain chemical transformation directly from the tablet during the dissolution experiment. Moreover, Raman spectroscopy can be accompanied with MRI in order to obtain both chemical and physical information directly from the dosage form during the dissolution process.

To conclude, the work in the present thesis has shown that the FDM 3D printing technology has the ability to build better test model tablets to study the failure mode of the APIs from the the ASD tablets during dissolution testing in comparison to the typical tableting methods. Thus, the FDM 3D printer can be employed by the manufacturer and pharmaceutical companies to fabricate model tablets in order to assess the performance and the bioavailability of the ASDs tablets.

## 7. References

- [1] D. Attwood and A. T. Florence, *Physicochemical principles of pharmacy*. Macmillan, 1998.
- [2] V. R. Vemula, V. Lagishetty, and S. Lingala, "Solubility enhancement techniques," *Int. J. Pharm. Sci. Rev. Res.*, vol. 5, no. 1, pp. 41–51, 2010.
- [3] N. J. Babu and A. Nangia, "Solubility advantage of amorphous drugs and pharmaceutical cocrystals," *Cryst. Growth Des.*, vol. 11, no. 7, pp. 2662–2679, 2011.
- [4] F. Tres *et al.*, "Monitoring the dissolution mechanisms of amorphous bicalutamide solid dispersions via real-time raman mapping," *Mol. Pharm.*, vol. 12, no. 5, pp. 1512–1522, 2015.
- [5] C. Leuner and J. Dressman, "Improving drug solubility for oral delivery using solid dispersions," *Eur. J. Pharm. Biopharm.*, vol. 50, no. 1, pp. 47–60, 2000.
- [6] W. H. Organization and others, "Multisource (generic) pharmaceutical products: guidelines on registration requirements to establish interchangeability," *WHO Tech. Rep. Ser.*, vol. 937, pp. 347–390, 2006.
- [7] M. Savolainen *et al.*, "Better understanding of dissolution behaviour of amorphous drugs by in situ solid-state analysis using Raman spectroscopy," *Eur. J. Pharm. Biopharm.*, vol. 71, no. 1, pp. 71–79, 2009.
- [8] A. Newman, *Pharmaceutical amorphous solid dispersions*. John Wiley & Sons, 2015.
- [9] J. M. Butler and J. B. Dressman, "The developability classification system: application of biopharmaceutics concepts to formulation development," *J. Pharm. Sci.*, vol. 99, no. 12, pp. 4940–4954, 2010.
- [10] F. Tres, "Raman chemical and physical mapping of oral dosage forms," PhD Thesis, University of Nottingham, 2015.
- [11] M. E. Aulton and K. M. Taylor, *Aulton's pharmaceuticals: the design and manufacture of medicines*. Elsevier Health Sciences, 2013.
- [12] A. A. Noyes and W. R. Whitney, "The rate of solution of solid substances in their own solutions.," *J. Am. Chem. Soc.*, vol. 19, no. 12, pp. 930–934, 1897.
- [13] A. Dokoumetzidis and P. Macheras, "A century of dissolution research: from Noyes and Whitney to the biopharmaceutics classification system," *Int. J. Pharm.*, vol. 321, no. 1–2, pp. 1–11, 2006.
- [14] A. T. Serajuddin, "Salt formation to improve drug solubility," *Adv. Drug Deliv. Rev.*, vol. 59, no. 7, pp. 603–616, 2007.
- [15] A. C. Rumondor, S. S. Dhareshwar, and F. Kesisoglou, "Amorphous solid dispersions or prodrugs: complementary strategies to increase drug absorption," *J. Pharm. Sci.*, vol. 105, no. 9, pp. 2498–2508, 2016.

- [16] G. Sandri, M. C. Bonferoni, F. Ferrari, S. Rossi, and C. M. Caramella, "The role of particle size in drug release and absorption," in *Particulate Products*, Springer, 2014, pp. 323–341.
- [17] P. Khadka *et al.*, "Pharmaceutical particle technologies: an approach to improve drug solubility, dissolution and bioavailability," *Asian J. Pharm. Sci.*, vol. 9, no. 6, pp. 304–316, 2014.
- [18] E. Nelson, "Solution rate of theophylline salts and effects from oral administration," *J. Am. Pharm. Assoc.*, vol. 46, no. 10, pp. 607–614, 1957.
- [19] E. Nelson, "Comparative dissolution rates of weak acids and their sodium salts," *J. Am. Pharm. Assoc.*, vol. 47, no. 4, pp. 297–299, 1958.
- [20] P. Makary, "Principles of salt formation," *UK J Pharm Biosci*, vol. 2, no. 4, pp. 1–4, 2014.
- [21] L. Kumar, A. Amin, and A. K. Bansal, "Salt selection in drug development," *Pharm. Technol.*, vol. 3, no. 32, 2008.
- [22] V. J. Stella and K. W. Nti-Addae, "Prodrug strategies to overcome poor water solubility," *Adv. Drug Deliv. Rev.*, vol. 59, no. 7, pp. 677–694, 2007.
- [23] B. Testa, "Prodrug research: futile or fertile?," *Biochem. Pharmacol.*, vol. 68, no. 11, pp. 2097–2106, 2004.
- [24] R. Ho, S. E. Dilworth, D. R. Williams, and J. Y. Heng, "Role of surface chemistry and energetics in high shear wet granulation," *Ind. Eng. Chem. Res.*, vol. 50, no. 16, pp. 9642–9649, 2011.
- [25] R. M. Atkinson, C. Bedford, K. J. Child, and E. G. Tomich, "Effect of particle size on blood griseofulvin-levels in man," *Nature*, vol. 193, no. 4815, p. 588, 1962.
- [26] A. Krupa, M. Descamps, J.-F. Willart, R. Jachowicz, and F. Danède, "High energy ball milling and supercritical carbon dioxide impregnation as co-processing methods to improve dissolution of tadalafil," *Eur. J. Pharm. Sci.*, vol. 95, pp. 130–137, 2016.
- [27] S. M. Wong, I. W. Kellaway, and S. Murdan, "Enhancement of the dissolution rate and oral absorption of a poorly water soluble drug by formation of surfactant-containing microparticles," *Int. J. Pharm.*, vol. 317, no. 1, pp. 61–68, 2006.
- [28] T. Loftsson and M. E. Brewster, "Pharmaceutical applications of cyclodextrins. 1. Drug solubilization and stabilization," *J. Pharm. Sci.*, vol. 85, no. 10, pp. 1017–1025, 1996.
- [29] M. E. Brewster and T. Loftsson, "Cyclodextrins as pharmaceutical solubilizers," *Adv. Drug Deliv. Rev.*, vol. 59, no. 7, pp. 645–666, 2007.
- [30] P. G. Debenedetti and F. H. Stillinger, "Supercooled liquids and the glass transition," *Nature*, vol. 410, no. 6825, pp. 259–267, 2001.
- [31] B. C. Hancock and S. L. Shamblin, "Molecular mobility of amorphous pharmaceuticals determined using differential scanning calorimetry," *Thermochim. Acta*, vol. 380, no. 2, pp. 95–107, 2001.
- [32] A. Newman and G. Zografi, "Commentary: Considerations in the Measurement of Glass Transition Temperatures of Pharmaceutical Amorphous Solids," *AAPS PharmSciTech*, vol. 21, no. 1, p. 26, 2020.

- [33] Y. Aso, S. Yoshioka, and S. Kojima, "Relationship between the crystallization rates of amorphous nifedipine, phenobarbital, and flopropione, and their molecular mobility as measured by their enthalpy relaxation and <sup>1</sup>H NMR relaxation times," *J. Pharm. Sci.*, vol. 89, no. 3, pp. 408–416, 2000.
- [34] B. C. Hancock and M. Parks, "What is the true solubility advantage for amorphous pharmaceuticals?," *Pharm. Res.*, vol. 17, no. 4, pp. 397–404, 2000.
- [35] D. E. Alonzo, Y. Gao, D. Zhou, H. Mo, G. G. Zhang, and L. S. Taylor, "Dissolution and precipitation behavior of amorphous solid dispersions," *J. Pharm. Sci.*, vol. 100, no. 8, pp. 3316–3331, 2011.
- [36] L. S. Taylor and B. C. Hancock, "George Zografi and the science of solids and surfaces," *J. Pharm. Sci.*, vol. 103, no. 9, pp. 2592–2594, 2014.
- [37] A. Newman, G. Knipp, and G. Zografi, "Assessing the performance of amorphous solid dispersions," *J. Pharm. Sci.*, vol. 101, no. 4, pp. 1355–1377, 2012.
- [38] C. L.-N. Vo, C. Park, and B.-J. Lee, "Current trends and future perspectives of solid dispersions containing poorly water-soluble drugs," *Eur. J. Pharm. Biopharm.*, vol. 85, no. 3, pp. 799–813, 2013.
- [39] S. Janssens and G. Van den Mooter, "Physical chemistry of solid dispersions," *J. Pharm. Pharmacol.*, vol. 61, no. 12, pp. 1571–1586, 2009.
- [40] N. Shah, H. Sandhu, D. S. Choi, H. Chokshi, and A. W. Malick, "Amorphous solid dispersions," *Theory Pract. Springer*, 2014, [Online]. Available: <http://link.springer.com/content/pdf/10.1007/978-1-4939-1598-9.pdf>.
- [41] S. Baghel, H. Cathcart, and N. J. O'Reilly, "Polymeric amorphous solid dispersions: a review of amorphization, crystallization, stabilization, solid-state characterization, and aqueous solubilization of biopharmaceutical classification system class II drugs," *J. Pharm. Sci.*, vol. 105, no. 9, pp. 2527–2544, 2016.
- [42] A. Samir, N. El-Megrab, H. A. Fattah, and W. Barakat, "Solubility Enhancement of Poorly Water Soluble Drug by Solid Dispersion," *Asian J Res. Chem*, vol. 5, no. 4, pp. 359–367, 2012.
- [43] A. Newman, G. Knipp, and G. Zografi, "Assessing the performance of amorphous solid dispersions," *J. Pharm. Sci.*, vol. 101, no. 4, pp. 1355–1377, 2012.
- [44] A. Goyanes, A. B. M. Buanz, G. B. Hatton, S. Gaisford, and A. W. Basit, "3D printing of modified-release aminosalicylate (4-ASA and 5-ASA) tablets," *Eur. J. Pharm. Biopharm.*, vol. 89, pp. 157–162, 2015, doi: 10.1016/j.ejpb.2014.12.003.
- [45] Y. He and C. Ho, "Amorphous solid dispersions: utilization and challenges in drug discovery and development," *J. Pharm. Sci.*, vol. 104, no. 10, pp. 3237–3258, 2015.
- [46] Y. Huang and W.-G. Dai, "Fundamental aspects of solid dispersion technology for poorly soluble drugs," *Acta Pharm. Sin. B*, vol. 4, no. 1, pp. 18–25, Feb. 2014, doi: 10.1016/j.apsb.2013.11.001.

- [47] T. Vilhelmsen, H. Eliassen, and T. Schøfer, "Effect of a melt agglomeration process on agglomerates containing solid dispersions," *Int. J. Pharm.*, vol. 303, no. 1, pp. 132–142, 2005.
- [48] G. Van den Mooter, I. Weuts, T. De Ridder, and N. Blaton, "Evaluation of Inutec SP1 as a new carrier in the formulation of solid dispersions for poorly soluble drugs," *Int. J. Pharm.*, vol. 316, no. 1, pp. 1–6, 2006.
- [49] D.-H. Won, M.-S. Kim, S. Lee, J.-S. Park, and S.-J. Hwang, "Improved physicochemical characteristics of felodipine solid dispersion particles by supercritical anti-solvent precipitation process," *Int. J. Pharm.*, vol. 301, no. 1, pp. 199–208, 2005.
- [50] A. L. Sarode, H. Sandhu, N. Shah, W. Malick, and H. Zia, "Hot melt extrusion (HME) for amorphous solid dispersions: predictive tools for processing and impact of drug–polymer interactions on supersaturation," *Eur. J. Pharm. Sci.*, vol. 48, no. 3, pp. 371–384, 2013.
- [51] R. J. Chokshi, H. K. Sandhu, R. M. Iyer, N. H. Shah, A. W. Malick, and H. Zia, "Characterization of physico-mechanical properties of indomethacin and polymers to assess their suitability for hot-melt extrusion processes as a means to manufacture solid dispersion/solution," *J. Pharm. Sci.*, vol. 94, no. 11, pp. 2463–2474, 2005.
- [52] S. Qi, A. Gryczke, P. Belton, and D. Q. Craig, "Characterisation of solid dispersions of paracetamol and EUDRAGIT® E prepared by hot-melt extrusion using thermal, microthermal and spectroscopic analysis," *Int. J. Pharm.*, vol. 354, no. 1–2, pp. 158–167, 2008.
- [53] H. Patil, R. V. Tiwari, and M. A. Repka, "Hot-melt extrusion: from theory to application in pharmaceutical formulation," *Aaps Pharmscitech*, vol. 17, no. 1, pp. 20–42, 2016.
- [54] C. W. Pouton, "Formulation of poorly water-soluble drugs for oral administration: physicochemical and physiological issues and the lipid formulation classification system," *Eur. J. Pharm. Sci.*, vol. 29, no. 3, pp. 278–287, 2006.
- [55] A. Narang and A. Shrivastava, "Melt extrusion solid dispersion technique," *Drug Dev Ind Pharm*, vol. 26, no. 8, pp. 111–115, 2002.
- [56] R. S. Dhumal, A. L. Kelly, P. York, P. D. Coates, and A. Paradkar, "Cocrystallization and simultaneous agglomeration using hot melt extrusion," *Pharm. Res.*, vol. 27, no. 12, pp. 2725–2733, 2010.
- [57] G. Verreck, K. Six, G. Van den Mooter, L. Baert, J. Peeters, and M. E. Brewster, "Characterization of solid dispersions of itraconazole and hydroxypropylmethylcellulose prepared by melt extrusion—part I," *Int. J. Pharm.*, vol. 251, no. 1–2, pp. 165–174, 2003.
- [58] M. Alhijaj, P. Belton, and S. Qi, "An investigation into the use of polymer blends to improve the printability of and regulate drug release from pharmaceutical solid dispersions prepared via fused deposition modeling (FDM) 3D printing," *Eur. J. Pharm. Biopharm.*, vol. 108, pp. 111–125, 2016.
- [59] A. Paudel, Z. A. Worku, J. Meeus, S. Guns, and G. Van den Mooter, "Manufacturing of solid dispersions of poorly water soluble

- drugs by spray drying: formulation and process considerations," *Int. J. Pharm.*, vol. 453, no. 1, pp. 253–284, 2013.
- [60] A. Paudel and G. Van den Mooter, "Influence of solvent composition on the miscibility and physical stability of naproxen/PVP K 25 solid dispersions prepared by cosolvent spray-drying," *Pharm. Res.*, vol. 29, no. 1, pp. 251–270, 2012.
- [61] T. Vasconcelos, B. Sarmiento, and P. Costa, "Solid dispersions as strategy to improve oral bioavailability of poor water soluble drugs," *Drug Discov. Today*, vol. 12, no. 23–24, pp. 1068–1075, 2007.
- [62] G. Van den Mooter *et al.*, "Physical stabilisation of amorphous ketoconazole in solid dispersions with polyvinylpyrrolidone K25," *Eur. J. Pharm. Sci.*, vol. 12, no. 3, pp. 261–269, 2001.
- [63] S. Janssens and G. Van den Mooter, "Physical chemistry of solid dispersions," *J. Pharm. Pharmacol.*, vol. 61, no. 12, pp. 1571–1586, 2009.
- [64] A. T. Serajuddin, "Solid dispersion of poorly water-soluble drugs: Early promises, subsequent problems, and recent breakthroughs," *J. Pharm. Sci.*, vol. 88, no. 10, pp. 1058–1066, 1999.
- [65] H. Konno and L. S. Taylor, "Influence of different polymers on the crystallization tendency of molecularly dispersed amorphous felodipine," *J. Pharm. Sci.*, vol. 95, no. 12, pp. 2692–2705, 2006.
- [66] R. J. Chokshi, N. H. Shah, H. K. Sandhu, A. W. Malick, and H. Zia, "Stabilization of low glass transition temperature indomethacin formulations: Impact of polymer-type and its concentration," *J. Pharm. Sci.*, vol. 97, no. 6, pp. 2286–2298, 2008.
- [67] B. C. Hancock and G. Zografi, "Characteristics and significance of the amorphous state in pharmaceutical systems," *J. Pharm. Sci.*, vol. 86, no. 1, pp. 1–12, 1997.
- [68] Y. Hu *et al.*, "Formation, physical stability, and quantification of process-induced disorder in cryomilled samples of a model polymorphic drug," *J. Pharm. Sci.*, vol. 102, no. 1, pp. 93–103, 2013.
- [69] V. Caron, L. Tajber, O. I. Corrigan, and A. M. Healy, "A comparison of spray drying and milling in the production of amorphous dispersions of sulfathiazole/polyvinylpyrrolidone and sulfadimidine/polyvinylpyrrolidone," *Mol. Pharm.*, vol. 8, no. 2, pp. 532–542, 2011.
- [70] G. Van den Mooter, "The use of amorphous solid dispersions: A formulation strategy to overcome poor solubility and dissolution rate," *Drug Discov. Today Technol.*, vol. 9, no. 2, pp. e79–e85, 2012.
- [71] P. J. Marsac, S. L. Shamblin, and L. S. Taylor, "Theoretical and practical approaches for prediction of drug–polymer miscibility and solubility," *Pharm. Res.*, vol. 23, no. 10, p. 2417, 2006.
- [72] F. Qian, J. Huang, and M. A. Hussain, "Drug–polymer solubility and miscibility: stability consideration and practical challenges in amorphous solid dispersion development," *J. Pharm. Sci.*, vol. 99, no. 7, pp. 2941–2947, 2010.
- [73] A. C. Rumondor, I. Ivanisevic, S. Bates, D. E. Alonzo, and L. S. Taylor, "Evaluation of drug-polymer miscibility in amorphous solid

- dispersion systems," *Pharm. Res.*, vol. 26, no. 11, pp. 2523–2534, 2009.
- [74] P. J. Marsac, H. Konno, and L. S. Taylor, "A comparison of the physical stability of amorphous felodipine and nifedipine systems," *Pharm. Res.*, vol. 23, no. 10, pp. 2306–2316, 2006.
- [75] H. Konno, T. Handa, D. E. Alonzo, and L. S. Taylor, "Effect of polymer type on the dissolution profile of amorphous solid dispersions containing felodipine," *Eur. J. Pharm. Biopharm.*, vol. 70, no. 2, pp. 493–499, 2008.
- [76] Y. Tian, J. Booth, E. Meehan, D. S. Jones, S. Li, and G. P. Andrews, "Construction of drug–polymer thermodynamic phase diagrams using Flory–Huggins interaction theory: identifying the relevance of temperature and drug weight fraction to phase separation within solid dispersions," *Mol. Pharm.*, vol. 10, no. 1, pp. 236–248, 2012.
- [77] S. Dalsania, J. Sharma, B. Munjal, and A. K. Bansal, "Impact of drug-polymer miscibility on enthalpy relaxation of Irbesartan amorphous solid dispersions," *Pharm. Res.*, vol. 35, no. 2, p. 29, 2018.
- [78] G. Hameed, "Investigation of cryomilling as a potential tool for the production of amorphous solid dispersions," PhD Thesis, University of Nottingham, 2017.
- [79] Y. Zhao, P. Inbar, H. P. Chokshi, A. W. Malick, and D. S. Choi, "Prediction of the thermal phase diagram of amorphous solid dispersions by Flory–Huggins theory," *J. Pharm. Sci.*, vol. 100, no. 8, pp. 3196–3207, 2011.
- [80] S. Baghel, H. Cathcart, and N. J. O'reilly, "Theoretical and experimental investigation of drug-polymer interaction and miscibility and its impact on drug supersaturation in aqueous medium," *Eur. J. Pharm. Biopharm.*, vol. 107, pp. 16–31, 2016.
- [81] Y. E. Sun, J. Tao, G. G. Zhang, and L. Yu, "Solubilities of crystalline drugs in polymers: an improved analytical method and comparison of solubilities of indomethacin and nifedipine in PVP, PVP/VA, and PVAc," *J. Pharm. Sci.*, vol. 99, no. 9, pp. 4023–4031, 2010.
- [82] P. J. Marsac, T. Li, and L. S. Taylor, "Estimation of drug–polymer miscibility and solubility in amorphous solid dispersions using experimentally determined interaction parameters," *Pharm. Res.*, vol. 26, no. 1, p. 139, 2009.
- [83] J. Tao, Y. Sun, G. G. Zhang, and L. Yu, "Solubility of small-molecule crystals in polymers: D-mannitol in PVP, indomethacin in PVP/VA, and nifedipine in PVP/VA," *Pharm. Res.*, vol. 26, no. 4, pp. 855–864, 2009.
- [84] Y.-C. Chen, H.-O. Ho, D.-Z. Liu, W.-S. Siow, and M.-T. Sheu, "Swelling/floating capability and drug release characterizations of gastroretentive drug delivery system based on a combination of hydroxyethyl cellulose and sodium carboxymethyl cellulose," *PLoS One*, vol. 10, no. 1, p. e0116914, 2015.
- [85] A. Fick, "Poggendorff's Flannel," *Physik*, vol. 94, no. 59, p. 297, 1855.

- [86] C. K. Sackett and B. Narasimhan, "Mathematical modeling of polymer erosion: Consequences for drug delivery," *Int. J. Pharm.*, vol. 418, no. 1, pp. 104–114, 2011.
- [87] K. E. Uhrich, S. M. Cannizzaro, R. S. Langer, and K. M. Shakesheff, "Polymeric systems for controlled drug release," *Chem. Rev.*, vol. 99, no. 11, pp. 3181–3198, 1999.
- [88] J. Siepmann and A. Göpferich, "Mathematical modeling of bioerodible, polymeric drug delivery systems," *Adv. Drug Deliv. Rev.*, vol. 48, no. 2–3, pp. 229–247, 2001.
- [89] B. P. Gupta, N. Thakur, N. P. Jain, J. Banweer, and S. Jain, "Osmotically controlled drug delivery system with associated drugs," *J. Pharm. Pharm. Sci.*, vol. 13, no. 4, pp. 571–588, 2010.
- [90] A. A. Robitzki and R. Kurz, "Biosensing and drug delivery at the microscale," in *Drug Delivery*, Springer, 2010, pp. 87–112.
- [91] D. J. Mastropietro, K. Park, and H. Omidian, "Polymers in Oral Drug Delivery," 2017.
- [92] S. N. Makhija and P. R. Vavia, "Controlled porosity osmotic pump-based controlled release systems of pseudoephedrine: I. Cellulose acetate as a semipermeable membrane," *J. Controlled Release*, vol. 89, no. 1, pp. 5–18, 2003.
- [93] G. Santus and R. W. Baker, "Osmotic drug delivery: a review of the patent literature," *J. Controlled Release*, vol. 35, no. 1, pp. 1–21, 1995.
- [94] O. Mahmah, R. Tabbakh, A. Kelly, and A. Paradkar, "A comparative study of the effect of spray drying and hot-melt extrusion on the properties of amorphous solid dispersions containing felodipine," *J. Pharm. Pharmacol.*, vol. 66, no. 2, pp. 275–284, 2014.
- [95] N. Setiawan, "Understanding the Thermodynamics and Oral Absorption Potential of Pharmaceutical Amorphous Solid Dispersions," 2018.
- [96] A. S. Keys, J. P. Garrahan, and D. Chandler, "Calorimetric glass transition explained by hierarchical dynamic facilitation," *Proc. Natl. Acad. Sci.*, vol. 110, no. 12, pp. 4482–4487, 2013.
- [97] K. Kawakami, "Crystallization Tendency of Pharmaceutical Glasses: Relevance to Compound Properties, Impact of Formulation Process, and Implications for Design of Amorphous Solid Dispersions," *Pharmaceutics*, vol. 11, no. 5, p. 202, 2019.
- [98] T. Xie and L. S. Taylor, "Effect of temperature and moisture on the physical stability of binary and ternary amorphous solid dispersions of celecoxib," *J. Pharm. Sci.*, vol. 106, no. 1, pp. 100–110, 2017.
- [99] A. Prudic, Y. Ji, and G. Sadowski, "Thermodynamic phase behavior of API/polymer solid dispersions," *Mol. Pharm.*, vol. 11, no. 7, pp. 2294–2304, 2014.
- [100] P. J. Marsac, A. C. Rumondor, D. E. Nivens, U. S. Kestur, L. Stanciu, and L. S. Taylor, "Effect of temperature and moisture on the miscibility of amorphous dispersions of felodipine and poly (vinyl pyrrolidone)," *J. Pharm. Sci.*, vol. 99, no. 1, pp. 169–185, 2010.

- [101] F. Tres *et al.*, “Real time Raman imaging to understand dissolution performance of amorphous solid dispersions,” *J. Controlled Release*, vol. 188, pp. 53–60, 2014.
- [102] D. Q. Craig, “The mechanisms of drug release from solid dispersions in water-soluble polymers,” *Int. J. Pharm.*, vol. 231, no. 2, pp. 131–144, 2002.
- [103] Z. A. Langham, J. Booth, L. P. Hughes, G. K. Reynolds, and S. A. Wren, “Mechanistic insights into the dissolution of spray-dried amorphous solid dispersions,” *J. Pharm. Sci.*, vol. 101, no. 8, pp. 2798–2810, 2012.
- [104] D. E. Alonzo, G. G. Zhang, D. Zhou, Y. Gao, and L. S. Taylor, “Understanding the behavior of amorphous pharmaceutical systems during dissolution,” *Pharm. Res.*, vol. 27, no. 4, pp. 608–618, 2010.
- [105] I. Tho, B. Liepold, J. Rosenberg, M. Maegerlein, M. Brandl, and G. Fricker, “Formation of nano/micro-dispersions with improved dissolution properties upon dispersion of ritonavir melt extrudate in aqueous media,” *Eur. J. Pharm. Sci.*, vol. 40, no. 1, pp. 25–32, 2010.
- [106] E. Karavas, G. Ktistis, A. Xenakis, and E. Georgarakis, “Effect of hydrogen bonding interactions on the release mechanism of felodipine from nanodispersions with polyvinylpyrrolidone,” *Eur. J. Pharm. Biopharm.*, vol. 63, no. 2, pp. 103–114, 2006.
- [107] W. L. Hulse, J. Gray, and R. T. Forbes, “A discriminatory intrinsic dissolution study using UV area imaging analysis to gain additional insights into the dissolution behaviour of active pharmaceutical ingredients,” *Int. J. Pharm.*, vol. 434, no. 1–2, pp. 133–139, 2012.
- [108] J. P. Boetker *et al.*, “Insights into the early dissolution events of amlodipine using UV imaging and Raman spectroscopy,” *Mol. Pharm.*, vol. 8, no. 4, pp. 1372–1380, 2011.
- [109] L. H. Nielsen, S. Gordon, J. P. Pajander, J. Østergaard, T. Rades, and A. Müllertz, “Biorelevant characterisation of amorphous furosemide salt exhibits conversion to a furosemide hydrate during dissolution,” *Int. J. Pharm.*, vol. 457, no. 1, pp. 14–24, 2013.
- [110] S. G. Kazarian and K. A. Chan, “‘Chemical photography’ of drug release,” *Macromolecules*, vol. 36, no. 26, pp. 9866–9872, 2003.
- [111] J. van der Weerd, K. A. Chan, and S. G. Kazarian, “An innovative design of compaction cell for in situ FT-IR imaging of tablet dissolution,” *Vib. Spectrosc.*, vol. 35, no. 1–2, pp. 9–13, 2004.
- [112] J. van der Weerd and S. G. Kazarian, “Combined approach of FTIR imaging and conventional dissolution tests applied to drug release,” *J. Controlled Release*, vol. 98, no. 2, pp. 295–305, 2004.
- [113] L. K. Prasad and H. Smyth, “3D Printing technologies for drug delivery: a review,” *Drug Dev. Ind. Pharm.*, vol. 42, no. 7, pp. 1019–1031, 2016.
- [114] I. D. Urgan, L. Chiu, and A. Pierce, “Three-dimensional drug printing: a structured review,” *J. Am. Pharm. Assoc.*, vol. 53, no. 2, pp. 136–144, 2013.

- [115] C.-C. Wang *et al.*, "Development of near zero-order release dosage forms using three-dimensional printing (3-DP™) technology," *Drug Dev. Ind. Pharm.*, vol. 32, no. 3, pp. 367–376, 2006.
- [116] M. Saviano, R. P. Aquino, P. Del Gaudio, F. Sansone, and P. Russo, "Poly (vinyl alcohol) 3D printed tablets: The effect of polymer particle size on drug loading and process efficiency," *Int. J. Pharm.*, vol. 561, pp. 1–8, 2019.
- [117] S. S. Crump, *Apparatus and method for creating three-dimensional objects*. Google Patents, 1992.
- [118] D. G. Yu, X. L. Yang, W. D. Huang, J. Liu, Y. G. Wang, and H. Xu, "Tablets with material gradients fabricated by three-dimensional printing," *J. Pharm. Sci.*, vol. 96, no. 9, pp. 2446–2456, 2007.
- [119] J. Jacob, N. Coyle, T. G. West, D. C. Monkhouse, H. L. Surprenant, and N. B. Jain, *Rapid disperse dosage form containing levetiracetam*. Google Patents, 2016.
- [120] D.-G. Yu, C. Branford-White, Z.-H. Ma, L.-M. Zhu, X.-Y. Li, and X.-L. Yang, "Novel drug delivery devices for providing linear release profiles fabricated by 3DP," *Int. J. Pharm.*, vol. 370, no. 1, pp. 160–166, 2009.
- [121] S. A. Khaled, J. C. Burley, M. R. Alexander, and C. J. Roberts, "Desktop 3D printing of controlled release pharmaceutical bilayer tablets," *Int. J. Pharm.*, vol. 461, no. 1–2, pp. 105–111, 2014, doi: 10.1016/j.ijpharm.2013.11.021.
- [122] S. A. Khaled, J. C. Burley, M. R. Alexander, J. Yang, and C. J. Roberts, "3D printing of five-in-one dose combination polypill with defined immediate and sustained release profiles," *J. Controlled Release*, vol. 217, pp. 308–314, 2015, doi: 10.1016/j.jconrel.2015.09.028.
- [123] A. Goyanes, A. B. Buanz, A. W. Basit, and S. Gaisford, "Fused-filament 3D printing (3DP) for fabrication of tablets," *Int. J. Pharm.*, vol. 476, no. 1, pp. 88–92, 2014.
- [124] J. Skowrya, K. Pietrzak, and M. A. Alhnan, "Fabrication of extended-release patient-tailored prednisolone tablets via fused deposition modelling (FDM) 3D printing," *Eur. J. Pharm. Sci.*, vol. 68, pp. 11–17, 2015.
- [125] A. Goyanes, P. R. Martinez, A. Buanz, A. W. Basit, and S. Gaisford, "Effect of geometry on drug release from 3D printed tablets," *Int. J. Pharm.*, vol. 494, no. 2, pp. 657–663, 2015.
- [126] A. Goyanes *et al.*, "3D printing of medicines: engineering novel oral devices with unique design and drug release characteristics," *Mol. Pharm.*, vol. 12, no. 11, pp. 4077–4084, 2015.
- [127] B. C. Gross, J. L. Erkal, S. Y. Lockwood, C. Chen, and D. M. Spence, *Evaluation of 3D printing and its potential impact on biotechnology and the chemical sciences*. ACS Publications, 2014.
- [128] X. Cui, T. Boland, D. D D'Lima, and M. K Lotz, "Thermal inkjet printing in tissue engineering and regenerative medicine," *Recent Pat. Drug Deliv. Formul.*, vol. 6, no. 2, pp. 149–155, 2012.

- [129] C. Schubert, M. C. Van Langeveld, and L. A. Donoso, "Innovations in 3D printing: a 3D overview from optics to organs," *Br. J. Ophthalmol.*, p. bjophthalmol-2013-304446, 2013.
- [130] J. Banks, "Adding value in additive manufacturing: Researchers in the United Kingdom and Europe look to 3D printing for customization," *IEEE Pulse*, vol. 4, no. 6, pp. 22–26, 2013.
- [131] U. K. Roopavath and D. M. Kalaskar, "1 - Introduction to 3D printing in medicine," in *3D Printing in Medicine*, Woodhead Publishing, 2017, pp. 1–20.
- [132] J. Wang, A. Goyanes, S. Gaisford, and A. W. Basit, "Stereolithographic (SLA) 3D printing of oral modified-release dosage forms," *Int. J. Pharm.*, vol. 503, no. 1, pp. 207–212, 2016.
- [133] K. S. Munir, Y. Li, and C. Wen, "1 - Metallic scaffolds manufactured by selective laser melting for biomedical applications," in *Metallic Foam Bone*, Woodhead Publishing, 2017, pp. 1–23.
- [134] G. Ryder, B. Ion, G. Green, D. Harrison, and B. Wood, "Rapid design and manufacture tools in architecture," *Autom. Constr.*, vol. 11, no. 3, pp. 279–290, 2002, doi: 10.1016/S0926-5805(00)00111-4.
- [135] I. T. Ozbolat and M. Hospodiuk, "Current advances and future perspectives in extrusion-based bioprinting," *Biomaterials*, vol. 76, pp. 321–343, 2016, doi: 10.1016/j.biomaterials.2015.10.076.
- [136] X. Wang, M. Jiang, Z. Zhou, J. Gou, and D. Hui, "3D printing of polymer matrix composites: A review and prospective," *Compos. Part B Eng.*, vol. 110, pp. 442–458, Feb. 2017, doi: 10.1016/j.compositesb.2016.11.034.
- [137] G. B. Kim *et al.*, "Three-Dimensional Printing: Basic Principles and Applications in Medicine and Radiology," *Korean J. Radiol.*, vol. 17, no. 2, pp. 182–197, Apr. 2016, doi: 10.3348/kjr.2016.17.2.182.
- [138] J. J. Beaman and C. R. Deckard, *Selective laser sintering with assisted powder handling*. Google Patents, 1990.
- [139] S. Kumar, "Selective laser sintering: a qualitative and objective approach," *JOM J. Miner. Met. Mater. Soc.*, vol. 55, no. 10, pp. 43–47, 2003.
- [140] P. Gu and X. Yan, "Neural network approach to the reconstruction of freeform surfaces for reverse engineering," *Comput.-Aided Des.*, vol. 27, no. 1, pp. 59–64, 1995.
- [141] S. H. Ko, H. Pan, C. P. Grigoropoulos, C. K. Luscombe, J. M. Fréchet, and D. Poulikakos, "All-inkjet-printed flexible electronics fabrication on a polymer substrate by low-temperature high-resolution selective laser sintering of metal nanoparticles," *Nanotechnology*, vol. 18, no. 34, p. 345202, 2007.
- [142] N. Raghunath and P. M. Pandey, "Improving accuracy through shrinkage modelling by using Taguchi method in selective laser sintering," *Int. J. Mach. Tools Manuf.*, vol. 47, no. 6, pp. 985–995, 2007.

- [143] N. Sandler *et al.*, "Inkjet printing of drug substances and use of porous substrates-towards individualized dosing," *J. Pharm. Sci.*, vol. 100, no. 8, pp. 3386–3395, 2011.
- [144] G. D. Martin, S. D. Hoath, and I. M. Hutchings, "Inkjet printing-the physics of manipulating liquid jets and drops," in *Journal of Physics: Conference Series*, 2008, vol. 105, p. 012001.
- [145] J. G. Khinast *et al.*, "Printable medicines: a microdosing device for producing personalized medicines," *Pharm. Technol. Eur.*, vol. 23, no. 1, 2011.
- [146] C. S. Dollery, *Therapeutic drugs*. Churchill Livingstone, 1999.
- [147] D. R. Abernethy and J. B. Schwartz, "Calcium-antagonist drugs," *N. Engl. J. Med.*, vol. 341, no. 19, pp. 1447–1457, 1999.
- [148] E. Blychert, B. Edgar, D. Elmfeldt, and T. Hedner, "A population study of the pharmacokinetics of felodipine.," *Br. J. Clin. Pharmacol.*, vol. 31, no. 1, pp. 15–24, 1991.
- [149] A. C. Moffat, M. D. Osselton, B. Widdop, and J. Watts, *Clarke's analysis of drugs and poisons*, vol. 3. Pharmaceutical press London, 2011.
- [150] S. Budavari, M. J. O'Neil, A. Smith, P. E. Heckelman, and J. F. Kinneary, "The Merck Index; Merck Research Laboratories," *N. J.*, 1996.
- [151] Y. Tian, V. Caron, D. S. Jones, A.-M. Healy, and G. P. Andrews, "Using Flory–Huggins phase diagrams as a pre-formulation tool for the production of amorphous solid dispersions: a comparison between hot-melt extrusion and spray drying," *J. Pharm. Pharmacol.*, vol. 66, no. 2, pp. 256–274, 2014.
- [152] P. G. Bhole and V. R. Patil, "Enhancement of water solubility of felodipine by preparing solid dispersion using poly-ethylene glycol 6000 and poly-vinyl alcohol," *Asian J. Pharm. AJP Free Full Text Artic. Asian J Pharm*, vol. 3, no. 3, 2014.
- [153] O. M. Koo *et al.*, "Investigation into stability of poly (vinyl alcohol)-based Opadry® II films," *AAPS PharmSciTech*, vol. 12, no. 2, pp. 746–754, 2011.
- [154] S. Muppalaneni and H. Omidian, "Polyvinyl alcohol in medicine and pharmacy: a perspective," *J Dev Drugs*, vol. 2, no. 3, pp. 1–5, 2013.
- [155] H. Yu, D. Xia, Q. Zhu, C. Zhu, D. Chen, and Y. Gan, "Supersaturated polymeric micelles for oral cyclosporine A delivery," *Eur. J. Pharm. Biopharm.*, vol. 85, no. 3, pp. 1325–1336, 2013.
- [156] K. M. Huh, S. C. Lee, Y. W. Cho, J. Lee, J. H. Jeong, and K. Park, "Hydrotropic polymer micelle system for delivery of paclitaxel," *J. Controlled Release*, vol. 101, no. 1–3, pp. 59–68, 2005.
- [157] M. Linn *et al.*, "Soluplus® as an effective absorption enhancer of poorly soluble drugs in vitro and in vivo," *Eur. J. Pharm. Sci.*, vol. 45, no. 3, pp. 336–343, 2012.
- [158] J. Djuris, N. Ioannis, S. Ibrić, Z. Djurić, and K. Kachrimanis, "Effect of composition in the development of carbamazepine hot-melt extruded solid dispersions by application of mixture

- experimental design," *J. Pharm. Pharmacol.*, vol. 66, no. 2, pp. 232–243, 2014.
- [159] "Soluplus - For better solubility & bioavailability," *BASF*. <https://pharmaceutical.basf.com/en/Drug-Formulation/Soluplus.html> (accessed Sep. 04, 2019).
- [160] I. Salah, M. A. Shamat, and M. T. Cook, "Soluplus solutions as thermothickening materials for topical drug delivery," *J. Appl. Polym. Sci.*, vol. 136, no. 1, p. 46915, 2019.
- [161] U. Paaver *et al.*, "Soluplus graft copolymer: potential novel carrier polymer in electrospinning of nanofibrous drug delivery systems for wound therapy," *BioMed Res. Int.*, vol. 2014, 2014.
- [162] A. Cossé, C. König, A. Lamprecht, and K. G. Wagner, "Hot melt extrusion for sustained protein release: matrix erosion and in vitro release of PLGA-based implants," *AAPS PharmSciTech*, vol. 18, no. 1, pp. 15–26, 2017.
- [163] S. Qi and D. Q. Craig, "Hot melt extruded transdermal films based on amorphous solid dispersions in Eudragit RS PO: The inclusion of hydrophilic additives to develop moisture-activated release systems," *Int. J. Pharm.*, vol. 514, no. 1, pp. 270–281, 2016.
- [164] I. Ghebre-Selassie, C. E. Martin, F. Zhang, and J. DiNunzio, *Pharmaceutical extrusion technology*. CRC Press, 2018.
- [165] J. W. McGinity, F. Zhang, J. J. Koleng, and M. A. Repka, "Hot-melt extrusion as a pharmaceutical process," *Am. Pharm. Rev.*, vol. 4, pp. 25–37, 2001.
- [166] N. P. Cheremisinoff, *Guidebook to extrusion technology*. Prentice-Hall, 1993.
- [167] M. M. Crowley *et al.*, "Pharmaceutical applications of hot-melt extrusion: part I," *Drug Dev. Ind. Pharm.*, vol. 33, no. 9, pp. 909–926, 2007.
- [168] G. P. Andrews, O. A. AbuDiak, and D. S. Jones, "Physicochemical characterization of hot melt extruded bicalutamide–polyvinylpyrrolidone solid dispersions," *J. Pharm. Sci.*, vol. 99, no. 3, pp. 1322–1335, 2010.
- [169] Y. Song *et al.*, "Physicochemical characterization of felodipine-kollidon VA64 amorphous solid dispersions prepared by hot-melt extrusion," *J. Pharm. Sci.*, vol. 102, no. 6, pp. 1915–1923, 2013.
- [170] S. R. Byrn, G. Zografi, and X. S. Chen, *Solid-state properties of pharmaceutical materials*. John Wiley & Sons, 2017.
- [171] S. S. Afanasyev, T. V. Kychkina, and L. N. Savvinova, "SCANNING ELECTRON MICROSCOPE (ADVANTAGES AND DISADVANTAGES)," 2019.
- [172] E. Verdonck, K. Schaap, and L. C. Thomas, "A discussion of the principles and applications of modulated temperature DSC (MTDSC)," *Int. J. Pharm.*, vol. 192, no. 1, pp. 3–20, 1999.
- [173] D. J. Gardiner, "Introduction to Raman scattering," in *Practical Raman Spectroscopy*, Springer, 1989, pp. 1–12.
- [174] C. V. Raman, "A new radiation," *Indian J. Phys.*, vol. 2, pp. 387–398, 1928.

- [175] D. C. Harris and M. D. Bertolucci, *Symmetry and spectroscopy: an introduction to vibrational and electronic spectroscopy*. Courier Corporation, 1989.
- [176] R. S. Das and Y. K. Agrawal, "Raman spectroscopy: recent advancements, techniques and applications," *Vib. Spectrosc.*, vol. 57, no. 2, pp. 163–176, 2011.
- [177] B. Mercier, T. Castelain, E. Jondeau, and C. Bailly, "Density fluctuations measurement by rayleigh scattering using a single photomultiplier," *AIAA J.*, vol. 56, no. 4, pp. 1310–1316, 2017.
- [178] Z. Xu *et al.*, "Topic review: application of Raman spectroscopy characterization in micro/nano-machining," *Micromachines*, vol. 9, no. 7, p. 361, 2018.
- [179] K. A. Chan and S. G. Kazarian, "FTIR spectroscopic imaging of dissolution of a solid dispersion of nifedipine in poly (ethylene glycol)," *Mol. Pharm.*, vol. 1, no. 4, pp. 331–335, 2004.
- [180] S. Khaled, "Extrusion based 3D printing as a novel technique for fabrication of oral solid dosage forms," PhD Thesis, University of Nottingham, 2016.
- [181] S. E. Glassford, B. Byrne, and S. G. Kazarian, "Recent applications of ATR FTIR spectroscopy and imaging to proteins," *Biochim. Biophys. Acta BBA-Proteins Proteomics*, vol. 1834, no. 12, pp. 2849–2858, 2013.
- [182] S. Thakral, M. W. Terban, N. K. Thakral, and R. Suryanarayanan, "Recent advances in the characterization of amorphous pharmaceuticals by X-ray diffractometry," *Adv. Drug Deliv. Rev.*, vol. 100, pp. 183–193, 2016.
- [183] X. Liu, X. Feng, R. O. Williams, and F. Zhang, "Characterization of amorphous solid dispersions," *J. Pharm. Investig.*, vol. 48, no. 1, pp. 19–41, 2018.
- [184] A. A. Bunaciu, E. G. UdriŞtioiu, and H. Y. Aboul-Enein, "X-ray diffraction: instrumentation and applications," *Crit. Rev. Anal. Chem.*, vol. 45, no. 4, pp. 289–299, 2015.
- [185] C. Telang, S. Mujumdar, and M. Mathew, "Improved physical stability of amorphous state through acid base interactions," *J. Pharm. Sci.*, vol. 98, no. 6, pp. 2149–2159, 2009.
- [186] S. A. Raina, D. E. Alonzo, G. G. Zhang, Y. Gao, and L. S. Taylor, "Impact of polymers on the crystallization and phase transition kinetics of amorphous nifedipine during dissolution in aqueous media," *Mol. Pharm.*, vol. 11, no. 10, pp. 3565–3576, 2014.
- [187] X. Liu, M. Lu, Z. Guo, L. Huang, X. Feng, and C. Wu, "Improving the chemical stability of amorphous solid dispersion with cocrystal technique by hot melt extrusion," *Pharm. Res.*, vol. 29, no. 3, pp. 806–817, 2012.
- [188] T. Cai, L. Zhu, and L. Yu, "Crystallization of organic glasses: effects of polymer additives on bulk and surface crystal growth in amorphous nifedipine," *Pharm. Res.*, vol. 28, no. 10, pp. 2458–2466, 2011.
- [189] W. L. Chiou and S. Riegelman, "Pharmaceutical applications of solid dispersion systems," *J. Pharm. Sci.*, vol. 60, no. 9, pp. 1281–1302, 1971.

- [190] I. Weuts *et al.*, “Physicochemical properties of the amorphous drug, cast films, and spray dried powders to predict formulation probability of success for solid dispersions: etravirine,” *J. Pharm. Sci.*, vol. 100, no. 1, pp. 260–274, 2011.
- [191] L. H. Emara, R. M. Badr, and A. Abd Elbary, “Improving the dissolution and bioavailability of nifedipine using solid dispersions and solubilizers,” *Drug Dev. Ind. Pharm.*, vol. 28, no. 7, pp. 795–807, 2002.
- [192] F. Tanno, Y. Nishiyama, H. Kokubo, and S. Obara, “Evaluation of hypromellose acetate succinate (HPMCAS) as a carrier in solid dispersions,” *Drug Dev. Ind. Pharm.*, vol. 30, no. 1, pp. 9–17, 2004.
- [193] A. Mahieu, J.-F. Willart, E. Dudognon, F. Danède, and M. Descamps, “A new protocol to determine the solubility of drugs into polymer matrixes,” *Mol. Pharm.*, vol. 10, no. 2, pp. 560–566, 2013.
- [194] B. Tian, X. Wang, Y. Zhang, K. Zhang, Y. Zhang, and X. Tang, “Theoretical prediction of a phase diagram for solid dispersions,” *Pharm. Res.*, vol. 32, no. 3, pp. 840–851, 2015.
- [195] A. Paudel, J. Van Humbeeck, and G. Van den Mooter, “Theoretical and experimental investigation on the solid solubility and miscibility of naproxen in poly (vinylpyrrolidone),” *Mol. Pharm.*, vol. 7, no. 4, pp. 1133–1148, 2010.
- [196] D. Lin and Y. Huang, “A thermal analysis method to predict the complete phase diagram of drug–polymer solid dispersions,” *Int. J. Pharm.*, vol. 399, no. 1–2, pp. 109–115, 2010.
- [197] D. Medarević, J. Djuriš, P. Barmpalexis, K. Kachrimanis, and S. Ibrić, “Analytical and computational methods for the estimation of drug-polymer solubility and miscibility in solid dispersions development,” *Pharmaceutics*, vol. 11, no. 8, p. 372, 2019.
- [198] P. J. Flory, *Principles of polymer chemistry*. Cornell University Press, 1953.
- [199] P. J. Marsac, S. L. Shamblin, and L. S. Taylor, “Theoretical and practical approaches for prediction of drug–polymer miscibility and solubility,” *Pharm. Res.*, vol. 23, no. 10, p. 2417, 2006.
- [200] “Polymer Density.”  
<https://polymerdatabase.com/polymer%20physics/Polymer%20Density.html> (accessed Jun. 08, 2020).
- [201] M. Rubinstein and R. H. Colby, *Polymer physics*, vol. 23. Oxford university press New York, 2003.
- [202] M. Yang, P. Wang, and C. Gogos, “Prediction of acetaminophen’s solubility in poly (ethylene oxide) at room temperature using the Flory–Huggins theory,” *Drug Dev. Ind. Pharm.*, vol. 39, no. 1, pp. 102–108, 2013.
- [203] Q. Lu and G. Zografis, “Phase behavior of binary and ternary amorphous mixtures containing indomethacin, citric acid, and PVP,” *Pharm. Res.*, vol. 15, no. 8, pp. 1202–1206, 1998.
- [204] J. E. Patterson, M. B. James, A. H. Forster, and T. Rades, “Melt extrusion and spray drying of carbamazepine and dipyridamole with polyvinylpyrrolidone/vinyl acetate copolymers,” *Drug Dev. Ind. Pharm.*, vol. 34, no. 1, pp. 95–106, 2008.

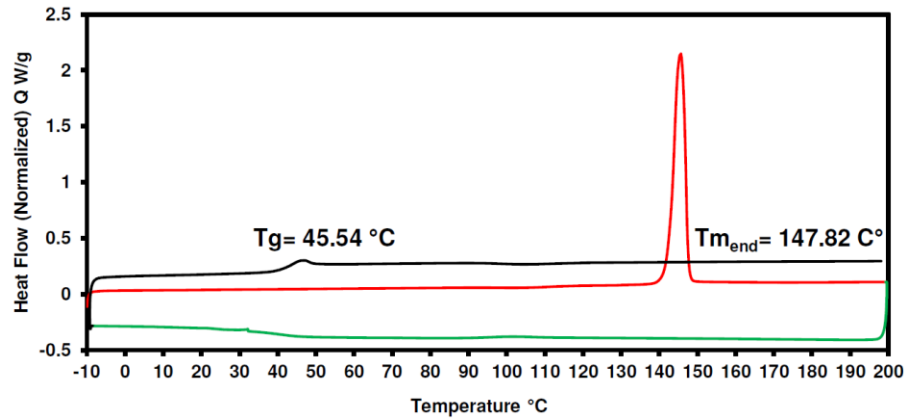
- [205] A. Forster, J. Hempenstall, I. Tucker, and T. Rades, "Selection of excipients for melt extrusion with two poorly water-soluble drugs by solubility parameter calculation and thermal analysis," *Int. J. Pharm.*, vol. 226, no. 1–2, pp. 147–161, 2001.
- [206] D. J. Greenhalgh, A. C. Williams, P. Timmins, and P. York, "Solubility parameters as predictors of miscibility in solid dispersions," *J. Pharm. Sci.*, vol. 88, no. 11, pp. 1182–1190, 1999.
- [207] M. Langer, M. Höltje, N. A. Urbanetz, B. Brandt, H.-D. Höltje, and B. C. Lippold, "Investigations on the predictability of the formation of glassy solid solutions of drugs in sugar alcohols," *Int. J. Pharm.*, vol. 252, no. 1–2, pp. 167–179, 2003.
- [208] "Solubility Parameter."  
<http://polymerdatabase.com/polymer%20physics/delta%20Table.html> (accessed Jul. 31, 2019).
- [209] S. Baghel, H. Cathcart, W. Redington, and N. J. O'Reilly, "An investigation into the crystallization tendency/kinetics of amorphous active pharmaceutical ingredients: A case study with dipyridamole and cinnarizine," *Eur. J. Pharm. Biopharm.*, vol. 104, pp. 59–71, 2016.
- [210] O. A. Abu-Diak, D. S. Jones, and G. P. Andrews, "Understanding the performance of melt-extruded poly (ethylene oxide)–bicalutamide solid dispersions: Characterisation of microstructural properties using thermal, spectroscopic and drug release methods," *J. Pharm. Sci.*, vol. 101, no. 1, pp. 200–213, 2012.
- [211] J. Holländer *et al.*, "Three-dimensional printed PCL-based implantable prototypes of medical devices for controlled drug delivery," *J. Pharm. Sci.*, vol. 105, no. 9, pp. 2665–2676, 2016.
- [212] A. Le Bras, *3D printing of personalized implants for left atrial appendage occlusion*. Nature Publishing Group 75 VARICK ST, 9TH FLR, NEW YORK, NY 10013-1917 USA, 2018.
- [213] J. Londono, M. Tadros, M. Salgueiro, and P. S. Baker, "Digital design and 3D printing of an implant-supported prosthetic stent for protecting complete arch soft tissue grafts around dental implants: A dental technique," *J. Prosthet. Dent.*, vol. 120, no. 6, pp. 801–804, 2018.
- [214] Z. Muwaffak, A. Goyanes, V. Clark, A. W. Basit, S. T. Hilton, and S. Gaisford, "Patient-specific 3D scanned and 3D printed antimicrobial polycaprolactone wound dressings," *Int. J. Pharm.*, vol. 527, no. 1–2, pp. 161–170, 2017.
- [215] A. Melocchi *et al.*, "Industrial development of a 3D-printed nutraceutical delivery platform in the form of a multicompartiment HPC capsule," *AAPS PharmSciTech*, vol. 19, no. 8, pp. 3343–3354, 2018.
- [216] M. Sadia, B. Arafat, W. Ahmed, R. T. Forbes, and M. A. Alhnan, "Channelled tablets: An innovative approach to accelerating drug release from 3D printed tablets," *J. Controlled Release*, vol. 269, pp. 355–363, 2018.
- [217] A. Goyanes *et al.*, "Fabrication of controlled-release budesonide tablets via desktop (FDM) 3D printing," *Int. J. Pharm.*, vol. 496, no. 2, pp. 414–420, 2015.

- [218] D. K. Tan, M. Maniruzzaman, and A. Nokhodchi, "Advanced pharmaceutical applications of hot-melt extrusion coupled with fused deposition modelling (FDM) 3D printing for personalised drug delivery," *Pharmaceutics*, vol. 10, no. 4, p. 203, 2018.
- [219] A. Goyanes *et al.*, "3D printing of medicines: engineering novel oral devices with unique design and drug release characteristics," *Mol. Pharm.*, vol. 12, no. 11, pp. 4077–4084, 2015.
- [220] A. Liu *et al.*, "3D printing surgical implants at the clinic: a experimental study on anterior cruciate ligament reconstruction," *Sci. Rep.*, vol. 6, no. 1, pp. 1–13, 2016.
- [221] K. Tappa *et al.*, "3D printing custom bioactive and absorbable surgical screws, pins, and bone plates for localized drug delivery," *J. Funct. Biomater.*, vol. 10, no. 2, p. 17, 2019.
- [222] S. N. Cassu and M. I. Felisberti, "Poly (vinyl alcohol) and poly (vinyl pyrrolidone) blends: miscibility, microheterogeneity and free volume change," *Polymer*, vol. 38, no. 15, pp. 3907–3911, 1997.
- [223] N. JAMIL, H. HUSIN, A. W. ALFIDA, Z. AMAN, and Z. HASSAN, "Characterization and Preparation of Polyvinyl Alcohol (PVA) as Inhibitor in Formation of Hydrates," *AMCT 2017 Malaysisa*, p. 578.
- [224] B. Shah, V. K. Kakumanu, and A. K. Bansal, "Analytical techniques for quantification of amorphous/crystalline phases in pharmaceutical solids," *J. Pharm. Sci.*, vol. 95, no. 8, pp. 1641–1665, 2006.
- [225] J. F. Young, "Humidity control in the laboratory using salt solutions—a review," *J. Appl. Chem.*, vol. 17, no. 9, pp. 241–245, 1967.
- [226] S. Al-Dulaimi, A. Aina, and J. Burley, "Rapid polymorph screening on milligram quantities of pharmaceutical material using phonon-mode Raman spectroscopy," *CrystEngComm*, vol. 12, no. 4, pp. 1038–1040, 2010.
- [227] A. Alkhalil, J. B. Nanubolu, and J. C. Burley, "Analysis of phase transitions in molecular solids: quantitative assessment of phonon-mode vs intra-molecular spectral data," *RSC Adv.*, vol. 2, no. 1, pp. 209–216, 2012.
- [228] H. Konno and L. S. Taylor, "Ability of different polymers to inhibit the crystallization of amorphous felodipine in the presence of moisture," *Pharm. Res.*, vol. 25, no. 4, pp. 969–978, 2008.
- [229] M. A. Kalam *et al.*, "Release kinetics of modified pharmaceutical dosage forms: a review," *Cont J Pharm Sci*, vol. 1, no. 1, pp. 30–5, 2007.
- [230] C. G. Varelas, D. G. Dixon, and C. A. Steiner, "Zero-order release from biphasic polymer hydrogels," *J. Controlled Release*, vol. 34, no. 3, pp. 185–192, 1995.
- [231] Y.-N. Zhao *et al.*, "A drug carrier for sustained zero-order release of peptide therapeutics," *Sci. Rep.*, vol. 7, no. 1, pp. 1–9, 2017.
- [232] D. W. Bourne, "Pharmacokinetics In: Modern pharmaceuticals; Banker, GS, Rhodes, CT, Eds," *Marcel Dekker Inc N. Y.*, 2002.
- [233] B. Narsimhan, S. K. Mallapragada, and N. A. Peppas, *Release Kinetics, Data Interpretation, Encyclopedia of Controlled Drug Delivery*, E. Mathiowitz. John Wiley & Sons, 1999.

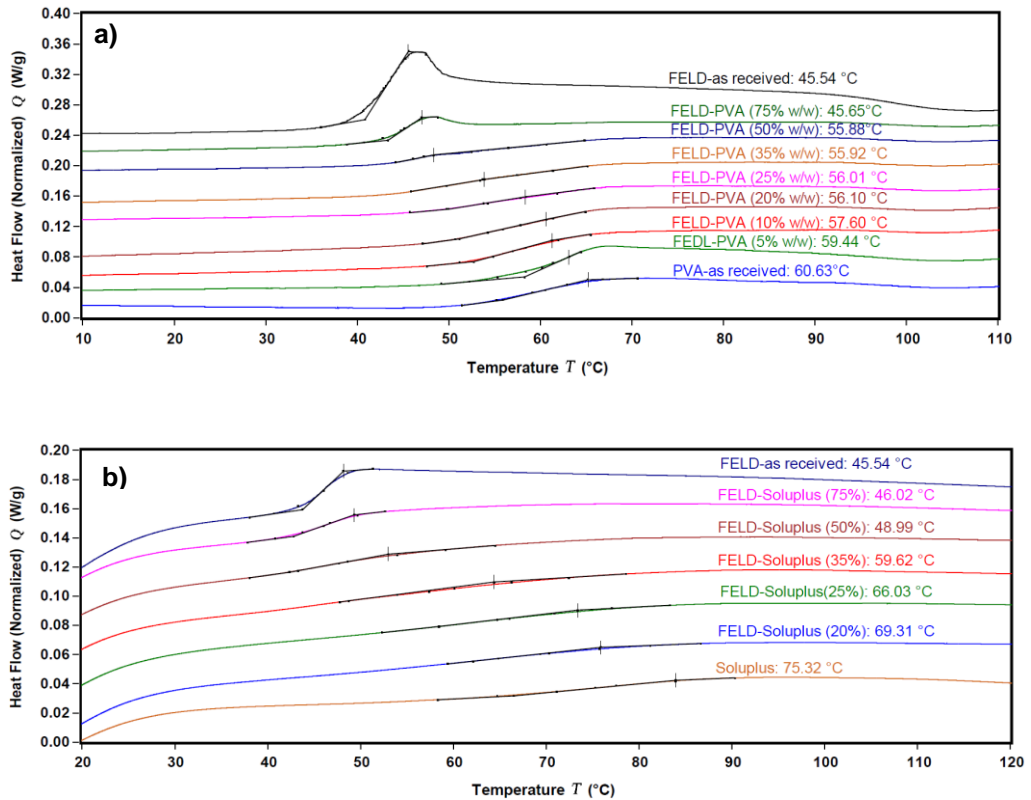
- [234] S. A. Bravo, M. C. Lamas, and C. J. Salomón, "In-vitro studies of diclofenac sodium controlled-release from biopolymeric hydrophilic matrices," *J Pharm Pharm Sci*, vol. 5, no. 3, pp. 213–219, 2002.
- [235] T. Higuchi, "Mechanism of sustained-action medication. Theoretical analysis of rate of release of solid drugs dispersed in solid matrices," *J. Pharm. Sci.*, vol. 52, no. 12, pp. 1145–1149, 1963.
- [236] J. Siepmann and N. A. Peppas, "Higuchi equation: derivation, applications, use and misuse," *Int. J. Pharm.*, vol. 418, no. 1, pp. 6–12, 2011.
- [237] R. W. Korsmeyer, R. Gurny, E. Doelker, P. Buri, and N. A. Peppas, "Mechanisms of solute release from porous hydrophilic polymers," *Int. J. Pharm.*, vol. 15, no. 1, pp. 25–35, 1983.
- [238] Y. Gao *et al.*, "In vitro release kinetics of antituberculosis drugs from nanoparticles assessed using a modified dissolution apparatus," *BioMed Res. Int.*, vol. 2013, 2013.
- [239] T. Feng, R. Pinal, and M. T. Carvajal, "Process induced disorder in crystalline materials: differentiating defective crystals from the amorphous form of griseofulvin," *J. Pharm. Sci.*, vol. 97, no. 8, pp. 3207–3221, 2008.
- [240] G. Van den Mooter *et al.*, "Physical stabilisation of amorphous ketoconazole in solid dispersions with polyvinylpyrrolidone K25," *Eur. J. Pharm. Sci.*, vol. 12, no. 3, pp. 261–269, Jan. 2001, doi: 10.1016/S0928-0987(00)00173-1.
- [241] "USP Monographs: Felodipine Extended-Release Tablets." [http://www.pharmacopeia.cn/v29240/usp29nf24s0\\_m32660.html](http://www.pharmacopeia.cn/v29240/usp29nf24s0_m32660.html) (accessed Oct. 06, 2020).
- [242] A. Goyanes, F. Fina, A. Martorana, D. Sedough, S. Gaisford, and A. W. Basit, "Development of modified release 3D printed tablets (printlets) with pharmaceutical excipients using additive manufacturing," *Int. J. Pharm.*, 2017.
- [243] D. Markl *et al.*, "Analysis of 3D Prints by X-ray Computed Microtomography and Terahertz Pulsed Imaging," *Pharm. Res.*, vol. 34, no. 5, pp. 1037–1052, May 2017, doi: 10.1007/s11095-016-2083-1.
- [244] J. S. LaFontaine, L. K. Prasad, C. Brough, D. A. Miller, J. W. McGinity, and R. O. Williams, "Thermal Processing of PVP- and HPMC-Based Amorphous Solid Dispersions," *AAPS PharmSciTech*, vol. 17, no. 1, pp. 120–132, Feb. 2016, doi: 10.1208/s12249-015-0417-7.
- [245] "Felodipine." <https://www.drugbank.ca/drugs/DB01023> (accessed Apr. 04, 2019).
- [246] K. Deshmukh *et al.*, "Influence of K<sub>2</sub>CrO<sub>4</sub> doping on the structural, optical and dielectric properties of polyvinyl alcohol/K<sub>2</sub>CrO<sub>4</sub> composite films," *Polym.-Plast. Technol. Eng.*, vol. 55, no. 3, pp. 231–241, 2016.
- [247] M. Mosharraf and C. Nyström, "The effect of dry mixing on the apparent solubility of hydrophobic, sparingly soluble drugs," *Eur. J. Pharm. Sci.*, vol. 9, no. 2, pp. 145–156, 1999.

- [248] A. M. Atta, N. E. Maysour, and K. F. Arndt, "Swelling characteristics of pH-and thermo-sensitive crosslinked poly (vinyl alcohol) grafts," *J. Polym. Res.*, vol. 13, no. 1, pp. 53–63, 2006.
- [249] S. Jiang, S. Liu, and W. Feng, "PVA hydrogel properties for biomedical application," *J. Mech. Behav. Biomed. Mater.*, vol. 4, no. 7, pp. 1228–1233, 2011.
- [250] P. Colombo, R. Bettini, P. Santi, and N. A. Peppas, "Swellable matrices for controlled drug delivery: gel-layer behaviour, mechanisms and optimal performance," *Pharm. Sci. Technol. Today*, vol. 3, no. 6, pp. 198–204, 2000.

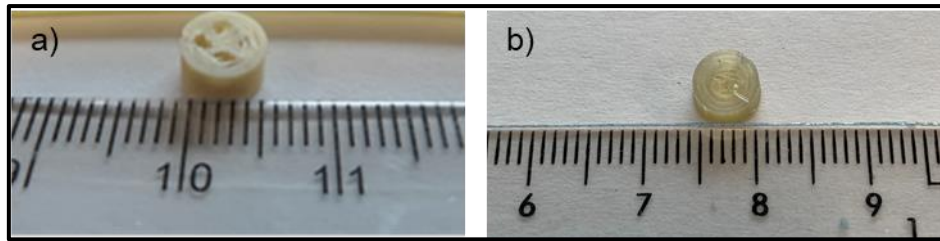
## 8. Appendix



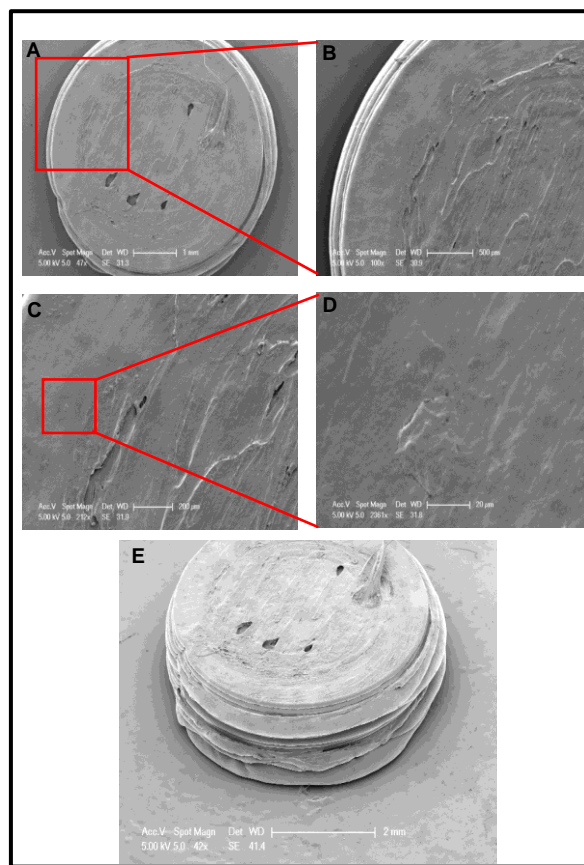
**Figure 1.** DSC thermogram of the crystalline FELD. 1<sup>st</sup> heating (red), cooling cycle (green), and 2<sup>nd</sup> heating (black).



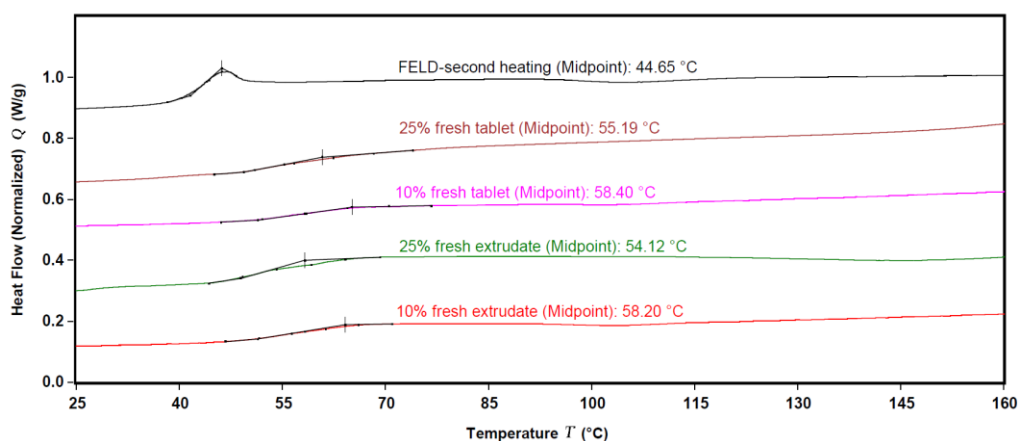
**Figure 2.**  $T_g$  regions of a) FELD-PVA system, from top to bottom (crystalline FELD, 75%, 50%, 35%, 25%, 20%, 10%, 5% FELD-PVA w/w %, and PVA), and b) FELD-Soluplus system, from top to bottom (crystalline FELD, 75%, 50%, 35%, 25%, and 20% FELD-Soluplus w/w %, and Soluplus).



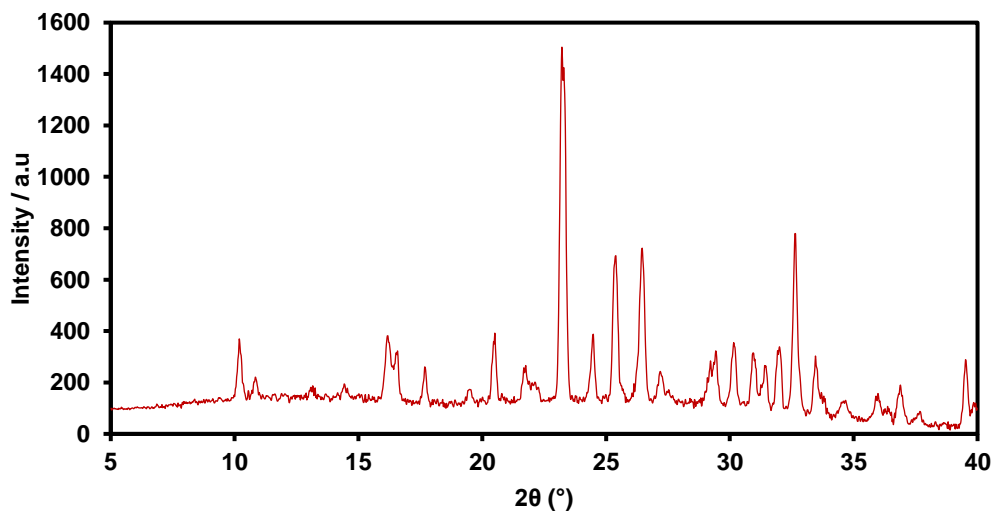
**Figure 3.** Photographic images of a) pre-optimised, and b) post-optimised FELD-PVA model tablet fabricated using FDM 3D printer.



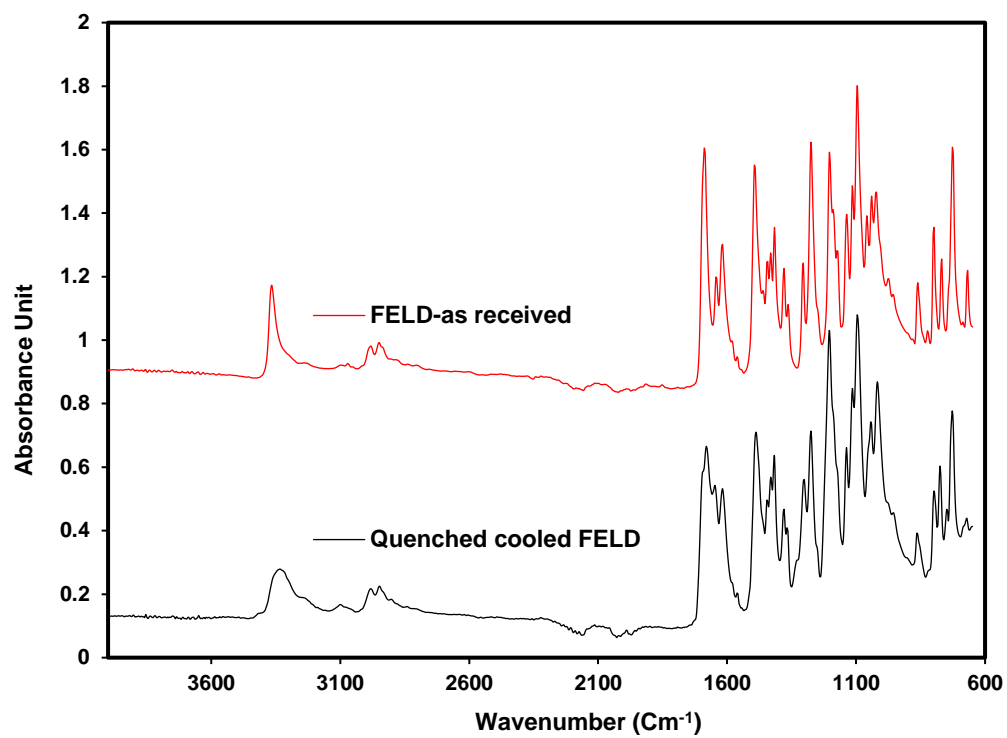
**Figure 4.** SEM images of the fabricated FELD-PVA tablet (10% w/w) utilising FDM 3D printer.



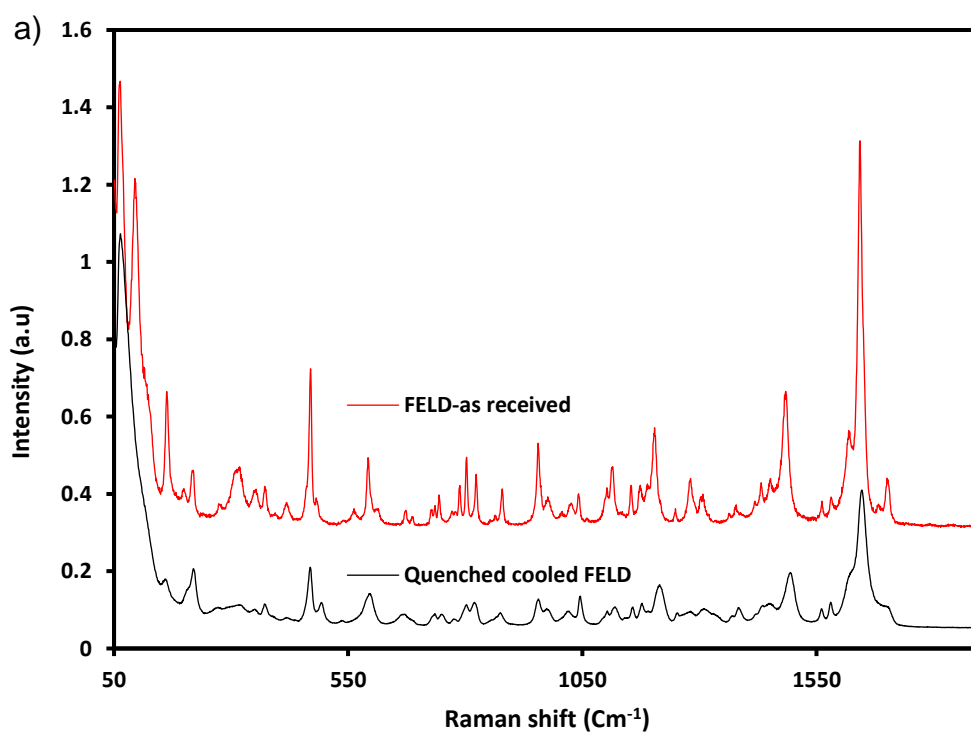
**Figure 5.** DSC thermograms of the  $T_g$  regions of 2<sup>nd</sup> heating of FELD (black), heating of 25% tablet (brown), heating of 10% tablet (pink), heating of 25% filament (green), heating of 10% filament (red). (Endotherm upward in the thermogram).



**Figure 6.** PXRD patterns of crystalline FELD.



**Figure 7.** FTIR spectra of crystalline FELD and quenched cooled FELD.



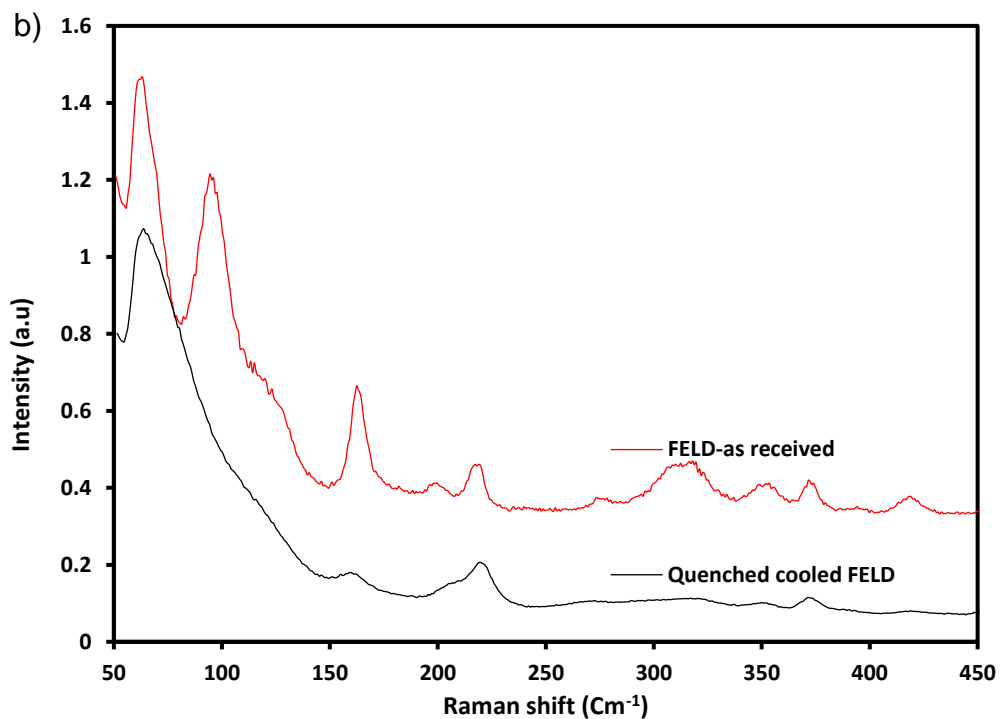


**Figure 8.** Raman spectra of crystalline FELD and quenched cooled FELD in a) molecular region, and b) phonon mode.

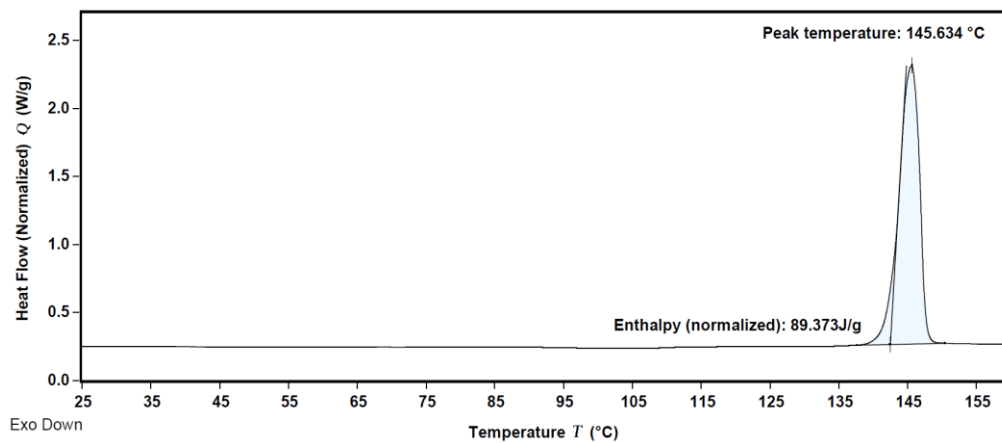


**Figure 9.** DSC thermogram of the crystalline FELD.

**Table 1.** Estimation of the aged tablet crystallinity calculated from the DSC data of 25% (w/w FELD-PVA) 3D printed model tablets after seven days in 75% RH media (n=3).

$\Delta H_f$ J/g of the FELD in the aged samples	$\Delta H_c$ J/g	$\Delta H_f^{cryst}$ (pure FELD) J/g	% crystallinity
2.61	0	89.37	2.92
2.46	0	89.37	2.75
4.93	0	89.37	5.52
<b>Average</b>			<b>3.73</b>
<b>STDEV</b>			<b>1.55</b>

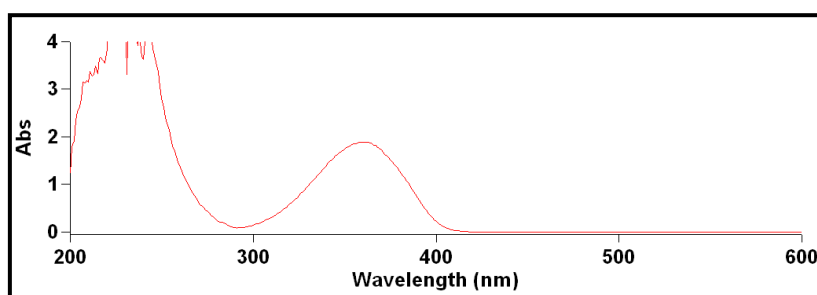


**Figure 10.** FELD absorbance wavelength determined using UV-vis spectrophotometer.

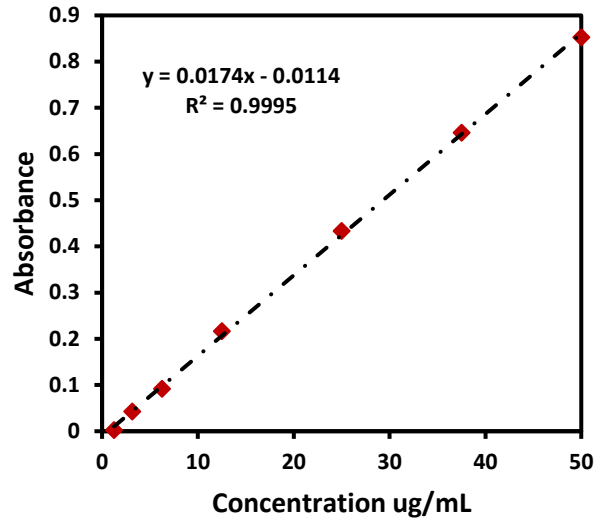


**Figure 11.** FELD calibration curve.



**Figure 12.** Photographic image of fabricated formulation after 10 hours in pH2 dissolution medium.

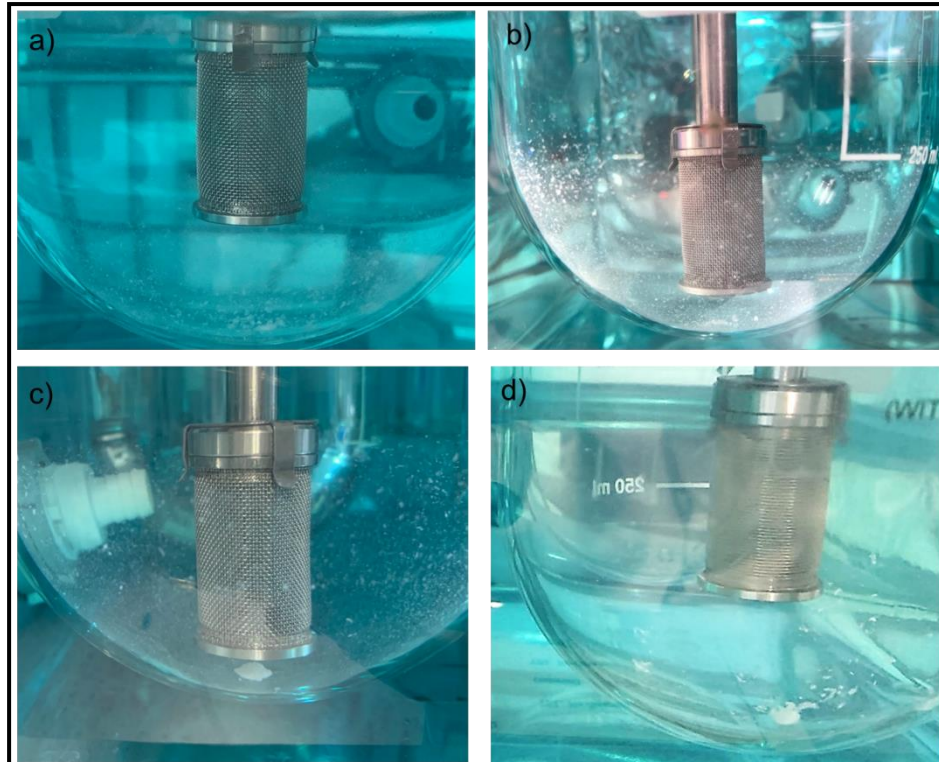


**Figure 13.** Photographic images of the utilised model tablets after 10 hours in pH6.8 dissolution medium: a) fresh control, b) fresh shell-aged core, c) aged control, and d) aged shell-fresh core.